frontiers | Research Topics

The role of metabolism and endocrinology in eye diseases

Edited by
Lvzhen Huang, Lian Zhao and Jing Li

Published in
Frontiers in Endocrinology

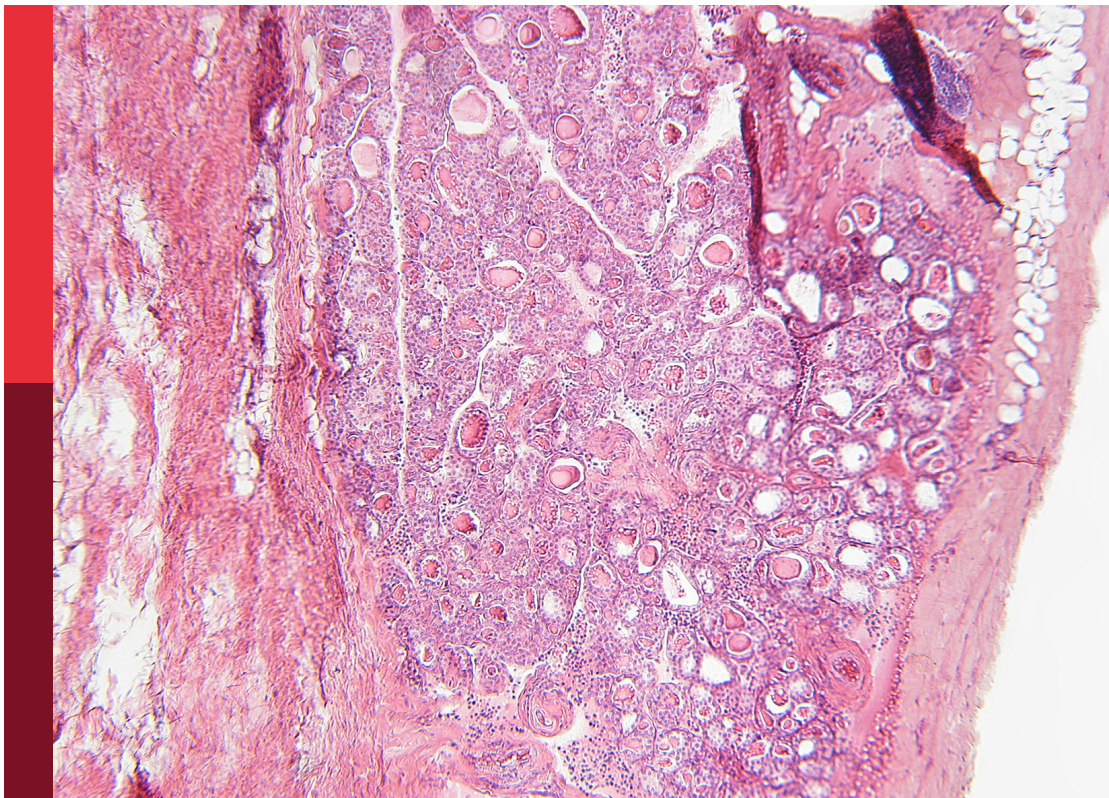

ISSN 1664-8714
ISBN 978-2-83251-085-8
DOI 10.3389/978-2-83251-085-8

About Frontiers

Frontiers is more than just an open access publisher of scholarly articles: it is a pioneering approach to the world of academia, radically improving the way scholarly research is managed. The grand vision of Frontiers is a world where all people have an equal opportunity to seek, share and generate knowledge. Frontiers provides immediate and permanent online open access to all its publications, but this alone is not enough to realize our grand goals.

Frontiers journal series

The Frontiers journal series is a multi-tier and interdisciplinary set of open-access, online journals, promising a paradigm shift from the current review, selection and dissemination processes in academic publishing. All Frontiers journals are driven by researchers for researchers; therefore, they constitute a service to the scholarly community. At the same time, the *Frontiers journal series* operates on a revolutionary invention, the tiered publishing system, initially addressing specific communities of scholars, and gradually climbing up to broader public understanding, thus serving the interests of the lay society, too.

Dedication to quality

Each Frontiers article is a landmark of the highest quality, thanks to genuinely collaborative interactions between authors and review editors, who include some of the world's best academicians. Research must be certified by peers before entering a stream of knowledge that may eventually reach the public - and shape society; therefore, Frontiers only applies the most rigorous and unbiased reviews. Frontiers revolutionizes research publishing by freely delivering the most outstanding research, evaluated with no bias from both the academic and social point of view. By applying the most advanced information technologies, Frontiers is catapulting scholarly publishing into a new generation.

What are Frontiers Research Topics?

Frontiers Research Topics are very popular trademarks of the *Frontiers journals series*: they are collections of at least ten articles, all centered on a particular subject. With their unique mix of varied contributions from Original Research to Review Articles, Frontiers Research Topics unify the most influential researchers, the latest key findings and historical advances in a hot research area.

Find out more on how to host your own Frontiers Research Topic or contribute to one as an author by contacting the Frontiers editorial office: frontiersin.org/about/contact

The role of metabolism and endocrinology in eye diseases

Topic editors

Lvzhen Huang — Peking University People's Hospital, China
Lian Zhao — National Eye Institute (NIH), United States
Jing Li — Capital Normal University, China

Citation

Huang, L., Zhao, L., Li, J., eds. (2023). *The role of metabolism and endocrinology in eye diseases*. Lausanne: Frontiers Media SA. doi: 10.3389/978-2-83251-085-8

Table of contents

frontiers in Endocrinology

ORIGINAL RESEARCH
published: 17 March 2022
doi: 10.3389/fendo.2022.861757

The Changes of Irisin and Inflammatory Cytokines in the Age-Related Macular Degeneration and Retinal Vein Occlusion

Xiaochun Li[1,2†], *Xiaoguang Cao*[1†], *Mingwei Zhao*[1] *and Yongzhen Bao*[1*]

[1] Department of Ophthalmology, Peking University People's Hospital; Eye Diseases and Optometry Institute; Beijing Key Laboratory of Diagnosis and Therapy of Retinal and Choroid Diseases; College of Optometry, Peking University Health Science Center, Beijing, China, [2] Department of Ophthalmology, Peking University International Hospital, Beijing, China

OPEN ACCESS

Edited by:
Lian Zhao,
National Eye Institute (NIH),
United States

Reviewed by:
Qin Long,
Peking Union Medical College Hospital (CAMS), China
Xu Hou,
Fourth Military Medical University, China
Xiaoyong Chen,
Peking University Third Hospital, China

***Correspondence:**
Yongzhen Bao
drbaoyz@sina.com

[†]These authors have contributed equally to this work and share first authorship

Specialty section:
This article was submitted to Molecular and Structural Endocrinology, a section of the journal Frontiers in Endocrinology

Received: 25 January 2022
Accepted: 08 February 2022
Published: 17 March 2022

Citation:
Li X, Cao X, Zhao M and Bao Y (2022) The Changes of Irisin and Inflammatory Cytokines in the Age-Related Macular Degeneration and Retinal Vein Occlusion. Front. Endocrinol. 13:861757. doi: 10.3389/fendo.2022.861757

Purpose: Age-related macular degeneration (AMD) and retinal vein occlusion (RVO) are irreversible chorioretinal diseases, which might induce severe damage in visual function. The metabolic factor and inflammatory factors might play important roles in the pathogenesis of AMD and RVO. The levels of irisin and 14 cytokines were analyzed in aqueous humor of AMD and RVO eyes to evaluate the roles of irisin and inflammatory factors.

Methods: We collected aqueous humor samples from patients with AMD (n = 27), RVO (n = 30), and cataract (as control, n = 23) eyes. Samples were assayed using ELISA kit for irisin and a multiplex immunoassay kit for 14 cytokines. The macular thickness (MT) was measured with OCT in all included eyes.

Results: MT in the RVO group is significantly higher than that in the AMD or control group. Irisin levels in the aqueous samples of AMD and RVO eyes were both significantly lower than that in the control. Furthermore, a positive correlation was found between irisin and MT in the RVO. Compared with the controls, AMD eyes had significantly higher levels of BDNF, VEGF-A, VEGF-R1, VEGF-R2, IL-10, TNF-α, VCAM-1, IP-10, and MCP-1. Similarly, RVO eyes had significantly higher levels of BDNF, VEGF-A, VEGF-R1, VEGF-R2, IL-6, IL-8, IL-10, TNF-α, ICAM-1, VCAM-1, IP-10, and MCP-1. However, there was no significant difference between the levels of PDGF-BB or TNF-β in these three groups. A negative correlation was found between VEGF-A and MT in AMD, as well as in control. Furthermore, a positive correlation was found between IL-6 and MT in the 80 included eyes, as well as in RVO. A positive correlation was found between ICAM-1 and MT in the 80 included eyes, as well as in RVO.

Conclusions: The metabolic factor, irisin levels in the aqueous humor are decreased in AMD and RVO eyes and show a positive correlation between irisin and MT in RVO eyes, prompting researchers to explore the relationship between irisin and macular edema. We

also identified the higher expression of vascular growth factors (VEGF-A, VEGF-R1, and PDGF-BB), inflammatory cytokines (IL-6, IL-8, IL-10, and TNF-α), and chemokines (ICAM-1, VCAM-1, IP-10, and MCP-1) in AMD and RVO eyes.

Keywords: irisin, age-related macular degeneration (AMD), retinal vein occlusion (RVO), macular thickness, inflammatory factor

INTRODUCTION

In human sensory organs, the eye is the primary means to obtain information. With the development of technology, many parts of human eyes, such as the cornea and lens, have artificial substitutes, but there is no substitute for the retina. The retina is a nerve tissue that is responsible for converting light signals into nerve signals, which are then transmitted to the visual center of the brain by the optic nerve (1). Various retinal diseases may seriously damage visual function and even lead to blindness (2).

With the process of aging society, age-related macular degeneration (AMD) has become one of the leading causes for inevitable blindness in China and worldwide, as an estimated 288 million people worldwide will suffer from AMD by 2040 (3, 4). The etiology of AMD is complex and several possible risk factors for the development of AMD had been reported, the major one being aging, and others such as oxidative stress and inflammatory damage. Moreover, the association between AMD and some systemic disorders has also been reported. Previous studies have shown a significant link between AMD occurrence and diabetes, obesity, high body mass index, hypertension, coronary heart disease, dyslipidemia, chronic kidney disease, and Alzheimer's disease (5–7).

Retinal vein occlusion (RVO) is caused by retinal vein thrombosis and affects 16 million people worldwide. It is the second most common retinal disease after diabetic retinopathy and may be related to severe consequences such as neurovascular glaucoma, retinal detachment, and eventual blindness (8). As categorized according to the site of vascular occlusion, RVO includes branch RVO (BRVO), central RVO (CRVO), and hemi-RVO (9). As the occurrence of hemorrhages and macular edema (ME), RVO could lend to significant visual impairment (10). Several common cardiovascular risk factors, such as hypertension, diabetes, and hyperlipemia, were reported to be predisposing factors for RVO and to enhance the risk of RVO recurrence (11, 12).

Irisin is a cleavage product of fibronectin type III domain-containing protein 5 (FNDC5) and can act on white adipocytes and induce them to transform into brown adipocytes. Irisin exists in various organs, including brain, heart, liver, and skeletal muscle and was reported to control glucose metabolism, lipid metabolism and energy homeostasis in skeletal muscle and adipose tissue (13–16). In addition, a recent study showed that irisin had anti-inflammatory, antioxidant, and anti-apoptotic effects (17). Irisin could cross the blood–brain barrier, and its expression had been found in some sites of the central nervous system (CNS) (18, 19). Previous studies had shown that irisin could enhance the expression of brain-derived neurotrophic factor (BDNF) in various brain regions with subsequent beneficial effects on brain health and cognitive function (20, 21).

One previous study reported that irisin could be detected in the retinae and other studies reported the level of irisin in the aqueous humor of cataract with/without pseudoexfoliation, and high myopia (22–25). Moreover, the concentration of serum irisin was lower in those patients with type 2 diabetes mellitus, and was associated with the presence of diabetic nephropathy and diabetic retinopathy (26). The goals of our study are to identify the expression of irisin in AMD and RVO and to explore its role and potential application in those ocular diseases. On the other hand, previous studies have reported the association of AMD and RVO with inflammatory stress; the relationship of irisin and inflammatory cytokines is also explored.

METHODS

Study Design

Twenty-seven eyes from 27 patients with AMD, thirty eyes from 30 patients with RVO, and twenty-three eyes from 23 patients with cataract were studied from December 2020 to September 2021, and comprise the AMD group, RVO group, and control group, respectively. All included AMD and RVO eyes were planned to have an uneventful intra-vitreal anti-VEGF therapy. The inclusion criterion for those patients with AMD was diagnosed with AMD, exclusive of any other retinal disorder. The inclusion criterion for those patients with RVO was diagnosed with RVO, exclusive of any other retinal disorder. The inclusion criterion for those patients with cataract was an uneventful cataract surgery. Eyes with glaucoma, uveitis, zonular weakness, previous trauma, previous intraocular surgery, or fundus pathology were excluded from the study. Patients with diabetes mellitus were excluded. The study was approved by the Human Research Ethics Committee of Peking University People's Hospital and Peking University International Hospital, and adhered to the guidelines of the Declaration of Helsinki. Written informed consent was obtained from all included patients.

Sample Collection

We administered Oxybuprocaine Hydrochloride Eye Drop (Santen Pharmaceutical Co., Ltd., Osaka, Japan) to the patients 4 times every 5 min before the surgery as the local anesthesia. Eyelids and the surrounding skin were swabbed with povidone iodine. Samples of aqueous humor (90–120 μl) were aspirated by inserting a 29-gauge needle through the corneal paracentesis into

the anterior chamber before surgery. Samples were immediately stored at −80°C until sample analysis.

Irisin Analysis

Samples were harvested and assayed using the enzyme-linked immunosorbent assay (ELISA) kit for irisin (Irisin ELISA Kit; Beijing Dongge Boye Biotechnology Co. Ltd., Beijing, China) and were measured according to the manufacturer's instructions. The stop solution changes the color from blue to yellow and the intensity of the color is measured at 450 nm using a spectrophotometer. In order to measure the concentration of irisin in the sample, the Irisin ELISA Kit includes a set of calibration standards. The calibration standards are assayed at the same time as the samples and allow the operator to produce a standard curve of optical density (OD) compared to irisin concentration. The concentration of irisin in the samples is then determined by comparing the OD of the samples to the standard curve.

Cytokine Analysis

We simultaneously analyzed a selection of 14 cytokines, namely BDNF, intercellular cell adhesion molecule-1 (ICAM-1), interleukin (IL)-10, IL-8, IL-6, inducible protein-10 (IP-10), monocyte chemoattractant protein-1 (MCP-1), platelet-derived growth factor BB (PDGF-BB), tumor necrosis factor α (TNF-α) and β (TNF-β), vascular cell adhesion molecule-1 (VCAM-1), vascular endothelial growth factor (VEGF), and vascular endothelial growth factor receptor 1 (VEGF-R1) and 2 (VEGF-R2). Cytokine concentrations were quantified in duplicate using a magnetic bead 14-plex panel assay (Human ProcartaPlex Mix&Match 14-plex, PPX-14-MX9HJ62; Thermo Fisher Scientific, Waltham, USA) performed according to the manufacturer's recommended protocol and read using a Bio-Plex 200 array reader (Bio-Rad, Hercules, California, USA). The standard curve was based on five-parameter nonlinear regression. Each cytokine concentration was then calculated by the curve.

Measurement of Macular Thickness

All included eyes were measured using a spectral-domain OCT (3D OCT-1, Topcon, Tokyo, Japan) without dilating the pupil. The macula full retinal thickness was defined as the distance between the inner limiting membrane and the outer segments/retinal pigment epithelium junction boundary. It was divided into nine quadrants based on the ETDRS (Early Treatment Diabetic Retinopathy Study) map. The value of average thickness read from the OCT report was set as the macular thickness (MT).

Statistical Analysis

The data were processed and statistically analyzed using IBM SPSS Statistics for Windows, v. 20.0 (IBM Corp., Armonk, USA). All data are presented as means ± standard deviations (SD). Categorical data were compared between groups using χ^2 test. Student's *t*-test and Mann–Whitney *U* test were used to detect differences between AMD, RVO, and control groups. Pearson's correlation analysis was adopted to analyze the relationships among the cytokines and MT in our study. Values of $p < 0.05$ were considered statistically significant.

RESULTS

Baseline Characteristics of the Participants

The distributions of age, gender, and eye are summarized in **Table 1**. All included AMD eyes were wet-AMD. The included 30 RVO eyes had 13 eyes with BRVO and 17 eyes with CRVO. There was a significant difference in age and no significant difference in gender or eye in the three groups.

Macular Thickness Measurement

The measurement of MT is shown in **Table 1**. MT in the RVO groups is higher than that in the AMD group ($t = -5.016$, $p = 0.000$) or the control group, significantly ($t = 5.75$, $p = 0.000$). There is no significant difference in MTs between the AMD and control groups.

Irisin Levels in the Aqueous Humor of the Study Eyes

The irisin levels in the aqueous samples of AMD, RVO, and control groups are shown in **Table 2**. Student's *t*-test revealed that irisin level in the aqueous samples of the AMD group was significantly lower than that of the control group ($t = -3.357$, $p = 0.002$). The irisin level of RVO group was similarly lower than that of the control group ($t = -3.221$, $p = 0.002$). Those of the AMD and RVO groups have no significant difference ($t = 0.243$,

TABLE 1 | Baseline characteristics of the patients in respective groups.

Group (n = 80)	Age (years)	Gender	Eye	Macular thickness (MT) (um)
AMD (n = 27)	71.07 ± 8.77	Male (n = 19) 70.37% Female (n = 8) 29.63%	Right eye (n = 12) 44.44% Left eye (n = 15) 55.56%	275.20 ± 27.83
RVO (n = 30)	59.40 ± 14.52$	Male (n = 18) 60.00% Female (n = 12) 40.00%	Right eye (n = 12) 40.00% Left eye (n = 18) 60.00%	359.61 ± 87.39$
Control (n = 23)	71.78 ± 13.27	Male (n = 13) 56.52% Female (n = 10) 43.48%	Right eye (n = 15) 65.22% Left eye (n = 8) 34.78%	265.66 ± 16.89
p-value	0.000	0.07	0.293	0.000

The difference in age and macular thickness (MT) between the three groups was tested using one-way ANOVA. The difference in age and MT between AMD and control groups, and that between the RVO and control group were tested using independent Student's t-test, and $ p < 0.05. The difference in gender and eye distribution between the three groups was tested using χ^2 test.

TABLE 2 | The levels of irisin, BDNF, VEGF-A, VEGF-R1, VEGF-R2, and PDGF-BB in the aqueous humor.

Group (n = 80)	Irisin	BDNF	VEGF-A	VEGF-R1	VEGF-R2	PDGF-BB
AMD (n = 27)	64.81 ± 24.40	1.26 ± 0.72	7,094.78 ± 5,961.80	4,650.89 ± 6,590.30	863.68 ± 428.65	6.10 ± 22.21
RVO (n = 30)	63.00 ± 30.92	0.97 ± 0.39	11,291.77 ± 14,146.21	1,732.77 ± 3,109.11$^{\#}$	1,023.11 ± 511.22	3.14 ± 12.13
Control (n = 23)	88.92 ± 26.34$^{*\$}$	0.67 ± 0.19$^{*\$}$	2,518.33 ± 2,098.66$^{*\$}$	435.28 ± 336.12$^{*\$}$	633.96 ± 327.34$^{*\$}$	1.24 ± 4.70

Brain-derived neurotrophic factor (BDNF), Vascular endothelial growth factor (VEGF), Vascular endothelial growth factor receptor 1 (VEGF-R1) and 2 (VEGF-R2), Platelet derived growth factor BB (PDGF-BB). Data are expressed as the means ± standard deviations (SD), in pg/ml. The differences in cytokines between the 2 groups were tested using Student's t-test. $^{*}p < 0.05$ between the AMD and control group; $^{\$}p < 0.05$ between the RVO and control group; $^{\#}p < 0.05$ between the AMD and RVO group.

p = 0.809). Furthermore, a positive correlation was found between irisin and MT in the RVO group (Pearson = 0.468, p = 0.009).

BDNF Levels in the Aqueous Humor of the Study Eyes

As shown in **Table 2**, the levels of BDNF of the AMD group and RVO group were higher than that of the control group significantly (p = 0.000 and p = 0.001, respectively). However, there is no significant difference between the levels of BDNF in AMD and RVO groups (p = 0.068).

VEGF-A, VEGF-R1, VEGF-R2, and PDGF-BB Levels in the Aqueous Humor of the Study Eyes

As shown in **Table 2**, the levels of VEGF-A, VEGF-R1, and VEGF-R2 of the AMD group and RVO group were higher than that of the control group significantly (VEGF-A, p = 0.001 and p = 0.002; VEGF-R1, p = 0.003 and p = 0.031; VEGF-R2, p = 0.041 and p = 0.002, respectively). The level of VEGF-R1 in the AMD group was higher than that in the RVO group significantly (p = 0.034). However, there was no significant difference between the levels of PDGF-BB in these three groups. Furthermore, a positive correlation was found between VEGF-R2 and MT in the total 80 included eyes (Pearson = 0.339, p = 0.002). A negative correlation was found between VEGF-A and MT in the AMD group (Pearson = −0.435, p = 0.023) and also in the control group (Pearson = −0.479, p = 0.021).

Interleukin 6, 8, and 10 levels in the Aqueous Humor of the Study Eyes

As shown in **Table 3**, the level of IL-10 in the AMD group was higher than that of the control group significantly (p = 0.013). The levels of IL-6, IL-8, and IL-10 in the RVO group were higher than those of the control group (p = 0.036, 0.007, and 0.003, respectively). Moreover, the level of IL-8 in the AMD group was lower than that in the RVO group (p = 0.029). Furthermore, a positive correlation was found between IL-6 and MT in the total 80 included eyes (Pearson = 0.429, p = 0.000), and also in the RVO group (Pearson = 0.508, p = 0.004).

Tumor Necrosis Factor α and β levels in the Aqueous Humor of the Study Eyes

As shown in **Table 3**, the levels of TNF-α in AMD and RVO groups were higher than those of the control group (p = 0.005 and p = 0.000, respectively). However, there was no significant difference between the levels of TNF-β in these three groups.

ICAM-1, VCAM-1, IP-10, and MCP-1 Levels in the Aqueous Humor of the Study Eyes

As shown in **Table 4**, the AMD group had significantly higher levels of VCAM-1, IP-10, and MCP-1, compared with the control group (p = 0.036, 0.045, and 0.010, respectively). Moreover, the RVO group had significantly higher levels of ICAM-1, VCAM-1, IP-10, and MCP-1, compared with the control group (p = 0.000, 0.002, 0.000, and 0.005, respectively). However, the AMD group had a lower level of ICAM-1 than that of the RVO group (p = 0.000). Furthermore, a positive correlation was found between ICAM-1 and MT in the total 80 included eyes (Pearson = 0.530, p = 0.000) and also in the RVO group (Pearson = 0.407, p = 0.026).

DISCUSSION

As one of the leading cause of inevitable blindness, AMD is very important in the ocular clinic and research. Besides it, another retinal disease, RVO, could lead to severe ocular disorders and the loss of visual function. The cytokine signal pathway and possible treatment factors are interesting.

Almost 10 years ago, irisin was identified as an exercise-induced hormone and found to be synthesized in some different tissues of several species (27, 28). Its cellular form, called FNDC5, is proteolytic cleavaged to be the secret form, irisin, and released into the circulation, which could be found not only in skeletal muscle cells, but also in nerve tissues, such in some sites of human brain, Purkinje cells, paraventricular nucleus, and cerebrospinal fluid (29–31). Several previous studies had investigated the immunoreactivity of irisin in one type of

TABLE 3 | The levels of, IL-6, IL-8, IL-10, TNF-α, and TNF-β in the aqueous.

Group (n = 80)	IL-6	IL-8	IL-10	TNF-α	TNF-β
AMD (n = 27)	43.98 ± 73.26	13.33 ± 22.44$^{\#}$	1.37 ± 0.97	13.01 ± 10.84	0.82 ± 3.78
RVO (n = 30)	67.03 ± 120.68	45.54 ± 73.83	1.16 ± 0.46	10.85 ± 5.33	17.55 ± 96.14
Control (n = 23)	17.47 ± 23.54$^{\$}$	6.08 ± 5.93$^{\$}$	0.87 ± 0.17$^{*\$}$	6.53 ± 2.28$^{*\$}$	0.00 ± 0.00

Interleukin (IL), Tumor necrosis factor α (TNF-α) and β (TNF-β). Data are expressed as the means ± standard deviations (SD), in pg/ml. The differences in cytokines between the 2 groups were tested using Student's t-test. $^{*}p < 0.05$ between the AMD and control group; $^{\$}p < 0.05$ between the RVO and control group; $^{\#}p < 0.05$ between the AMD and RVO group.

TABLE 4 | The levels of ICAM-1, VCAM-1, IP-10, and MCP-1 in the aqueous.

Group (n = 80)	ICAM-1	VCAM-1	IP-10	MCP-1
AMD (n = 27)	1,678.00 ± 1,205.49$^{\#}$	857.90 ± 724.14	54.99 ± 101.81	1,368.95 ± 678.02
RVO (n = 30)	3,323.35 ± 1,824.91	849.62 ± 415.38	38.67 ± 25.37	1,335.95 ± 582.13
Control (n = 23)	1,162.56 ± 773.04$^{\$}$	525.30 ± 299.90$^{*\$}$	13.62 ± 8.77$^{*\$}$	977.97 ± 290.40$^{*\$}$

*Intercellular cell adhesion molecule-1 (ICAM-1), Inducible protein-10 (IP-10), Monocyte chemoattractant protein-1 (MCP-1), Vascular cell adhesion molecule-1 (VCAM-1). Data are expressed as the means ± standard deviations (SD), in pg/ml. The differences in cytokines between the 2 groups were tested using Student's t-test. *$p < 0.05$ between the AMD and control group; $^{\$}p < 0.05$ between the RVO and control group; $^{\#}p < 0.05$ between the AMD and RVO group.*

rodent, dwarf hamsters (*Phodopus roborovskii*), and irisin was found almost in all layers of retinae, except the outer nuclear layer (23). Moreover, the immunoreactivity of irisin was observed in the cornea (23). Another study of crested porcupine (*Hystrix cristata*) showed the immunoreactivity of irisin in the neural retina (24). Recently, two studies identified that irisin could be detected in the human aqueous humor and one study found that it could be detected in the vitreous humor (22, 25, 26). In our study, the AMD and RVO groups have significantly lower irisin in the aqueous than the control group. It could be that irisin is a retinal injury marker. As a positive correlation was found between irisin and MT in the RVO group, irisin could quantitatively reflect the MT in retinal disorders, especially in retinal vascular diseases.

In the pathogenic process of AMD, VEGF plays a very important role. Bis-retinoid N-retinyl-N-retinylidene ethanolamine (A2E) is found to accumulate in the retinae as aging and may induce oxidative damage (32) and cell damage and then finally stimulate cell death (33). In RPE cells, A2E was found to increase the level of VEGF mRNA and protein but did not affect the expression of VEGF-R1 or VEGF-R2. However, blue light exposure in A2E-loaded cells stimulated VEGF-R1 but not the levels of VEGF mRNA and protein (34). Currently, the intra-vitreal injection of anti-VEGF drugs has already become the standard treatment for wet-AMD (35). VEGF has been implicated in the etiology of various diseases of the retina including diabetic retinopathy (DR) and RVO. The use of anti-VEGF intra-vitreal injections has also profoundly impacted the treatment and visual outcomes in many of these entities, including macular edema (ME) secondary to RVO (36). Our study showed the level of VEGF-A in the aqueous of AMD and RVO groups to be higher than that in the control group, which also identified the role of VEGF in the pathogenesis of AMD and RVO, and the necessity of anti-VEGF treatment. Besides VEGF-A, the higher levels of VEGF-R1 in the AMD and RVO groups report of previous and identified VEGF-R1 could be a candidate molecular target whose suppression could supplement VEGF neutralization for treatment of RVO and AMD (37, 38). Although PDGF-BB could be induced by hypoxia and a previous study showed that combined suppression of VEGF and PDGF-BB provided superior outcomes versus suppression of VEGF alone in an early-phase clinical trial in patients with exudative AMD (39), our study showed higher levels of PDGF-BB in the AMD and RVO groups, but there was no significance.

On the other hand, many studies have reported the relationship between inflammatory stress and AMD or RVO. IL-6 is released from the lymphocytes and macrophages, as well as from the skeletal muscle cells, and acts both as a pro-inflammatory cytokine and as an anti-inflammatory myokine, depending on the stimuli (40). IL-6 might be one of the key molecules in the RPE response to oxidative stress (41). A recently study reported that IL-6 was higher in AMD patients than in cataract patients, who all also had AIDS (42). One study reported IL-6 values remaining within the normal range before and after the treatment of anti-VEGF (43). IL-8 is a main chemoattractant for neutrophils. It has been shown that intraocular IL-8 levels are higher in AMD, retinitis pigmentosa (RP), and glaucoma patients (25, 44). Also, one study showed that IL-8 was higher in AMD, and enhanced by A2E (45, 46). IL-10 is an anti-inflammatory cytokine that reduces activation of T cells. A previous study has also shown that IL-10 promotes ocular neovascularization (NV) through macrophage response to retina ischemia (47). No significant difference in IL-10 level between RP, AMD, glaucoma, and cataract patients has been found by one previous study (48). However, another study reported higher levels of IL-10 could be associated with AMD (49). Our study showed that the levels of IL-6, IL-8, and IL-10 in the aqueous of AMD groups were higher than those of controls, but only IL-10 had a significant difference. On the contrary, the levels of IL-6, IL-8, and IL-10 in the aqueous of the RVO group were significantly higher, which is consistent with previous studies (50, 51). TNF-α also plays a very important role in the pathogenesis of AMD as lower serum TNF-α levels were associated with an increase in visual acuity after anti-VEGF therapy in AMD patients (52). Bevacizumab, an anti-VEGF drug, was found to reduce the expression of IL-8 and TNF-α in RPE cells (53). Also, one study reported that TNF-α had a more than sixfold increase in RVO eyes versus controls (51). Our study showed higher levels of TNF-α in the AMD and RVO groups, significantly consistent with those of previous studies. It is interesting that the level of TNF-β in the RVO group was quite high in our study, but there was no significance. The role of TNF-β in the pathogenesis of AMD or RVO has not been reported. We might need more samples to explore the role of TNF-β in those retinal diseases.

ICAM-1, VCAM-1, IP-10, and MCP-1 are chemokines. VCAM-1 and ICAM-1 might be associated with dry-AMD (54). The inhibition of MCP-1 or ICAM-1 could protect RPE from inflammatory stress (55). A previous study suggested that IP-10 played a critical role as an antiangiogenic factor and, at the same time, as an inflammatory factor in the pathogenesis and pathophysiology of NV AMD eyes at onset and after IVA initiation (56). ICAM-1, VCAM-1, and IP-10 levels were higher in RVO patients (57, 58). The MCP-1 level in the

aqueous humor of patients with RVO-ME was significantly higher compared with control and was positively correlated with the central retinal thickness (50). Diabetic ME patients with normal VEGF levels but with high levels of IL-8, IP-10, and MCP-1 showed more resistance to the anti-VEGF treatment (59). Our study showed significantly higher levels of ICAM-1 (no significance), VCAM-1, IP-10, and MCP-1 in AMD and RVO eyes, which are consistent with the results of previous studies. It also indicated the very important roles of inflammatory stress in the pathogenesis and treatment of retinal diseases, such as AMD and RVO.

LIMITATIONS

Our samples are from the elderly, which may create a selection bias. Another limitation is the lack of serum level of irisin from the subjects. Moreover, the average age of RVO patients was relatively younger than that of the AMD and control groups. Further experiments are needed to clarify the detailed mechanisms underlying the relationship between irisin and cytokines with AMD and RVO.

CONCLUSIONS

The metabolic factor, irisin levels in the aqueous humor are decreased in AMD and RVO eyes and show a positive correlation between irisin and MT in RVO eyes, prompting researchers to explore the relationship between irisin and macular edema. We also identified the higher expression of vascular growth factors (VEGF-A, VEGF-R1, and PDGF-BB), inflammatory cytokines (IL-6, IL-8, IL-10, and TNF-α), and chemokines (ICAM-1, VCAM-1, IP-10, and MCP-1) in AMD and RVO eyes.

DATA AVAILABILITY STATEMENT

The original contributions presented in the study are included in the article/supplementary material. Further inquiries can be directed to the corresponding author.

ETHICS STATEMENT

The studies involving human participants were reviewed and approved by the Human Research Ethics Committee of Peking University People's Hospital and Peking University International Hospital. The patients/participants provided their written informed consent to participate in this study.

AUTHOR CONTRIBUTIONS

XL and XC contributed to collection of samples, data analysis, and writing. MZ revised this manuscript. YB designed and directed the manuscript. All authors contributed to manuscript revision, read, and approved the submitted version.

REFERENCES

1. Balasubramanian V, Sterling P. Receptive Fields and Functional Architecture in the Retina. *J Physiol* (2009) 587:2753–67. doi: 10.1113/jphysiol.2009.170704
2. Ahmad A, Ahsan H. Biomarkers of Inflammation and Oxidative Stress in Ophthalmic Disorders. *J Immunoassay Immunochem* (2020) 41:257–71. doi: 10.1080/15321819.2020.1726774
3. Wang W, Gawlik K, Lopez J, Wen C, Zhu J, Wu F, et al. Erratum: Genetic and Environmental Factors Strongly Influence Risk, Severity and Progression of Age-Related Macular Degeneration. *Signal Transduct Target Ther* (2016) 1:16023. doi: 10.1038/sigtrans.2016.23
4. Wong WL, Su X, Li X, Cheung CM, Klein R, Cheng CY, et al. Global Prevalence of Age-Related Macular Degeneration and Disease Burden Projection for 2020 and 2040: A Systematic Review and Meta-Analysis. *Lancet Global Health* (2014) 2:e106–116. doi: 10.1016/s2214-109x(13)70145-1
5. Di Carlo E, Augustin AJ. Prevention of the Onset of Age-Related Macular Degeneration. *J Clin Med* (2021) 10(15):3297. doi: 10.3390/jcm10153297
6. Zhang QY, Tie LJ, Wu SS, Lv PL, Huang HW, Wang WQ, et al. Overweight, Obesity, and Risk of Age-Related Macular Degeneration. *Invest Ophthalmol Visual Sci* (2016) 57:1276–83. doi: 10.1167/iovs.15-18637
7. Cheung CM, Wong TY. Is Age-Related Macular Degeneration a Manifestation of Systemic Disease? New Prospects for Early Intervention and Treatment. *J Internal Med* (2014) 276:140–53. doi: 10.1111/joim.12227
8. Sivaprasad S, Amoaku WM, Hykin P. The Royal College of Ophthalmologists Guidelines on Retinal Vein Occlusions: Executive Summary. *Eye (London England)* (2015) 29:1633–8. doi: 10.1038/eye.2015.164
9. Zhang Y, Duan J, Chang T, Li X, Wang M, Zhang M. Comparative Efficacy of Intravitreal Pharmacotherapy for Macular Edema Secondary to Retinal Vein Occlusion: A Protocol for the Systematic Review and Network Meta-Analysis. *Medicine* (2020) 99:e22267. doi: 10.1097/md.0000000000022267
10. Xia JP, Wang S, Zhang JS. The Anti-Inflammatory and Anti-Oxidative Effects of Conbercept in Treatment of Macular Edema Secondary to Retinal Vein Occlusion. *Biochem Biophys Res Commun* (2019) 508:1264–70. doi: 10.1016/j.bbrc.2018.12.049
11. Garcia-Horton A, Al-Ani F, Lazo-Langner A. Retinal Vein Thrombosis: The Internist's Role in the Etiologic and Therapeutic Management. *Thromb Res* (2016) 148:118–24. doi: 10.1016/j.thromres.2016.11.004
12. Ponto KA, Scharrer I, Binder H, Korb C, Rosner AK, Ehlers TO, et al. Hypertension and Multiple Cardiovascular Risk Factors Increase the Risk for Retinal Vein Occlusions: Results From the Gutenberg Retinal Vein Occlusion Study. *J Hypertension* (2019) 37:1372–83. doi: 10.1097/hjh.0000000000002057
13. Ferrer-Martínez A, Ruiz-Lozano P, Chien KR. Mouse PeP: A Novel Peroxisomal Protein Linked to Myoblast Differentiation and Development. *Dev Dynamics an Off Publ Am Assoc Anatomists* (2002) 224:154–67. doi: 10.1002/dvdy.10099
14. Xin C, Liu J, Zhang J, Zhu D, Wang H, Xiong L, et al. Irisin Improves Fatty Acid Oxidation and Glucose Utilization in Type 2 Diabetes by Regulating the AMPK Signaling Pathway. *Int J Obes (2005)* (2016) 40:443–51. doi: 10.1038/ijo.2015.199
15. Crujeiras AB, Zulet MA, Lopez-Legarrea P, de la Iglesia R, Pardo M, Carreira MC, et al. Association Between Circulating Irisin Levels and the Promotion of Insulin Resistance During the Weight Maintenance Period After a Dietary Weight-Lowering Program in Obese Patients. *Metab: Clin Exp* (2014) 63:520–31. doi: 10.1016/j.metabol.2013.12.007
16. Choi YK, Kim MK, Bae KH, Seo HA, Jeong JY, Lee WK, et al. Serum Irisin Levels in New-Onset Type 2 Diabetes. *Diabetes Res Clin Pract* (2013) 100:96–101. doi: 10.1016/j.diabres.2013.01.007
17. Askari H, Rajani SF, Poorebrahim M, Haghi-Aminjan H, Raeis-Abdollahi E, Abdollahi M. A Glance at the Therapeutic Potential of Irisin Against Diseases Involving Inflammation, Oxidative Stress, and Apoptosis: An Introductory Review. *Pharmacol Res* (2018) 129:44–55. doi: 10.1016/j.phrs.2018.01.012

18. Phillips C, Baktir MA, Srivatsan M, Salehi A. Neuroprotective Effects of Physical Activity on the Brain: A Closer Look at Trophic Factor Signaling. *Front Cell Neurosci* (2014) 8:170. doi: 10.3389/fncel.2014.00170
19. Zsuga J, Biro K, Papp C, Tajti G, Gesztelyi R. The "Proactive" Model of Learning: Integrative Framework for Model-Free and Model-Based Reinforcement Learning Utilizing the Associative Learning-Based Proactive Brain Concept. *Behav Neurosci* (2016) 130:6–18. doi: 10.1037/bne0000116
20. Papp C, Pak K, Erdei T, Juhasz B, Seres I, Szentpéteri A, et al. Alteration of the Irisin-Brain-Derived Neurotrophic Factor Axis Contributes to Disturbance of Mood in COPD Patients. *Int J chronic obstructive pulm Dis* (2017) 12:2023–33. doi: 10.2147/copd.S135701
21. Wrann CD, White JP, Salogiannnis J, Laznik-Bogoslavski D, Wu J, Ma D, et al. Exercise Induces Hippocampal BDNF Through a PGC-1α/FNDC5 Pathway. *Cell Metab* (2013) 18:649–59. doi: 10.1016/j.cmet.2013.09.008
22. Güler M, Aydın S, Urfalıoğlu S, Yardım M. Aqueous Humor Heat-Shock Protein 70, Periostin, and Irisin Levels in Patients With Pseudoexfoliation Syndrome. *Arquivos Brasileiros Oftalmologia* (2020) 83:378–82. doi: 10.5935/0004-2749.20200046
23. Gür FM, Timurkaan S, Gençer Tarakçi B, Yalçin MH, Özkan ZE, Baygeldi SB, et al. Identification of Immunohistochemical Localization of Irisin in the Dwarf Hamster (Phodopus Roborovskii) Tissues. *Anatomia Histologia Embryologia* (2018) 47:174–9. doi: 10.1111/ahe.12345
24. Gençer Tarakçı B, Girgin A, Timurkaan A, Yalçın MH, Gür FM, Karan M. Immunohistochemical Localization of Irisin in Skin, Eye, and Thyroid and Pineal Glands of the Crested Porcupine (Hystrix Cristata). *Biotech Histochem Off Publ Biol Stain Commission* (2016) 91:423–7. doi: 10.1080/10520295.2016.1183820
25. Wang X, Li M, Zheng R, Cui T, Qin J, Su Z, et al. High Irisin and Low BDNF Levels in Aqueous Humor of High Myopia. *Adv Clin Exp Med Off Organ Wroclaw Med Univ* (2021) 30:893–904. doi: 10.17219/acem/125428
26. Hu W, Wang R, Li J, Zhang J, Wang W. Association of Irisin Concentrations With the Presence of Diabetic Nephropathy and Retinopathy. *Ann Clin Biochem* (2016) 53:67–74. doi: 10.1177/0004563215582072
27. Boström P, Wu J, Jedrychowski MP, Korde A, Ye L, Lo JC, et al. A PGC1-α-Dependent Myokine That Drives Brown-Fat-Like Development of White Fat and Thermogenesis. *Nature* (2012) 481:463–8. doi: 10.1038/nature10777
28. Peng J, Deng X, Huang W, Yu JH, Wang JX, Wang JP, et al. Irisin Protects Against Neuronal Injury Induced by Oxygen-Glucose Deprivation in Part Depends on the Inhibition of ROS-NLRP3 Inflammatory Signaling Pathway. *Mol Immunol* (2017) 91:185–94. doi: 10.1016/j.molimm.2017.09.014
29. Dun SL, Lyu RM, Chen YH, Chang JK, Luo JJ, Dun NJ. Irisin-Immunoreactivity in Neural and Non-Neural Cells of the Rodent. *Neuroscience* (2013) 240:155–62. doi: 10.1016/j.neuroscience.2013.02.050
30. Martinez Munoz IY, Camarillo Romero EDS, Garduno Garcia JJ. Irisin a Novel Metabolic Biomarker: Present Knowledge and Future Directions. *Int J Endocrinol* (2018) 2018:7816806. doi: 10.1155/2018/7816806
31. Piya MK, Harte AL, Sivakumar K, Tripathi G, Voyias PD, James S, et al. The Identification of Irisin in Human Cerebrospinal Fluid: Influence of Adiposity, Metabolic Markers, and Gestational Diabetes. *Am J Physiol Endocrinol Metab* (2014) 306:E512–8. doi: 10.1152/ajpendo.00308.2013
32. Yin D. Biochemical Basis of Lipofuscin, Ceroid, and Age Pigment-Like Fluorophores. *Free Radical Biol Med* (1996) 21:871–88. doi: 10.1016/0891-5849(96)00175-x
33. Sparrow JR, Vollmer-Snarr HR, Zhou J, Jang YP, Jockusch S, Itagaki Y, et al. A2E-Epoxides Damage DNA in Retinal Pigment Epithelial Cells. Vitamin E and Other Antioxidants Inhibit A2E-Epoxide Formation. *J Biol Chem* (2003) 278:18207–13. doi: 10.1074/jbc.M300457200
34. Marie M, Gondouin P, Pagan D, Barrau C, Villette T, Sahel J, et al. Blue-Violet Light Decreases VEGFa Production in an. *Vitro Model AMD. PloS One* (2019) 14:e0223839. doi: 10.1371/journal.pone.0223839
35. Shinojima A, Lee D, Tsubota K, Negishi K, Kurihara T. Retinal Diseases Regulated by Hypoxia-Basic and Clinical Perspectives: A Comprehensive Review. *J Clin Med* (2021) 10(23):5496. doi: 10.3390/jcm10235496
36. Jiang Y, Mieler WF. Update on the Use of Anti-VEGF Intravitreal Therapies for Retinal Vein Occlusions. *Asia-Pacific J Ophthalmol (Philadelphia Pa.)* (2017) 6:546–53. doi: 10.22608/apo.2017459
37. Liu Y, Shen J, Fortmann SD, Wang J, Vestweber D, Campochiaro PA. Reversible Retinal Vessel Closure From VEGF-Induced Leukocyte Plugging. *JCI Insight* (2017) 2(18):e95530. doi: 10.1172/jci.insight.95530
38. Cobos E, Recalde S, Anter J, Hernandez-Sanchez M, Barreales C, Olavarrieta L, et al. CFB, ARMS2, SERPINF1, VEGFR1 and VEGF Polymorphisms and Anatomical and Functional Response to Ranibizumab Treatment in Neovascular Age-Related Macular Degeneration. *Acta Ophthalmologica* (2018) 96:e201–12. doi: 10.1111/aos.13519
39. Ding K, Eaton L, Bowley D, Rieser M, Chang Q, Harris MC, et al. Generation and Characterization of ABBV642, a Dual Variable Domain Immunoglobulin Molecule (DVD-Ig) That Potently Neutralizes VEGF and PDGF-BB and is Designed for the Treatment of Exudative Age-Related Macular Degeneration. *mAbs* (2017) 9:269–84. doi: 10.1080/19420862.2016.1268305
40. Pedersen BK. The Diseasome of Physical Inactivity–and the Role of Myokines in Muscle–Fat Cross Talk. *J Physiol* (2009) 587:5559–68. doi: 10.1113/jphysiol.2009.179515
41. Lazzarini R, Nicolai M, Lucarini G, Pirani V, Mariotti C, Bracci M, et al. Oxidative Stress in Retinal Pigment Epithelium Impairs Stem Cells: A Vicious Cycle in Age-Related Macular Degeneration. *Mol Cell Biochem* (2021) 477(1):67–77. doi: 10.1007/s11010-021-04258-3
42. Jabs DA, Van Natta ML, Schneider MF, Pak JW, Trang G, Jones NG, et al. Association of Elevated Plasma Inflammatory Biomarker Levels With Age-Related Macular Degeneration But Not Cataract in Persons With AIDS. *AIDS (London England)* (2022) 36:177–84. doi: 10.1097/qad.0000000000003104
43. Wiciński M, Seredyka-Burduk M, Liberski S, Marczak D, Pol M, Malinowski B, et al. Evaluation of Blood Coagulation Parameters and ADMA, NO, IL-6, and IL-18 Serum Levels in Patients With Neovascular AMD Before, During, and After the Initial Loading Phase of Intravitreal Aflibercept. *Life (Basel Switzerland)* (2021) 11(5):441. doi: 10.3390/life11050441
44. Jonas JB, Tao Y, Neumaier M, Findeisen P. Cytokine Concentration in Aqueous Humour of Eyes With Exudative Age-Related Macular Degeneration. *Acta Ophthalmologica* (2012) 90:e381–8. doi: 10.1111/j.1755-3768.2012.02414.x
45. Liukkonen MPK, Paterno JJ, Kivinen N, Siintamo L, Koskela AKJ, Kaarniranta K. Epithelial-Mesenchymal Transition-Related Serum Markers ET-1, IL-8 and TGF-β2 are Elevated in a Finnish Wet Age-Related Macular Degeneration Cohort. *Acta Ophthalmologica* (2021). doi: 10.1111/aos.15051
46. Fontaine V, Fournié M, Monteiro E, Boumedine T, Balducci C, Guibout L, et al. A2E-Induced Inflammation and Angiogenesis in RPE Cells *In Vitro* are Modulated by PPAR-α, -β/δ, -γ, and RXR Antagonists and by Norbixin. *Aging* (2021) 13:22040–58. doi: 10.18632/aging.203558
47. Dace DS, Khan AA, Kelly J, Apte RS. Interleukin-10 Promotes Pathological Angiogenesis by Regulating Macrophage Response to Hypoxia During Development. *PloS One* (2008) 3:e3381. doi: 10.1371/journal.pone.0003381
48. Ten Berge JC, Fazil Z, van den Born I, Wolfs RCW, Schreurs MWJ, Dik WA, et al. Intraocular Cytokine Profile and Autoimmune Reactions in Retinitis Pigmentosa, Age-Related Macular Degeneration, Glaucoma and Cataract. *Acta Ophthalmologica* (2019) 97:185–92. doi: 10.1111/aos.13899
49. Vilkeviciute A, Cebatoriene D, Kriauciuniene L, Zemaitiene R, Liutkeviciene R. IL-9 and IL-10 Single-Nucleotide Variants and Serum Levels in Age-Related Macular Degeneration in the Caucasian Population. *Mediators Inflamm* (2021) 2021:6622934. doi: 10.1155/2021/6622934
50. Yong H, Qi H, Yan H, Wu Q, Zuo L. The Correlation Between Cytokine Levels in the Aqueous Humor and the Prognostic Value of Anti-Vascular Endothelial Growth Factor Therapy for Treating Macular Edema Resulting From Retinal Vein Occlusion. *Graefe's Arch Clin Exp Ophthalmol = Albrecht von Graefes Archiv fur Klinische und Experimentelle Ophthalmologie* (2021) 259:3243–50. doi: 10.1007/s00417-021-05211-2
51. Zeng Y, Cao D, Yu H, Zhuang X, Yang F, Hu Y, et al. Comprehensive Analysis of Vitreous Chemokines Involved in Ischemic Retinal Vein Occlusion. *Mol Vision* (2019) 25:756–65.
52. Khan AH, Pierce CO, De Salvo G, Griffiths H, Nelson M, Cree AJ, et al. The Effect of Systemic Levels of TNF-Alpha and Complement Pathway Activity on Outcomes of VEGF Inhibition in Neovascular AMD. *Eye (London England)* (2021). doi: 10.1038/s41433-021-01824-3
53. Hildebrandt J, Käckenmeister T, Winkelmann K, Dörschmann P, Roider J, Klettner A. Pro-Inflammatory Activation Changes Intracellular Transport of Bevacizumab in the Retinal Pigment Epithelium *In Vitro*. *Graefe's Arch Clin Exp Ophthalmol = Albrecht von Graefes Archiv fur Klinische und Experimentelle Ophthalmologie* (2021) 260(3):857–72. doi: 10.1007/s00417-021-05443-2

54. Baiula M, Caligiana A, Bedini A, Zhao J, Santino F, Cirillo M, et al. Leukocyte Integrin Antagonists as a Novel Option to Treat Dry Age-Related Macular Degeneration. *Front Pharmacol* (2020) 11:617836. doi: 10.3389/fphar.2020.617836
55. Huang WC, Liou CJ, Shen SC, Hu S, Hsiao CY, Wu SJ. Luteolin Attenuates IL-1β-Induced THP-1 Adhesion to ARPE-19 Cells *via* Suppression of NF-κb and MAPK Pathways. *Mediators Inflamm* (2020) 2020:9421340. doi: 10.1155/2020/9421340
56. Sato T, Takeuchi M, Karasawa Y, Enoki T, Ito M. Intraocular Inflammatory Cytokines in Patients With Neovascular Age-Related Macular Degeneration Before and After Initiation of Intravitreal Injection of Anti-VEGF Inhibitor. *Sci Rep* (2018) 8:1098. doi: 10.1038/s41598-018-19594-6
57. Yi QY, Wang YY, Chen LS, Li WD, Shen Y, Jin Y, et al. Implication of Inflammatory Cytokines in the Aqueous Humour for Management of Macular Diseases. *Acta Ophthalmologica* (2020) 98:e309–15. doi: 10.1111/aos.14248
58. Wautier JL, Wautier MP. Cellular and Molecular Aspects of Blood Cell-Endothelium Interactions in Vascular Disorders. *Int J Mol Sci* (2020) 21 (15):5315. doi: 10.3390/ijms21155315
59. Mao J, Zhang S, Zheng Z, Deng X, Liu C, Chen Y, et al. Prediction of Anti-VEGF Efficacy in Diabetic Macular Oedema Using Intraocular Cytokines and Macular Optical Coherence Tomography. *Acta Ophthalmologica* (2021). doi: 10.1111/aos.15008

Conflict of Interest: The authors declare that the research was conducted in the absence of any commercial or financial relationships that could be construed as a potential conflict of interest.

Publisher's Note: All claims expressed in this article are solely those of the authors and do not necessarily represent those of their affiliated organizations, or those of the publisher, the editors and the reviewers. Any product that may be evaluated in this article, or claim that may be made by its manufacturer, is not guaranteed or endorsed by the publisher.

frontiers | Frontiers in Molecular Biosciences

ORIGINAL RESEARCH
published: 09 June 2022
doi: 10.3389/fmolb.2022.871291

Serum Untargeted Metabolomics Reveal Potential Biomarkers of Progression of Diabetic Retinopathy in Asians

Zongyi Wang, Jiyang Tang, Enzhong Jin, Yusheng Zhong, Linqi Zhang, Xinyao Han, Jia Liu, Yong Cheng, Jing Hou, Xuan Shi, Huijun Qi, Tong Qian, Li Yuan, Xianru Hou, Hong Yin, Jianhong Liang, Mingwei Zhao, Lvzhen Huang and Jinfeng Qu**

Department of Ophthalmology, Peking University People's Hospital, Eye Diseases and Optometry Institute, Beijing Key Laboratory of Diagnosis and Therapy of Retinal and Choroid Diseases, College of Optometry, Peking University Health Science Center, Beijing, China

OPEN ACCESS

Edited by:
Ye Sun,
Boston Children's Hospital and Harvard Medical School, United States

Reviewed by:
Caroline Volpe,
Institute of Education and Research Santa Casa BH, Brazil
Cheng Guo,
Zhejiang University, China

***Correspondence:**
Lvzhen Huang
huanglvzhen@126.com
Jinfeng Qu
drbari@163.com

Specialty section:
This article was submitted to Metabolomics, a section of the journal Frontiers in Molecular Biosciences

Received: *15 February 2022*
Accepted: *25 April 2022*
Published: *09 June 2022*

Citation:
Wang Z, Tang J, Jin E, Zhong Y, Zhang L, Han X, Liu J, Cheng Y, Hou J, Shi X, Qi H, Qian T, Yuan L, Hou X, Yin H, Liang J, Zhao M, Huang L and Qu J (2022) Serum Untargeted Metabolomics Reveal Potential Biomarkers of Progression of Diabetic Retinopathy in Asians. Front. Mol. Biosci. 9:871291. doi: 10.3389/fmolb.2022.871291

Purpose: To reveal molecular mechanisms of diabetic retinopathy (DR) in Asians and facilitate the identification of new therapeutic targets through untargeted metabolomics. To determine the differences in serum metabolites and metabolic pathways between different stages of diabetic retinopathy in patients with type 2 diabetic mellitus (T2DM) and proliferative DR (PDR) and non-proliferative DR (NPDR) and identify differential metabolites between T2DM and DR (NPDR and PDR) patients.

Methods: This prospective observational registration study described the differential metabolites between 45 T2DM patients and 15 control cases with no significant differences in clinical characteristics. Their biospecimens and clinical information were collected and recorded in their medical reports. DR phenotypes of the subjects were verified by retina specialists. Serum metabolites were analyzed using high-resolution mass spectrometry with liquid chromatography. Untargeted metabolomics was performed on serum samples from 15 T2DM patients, 15 non-proliferative diabetic retinopathy patients, 15 proliferative diabetic retinopathy patients, and 15 diabetic controls. Discriminatory metabolic features were identified through partial least squares discriminant analysis (PLS-DA), hierarchical clustering analysis (HCA), and generalized linear regression models.

Result: Through untargeted metabolomics, 931 features (523 in positive and 408 in negative modes) with 102 common metabolites highly relevant to the presence of DR were detected. In the adjusted analysis, 67 metabolic features differed significantly between T2DM and NPDR patients. Pathway analysis revealed alterations in metabolisms of amino acids and fatty acids. Glutamate, phosphatidylcholine, and 13-hydroperoxyoctadeca-9,11-dienoic acid (13-PHODE) were key contributors to these pathway differences. A total of 171 features distinguished PDR patients from T2DM patients, and pathway analysis revealed alterations in amino acid metabolism, fatty acid metabolism, nitrogen metabolism, and tricarboxylic acid cycle. Aspartate, glutamate, glutamine, ornithine, N-acetyl-L-glutamate, N-acetyl-L-aspartate, citrate, succinate, N-(L-arginino)succinate, 2-oxoglutarate, 13-hydroperoxyoctadeca-9,11-dienoic acid, methionine, lysine, threonine,

phenylalanine, N(pi)-methyl-L-histidine, phosphatidylcholine, and linoleate were major contributors to the pathway differences. Between NPDR patients and PDR patients, there were 79 significant differential metabolites. Enrichment pathway analysis showed changes in amino acid metabolism, fatty acid metabolism, pantothenate, and CoA biosynthesis. Aspartate, glutamine, N-acetyl-L-glutamate, N-acetyl-L-aspartate, pantothenate, dihomo-gamma-linolenate, docosahexaenoic acid, and icosapentaenoic acid were key factors for the differences of these pathways.

Conclusion: This study demonstrated that the pathways of arginine biosynthesis metabolism, linoleic acid metabolism, alanine, aspartate, and glutamate metabolism, as well as D-glutamine and D-glutamate metabolism, were dysregulated in DR patients of the Asian population. Increased levels of glutamate, aspartate, glutamine, N-acetyl-L-glutamate, and N-acetyl-L-aspartate and decreased levels of dihomo-gamma-linolenate, docosahexaenoic, and icosapentaenoic were considered as the metabolic profile that could distinguish PDR from NPDR in Asians. Phosphatidylcholine and 13-PHODE were identified as two major novel metabolite markers in advanced stages of DR in our study.

Keywords: Type 2 diabetes, proliferative diabetic retinopathy, non-proliferative diabetic retinopathy, metabolomics, untargeted metabolomics, metabolic profiling, LC-MS

INTRODUCTION

Diabetes is a prevalent global health problem that currently affects 537 million patients around the world (Sun et al., 2022). Without appropriate intervention, this number is projected to reach 643 million by 2030. Diabetes could lead to serious and even life-threatening complications, most notably cardiovascular diseases, diabetic nephropathy, and diabetic retinopathy. These complications could increase medical and nursing needs, reduce the quality of life of the patients, and substantially increase health care costs (Ogurtsova et al., 2017). Diabetic retinopathy (DR) is the most serious microvascular complication of diabetes in the eyes (Sumarriva et al., 2019) (Cabrera et al., 2020). It is also the main cause of decreased vision and blindness among 20–74-year-old adults in developing and developed countries (Sabanayagam et al., 2019). While enabling the increase in life expectancy, advances in modern medicine lead to an aging population and rising numbers of diabetic patients with complications such as diabetic retinopathy worldwide, especially in Asia (Yang et al., 2019) (Wong et al., 2016). The prevalence of diabetic retinopathy in China was estimated to be 1.14% (Zhong et al., 2018) (Song et al., 2018). As a destructive and progressive disease, DR can be divided into two stages according to its severity: non-proliferative diabetic retinopathy (NPDR) and proliferative diabetic retinopathy (PDR) (2016) (Mahajan et al., 2019). Currently, no treatment strategy for DR can consistently control the progression of each DR patient. Studies have shown that systemic risk factors of DR include higher levels of blood glucose, blood lipids, blood pressure, and longer disease course of diabetes (Sumarriva et al., 2019) (Cabrera et al., 2020), though studies have shown that higher blood glucose level and longer disease course of diabetes are the main risk factors that should be considered in clinical settings (Jenkins et al., 2015) (Cheung et al., 2014). However, these two factors alone could not completely predict an individual's risk for developing diabetic retinopathy. In clinical practice, patients with similar durations of diabetes and similar levels of glycemic control could have tremendously different clinical outcomes in diabetic retinopathy. Some patients develop very mild retinopathy, while others seem to be significantly predisposed to severe retinopathy (Sun et al., 2011) (Gao et al., 2014) (Touzani et al., 2019). This phenomenon indicates that there may be other potential pathogenic factors behind DR and that there is still a lack of effective markers to detect and control the occurrence and progression of DR (Porta and Striglia, 2020). Therefore, it is of great importance to search for potential biomarkers that can predict the occurrence and development of DR, enabling better prevention and control of DR (Ting et al., 2016; Peng et al., 2018). Although there have been many metabolomic studies on DR, the identification of differential metabolites in critical periods of DR development (T2DM and NPDR periods) has been rarely attempted, especially in Asian populations. To address this gap and better understand the complicated metabolic state of DR, we performed untargeted metabolomics *via* LCMS in sera of the Asian patients with T2DM with and without DR. This study aimed to identify metabolites or metabolic pathways altered in DR in the Asian, as well as metabolic differences between patients with NPDR and PDR, especially the stage from T2DM to DR. Furthermore, we also compared the differential metabolism between DR group (including NPDR and PDR patients) and T2DM group as well as DR group and non-DR group (including T2DM and control patients). Identifying these differences in metabolic profiles could aid in the clarification of molecular mechanisms of DR and PDR and facilitate the identification of new therapeutic targets.

MATERIALS AND METHODS

Ethics Statement

This study adhered to the tenets of the Declaration of Helsinki and was approved by the Ethical Committee of Peking University People's Hospital. Signed informed consent was obtained from all participants.

Study Participants and Research Design

This prospective observational registration study was conducted from December 2020 to July 2021 at Peking University People's Hospital Ophthalmologic Center. A total of 618 patients with type 2 diabetes were screened. A cohort of 60 patients was randomly recruited from Peking University People's Hospital Ophthalmologic Center. The diabetic control (n = 15) were healthy individuals with no history of diabetes. The T2DM cases (n = 15) included patients diagnosed with T2DM for at least 10 years with no clinical signs of DR as determined by dilated fundus examination by a retina specialist. DR cases (n = 30) were patients with T2DM and DR diagnosed on dilated fundus examination by a retina specialist. In accordance with the Early Treatment Diabetic Retinopathy Study (ETDRS) criteria, DR was classified into three categories: no DR, non-proliferative diabetic retinopathy (NPDR), and proliferative diabetic retinopathy (PDR) (Wilkinson et al., 2003) (Wu, 2013). All patients underwent thorough ophthalmic examination, color fundus photography, and optical coherence tomography (OCT). Color fundus photography and fluorescein angiography (FA) were obtained with FF 540 Plus (Carl Zeiss Meditech, Jena, Germany) or Optos 200Tx (Optos plc, Dunfermline, Scotland, United Kingdom). Optical coherence tomography (OCT) was performed with RTVue XR Avanti (Optovue, Fremont, CA, United States) or Cirrus HD-OCT 5000 (Carl Zeiss Meditec Inc., Dublin, CA, United States). Classification of no DR, NPDR (n = 15), or PDR (n = 15) was done by retina specialists with dilated fundus examination with the aid of color fundus photography, FFA, and OCT. Two or more ophthalmologists classified the DR status based on the results of the exams to avoid potential diagnosis bias. If there were discordance between the specialists, an agreement on the final diagnosis by all parties would be reached by open arbitration. A diagnosis of NPDR was based on the presence of blot hemorrhages, microaneurysms, cotton-wool spots, or intraretinal microvascular abnormalities on dilated fundus examination and no evidence of active PDR or history of treatment for PDR. A PDR diagnosis was based on the presence of neovascularization on the iris or retina or documented history of PDR for which the patient has received treatment. Exclusion criteria included 1) presence or history of other eye diseases (retinal degeneration, glaucoma, active ocular inflammation, etc.) or history of intraocular surgery (vitreoretinal surgery, intravitreal injection, laser therapy, and trauma history); 2) cancer, infectious disease, hyperuricemia, inherited metabolic diseases, mental disorder, heart failure, severe hypertension (systolic blood pressure ≥180 mm Hg or diastolic blood pressure ≥110 mm Hg), acute myocardial infarction, pregnancy, liver disease, stroke or any other severe chronic systemic disease; 3) corneal and lens pathologies that prevent a clear view of the fundus.

Baseline Test/Data Collection and Definitions

All participants' demographic information and medical records, including sex, age, past medical history, current status of smoking and alcohol consumption, duration of diabetes, clinical and laboratory measurements, drugs used, and disease status, were obtained. Patients received a general physical examination that included blood pressure, height, and weight measurements. The body mass indexes (BMI) of all patients were calculated and recorded. Blood laboratory tests, including fasting plasma glucose (FPG), total cholesterol (TC), triglycerides (TG), high-density lipoprotein cholesterol (HDL-c), low-density lipoprotein cholesterol (LDL-c), serum creatinine (SCr), hemoglobin A1c (HbA1c), and blood urea nitrogen (BUN), were measured using standard automated assays and recorded in the electronic case report form. Medication records included insulin, metformin, and other antidiabetic agents; ACE inhibitors, angiotensin receptor blockers, and other antihypertensive drugs; and statins and other lipid-lowering drugs.

Blood Collection and Preparation

After at least 8 h overnight fasting, 6 ml of venous blood samples were collected under complete aseptic precautions using a 21 or 23 G butterfly needle from each study participant with tubes and stored at 4°C. The serum was separated by centrifugation at 3,000 rpm for 10 min (4°C) within 30 min to separate serum from whole blood and then transferred into a 1.5 ml sterile tube to be stored at −80°C ultra-low temperature allowing the serum to freeze immediately. Well-trained professional technicians carried out further measurements.

Untargeted Metabolomics Analysis

Ultra-high-performance liquid chromatography coupled with tandem mass spectrometry (UHPLC-MS/MS) analyses were performed using a Vanquish UHPLC system (Thermo Fisher, Germany) coupled with an Orbitrap Q Exactive™ HF mass spectrometer (Thermo Fisher, Germany) in Novogene Co., Ltd. (Beijing, China). Before the analysis, frozen serum samples (100 μL) were thawed, dissolved at 4°C, placed in the Eppendorf (EP) tubes, and resuspended with prechilled 80% methanol and 0.1% formic acid by a well vortex. The samples were incubated on ice for 5 min and centrifuged at 15,000 g at 4 °C for 20 min. Some of the supernatant was diluted to a final concentration containing 53% methanol by LC-MS grade water. The samples were subsequently transferred to a fresh EP tube and then centrifuged at 15,000 g at 4°C for 20 min. Finally, the supernatant was injected into the LC-MS/MS system for analysis [22]. Samples were injected onto a Hypesil Goldcolumn (100 × 2.1 mm, 1.9 μm) using a 17 min linear gradient at a flow rate of 0.2 ml/min. The eluents for the positive polarity mode were eluent A (0.1% FA in water) and

eluent B (methanol), and the eluents for the negative polarity mode were eluent A (5 mM ammonium acetate, pH 9.0) and eluent B (methanol). The solvent gradient was set as follows: 2% B, 1.5 min; 2%–100% B, 12.0 min; 100% B, 14.0 min; 100%–2% B, 14.1 min; and 2% B, 17 min. Q Exactive™ HF mass spectrometer was operated in positive/negative polarity mode with a spray voltage of 3.2 kV, capillary temperature of 320°C, sheath gas flow rate of 40 arb, and aux gas flow rate of 10 arb. Quality control (QC) samples were prepared by mixing the same amount of serum from each sample and using the same procedures as the test samples to extract metabolites. One QC was inserted into every 10 samples regularly before and after the operation. The raw data files generated by UHPLC-MS/MS were processed using the Compound Discoverer 3.1 (CD3.1, Thermo Fisher) to perform peak alignment, peak picking, and quantitation for each metabolite. The main parameters were set as follows: retention time tolerance, 0.2 min; actual mass tolerance, 5 ppm; signal intensity tolerance, 30%; signal/noise ratio, 3; and minimum intensity, 100,000. Peak intensities were normalized to the total spectral intensity. Based on additive ions, molecular ion peaks, and fragment ions, the normalized data were used to predict the molecular formula. Peaks were matched with the mzCloud, mzVault, and MassList database to obtain accurate qualitative and relative quantitative results.

Data Processing and Pathway Analysis for Metabolomic Study

Statistical analyses were performed using the statistical software R (R version R-3.4.3), Python (Python 2.7.6 version), and CentOS (CentOS release 6.6). Normal transformation of non-normally distributed data was done using the area normalization method. These metabolites were annotated using the KEGG, HMDB, and LIPIDMaps databases. Multivariate analysis, including partial least squares discriminant analysis (PLS-DA), was used to determine the distributions and performed at metaX (a flexible and comprehensive software for processing metabolomics data). Univariate analysis (*t*-test) was used to calculate the statistical significance (*p*-value). To select the metabolites responsible for these differences, variable importance in the projection (VIP), fold changes (FC), and *p*-value were mainly used. The VIP value is an important parameter for detecting potential biomarker candidates that reflects the correlation of the metabolites with different biological states. In our study, VIP values >1.0 of PLS–DAs were used. $p < 0.05$ was considered statistically significant when analyzing differences among means. For pairwise comparisons, adjusted *p*-values using the Bonferroni correction as calculated by statistical software R were used. Therefore, the adjusted *p*-value < 0.05 was still considered significant. The relative metabolite levels were converted into fold changes (FC), which was defined as the ratio of each metabolite to the mean of all biological repeat quantitative values between groups. FC > 1.2 and < 0.833 indicated the significantly upregulated and downregulated differential metabolites, respectively. Volcano plots were calculated using filter metabolites of interest, based on log2 (FC) and –log10 (*p*-value) of metabolites, and the peaks that exhibited a statistically significant difference between two groups were used to perform multivariate pattern recognition. For clustering heat maps, the data were normalized using z-scores of the intensity areas of differential metabolites and plotted by the Pheatmap package in R language. The correlation between differential metabolites was analyzed by cor () in R language (method = Pearson). Statistically significant correlations between differential metabolites were calculated by cor.mtest () in R language. A *p*-value < 0.05 was considered statistically significant, and correlation plots were plotted by the corrplot package in R language. The functions of these metabolites and metabolic pathways were studied using the KEGG database. The metabolic pathway enrichment analysis of differential metabolites was performed when ratios were satisfied by x/n > y/N; metabolic pathways were considered enrichment when the p-value of metabolic pathway <0.05; and metabolic pathways were considered statistically significant enrichment.

Bioinformatics Analysis

Descriptive statistics for demographic and clinical variables were calculated for the study population. Analysis of variance (ANOVA) was used to compare means of normally distributed data with homogeneity of variances. The Chi-square test was used for the analysis of categoric data (e.g., gender and presence of comorbidities). Wilcoxon rank-sum test was performed to compare age, diabetes duration, and biochemical parameters, including FPG, HbA1c, HDL-c, LDL-c, SCr, TC, TG, and BUN between the respective groups, as these values were not normally distributed within the groups.

RESULTS

Baseline Characteristics

The demographic characteristics of the study population are shown in **Table 1**. Of all the participants (60 cases), 15 were T2DM patients (mean age of 73.53 ± 7.54 years, 40.0% males), 15 were NPDR patients (mean age of 70.47 ± 8.28 years, 60.0% males), 15 were PDR patients (mean age of 57.53 ± 9.05 years, 60.0% males), and 15 were controls (mean age of 64.07 ± 15.15 years, 46.7% males). Compared with T2DM patients and controls, PDR patients had a longer mean diabetes duration ($p < 0.001$, $p < 0.001$), but no differences were observed between NPDR and PDR, as well as T2DM and NPDR. The PDR group was significantly younger than the other groups ($p = 0.028$, $p < 0.001$, $p < 0.001$). No statistically significant differences in gender and body mass index (BMI) were found between groups. In the analysis of serum, fasting plasma glucose ($p = 0.002$, $p = 0.001$, $p = 0.001$) and HbA1c ($p < 0.001$, $p < 0.001$, $p < 0.001$) in control group was significantly lower than T2DM, NPDR, and PDR groups. Serum creatinine in the control, T2DM, and NPDR groups were significantly lower than in the PDR group ($p = 0.045$, $p = 0.012$, $p = 0.032$). Blood urea nitrogen in PDR patients was significantly higher than the other groups ($p = 0.001$, $p < 0.001$, $p = 0.001$). No statistically significant differences were found in levels of HDL-c, LDL-c, total cholesterol, triacylglycerol, and rate of hypertension between groups (**Table 1**).

TABLE 1 | Demographics, comorbidities, and serum test results across groups.

	Control	T2DM	NPDR	PDR	P-value	P^a	P^b	P^c	P^d	P^e	P^f
Age	64.07 ± 15.15	73.53 ± 7.54	70.47 ± 8.28	57.53 ± 9.05	<0.001	0.082	0.209	0.028	0.965	<0.001	<0.001
Mean ± SD											
Gender, n (%)											
Male	7 (46.7)	6 (40)	9 (60)	9 (60)	0.615						
Female	8 (53.3)	9 (60)	6 (40)	6 (40)							
BMI	23.79 ± 3.26	23.90 ± 3.04	24.78 ± 3.90	24.65 ± 2.57	0.793	1.000	0.849	0.897	0.888	0.928	1.000
Diabetes duration, y	0	12.47 ± 2.94	16.67 ± 6.97	21.2 ± 6.10	<0.001	<0.001	<0.001	<0.001	0.113	<0.001	0.076
FPG (mm/L)	5.39 ± 0.66	7.89 ± 0.94	7.96 ± 1.65	8.06 ± 2.75	<0.001	0.002	0.001	0.001	1.000	0.994	0.999
HbA1 (mm/L)	5.13 ± 0.54	7.01 ± 0.67	7.21 ± 1.14	7.47 ± 0.93	<0.001	<0.001	<0.001	<0.001	0.925	0.501	0.861
HDL-c (mm/L)	1.35 ± 0.28	1.31 ± 0.22	1.24 ± 0.27	1.11 ± 0.17	0.057	0.965	0.625	0.051	0.884	0.145	0.483
LDL-c (mm/L)	2.95 ± 0.83	2.94 ± 0.98	3.06 ± 1.17	2.67 ± 0.74	0.724	>1.000	0.992	0.849	0.987	0.870	0.691
SCr (mm/L)	79.56 ± 17.83	71.33 ± 15.88	77.27 ± 15.47	122.40 ± 79.39	0.0082	0.955	0.999	0.045	0.982	0.012	0.032
TC (mm/L)	4.84 ± 0.94	4.81 ± 1.19	4.86 ± 1.41	5.03 ± 1.50	0.977	0.975	0.989	0.999	1.000	0.994	0.999
TG (mm/L)	1.26 ± 0.79	1.45 ± 0.70	1.79 ± 1.14	2.38 ± 2.43	0.196	0.984	0.762	0.181	0.926	0.337	0.707
BUN (mm/L)	5.55 ± 1.47	5.01 ± 1.31	5.64 ± 1.5	9.64 ± 4.80	<0.001	0.953	1.000	0.001	0.928	<0.001	0.001
HTN%	60.0%	66.7%	60.0%	73.3%	0.848						

For age, diabetes duration, FPG, HbA1c, HDL-c, LDL-c, SCr, TC, TG, and BUN, the mean and standard deviations are presented and comparisons were made by the Wilcoxon rank-sum test. Gender and rates of comorbidities were compared by X2 test. HbA1c and creatinine levels were taken from the date closest to the date of the blood draw. BMI, body mass index; FPG, fasting plasma glucose; HbA1c, hemoglobin A1c; HDL-c, high-density lipoprotein-cholesterol; LDL-c, low-density lipoprotein-cholesterol; SCr, serum creatinine; TC, total cholesterol; TG, triglycerides; BUN, blood urea nitrogen; HTN, hypertension. P^a, p-value of diabetic controls versus *T2DM patients. P^b*, p-value of diabetic controls* versus *NPDR patients. P^c*, p-value of diabetic controls* versus *PDR patients. P^d*, p-value of T2DM patients* versus *NPDR patients. P^e*, p-value of T2DM patients* versus *PDR patients. P^f*, p-value of NPDR patients* versus *PDR patients.*

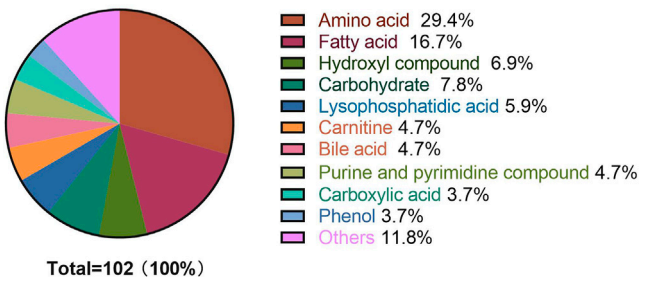

FIGURE 1 | Metabolite classification analysis. The pie chart shows the 60 metabolites, including amino acids (29.4%), fatty acids (16.7%), hydroxyl compounds (6.9%), carbohydrates (7.8%), lysophosphatidic acids (5.9%), carnitines (4.7%), bile acids (4.7%), purine and pyrimidine compounds (4.7%) carboxylic acids (3.7%), phenols (3.7%), and others (11.8%). The highest percentage (30 out of 102) of these metabolites were amino acids.

Metabolites Identification Analysis

A metabolome-wide association study (MWAS) was performed to determine which metabolic features differed between control (n = 15), T2DM patients (n = 15), NPDR patients (n = 15), and PDR patients (n = 15) in the Asian population. In addition, we also conducted a further comparative analysis of metabolomics between the DR group (NPDR and PDR groups) and T2DM group, as well as between the DR group (NPDR and PDR groups) and non-DR group (T2DM and control groups). Through untargeted metabolomics analysis, 931 metabolic features (including 523 features in positive mode and 408 features in negative mode) were detected. A total of 102 common metabolites were identified by comparing MS fragment patterns with commercial standard compounds, and various databases, including the Kyoto Encyclopedia of Genes and Genomes (KEGG), Human Metabolome Database (HMDB), and LIPIDMaps databases, were selected. These metabolites were identified as metabolites that differed significantly among the groups, including 30 amino acids, 7 hydroxyl compounds, 4 carboxylic acids, 5 carnitines, 17 fatty acids, 5 bile acids, 8 carbohydrates, 5 purine and pyrimidine compounds, 3 phenols, and 6 lysophosphatidic acids. Detailed information on these metabolites is presented in **Figure 1**. Hierarchical clustering analysis (HCA) showed the relationship between the metabolite content clustering between groups. In both positive and negative modes, the identified metabolites in the controls, T2DM, and PDR groups showed distinguishable clusters in groups, even though the sample clusters overlapped slightly (**Figure 2**).

Non-Proliferative DR *Versus* Type 2 Diabetic Mellitus

Based on PLS-DA and adjusted linear regression analysis (p < 0.05), there were 93 (40 in positive and 53 in negative modes) metabolic features that differed significantly between NPDR and T2DM patients in the adjusted analysis. These features were compared using hierarchical clustering analysis (**Figure 3**). The volcano maps visualized the differences between NPDR and T2DM patients in positive and negative modes based on log2 (FC) and −log10 (p-value) of metabolites (**Figure 4**). Excluding the metabolic features that could not be matched in mzCloud, mzVault, or MassList databases, 26 and 41 of the metabolites showed good discriminatory power for NPDR *versus* T2DM subjects with an area under the curve (95% CI) > 0.7 in positive and negative modes. We performed KEGG enrichment pathway analysis with VIP > 1.0 and AUC > 0.7 using the 67 features distinguishing NPDR patients and T2DM

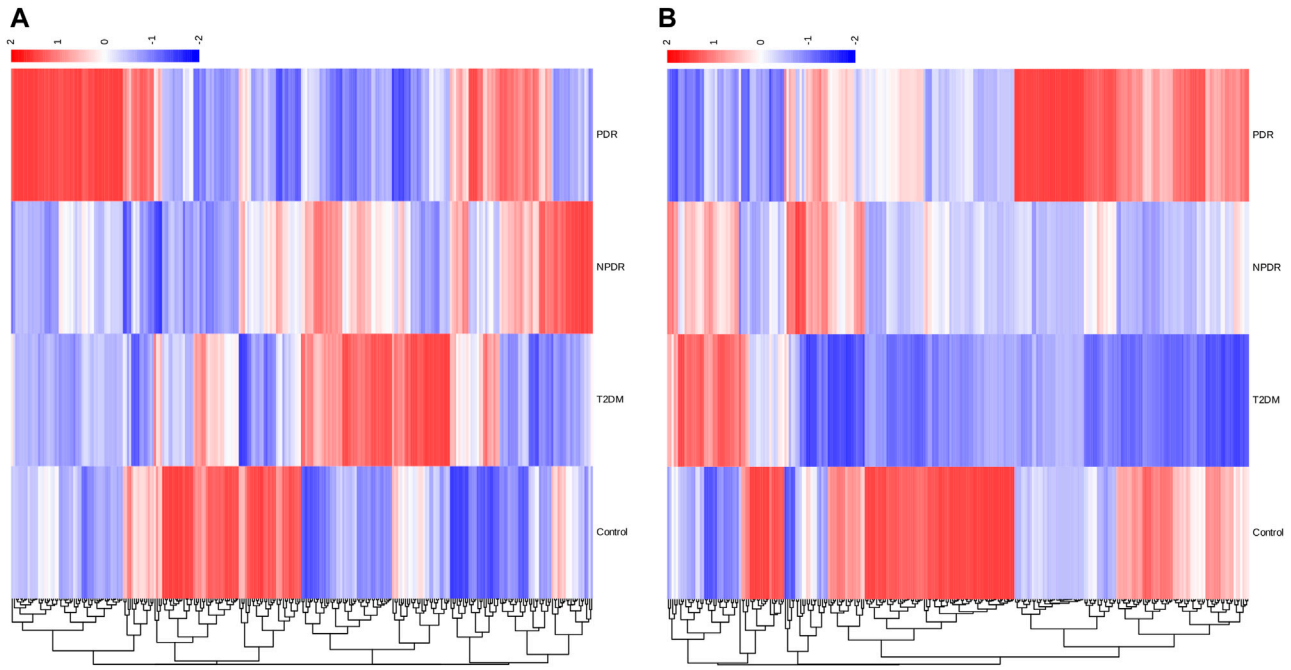

FIGURE 2 | (A) Positive mode. **(B)** Negative mode. Hierarchical clustering analysis (HCA) showed that the identified metabolites were clearly grouped into controls, T2DM, and PDR patient clusters with high repeatability, and the resulting data were reliable and logical. Significant metabolic features increased (red) or decreased (blue) compared with the others group.

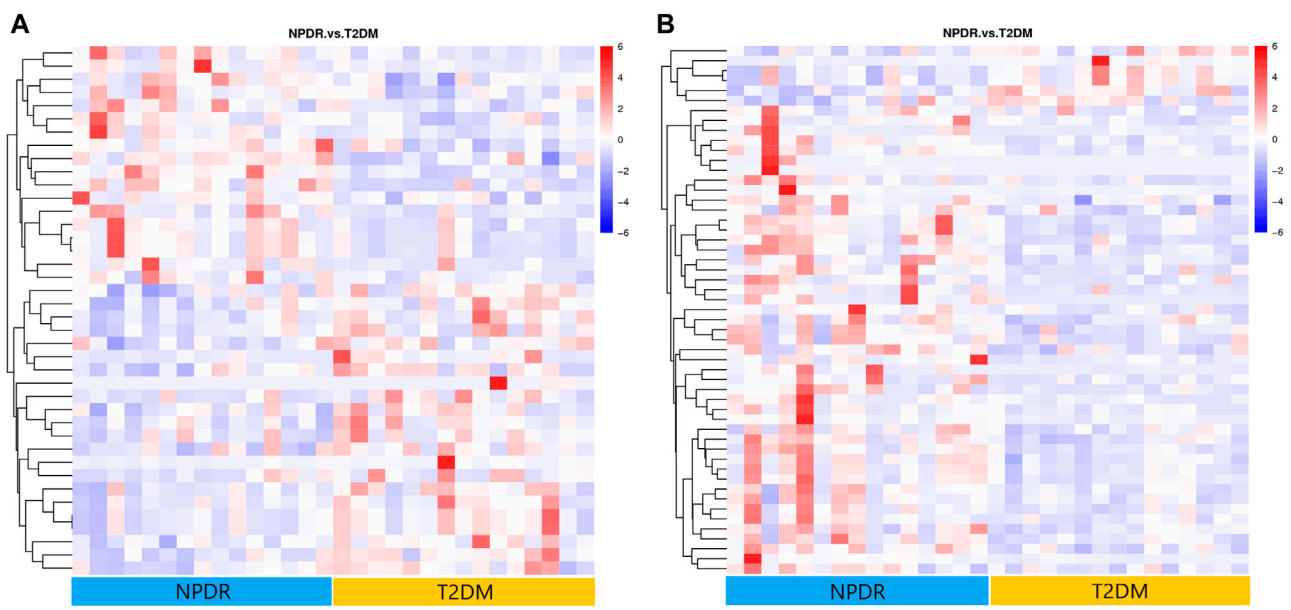

FIGURE 3 | (A) Positive mode. **(B)** Negative mode. Hierarchical clustering analysis based on the intensity of significant metabolite features selected by PLS-DA identified clusters of features that were increased (red) or decreased (blue) in NPDR and T2DM patients. There are 40 metabolic features shown in positive mode and 53 metabolic features shown in negative mode.

patients. This revealed enrichment of 22 metabolic pathways, three of which (metabolism of D-glutamine and D-glutamate, linoleic acid, and nitrogen) were considered to be the significant KEGG enrichment pathways with a p-value ≤ 0.05. The other pathways, including arginine biosynthesis, primary bile acid biosynthesis, metabolism of alpha-linolenic acid metabolism,

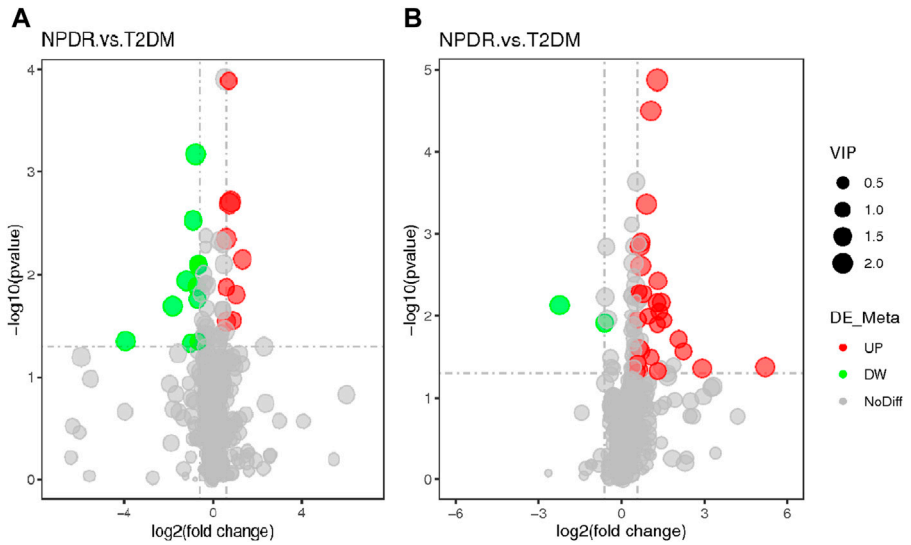

FIGURE 4 | (A) Positive mode. **(B)** Negative mode. The volcano map of the log2 (FC) and −log10 (*p*-value) shows that 93 features were significantly different between NPDR patients (*n* = 15) and T2DM patients (*n* = 15). Significant metabolic features that increased (red dots) or decreased (green dots) in NPDR patients compared with T2DM patients are indicated, and the dot size represents the VIP value. In the positive mode, compared with T2DM patients, 12 metabolic features increased significantly and 14 metabolic features decreased significantly in NPDR patients. In the negative mode, compared with T2DM patients, 35 metabolic features increased significantly and 6 metabolic features decreased significantly in NPDR patients.

TABLE 2 | KEGG enrichment pathways altered in NPDR patients compared with T2DM patients.

Pathway	Overlapping features	Pathway size	*p*-value
Linoleic acid metabolism	2	5	0.002
D-Glutamine and D-glutamate metabolism	1	6	0.038
Nitrogen metabolism	1	6	0.038
Arginine biosynthesis	1	14	0.204
primary bile acid biosynthesis	1	46	0.168
Alpha-linolenic acid metabolism	1	13	0.191
Histidine metabolism	1	16	0.230

With p-value ≤0.05, three metabolic pathways of linoleic acid (p = 0.0024), D-glutamine and D-glutamate (p = 0.0381), and nitrogen (p = 0.0381) were considered to be the significant KEGG enrichment pathways. Overlapping features represent the number of metabolites enriched in the pathway, while pathway size describes the total number of metabolites in each pathway.

and histidine, are shown in **Table 2** and **Supplementary Figure S1**. Metabolites that were key contributors to the pathway differences confirmed with the metabolomics standards initiative (MSI) including glutamate (p = 0.036, AUC = 0.733), phosphatidylcholine (p = 0.022, AUC = 0.740), and 13-hydroperoxyoctadeca-9,11-dienoic acid (13-HPODE) (p = 0.002, AUC = 0.835) showed marked increase in NPDR subjects (**Figure 5**).

Proliferative DR *Versus* Type 2 Diabetic Mellitus

To determine metabolic features that differed between PDR and T2DM, an MWAS was performed to compare PDR patients (n = 15) with T2DM patients (n = 15). In the adjusted analysis, 259 features distinguishing PDR and T2DM groups were identified based on PLS-DA with a VIP >1.0 and adjusted linear regression analysis ($p < 0.05$). Hierarchical clustering analysis showed that between and within T2DM and NPDR groups, there were 118 and 141 metabolic features in positive and negative modes, respectively (**Figure 6**). Based on log2 (FC) and −log10 (p-value) of metabolites, the volcano maps visualized the differences between PDR patients and T2DM patients in positive and negative modes (**Figure 7**). In positive and negative modes, 63 and 108 of the metabolites, respectively, showed good discriminatory power for PDR *versus* T2DM subjects, with an area under the curve (95% CI) > 0.7. In KEGG enrichment pathway analysis, 171 features between PDR patients and T2DM patients revealed enrichment of 39 metabolic pathways, nine of which (metabolism of arginine biosynthesis, linoleic acid, alanine, aspartate and glutamate, D-glutamine and D-glutamate, aminoacyl-tRNA biosynthesis, butanoate, nitrogen, histidine, and tricarboxylic acid cycle) were considered to be the significant KEGG enrichment

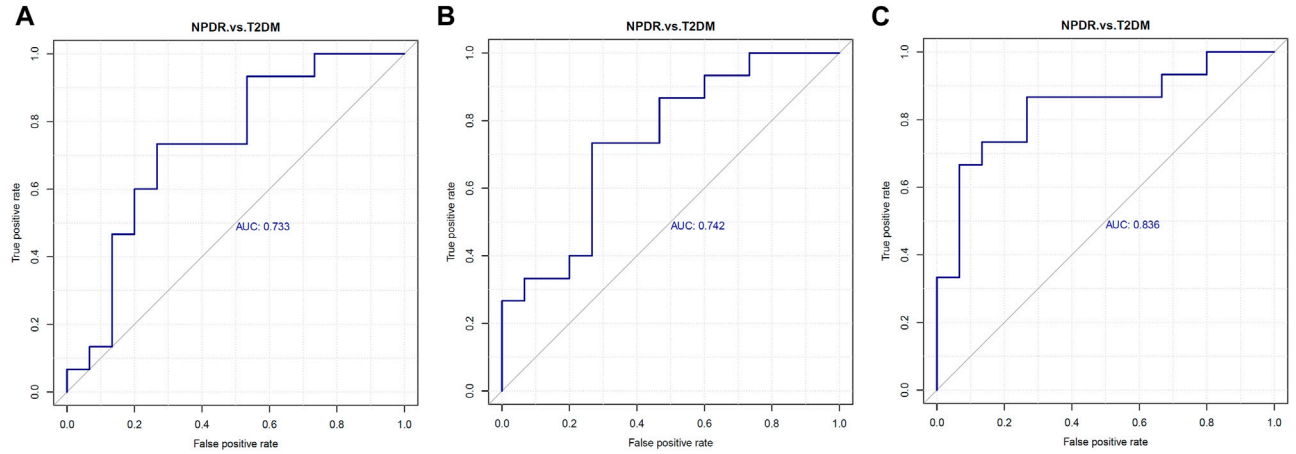

FIGURE 5 | Serum levels of **(A)** glutamate, **(B)** phosphatidylcholine, and **(C)** 13-hydroperoxyoctadeca-9,11-dienoic acid were elevated in NPDR patients. Metabolites enriched in the pathway analyses were further analyzed with $p \leq 0.05$ and using LC-MS/MS, revealing glutamate ($p = 0.036$, AUC = 0.733, VIP = 1.054), phosphatidylcholine ($p = 0.022$, AUC = 0.740,VIP = 1.581), and 13-hydroperoxyoctadeca-9,11-dienoic acid ($p = 0.002$, AUC = 0.835, VIP = 2.622) levels were significantly increased in NPDR patients compared with T2DM patients. AUC, area under the curve.

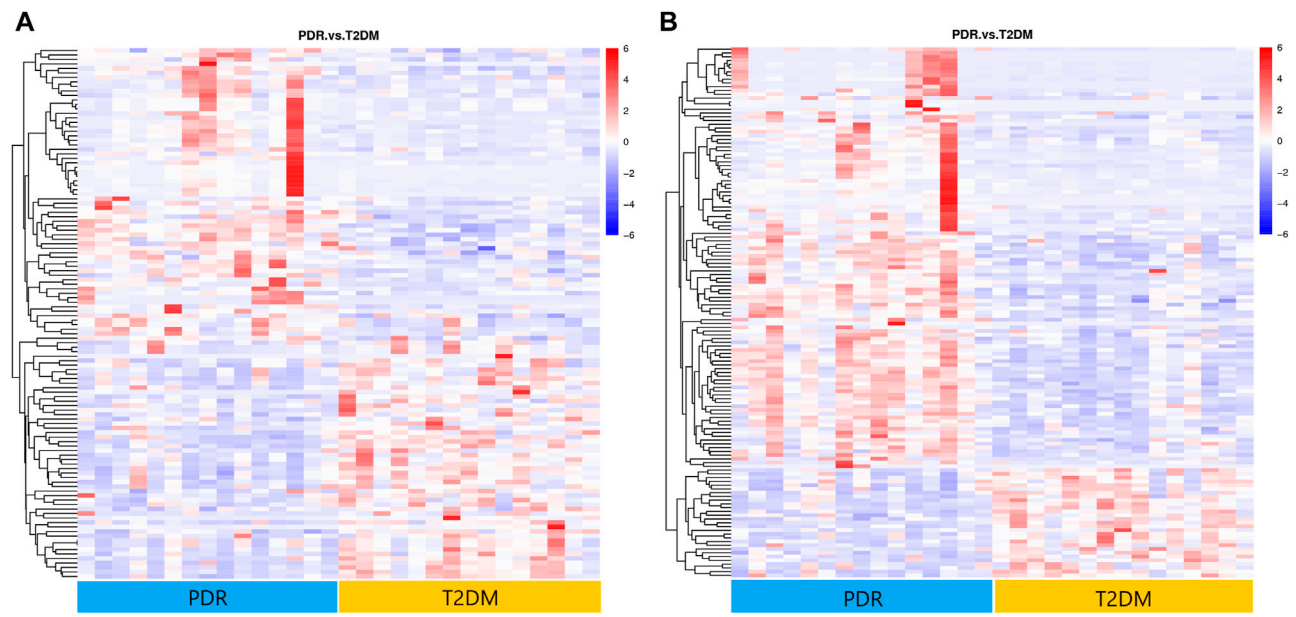

FIGURE 6 | (A) Positive mode. **(B)** Negative mode. Hierarchical clustering analysis based on the intensity of significant metabolite features selected by PLS-DA identified clusters of features that were increased (red) or decreased (blue) in PDR and T2DM patients. There were 141 metabolic features shown in positive mode and 118 metabolic features shown in negative mode.

pathways with p-value ≤ 0.05. The other pathways included biosynthesis of unsaturated fatty acids, glutathione metabolism and glyoxylate and dicarboxylate metabolism (**Table 3** and **Supplementary Figure S2**). Compared with T2DM, metabolites that were major contributors to the pathway differences were increased markedly in PDR subjects, including aspartate ($p = 0.001$, AUC = 0.996), glutamate ($p =$ 1.70E-05, AUC = 0.916), glutamine ($p = 6.43$E-05, AUC = 0.876), ornithine ($p = 9.50$E-04, AUC = 0.827), 2-oxoglutarate ($p = 0.007$, AUC = 0.822), N-acetyl-L-glutamate ($p = 0.002$, AUC = 0.871), N-acetyl-L-aspartate ($p = 0.004$, AUC = 0.813), citrate ($p = 0.011$, AUC = 0.813), phosphatidylcholine ($p = 0.001$, AUC = 0.871), 13-HPODE ($p = 0.001$, AUC = 0.796), methionine ($p = 0.001$, AUC = 0.840), lysine ($p = 0.001$, AUC = 0.831), threonine ($p = 0.002$, AUC = 0.836), phenylalanine ($p = 0.010$, AUC = 0.751), N-(L-arginino) succinate ($p = 0.026$, AUC = 0.796), succinate ($p =$ 0.030, AUC = 0.711), and N (pi)-methyl-L-histidine ($p = 0.031$, AUC = 0.716). On the contrary, linoleate level was ($p = 5.31$E-04,

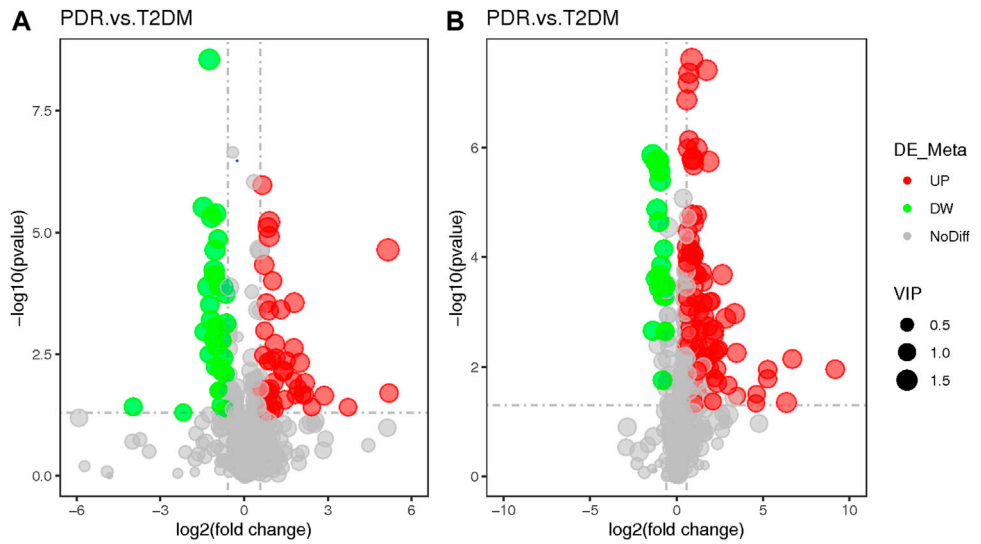

FIGURE 7 | (A) Positive mode. **(B)** Negative mode. The volcano map of the log2 (FC) and −log10 (*p*-value) showed that 259 features were significantly different between PDR patients (*n* = 15) and T2DM patients (*n* = 15). Significant metabolic features that increased (red dots) or decreased (green dots) in PDR patients compared with T2DM patients are indicated with dot size representing the VIP value. In the positive mode, compared with T2DM patients, 39 metabolic features were significantly increased and 24 metabolic features were significantly decreased in PDR patients. In the negative mode, compared with T2DM patients, there were 82 metabolic features.

TABLE 3 | KEGG enrichment pathways altered in PDR patients compared with T2DM patients.

Pathway	Overlapping features	Pathway size	*p*-value
Arginine biosynthesis	8	14	1.7 × 10−8
Alanine, aspartate, and glutamate metabolism	8	28	1.1 × 10−5
Linoleic acid metabolism	3	5	6.9 × 10−4
D-Glutamine and D-glutamate metabolism	3	6	1.3 × 10−3
Aminoacyl-tRNA biosynthesis	7	48	3.4 × 10−3
Butanoate metabolism	3	15	0.023
Nitrogen metabolism	2	6	0.024
Histidine metabolism	3	16	0.028
Tricarboxylic acid cycle	3	20	0.043

With p-value ≤ 0.05, nine metabolism pathways including arginine biosynthesis (p = 1.7 × 10−8), alanine, aspartate and glutamate (p = 1.1 × 10−5), linoleic acid (p = 6.9 × 10−4), D-glutamine and D-glutamate (p = 1.3 × 10−3), aminoacyl-tRNA, biosynthesis (p = 3.4 × 10−3), butanoate (p = 0.023), nitrogen (p = 0.024), histidine (p = 0.028), and tricarboxylic acid cycle (p = 0.049) were considered to be the significant KEGG enrichment pathways. Overlapping features represent the number of metabolites enriched in the pathway, while pathway size describes the total number of metabolites in each pathway.

AUC = 0.871) significantly lower in PDR subjects (**Supplementary Figure S3**).

Proliferative DR *Versus* Non-Proliferative DR

A total of 122 metabolic distinguishable features were detected between PDR patients (*n* = 15) and NPDR patients (*n* = 15) based on PLS-DA with a VIP >1.0 and adjusted linear regression analysis ($p < 0.05$). There were 61 and 61 distinguishable metabolic features in positive and negative modes, respectively, in hierarchical clustering analysis (**Figure 8**). According to log2 (FC) and −log10 (*p*-value) of metabolites, the volcano map could more intuitively display the upregulation and downregulation of differential metabolites in positive and negative patterns between PDR patients and NPDR patients (**Figure 9**). In positive and negative modes with an area under the curve (95% CI) > 0.7, 31 and 48 of the metabolites, respectively, show good discriminatory power for PDR *versus* NPDR subjects. KEGG enrichment pathway analysis using the 79 differential metabolites with VIP > 1.0 and AUC > 0.7 identified enrichment in arginine biosynthesis metabolism, alanine, aspartate and glutamate metabolism, D-glutamine and D-glutamate metabolism, biosynthesis of unsaturated fatty acids, and pantothenate and CoA biosynthesis (**Table 4** and **Supplementary Figure S4**). A Wilcoxon rank sum test was performed on the metabolites that contributed to the enrichment of these pathways to prioritize key metabolites. Compared with NPDR patients, in PDR patients, five key factors, including aspartate ($p = 0.004$, AUC = 0.853),

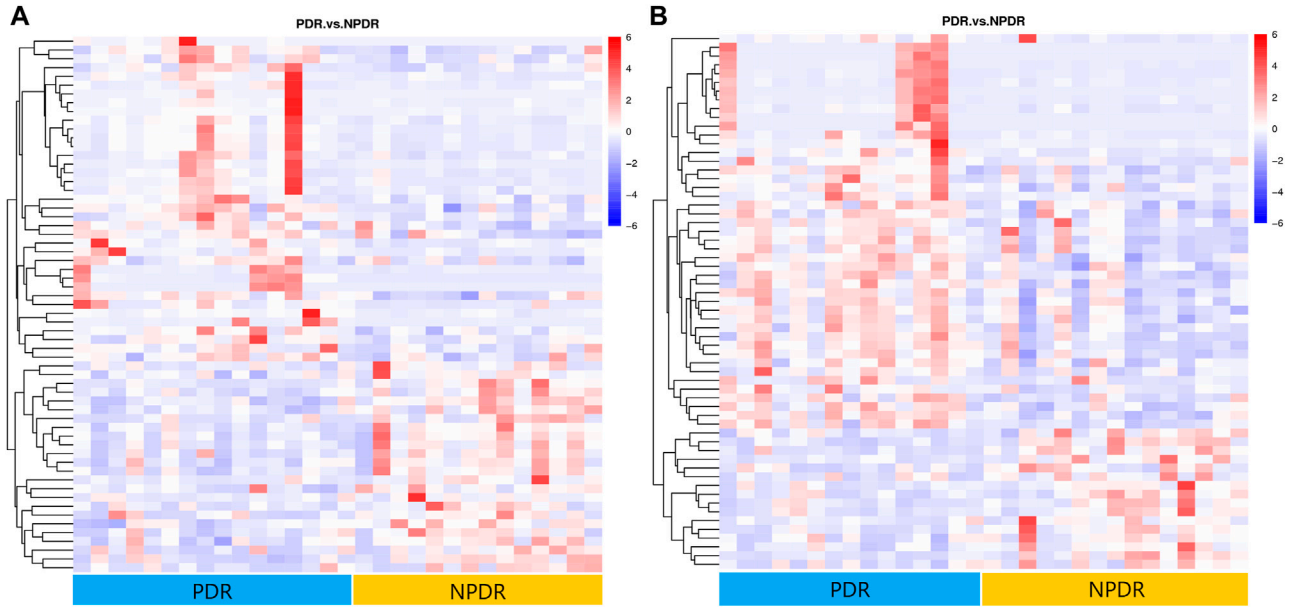

FIGURE 8 | (A) Positive mode. **(B)** Negative mode. Hierarchical clustering analysis based on the intensity of significant metabolite features selected by PLS-DA with a VIP > 1.0 identified clusters of features that were increased (red) or decreased (blue) in PDR patients and NPDR patients. There are 61 metabolic features shown in positive mode and 61 metabolic features shown in negative mode.

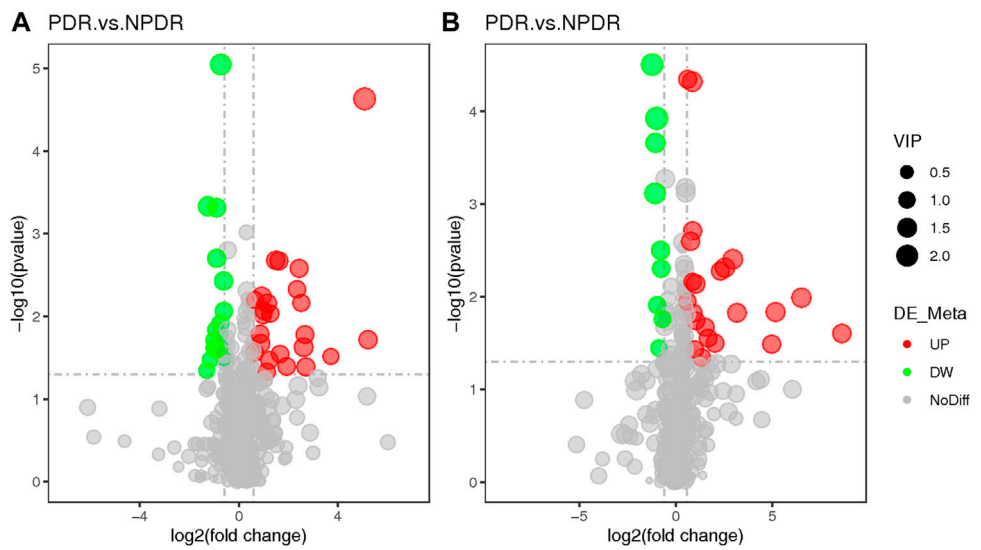

FIGURE 9 | (A) Positive mode. **(B)** Negative mode. Based on log2 (FC) and –log10 (*p*-value) of metabolites, the volcano map showed that 122 features were significantly different between PDR patients (*n* = 15) and T2DM patients (*n* = 15). Metabolic features that were significantly higher (red dots) or lower (green dots) in PDR patients compared with NPDR patients were indicated, with dot size representing the VIP value. In the positive mode, compared with NPDR patients, 20 metabolic features were significantly increased and 11 metabolic features were significantly decreased in PDR patients. In the negative mode, compared with NPDR patients, 33 metabolic features were significantly increased and 15 metabolic features were significantly decreased in PDR patients.

glutamine (p = 6.73E-04, AUC = 0.840), N-acetyl-L-glutamate (p = 0.028, AUC = 0.702), N-acetyl-L-aspartate (p = 0.021, AUC = 0.707), and pantothenate (p = 0.025, AUC = 0.729), significantly increased, and three key factors, including dihomo-gamma-linolenate (p = 5.65E-04, AUC = 0.849), docosahexaenoic acid (p = 0.005, AUC = 0.809), and icosapentaenoic (p = 0.012, AUC = 0.747) levels, were significantly lower (**Supplementary Figure S5**).

TABLE 4 | KEGG enrichment pathways altered in PDR patients compared with NPDR patients.

Pathway	Overlapping features	Pathway size	*p*-value
Arginine biosynthesis	4	14	1.1×10^{-4}
Alanine, aspartate, and glutamate metabolism	5	28	1.6×10^{-4}
D-Glutamine and D-glutamate metabolism	2	6	5.5×10^{-3}
Biosynthesis of unsaturated fatty acids	3	36	0.033
Pantothenate and CoA biosynthesis	2	19	0.043

With p-value ≤0.05 in the Wilcoxon rank-sum test, six metabolic pathways, including arginine biosynthesis metabolism (p = 1.1 × 10−4), alanine, aspartate and glutamate metabolism (p = 1.6 × 10−4), D-glutamine and D-glutamate metabolism (p = 5.5 × 10−3), biosynthesis of unsaturated fatty acids (p = 0.033), and pantothenate and CoA biosynthesis (p = 0.043), were considered to be the significant KEGG enrichment pathways. Overlapping features represent the number of metabolites enriched in the pathway, while pathway size describes the total number of metabolites in each pathway.

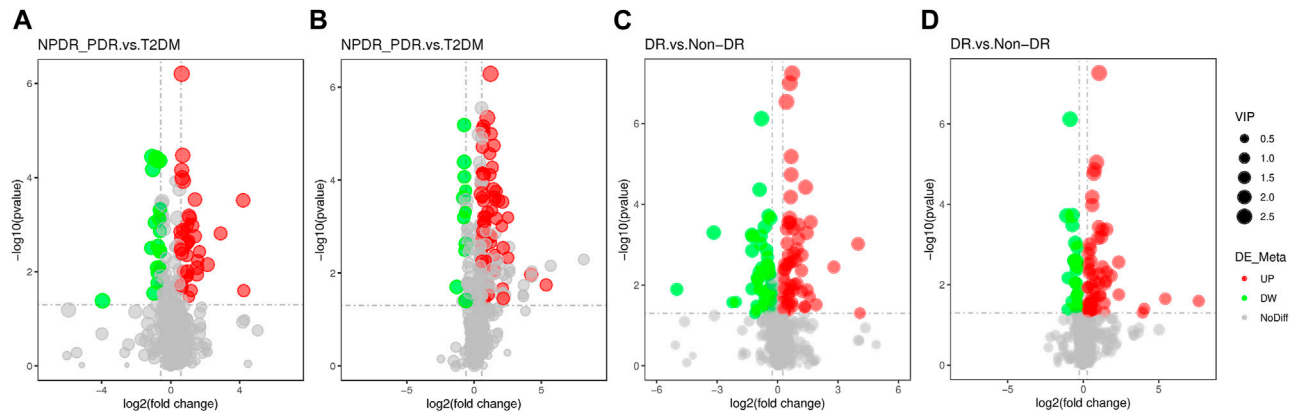

FIGURE 10 | (A) DR (including NPDR and PDR) *versus* T2DM in the positive mode. **(B)** DR (including NPDR and PDR) *versus* T2DM in the negative mode. **(C)** DR *versus* non-DR in the positive mode. **(D)** DR *versus* non-DR in the negative mode. Metabolic features were significantly increased (red dots) or decreased (green dots) in the volcano maps based on log2 (FC) and −log10 (*p*-value) of metabolites. **(A)** and **(B)** The volcano map, respectively, showed that 96 and 113 features were significantly different in positive and negative modes between DR patients (*n* = 30) and T2DM patients (*n* = 15). **(C)** and **(D)** The volcano map, respectively, showed that 112 and 86 features were significantly different in positive and negative modes between DR patients (*n* = 30) and non-DR patients (*n* = 30).

TABLE 5 | KEGG enrichment pathways altered in both DR *versus* T2DM and DR *versus* non-DR.

Pathway	DR *versus* T2DM		DR *versus* non-DR	
	Overlapping features/pathway size	*p*-value	Overlapping features/pathway size	*p*-value
Arginine biosynthesis	8/14	3.3×10^{-9}	5/14	1.0×10^{-4}
Alanine, aspartate, and glutamate metabolism	6/28	2.8×10^{-4}	6/28	4.6×10^{-4}
D-Glutamine and D-glutamate metabolism	3/6	7.4×10^{-4}	2/6	0.019
Linoleic acid metabolism	2/5	0.011	2/5	0.013

There were four enrichment pathways indicated simultaneously in DR versus *T2DM and DR* versus *non-DR in KEGG enrichment pathway analysis with* p-value *≤0.05 in the Wilcoxon rank-sum test.*

We further grouped and analyzed the differential metabolites between DR patients (including NPDR and PDR patients) (*n* = 30) and T2DM patients (*n* = 15), as well as DR patients (including NPDR and PDR patients) (*n* = 30) and non-DR patients (including T2DM patients and diabetic controls) (*n* = 30). In the adjusted analysis based on PLS-DA and adjusted linear regression analysis ($p < 0.05$), 209 and 198 distinguishable metabolic features were detected in DR *versus* T2DM and DR *versus* non-DR, respectively. With an area under the curve (95% CI) > 0.7 in the volcano maps, 138 and 133 metabolites showed good discriminatory power for DR *versus* T2DM subjects and DR *versus* non-DR subjects, respectively (**Figure10**). In KEGG enrichment pathway analysis, the pathways that showed significant enrichment in both DR *versus* T2DM and DR *versus* non-DR were arginine biosynthesis, alanine, aspartate and glutamate metabolism, linoleic acid metabolism, and D-glutamine and D-glutamate metabolism (**Table5** and **Supplementary Figure S6**). The other pathways included aminoacyl-tRNA biosynthesis ($p = 0.005$) and nitrogen metabolism ($p = 0.017$) in DR *versus* T2DM, and butanoate

metabolism ($p = 0.017$) in DR *versus* non-DR. There were 12 key contributors to these pathway differences between DR patients and T2DM patients, 11 of which (glutamate, N-acetyl-L-glutamate, 13-HPODE, aspartate, N-(L-arginino) succinate, threonine, methionine, phosphatidylcholine, oxoglutarate, glutamine, and ornithine) were significantly increased in DR patients, while only the level of eicosatrienoic acid was decreased in DR patients. Compared with non-DR patients, six key factors (glutamate, aspartate, N-acetyl-L-glutamate, 13-HPODE, phosphatidylcholine, and 3-hydroxybutanoate) were significantly increased in DR patients.

DISCUSSION

In order to identify complex endogenous metabolic phenotypes of multifactorial diseases, metabolomics is a powerful tool that can reflect the influence of pathological factors from different sources and the pathophysiological states of diseases (Alshehry et al., 2016) (Mapstone et al., 2014) (Zuo et al., 2021) (Baharum and Azizan, 2018) (Chen et al., 2016).

In our study, the metabolic pathways of arginine biosynthesis and alanine, aspartate, and glutamate metabolism were identified as the major specific metabolic pathways in PDR *versus* T2DM, PDR *versus* NPDR, DR *versus* T2DM, and DR *versus* non-DR. A similar result was observed in a vitreous humor liquid chromatography-mass spectrometry (LC-MS) based metabolomics study (Paris et al., 2016). Numerous studies on diabetic patients and a variety of experimental animal models have demonstrated the importance of the urea cycle and arginine metabolism in diabetes-induced oxidative stress, inflammation, and vascular dysfunction (Sumarriva et al., 2019) (Cao et al., 2019) (Caldwell et al., 2018). Arginine metabolism is a complex process. Ornithine, as a non-protein amino acid, is an intermediate in arginine-proline metabolism and a core part of the urea cycle (Tong et al., 2018). Consistent with our finding, Zuo et al. detected that the intensity of serum ornithine was positively linked to elevated odds of DR (Zuo et al., 2021). To our knowledge, the mechanism of ornithine in DR has not been examined so far. Ornithine is the substrate for the ornithine decarboxylase (ODC) pathway for the production of different polyamines through modulating ODC/polyamine systems. It is also a substrate for ornithine aminotransferase (OAT) to produce proline, which is a critical component for collagen formation (Morris, 2016). Under a hyperglycemic state, arginine produces ornithine and urea by arginine II enzyme (Arg-II enzyme). The elevation of ornithine level indicates the increased activity of the Arg-II enzyme, involved in microglia and macrophage-mediated chronic inflammation injury in type 2 diabetes (Narayanan et al., 2014). Meanwhile, the increased activity of the Arg-II enzyme declined the activity of the nitric oxide synthase (NOS) pathway, which mainly produces nitric oxide. Deficiency of nitric oxide and increased level of polyamine and proline could cause endothelial cell dysfunction, impaired vasodilation function, and inducement of cell proliferation and fibrosis (Stehouwer, 2018). We speculated that this might be closely related to the occurrence and development of DR. Meanwhile, the metabolic roles of serum glutamine, glutamate, and aspartate in diabetic retinopathy have not been clarified. A relevant study in 2021 reported that the pathogenesis of patients with impaired fasting glucose, diabetic microvascular complications, and diabetic peripheral vascular disease was highly correlated with serum glutamine, glutamate, and aspartate metabolism (Li et al., 2021). Another study reported similarly altered patterns of serum amino acids, including glutamine, asparagine, and aspartic acid, in diabetic patients compared with non-diabetic subjects (Zhou et al., 2013).

Another pathway highlighted in NPDR *versus* T2DM, PDR *versus* T2DM, and PDR *versus* NPDR comparisons was D-glutamine and D-glutamate metabolism. Glutamate, derived from glucose through the malate-aspartate shuttle, is not only the signal underlying incretin-induced insulin secretion (Gheni et al., 2014) but also the main excitatory neurotransmitter in the brain, spinal cord, and retina (Takahashi et al., 2019) (Liew et al., 2017) which further leads to the damage of oxidative tissue and increased level of free radicals (Du et al., 2018). Moreover, the ratio of glutamine to glutamate and serum glutamine concentration is closely related to various cellular functions and insulin resistance (Gheni et al., 2014) (Jenstad and Chaudhry, 2013) (Cheng et al., 2012). The roles of serum glutamine and glutamic acid in DR have not been elucidated yet. However, some evidence has pointed out that as diabetes progresses, the accumulation of glutamate in the retina will produce neurotoxic effects, generate an uncontrolled intracellular calcium response in postsynaptic neurons, and accelerate the development of DR and cell death (Coughlin et al., 2017) (Narayanan et al., 2019) (Lieth et al., 2000). In a serum-targeted metabolomics study of diabetic retinopathy, Rhee et al. indicated that serum levels of glutamine and glutamate and their ratios might be novel biomarkers for predicting DR in T2DM. Furthermore, glutamine and glutamate were considered the most unique metabolites in DR (Rhee et al., 2018). These results were consistent with our findings.

Normally, polyunsaturated fatty acids are highly expressed in the retina and regulate many biological processes, including nerve protection, regulation of vascular endothelial growth factor expression, inhibition of retinal neovascularization, prevention of pericyte loss caused by retinal vascular inflammation, and maintenance of retinal capillary structure and integrity (Sasaki et al., 2015). Studies on the relationship between polyunsaturated fatty acids and DR suggested that an elevated level of polyunsaturated fatty acids was negatively correlated with DR and was an independent protective factor for DR (Li et al., 2020) (Zuo et al., 2021). However, a metabolomics study on serum reported that no significant differences in linoleic acid and arachidonic acid intensities exist between DR patients and diabetic controls (Chen et al., 2016). It is not yet clear whether the reduction in polyunsaturated fatty acid composition in diabetic patients is due to increased lipid peroxidation or the changes in lipid synthesis or circulation (Augustine et al., 2020). In our study, linoleic acid metabolic pathways were highlighted by comparing between NPDR and T2DM, PDR and T2DM, DR

and T2DM, and DR and non-DR, which have also been reported in other metabolomics research on DR (Zuo et al., 2021) (Li et al., 2020).

To our knowledge, this study was the first to confirm that the serum levels of phosphatidylcholine and 13-PHODE were closely related to the different stages of diabetic retinopathy of type 2 diabetes in the Asian population. In our study, phosphatidylcholine and 13-PHODE levels were significantly elevated in DR patients compared with T2DM and non-DR patients. Although there is no relevant study on the pathogenesis of phosphatidylcholine in diabetic retinopathy at present, a large prospective study from Harvard University found that higher phosphatidylcholine intake was associated with an increased risk of type 2 diabetes (Li et al., 2015). In addition, a study using targeted metabolomics to identify serum metabolites associated with type 2 diabetes indicated that metabolic alterations, including amino acids and cholinergic phospholipids, were highly associated with a risk of early type 2 diabetes (Floegel et al., 2013). However, in an untargeted serum lipidomic analysis of diabetic retinopathy of type 1 diabetes, 104 lipids, including phosphatidylcholine, of five major lipids were identified as negatively associated with DR grading (Curovic et al., 2020). This discrepancy with our results may owe to the types of diabetes and distinct nationalities of the participants. Although the mechanism of 13-PHODE in the pathogenesis of diabetic retinopathy has not been clarified so far, 13-PHODE has been found to induce inflammatory responses in animal models, which could significantly induce pro-inflammatory gene expression of TNF-α and MCP-1 *in vitro*, most notably in differentiated intestinal epithelial cells (Keewan et al., 2020). The possible involvement of 13-PHODE in mitochondrial dysfunction-related disorders has also been reported (Faizo et al., 2021). Further studies are needed to confirm our findings.

In terms of differential metabolites, in our study, compared with T2DM patients, glutamate, phosphatidylcholine, and 13-PHODE were significantly increased in NPDR patients. The presence of these metabolites may suggest that the manifestations of ocular lesions in diabetic patients could shift from the T2DM stage to the DR stage. Furthermore, increased serum levels of glutamate, aspartate, glutamine, N-acetyl-L-glutamate, and N-acetyl-L-aspartate and decreased levels of dihomo-gamma-linolenate, docosahexaenoic, and cosapentaenoic could be used as differential metabolites between PDR and NPDR patients. These findings suggested that diabetes patients with these differential metabolite profiles should be observed more closely to avoid progression to PDR. Our findings may provide new insights into the management of DR patients and the development of novel treatments for DR patients.

The cohort of DR patients and diabetic controls in the Asian population enrolled from the same institution with standardized sample collection and processing are strengths of the study. Although the generalizability of these results is not yet certain because patients enrolled in this study were all from the same geographic region, the main DR metabolic pathways found in our study were mostly consistent with previous serum metabolomics analyses of DR in western countries. In recent years, there have been four serum untargeted metabolomic studies of diabetic retinopathy, three of which were analyzed through LC-MS (Zuo et al., 2021; Sumarriva et al., 2019; Zhu et al., 2019) and one using gas chromatography-mass spectrometry (GC-MS) (Rhee et al., 2018). Untargeted high-resolution LC-MS, used in this study, is a sensitive technology affected by diet, lifestyle, drugs, and gender that can reflect the overall dynamic changes of all endogenous metabolites such as nucleic acids, proteins, lipids, and other small molecules in organisms. Demographic information and comorbidities of enrolled patients were recorded in detail to minimize the effects of these confounding factors. A previous study by Zhu et al. on serum untargeted metabolomics of patients with DR in China identified four differential metabolites, including fumaric acid, uridine, acetic acid, and cytidine, as potential biomarkers for PDR, and nine KEGG pathways that were significantly enriched in PDR patients compared with NPDR patients (Zhu et al., 2019). Our study further analyzed the differences between NPDR and T2DM patients, PDR and T2DM patients, and DR and non-DR patients. However, studies with a larger sample size and targeted metabolomics validation are needed to determine the identification of metabolites and prevent potential confounding factors from untargeted studies. To our knowledge, this untargeted metabolomics study was the first to specifically compare the metabolic profiles of PDR and NPDR in the Asian population and analyze the metabolic differences between DR and T2DM patients, as well as DR patients and non-DR patients in the Asian population. In conclusion, this metabolomics analysis demonstrates that arginine metabolism, linoleic acid metabolism alanine, aspartate and glutamate metabolism, and D-glutamine and D-glutamate metabolism are dysregulated in the development of DR in the Asian population. Further studies are needed to clarify the roles these pathways and differential metabolites play in the pathogenesis and progression of DR.

DATA AVAILABILITY STATEMENT

The raw data supporting the conclusions of this article will be made available by the authors without undue reservation.

ETHICS STATEMENT

The studies involving human participants were reviewed and approved by Peking University People's Hospital. The patients/participants provided their written informed consent to participate in this study. Written informed consent was obtained from the individual(s) for the publication of any potentially identifiable images or data included in this article.

AUTHOR CONTRIBUTIONS

ZW drafted the work, revised it critically for important intellectual content, and provided approval for publication of the content. JT

revised the work critically for important intellectual content. EJ, YZ, LZ, YC, JH, XS, HQ, TQ, LY, XH, HY, JL, and MZ collected, analyzed, and interpreted data for the work. LH and JQ agreed to be accountable for all aspects of the work in ensuring that questions related to the accuracy or integrity of any part of the work are appropriately investigated and resolved.

FUNDING

This study was supported by the Beijing-Tianjin-Hebei Special Project (Grant Number J200014), Capital Clinical Diagnosis and Treatment Technology Research and Demonstration Application Project of China (Grant Number Z191100006619029), Science and Technology Innovation Project of Chinese Academy of Medical Sciences (2019-RC-HL-019) and the National Natural Science Foundation of China (Grant Number 81670870). The funders had no role in the study design, data collection and analysis, decision to publish or preparation of the manuscript.

SUPPLEMENTARY MATERIAL

The Supplementary Material for this article can be found online at: https://www.frontiersin.org/articles/10.3389/fmolb.2022.871291/full#supplementary-material

REFERENCES

Alshehry, Z. H., Mundra, P. A., Barlow, C. K., Mellett, N. A., Wong, G., Mcconville, M. J., et al. (2016). Plasma Lipidomic Profiles Improve on Traditional Risk Factors for the Prediction of Cardiovascular Events in Type 2 Diabetes Mellitus. *Circulation* 134, 1637–1650. doi:10.1161/circulationaha.116.023233

Augustine, J., Troendle, E. P., Barabas, P., Mcaleese, C. A., Friedel, T., Stitt, A. W., et al. (2020). The Role of Lipoxidation in the Pathogenesis of Diabetic Retinopathy. *Front. Endocrinol. (Lausanne)* 11, 621938. doi:10.3389/fendo.2020.621938

Baharum, S. N., and Azizan, K. A. (2018). Metabolomics in Systems Biology. *Adv. Exp. Med. Biol.* 1102, 51–68. doi:10.1007/978-3-319-98758-3_4

Cabrera, A. P., Monickaraj, F., Rangasamy, S., Hobbs, S., Mcguire, P., and Das, A. (2020). Do Genomic Factors Play a Role in Diabetic Retinopathy? *J. Clin. Med.* 9, 216. doi:10.3390/jcm9010216

Caldwell, R. W., Rodriguez, P. C., Toque, H. A., Narayanan, S. P., and Caldwell, R. B. (2018). Arginase: A Multifaceted Enzyme Important in Health and Disease. *Physiol. Rev.* 98, 641–665. doi:10.1152/physrev.00037.2016

Cao, Y.-F., Li, J., Zhang, Z., Liu, J., Sun, X.-Y., Feng, X.-F., et al. (2019). Plasma Levels of Amino Acids Related to Urea Cycle and Risk of Type 2 Diabetes Mellitus in Chinese Adults. *Front. Endocrinol.* 10, 50. doi:10.3389/fendo.2019.00050

Chen, L., Cheng, C.-Y., Choi, H., Ikram, M. K., Sabanayagam, C., Tan, G. S. W., et al. (2016). Plasma Metabonomic Profiling of Diabetic Retinopathy. *Diabetes* 65, 1099–1108. doi:10.2337/db15-0661

Cheng, S., Rhee, E. P., Larson, M. G., Lewis, G. D., Mccabe, E. L., Shen, D., et al. (2012). Metabolite Profiling Identifies Pathways Associated with Metabolic Risk in Humans. *Circulation* 125, 2222–2231. doi:10.1161/circulationaha.111.067827

Cheung, N., Wong, I. Y., and Wong, T. Y. (2014). Ocular Anti-VEGF Therapy for Diabetic Retinopathy: Overview of Clinical Efficacy and Evolving Applications. *Diabetes Care* 37, 900–905. doi:10.2337/dc13-1990

Coughlin, B. A., Feenstra, D. J., and Mohr, S. (2017). Müller Cells and Diabetic Retinopathy. *Vis. Res.* 139, 93–100. doi:10.1016/j.visres.2017.03.013

Curovic, V. R., Suvitaival, T., Mattila, I., Ahonen, L., Trošt, K., Theilade, S., et al. (2020). Circulating Metabolites and Lipids Are Associated to Diabetic Retinopathy in Individuals with Type 1 Diabetes. *Diabetes* 69, 2217–2226. doi:10.2337/db20-0104

Du, M.-R., Yan, L., Li, N.-S., Wang, Y.-J., Zhou, T., and Jiang, J.-L. (2018). Asymmetric Dimethylarginine Contributes to Retinal Neovascularization of Diabetic Retinopathy through EphrinB2 Pathway. *Vasc. Pharmacol.* 108, 46–56. doi:10.1016/j.vph.2018.05.004

Faizo, N., Narasimhulu, C. A., Forsman, A., Yooseph, S., and Parthasarathy, S. (2021). Peroxidized Linoleic Acid, 13-HPODE, Alters Gene Expression Profile in Intestinal Epithelial Cells. *Foods* 10, 314. doi:10.3390/foods10020314

Floegel, A., Stefan, N., Yu, Z., Mühlenbruch, K., Drogan, D., Joost, H.-G., et al. (2013). Identification of Serum Metabolites Associated with Risk of Type 2 Diabetes Using a Targeted Metabolomic Approach. *Diabetes* 62, 639–648. doi:10.2337/db12-0495

Gao, X., Gauderman, W. J., Marjoram, P., Torres, M., Chen, Y.-D. I., Taylor, K. D., et al. (2014). Native American Ancestry Is Associated with Severe Diabetic Retinopathy in Latinos. *Invest. Ophthalmol. Vis. Sci.* 55, 6041–6045. doi:10.1167/iovs.14-15044

Gheni, G., Ogura, M., Iwasaki, M., Yokoi, N., Minami, K., Nakayama, Y., et al. (2014). Glutamate Acts as a Key Signal Linking Glucose Metabolism to incretin/cAMP Action to Amplify Insulin Secretion. *Cell. Rep.* 9, 661–673. doi:10.1016/j.celrep.2014.09.030

Jenkins, A. J., Joglekar, M. V., Hardikar, A. A., Keech, A. C., O'neal, D. N., and Januszewski, A. S. (2015). Biomarkers in Diabetic Retinopathy. *Rev. Diabet. Stud.* 12, 159–195. doi:10.1900/rds.2015.12.159

Jenstad, M., and Chaudhry, F. A. (2013). The Amino Acid Transporters of the Glutamate/GABA-Glutamine Cycle and Their Impact on Insulin and Glucagon Secretion. *Front. Endocrinol.* 4, 199. doi:10.3389/fendo.2013.00199

Keewan, E., Narasimhulu, C. A., Rohr, M., Hamid, S., and Parthasarathy, S. (2020). Are Fried Foods Unhealthy? the Dietary Peroxidized Fatty Acid, 13-HPODE, Induces Intestinal Inflammation *In Vitro* and *In Vivo*. *Antioxidants (Basel)* 9, 926. doi:10.3390/antiox9100926

Li, J.-s., Wang, T., Zuo, J.-j., Guo, C.-n., Peng, F., Zhao, S.-z., et al. (2020). Association of N-6 PUFAs with the Risk of Diabetic Retinopathy in Diabetic Patients. *Endocr. Connect.* 9, 1191–1201. doi:10.1530/ec-20-0370

Li, X., Li, Y., Liang, Y., Hu, R., Xu, W., and Liu, Y. (2021). Plasma Targeted Metabolomics Analysis for Amino Acids and Acylcarnitines in Patients with Prediabetes, Type 2 Diabetes Mellitus, and Diabetic Vascular Complications. *Diabetes Metab. J.* 45, 195–208. doi:10.4093/dmj.2019.0209

Li, Y., Wang, D. D., Chiuve, S. E., Manson, J. E., Willett, W. C., Hu, F. B., et al. (2015). Dietary Phosphatidylcholine Intake and Type 2 Diabetes in Men and Women. *Diabetes Care* 38, e13–e14. doi:10.2337/dc14-2093

Lieth, E., Lanoue, K. F., LaNoue, K. F., Antonetti, D. A., and Ratz, M. (2000). Diabetes Reduces Glutamate Oxidation and Glutamine Synthesis in the Retina. *Exp. Eye Res.* 70, 723–730. doi:10.1006/exer.2000.0840

Liew, G., Lei, Z., Tan, G., Joachim, N., Ho, I.-V., Wong, T. Y., et al. (2017). Metabolomics of Diabetic Retinopathy. *Curr. Diab Rep.* 17, 102. doi:10.1007/s11892-017-0939-3

Mahajan, N., Arora, P., and Sandhir, R. (2019). Perturbed Biochemical Pathways and Associated Oxidative Stress Lead to Vascular Dysfunctions in Diabetic Retinopathy. *Oxid. Med. Cell. Longev.* 2019, 8458472. doi:10.1155/2019/8458472

Mapstone, M., Cheema, A. K., Fiandaca, M. S., Zhong, X., Mhyre, T. R., Macarthur, L. H., et al. (2014). Plasma Phospholipids Identify Antecedent Memory Impairment in Older Adults. *Nat. Med.* 20, 415–418. doi:10.1038/nm.3466

Morris, S. M., Jr. (2016). Arginine Metabolism Revisited. *J. Nutr.* 146, 2579S–2586S. doi:10.3945/jn.115.226621

Narayanan, S. P., Shosha, E., and D Palani, C. (2019). Spermine Oxidase: A Promising Therapeutic Target for Neurodegeneration in Diabetic Retinopathy. *Pharmacol. Res.* 147, 104299. doi:10.1016/j.phrs.2019.104299

Narayanan, S. P., Xu, Z., Putluri, N., Sreekumar, A., Lemtalsi, T., Caldwell, R. W., et al. (2014). Arginase 2 Deficiency Reduces Hyperoxia-Mediated Retinal Neurodegeneration through the Regulation of Polyamine Metabolism. *Cell. Death Dis.* 5, e1075. doi:10.1038/cddis.2014.23

Ogurtsova, K., Da Rocha Fernandes, J. D., Huang, Y., Linnenkamp, U., Guariguata, L., Cho, N. H., et al. (2017). IDF Diabetes Atlas: Global Estimates for the Prevalence of Diabetes for 2015 and 2040. *Diabetes Res. Clin. Pract.* 128, 40–50. doi:10.1016/j.diabres.2017.03.024

Paris, L. P., Johnson, C. H., Aguilar, E., Usui, Y., Cho, K., Hoang, L. T., et al. (2016). Global Metabolomics Reveals Metabolic Dysregulation in Ischemic Retinopathy. *Metabolomics* 12, 15. doi:10.1007/s11306-015-0877-5

Peng, L., Sun, B., Liu, M., Huang, J., Liu, Y., Xie, Z., et al. (2018). Plasma Metabolic Profile Reveals PGF2α Protecting against Non-proliferative Diabetic Retinopathy in Patients with Type 2 Diabetes. *Biochem. Biophysical Res. Commun.* 496, 1276–1283. doi:10.1016/j.bbrc.2018.01.188

Porta, M., and Striglia, E. (2020). Intravitreal Anti-vegf Agents and Cardiovascular Risk. *Intern Emerg. Med.* 15, 199–210. doi:10.1007/s11739-019-02253-7

Rhee, S. Y., Jung, E. S., Park, H. M., Jeong, S. J., Kim, K., Chon, S., et al. (2018). Plasma Glutamine and Glutamic Acid Are Potential Biomarkers for Predicting Diabetic Retinopathy. *Metabolomics* 14, 89. doi:10.1007/s11306-018-1383-3

Sabanayagam, C., Banu, R., Chee, M. L., Lee, R., Wang, Y. X., Tan, G., et al. (2019). Incidence and Progression of Diabetic Retinopathy: a Systematic Review. *Lancet Diabetes & Endocrinol.* 7, 140–149. doi:10.1016/s2213-8587(18)30128-1

Sasaki, M., Kawasaki, R., Rogers, S., Man, R. E. K., Itakura, K., Xie, J., et al. (2015). The Associations of Dietary Intake of Polyunsaturated Fatty Acids with Diabetic Retinopathy in Well-Controlled Diabetes. *Invest. Ophthalmol. Vis. Sci.* 56, 7473–7479. doi:10.1167/iovs.15-17485

Song, P., Yu, J., Chan, K. Y., Theodoratou, E., and Rudan, I. (2018). Prevalence, Risk Factors and Burden of Diabetic Retinopathy in China: a Systematic Review and Meta-Analysis. *J. Glob. Health* 8, 010803. doi:10.7189/jogh.08.010803

Stehouwer, C. D. A. (2018). Microvascular Dysfunction and Hyperglycemia: A Vicious Cycle with Widespread Consequences. *Diabetes* 67, 1729–1741. doi:10.2337/dbi17-0044

Sumarriva, K., Uppal, K., Ma, C., Herren, D. J., Wang, Y., Chocron, I. M., et al. (2019). Arginine and Carnitine Metabolites Are Altered in Diabetic Retinopathy. *Invest. Ophthalmol. Vis. Sci.* 60, 3119–3126. doi:10.1167/iovs.19-27321

Sun, H., Saeedi, P., Karuranga, S., Pinkepank, M., Ogurtsova, K., Duncan, B. B., et al. (2022). IDF Diabetes Atlas: Global, Regional and Country-Level Diabetes Prevalence Estimates for 2021 and Projections for 2045. *Diabetes Res. Clin. Pract.* 183, 109119. doi:10.1016/j.diabres.2021.109119

Sun, J. K., Keenan, H. A., Cavallerano, J. D., Asztalos, B. F., Schaefer, E. J., Sell, D. R., et al. (2011). Protection from Retinopathy and Other Complications in Patients with Type 1 Diabetes of Extreme Duration. *Diabetes Care* 34, 968–974. doi:10.2337/dc10-1675

Takahashi, H., Yokoi, N., and Seino, S. (2019). Glutamate as Intracellular and Extracellular Signals in Pancreatic Islet Functions. *Proc. Jpn. Acad. Ser. B Phys. Biol. Sci.* 95, 246–260. doi:10.2183/pjab.95.017

Ting, D. S. W., Cheung, G. C. M., and Wong, T. Y. (2016). Diabetic Retinopathy: Global Prevalence, Major Risk Factors, Screening Practices and Public Health Challenges: a Review. *Clin. Exp. Ophthalmol.* 44, 260–277. doi:10.1111/ceo.12696

Tong, F., Liu, S., Yan, B., Li, X., Ruan, S., and Yang, S. (2018). Endogenous Ornithine Decarboxylase/polyamine System Mediated the Antagonist Role of Insulin/PEG-CMCS Preconditioning against Heart Ischemia/reperfusion Injury in Diabetes Mellitus. *Ijn* 13, 2507–2520. doi:10.2147/ijn.s160848

Touzani, F., Geers, C., and Pozdzik, A. (2019). Intravitreal Injection of Anti-VEGF Antibody Induces Glomerular Endothelial Cells Injury. *Case Rep. Nephrol.* 2019, 2919080. doi:10.1155/2019/2919080

Wilkinson, C. P., Ferris, F. L., 3rd, Klein, R. E., Lee, P. P., Agardh, C. D., Davis, M., et al. (2003). Proposed International Clinical Diabetic Retinopathy and Diabetic Macular Edema Disease Severity Scales. *Ophthalmology* 110, 1677–1682. doi:10.1016/s0161-6420(03)00475-5

Wong, T. Y., Cheung, C. M. G, Larsen, M., Sharma, S., and Simó, R. (2016). Diabetic Retinopathy. *Nat. Rev. Dis. Prim.* 2, 16013. doi:10.1038/nrdp.2016.12

Wu, G. (2013). Functional Amino Acids in Nutrition and Health. *Amino acids* 45, 407–411. doi:10.1007/s00726-013-1500-6

Yang, Q. H., Zhang, Y., Zhang, X. M., and Li, X. R. (2019). Prevalence of Diabetic Retinopathy, Proliferative Diabetic Retinopathy and Non-proliferative Diabetic Retinopathy in Asian T2DM Patients: a Systematic Review and Meta-Analysis. *Int. J. Ophthalmol.* 12, 302–311. doi:10.18240/ijo.2019.02.19

Zhong, Y., Wu, J., Yue, S., Zhang, G., Liu, L., and Chen, L. (2018). Burden of Diabetic Retinopathy in Mainland China. *Med. Baltim.* 97, e13678. doi:10.1097/md.0000000000013678

Zhou, Y., Qiu, L., Xiao, Q., Wang, Y., Meng, X., Xu, R., et al. (2013). Obesity and Diabetes Related Plasma Amino Acid Alterations. *Clin. Biochem.* 46, 1447–1452. doi:10.1016/j.clinbiochem.2013.05.045

Zhu, X.-R., Yang, F.-y., Lu, J., Zhang, H.-r., Sun, R., Zhou, J.-B., et al. (2019). Plasma Metabolomic Profiling of Proliferative Diabetic Retinopathy. *Nutr. Metab. (Lond)* 16, 37. doi:10.1186/s12986-019-0358-3

Zuo, J., Lan, Y., Hu, H., Hou, X., Li, J., Wang, T., et al. (2021). Metabolomics-based Multidimensional Network Biomarkers for Diabetic Retinopathy Identification in Patients with Type 2 Diabetes Mellitus. *BMJ open diabetes Res. care* 9, e001443. doi:10.1136/bmjdrc-2020-001443

Conflict of Interest: The authors declare that the research was conducted in the absence of any commercial or financial relationships that could be construed as a potential conflict of interest.

Publisher's Note: All claims expressed in this article are solely those of the authors and do not necessarily represent those of their affiliated organizations or those of the publisher, the editors, and the reviewers. Any product that may be evaluated in this article, or claim that may be made by its manufacturer, is not guaranteed or endorsed by the publisher.

frontiers | Frontiers in Endocrinology

ORIGINAL RESEARCH
published: 28 June 2022
doi: 10.3389/fendo.2022.916789

Cytokine Concentrations in Aqueous Humor of Eyes With Circumscribed Choroidal Hemangioma

Kailin Liu[†], *Lili Guo*[†], *Yong Cheng*[†] *and Jianhong Liang*[*]

Beijing Key Laboratory of Diagnosis and Therapy of Retinal and Choroid Diseases, Eye Diseases and Optometry Institute, Department of Ophthalmology and Clinical Centre of Optometry, Peking University People's Hospital, College of Optometry, Peking University Health Science Center, Beijing, China

OPEN ACCESS

Edited by:
Lian Zhao,
National Eye Institute (NIH), United States

Reviewed by:
Dawei Sun,
The Second Affiliated Hospital of Harbin Medical University, China
Hai Lu,
Capital Medical University, China
Qianru Wu,
Capital Medical University, China

***Correspondence:**
Jianhong Liang
drliangjianhong@126.com

[†]*These authors have contributed equally to this work*

Specialty section:
This article was submitted to Molecular and Structural Endocrinology, a section of the journal Frontiers in Endocrinology

Received: *10 April 2022*
Accepted: *13 May 2022*
Published: *28 June 2022*

Citation:
Liu K, Guo L, Cheng Y and Liang J (2022) Cytokine Concentrations in Aqueous Humor of Eyes With Circumscribed Choroidal Hemangioma. Front. Endocrinol. 13:916789. doi: 10.3389/fendo.2022.916789

Purpose: Anti-vascular endothelial growth factor (anti-VEGF) treatment are now widely used in patients with circumscribed choroidal hemangioma (CCH), however the concentrations of VEGF and other cytokines in CCH patients have not been known before. The study was conducted to compare various cytokine concentrations in the aqueous humor of eyes with CCH and control.

Methods: A total of 16 eyes of 16 patients with CCH, and 15 eyes of 15 patients with cataract as the control group were examined. Aqueous humor samples were assessed for 30 angiogenic and inflammatory cytokines by Luminex bead-based multiplex array.

Results: Significantly, compared with control group, higher concentrations of VEGF-A and IP-10 were found in the CCH patients ($P = 0.002$ and $P < 0.001$).

Conclusions: VEGF-A and IP-10 might be involved with the angiogenic and antiangiogenic process in CCH patients, which provides new insight into the pathophysiology of CCH and could be potential targets for treatment.

Keywords: aqueous humor, cytokines, circumscribed choroidal hemangioma, VEGF - vascular endothelial growth factor, IP-10 (IFN-γ Inducible Protein 10)

INTRODUCTION

Choroidal hemangioma is a benign vascular tumor which is classified into two types based on the extent of choroidal involvement, circumscribed and diffuse. Circumscribed choroidal hemangioma (CCH) generally arises unilaterally and solitarily without systemic associations (1, 2). Although CCH is a benign tumor, it is still a vision threatening condition because of hyperopic shift or exudative retinal detachment (3). When it becomes symptomatic, treatment modalities include photodynamic therapy, laser photocoagulation, transpupillary thermotherapy, external beam and proton beam radiation (PDT), gamma knife radiosurgery, and plaque brachytherapy (4–9). However, because of complications associated with radiotherapy and the less favorable vision outcome, ophthalmologists seek other treatment options for CCH and start to use anti-vascular endothelial growth factor (anti-VEGF) agents to treat CCH and concomitant exudative retinal detachment. In 2009, Sagong et al. first reported that the use of intravitreal bevacizumab, alone or

combined with PDT may be helpful for symptomatic CCH (10). Several studies since then confirmed the effectiveness of intravitreal anti-VEGF agents used in CCH patients (11, 12). However, to our knowledge, there are no evidence showing that the ocular concentration of VEGF actually raises in CCH patients. While VEGF and other cytokines profile in aqueous humor in patients with CCH haven't been reported before, we aim to investigate both angiogenic and inflammatory cytokines in the aqueous humor among CCH patients and controls by using multiplex immunoassay.

METHODS

The Ethics Committee and Institutional Review Board of Peking University People's Hospital approved this study, and written informed consent was obtained from each patient in accordance with the Declaration of Helsinki. All the patients were diagnosed at Peking University People's Hospital. Exclusion criteria included previous intraocular surgery or previous treatment, such as PDT or plaque brachytherapy, concomitant ocular diseases, concomitant systemic diseases such as hypertension or diabetes, prior cardio-cerebrovascular accidents within the past 6 months. Undiluted aqueous humor samples were collected from 16 eyes with CCH before plaque brachytherapy and 15 eyes of cataract patients before cataract surgery. Aqueous samples of 0.05mL from each eye were extracted using a standard sterilization procedure and immediately stored in a freezer at -80°C until assay. And they were tested within 6 months of collection.

Cytokines were measured *via* Luminex X-MAP technology using the Procarta Immunoassay kit (Panomics Inc, Fremont, CA), as described previously (13).

All data were analyzed using SPSS 26.0 for Mac (SPSS, IBM Corp, New York). Data are presented as the mean ± standard deviation, and the normality of the distribution was assessed by the Shapiro–Wilk test. The nonparametric Mann–Whitney rank sum test and *t*-test were performed to compare the differences between the study group and the control group. Two-tailed probability of less than 0.05 was considered to be a statistically significant difference.

RESULTS

The study included 31 patients, with 16 patients in the study group and 15 patients in the control group. The details for all subjects including sex and age were listed in **Table 1**. Men in CCH group and control group were 11 (68.8%) and 7 (46.7%), respectively. Gender was not significantly different among the groups. The average age of the patients with CCH and control was 35.1 ± 17.6 and 65.2 ± 11.1 years old, respectively. However, age showed statistical difference among 2 groups. CCH patients were significantly younger than patients in the control group ($P < 0.001$).

The baseline ocular and tumor characteristics of CCH patients were summarized in **Table 2**. Right eye was involved in 9 patients. The mean largest basal tumor diameter was 11.8 mm (range, 8.2–15.0), and the mean tumor thickness was 3.9mm (range, 2.6-5.9). 10 patients were associated with exudative retinal detachment.

TABLE 1 | Demographics of study population.

Characteristic	CCH patients	Controls	*P* value
No. of patients	16	15	
Gender (male/female)	11/5	7/8	0.213*
Age (mean ± SD)	35.1 ± 17.6	65.2 ± 11.1	< 0.001†
Range	11-70	39-83	

Data are shown as mean ± SD or number.
**X^2 test.*
†Mann-Whitney U test.

TABLE 2 | Summary data on baseline ocular and tumor variables in patients with CCH.

Characteristic	
Eye	
Right	9 (56.3%)
Left	7 (43.7%)
Tumor size	
Base (mean ± SD)	11.8 ± 3.0 (8.2-15.0)
Thickness (mean ± SD)	3.9 ± 1.0 (2.6-5.9)
Exudative retinal detachment	
Yes	10 (62.5%)
No	6 (37.5%)

Data are shown as mean ± SD (range) or number (%).

Table 3 showed the concentrations of the 30 cytokines in the aqueous humor samples. Because the data on the aqueous concentration of IL-6, IL-8, IL-9, IL-23, IL-27, IL-1α, IL-1RA, TNF-β, Eotaxin, GRO-α, IP-10, RANTES, NGF-β, BDNF, EGF, HGF, LIF, PlGF-1, SCF, VEGF-A did not show a normal distribution according to Shapiro-Wilk test, we performed a Mann-Whitney rank-sum test on the data. Among the 30 cytokines, the aqueous humor levels of IP-10 and VEGF-A in the CCH group were significantly higher than the control group ($P = 0.002$, and $P < 0.001$). In contrast, the levels of IL-5, IL-22, IL-9, IL-31, TNF-β, GRO-α, RANTES, NGF-β in the aqueous humor were significantly lower in the CCH group than controls ($P = 0.027$, $P = 0.008$, $P < 0.001$, $P = 0.004$, $P = 0.001$, $P = 0.002$, $P = 0.011$, $P = 0.005$, respectively). **Figure 1** showed ocular examinations and cytokine concentrations in a representative CCH patient.

DISCUSSION

In the present study, we investigated the levels of 30 cytokines in aqueous humor from patients with CCH and controls, and explored whether there were differences among the two groups. Our results revealed that VEGF-A and IP-10 concentrations in aqueous humor of CCH patients were significantly higher than controls. In the meantime, the levels of IL-5, IL-22, IL-9, IL-31, TNF-β, GRO-α, RANTES, NGF-β in the aqueous humor were significantly lower in the CCH group than controls.

VEGF-A is an important pro-angiogenic factor associated with angiogenesis in tumors and retinal vascular disease. Anti-

TABLE 3 | Aqueous humor concentrations (pg/mL) (mean ± SD) of cytokines in CCH patients and subjects undergoing routine cataract surgery (control group).

Cytokine	CCH patients (pg/ml)	Controls (pg/ml)	*P* value
IL-5	6.87 ± 3.63	10.45 ± 4.86	**0.027**
IL-6*	363.38 ± 630.39	760.3 ± 1297.95	0.545
TNF-α	7.35 ± 4.69	9.49 ± 6.65	0.307
IL-22	18.33 ± 3.96	22.57 ± 4.29	**0.008**
IL-23*	17.1 ± 14.4	16.06 ± 8.98	0.711
IL-27*	11.55 ± 13.49	16.08 ± 25.37	0.984
IL-9*	2.81 ± 2.56	6.66 ± 2.88	**<0.001**
IFN-α	2.34 ± 1.13	2.86 ± 1.27	0.237
IL-31	5.18 ± 3.3	9.07 ± 3.55	**0.004**
IL-1α*	0.86 ± 0.76	1.06 ± 0.65	0.401
IL-1RA*	163.37 ± 112.76	522.88 ± 900.32	0.953
IL-7	4.1 ± 1.5	4.49 ± 1.39	0.460
TNF-β*	9.63 ± 10.58	17.73 ± 7.16	**0.001**
Eotaxin*	3.57 ± 1.64	3.75 ± 2.58	0.599
GRO-α*	1.34 ± 1.96	3.39 ± 2.51	**0.002**
IL-8*	9.56 ± 5.46	15.49 ± 11.21	0.093
IP-10*	114.73 ± 63.29	37.48 ± 43.75	**<0.001**
MCP-1	1372.67 ± 260.18	1329.86 ± 376.34	0.714
MIP-1α	1.54 ± 1.13	2.47 ± 1.87	0.104
MIP-1β	19.84 ± 10.42	25.6 ± 17.88	0.278
SDF-1α	184.19 ± 86.93	130.28 ± 70.14	0.068
RANTES*	0.32 ± 0.31	0.63 ± 0.21	**0.011**
NGF-β*	2.6 ± 0.33	2.89 ± 0.32	**0.005**
BDNF*	0.74 ± 0.57	0.79 ± 0.2	0.423
EGF*	1.57 ± 1.61	2 ± 2.46	0.861
HGF*	885.18 ± 364.99	798.38 ± 617.26	0.318
LIF*	19.22 ± 18.25	10.37 ± 7.68	**0.047**
PlGF-1*	2.45 ± 2.85	1.57 ± 1.54	0.682
SCF*	4.63 ± 2.23	4.83 ± 2.48	1.000
VEGF-A*	1217.93 ± 891.82	300.36 ± 152.61	**<0.001**

Data are shown as mean ± SD or number.

*SD, Standard deviation, IL, Interleukin; TNF, tumor necrosis factor; IFNα, interferon-α; GROα, growth-related gene product α; IP-10, interferon inducible protein 10; MCP-1, monocyte chemoattractant protein; MIP-1, macrophage inflammatory protein 1; SDF1-α, stromal-derived factor 1-α; RANTES, regulated upon the activation of normal T cell expressed and secreted; NGF, nerve growth factor; BDNF, brain-derived neurotrophic factor; EGF, epidermal growth factor; HGF, hepatocyte Growth Factor; LIF, leukemia inhibitory factor; PlGF, placental growth factor; SCF, stem cell factor; VEGF, vascular endothelial growth factor. Bold = P value was statistically significant (P < 0.05 was deemed to be statistically significant which using Student t test when data were normal distributed or Mann-Whitney U test when data were unnormal distributed. * means unnormal distribution including IL-6, IL-8, IL-9, IL-23, IL-27, IL-1α, IL-1RA, TNF-β, Eotaxin, GRO-α, IP-10, RANTES, NGF-β, BDNF, EGF, HGF, LIF, PlGF-1, SCF, VEGF-A.*

VEGF therapy has been widely used in the treatment of diabetic retinopathy, retinal vein occlusion and neovascular age-related macular degeneration. With regard to management of intraocular tumors, Kenawy et al. reported that intravitreal anti-VEGF therapy could reduce vasoproliferative retinal tumor-associated exudation (14). Ziemssen et al. reported a rapid decrease in exudation after intravitreal bevacizumab in a patient with juxtapapillary retinal capillary hemangioma (15). On the basis of these observations, Sagong et al. first reported 3 cases of CCH effectively managed with intravitreal bevacizumab alone or combined with PDT (10). Since then, Mandal et al. has documented the complete resolution of leakage after intravitreal bevacizumab in 3 cases of CCH patients and Lai et al. showed that using intravitreal conbercept as primary treatment for exudative CCH was effective in maintaining BCVA and decreasing the central foveal thickness (11, 12). Although anti-VEGF therapy has been proved effective in treating CCH with exudative retinal detachment, the current study is the first report which actually shows the elevation of VEGF-A in aqueous humor of from patients with CCH. This provides a reasonable explanation for the effectiveness of intravitreal anti-VEGF treatment in CCH patients. In the meantime, this indicates further studies are needed to observe the changes of VEGF-A before and after treatment in CCH patients, and the aqueous humor level of VEGF-A in treatment-naïve CCH patients may be a prognostic factor of anti-VEGF treatment responses.

Interferon-inducible protein 10 (IP-10) belongs to a group of α-chemokines and possess high affinity for the CXCR3 receptors found on activated T cells and natural killer cells (16). IP-10 is a chemoattractant to Th1 lymphocytes and monocytes and has antiangiogenic and antifibrotic effect (17). The antiangiogenic effect of IP-10 works through the inhibition of proliferation of endothelial cells and the induced apoptosis of them (18). Furthermore, Bodnar *et al.* found that IP-10 could inhibits VEGF-Induced endothelial tube formation (19). Elevation of IP-10 has been reported in uveal melanoma, diabetic Macular Edema, age-related macular degeneration and polypoidal choroidal vasculopathy (20–23). Our results showed that IP-10 also played a role in the pathophysiology in CCH, probably was a biomarker of angiogenic and antiangiogenic process.

The present study had several limitations, including the relatively small sample size, and the possible bias caused by

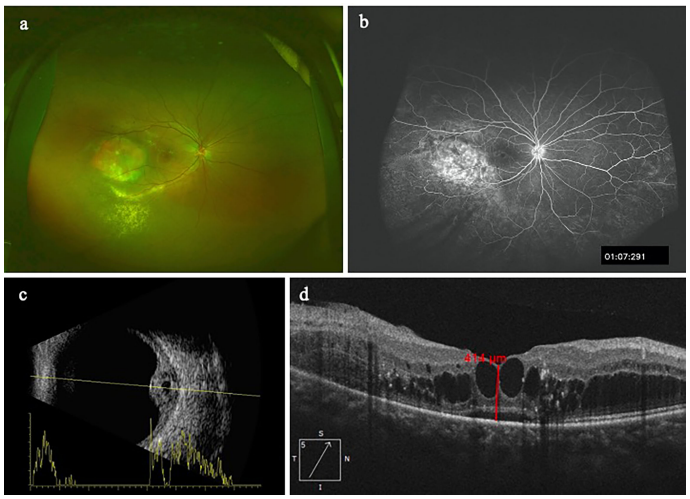

FIGURE 1 | A patient with CCH. The concentration of IP-10 in aqueous humor is 76.4 pg/ml while the concentration of VEGF-A is 987.57pg/ml. **(A)** CCH temporal to the fovea; **(B)** The FFA clearly delineates the hemangioma with leakage; **(C)** Ultrasonography reveals a tumor thickness of 4.3mm; **(D)** OCT image shows intraretinal cystic edema and subretinal fluid.

sample selection. Furthermore, the study design did not allow examination and comparison of the changes of the cytokine concentrations in aqueous humor before and after treatment. Further studies with a larger number of the patients and the investigation of changes of cytokine concentrations are crucial for confirming the role of these angiogenesis and inflammation associated cytokines in the pathophysiology of CCH.

CONCLUSION

Our research studied the concentrations of 30 cytokines in aqueous humor of patients with CCH and the controls. To the best of our knowledge, the cytokine concentrations in aqueous humor of patients with CCH have not been reported in previous researches. In the current study, we found intraocular levels of VEGF-A and IP-10 significantly elevated in patients with CCH, which may be associated with the pathophysiology of CCH. Importantly, these angiogenic and inflammatory cytokines may be potential novel therapeutic target for CCH.

DATA AVAILABILITY STATEMENT

The raw data supporting the conclusions of this article will be made available by the authors, without undue reservation.

ETHICS STATEMENT

The studies involving human participants were reviewed and approved by the Ethics Committee and Institutional Review Board of Peking University People's Hospital. The patients/participants provided their written informed consent to participate in this study.

AUTHOR CONTRIBUTIONS

JL and YC contributed to conception and design of the study. KL and LG organized the database. LG performed the statistical analysis. KL wrote the first draft of the manuscript. LG and YC wrote sections of the manuscript. All authors contributed to manuscript revision, read, and approved the submitted version.

FUNDING

This study was supported by the National Key R&D Program of China (2020YFC2008200); Beijing Municipal Science and Technology Commission (Grant Number Z191100007619041. The funders had no role in the study design, data collection and analysis, decision to publish or preparation of the manuscript.

REFERENCES

1. Shields CL, Honavar SG, Shields JA, Cater J, Demirci H. Circumscribed Choroidal Hemangioma: Clinical Manifestations and Factors Predictive of Visual Outcome in 200 Consecutive Cases. *Ophthalmol* (2001) 108(12):2237–48. doi: 10.1016/s0161-6420(01)00812-0
2. Sen M, Honavar SG. Circumscribed Choroidal Hemangioma: An Overview of Clinical Manifestation, Diagnosis and Management. *Indian J Ophthalmol* (2019) 67(12):1965–73. doi: 10.4103/ijo.IJO_2036_19
3. Stehouwer M, Schlingemann RO, Verbraak FD. High Recurrence Rate in Patients With Choroidal Hemangioma Treated With Limited Single Spot Photodynamic Therapy During Long-Term Follow-Up. *Acta Ophthalmol* (2020) 98(7):679–86. doi: 10.1111/aos.14409
4. Lee JH, Lee CS, Lee SC. Efficacy of Double Dose Photodynamic Therapy for Circumscribed Choroidal Hemangioma. *Retina J Retinal Vitreous Dis* (2019) 39(2):392–7. doi: 10.1097/Iae.0000000000001967
5. Scott IU, Gorscak J, Gass JDM, Feuer WJ, Murray TG. Anatomic and Visual Acuity Outcomes Following Thermal Laser Photocoagulation or

Photodynamic Therapy for Symptomatic Circumscribed Choroidal Hemangioma With Associated Serous Retinal Detachment. *Ophthal Surg Las Im* (2004) 35(4):281–91. doi: 10.3928/1542-8877-20040701-04
6. Cennamo G, Breve MA, Rossi C, Romano MR, de Crecchio G, Cennamo G. Transpupillary Thermotherapy as a Primary Treatment for Circumscribed Choroidal Haemangioma. *Acta Ophthalmol* (2016) 94(2):E167–E9. doi: 10.1111/aos.12810
7. Levy-Gabriel C, Rouic LLL, Plancher C, Dendale R, Delacroix S, Asselain B, et al. Long-Term Results of Low-Dose Proton Beam Therapy for Circumscribed Choroidal Hemangiomas. *Retina J Retinal Vitreous Dis* (2009) 29(2):170–5. doi: 10.1097/IAE.0b013e31818bccfb
8. Chung KS, Chang WS, Chang JH, Lee SC, Chang JW, Park YG, et al. Gamma Knife Radiosurgery for Choroidal Hemangioma: A Single-Institute Series. *World Neurosurg* (2020) 133:E129–E34. doi: 10.1016/j.wneu.2019.08.138
9. Li J, Jin EZ, Liang JH. High-Dose Ruthenium-106 Plaque Therapy for Circumscribed Choroidal Hemangioma: A Retrospective Study of 25 Chinese Patients. *Int J Ophthalmol* (2020) 13(3):425–30. doi: 10.18240/ijo.2020.03.09
10. Sagong M, Lee J, Chang W. Application of Intravitreal Bevacizumab for Circumscribed Choroidal Hemangioma. *Korean J Ophthalmol* (2009) 23 (2):127–31. doi: 10.3341/kjo.2009.23.2.127
11. Mandal S, Naithani P, Venkatesh P, Garg S. Intravitreal Bevacizumab (Avastin) for Circumscribed Choroidal Hemangioma. *Indian J Ophthalmol* (2011) 59(3):248–51. doi: 10.4103/0301-4738.81051
12. Lai K, Gong Y, Xu F, Li L, Huang C, Zhou L, et al. Effectiveness and Safety of Intravitreal Injection of Conbercept as an Initial Treatment for Exudative Circumscribed Choroidal Hemangioma. *Ophthalmologica* (2020) 243(6):436–43. doi: 10.1159/000505753
13. Feng J, Zheng X, Li B, Jiang Y. Differences in Aqueous Concentrations of Cytokines in Paediatric and Adult Patients With Coats' Disease. *Acta Ophthalmol* (2017) 95(6):608–12. doi: 10.1111/aos.13151
14. Kenawy N, Groenwald C, Damato B. Treatment of a Vasoproliferative Tumour With Intravitreal Bevacizumab (Avastin). *Eye (Lond)* (2007) 21 (6):893–4. doi: 10.1038/sj.eye.6702782
15. Ziemssen F, Voelker M, Inhoffen W, Bartz-Schmidt KU, Gelisken F. Combined Treatment of a Juxtapapillary Retinal Capillary Haemangioma With Intravitreal Bevacizumab and Photodynamic Therapy. *Eye (Lond)* (2007) 21(8):1125–6. doi: 10.1038/sj.eye.6702896
16. Luster AD. Chemokines - Chemotactic Cytokines That Mediate Inflammation. *N Engl J Med* (1998) 338(7):436–45. doi: 10.1056/Nejm199802123380706
17. Angiolillo AL, Sgadari C, Taub DD, Liao F, Farber JM, Maheshwari S, et al. Human Interferon-Inducible Protein-10 Is a Potent Inhibitor of Angiogenesis in-Vivo. *J Exp Med* (1995) 182(1):155–62. doi: 10.1084/jem.182.1.155
18. Feldman ED, Weinreich DM, Carroll NM, Burness ML, Feldman AL, Turner E, et al. Interferon Gamma-Inducible Protein 10 Selectively Inhibits Proliferation and Induces Apoptosis in Endothelial Cells. *Ann Surg Oncol* (2006) 13(1):125–33. doi: 10.1245/ASO.2006.03.038
19. Bodnar RJ, Yates CC, Wells A. IP-10 Blocks Vascular Endothelial Growth Factor-Induced Endothelial Cell Motility and Tube Formation *via* Inhibition of Calpain. *Circ Res* (2006) 98(5):617–25. doi: 10.1161/01.RES.0000209968.66606.10
20. Sakurada Y, Nakamura Y, Yoneyama S, Mabuchi F, Gotoh T, Tateno Y, et al. Aqueous Humor Cytokine Levels in Patients With Polypoidal Choroidal Vasculopathy and Neovascular Age-Related Macular Degeneration. *Ophthal Res* (2015) 53(1):2–7. doi: 10.1159/000365487
21. Mo FM, Proia AD, Johnson WH, Cyr D, Lashkari K. Interferon Gamma-Inducible Protein-10 (IP-10) and Eotaxin as Biomarkers in Age-Related Macular Degeneration. *Invest Ophthalmol Visual Sci* (2010) 51(8):4226–36. doi: 10.1167/iovs.09-3910
22. Nagarkatti-Gude N, Bronkhorst IHG, van Duinen SG, Luyten GPM, Jager MJ. Cytokines and Chemokines in the Vitreous Fluid of Eyes With Uveal Melanoma. *Invest Ophthalmol Visual Sci* (2012) 53(11):6748–55. doi: 10.1167/iovs.12-10123
23. Noma H, Mimura T, Yasuda K, Motohashi R, Kotake O, Shimura M. Aqueous Humor Levels of Soluble Vascular Endothelial Growth Factor Receptor and Inflammatory Factors in Diabetic Macular Edema. *Ophthalmol* (2017) 238(1-2):81–8. doi: 10.1159/000475603

Conflict of Interest: The authors declare that the research was conducted in the absence of any commercial or financial relationships that could be construed as a potential conflict of interest.

frontiers | Frontiers in Endocrinology

ORIGINAL RESEARCH
published: 15 July 2022
doi: 10.3389/fendo.2022.899271

Systemic and Ocular Anti-Inflammatory Mechanisms of Green Tea Extract on Endotoxin-Induced Ocular Inflammation

*Kai On Chu[1,2], Kwok Ping Chan[1], Yolanda Wong Ying Yip[1], Wai Kit Chu[1], Chi Chiu Wang[2,3] and Chi Pui Pang[1]**

[1] Department of Ophthalmology and Visual Sciences, The Chinese University of Hong Kong, Hong Kong, Hong Kong SAR, China, [2] Department of Obstetrics and Gynaecology, the Chinese University of Hong Kong, Hong Kong, Hong Kong SAR, China, [3] Li Ka Shing Institute of Health Science, the Chinese University of Hong Kong, Hong Kong, Hong Kong SAR, China

OPEN ACCESS

Edited by:
Lvzhen Huang,
Peking University People's Hospital, China

Reviewed by:
Lian Zhao,
National Eye Institute (NIH), United States
Peizeng Yang,
First Affiliated Hospital of Chongqing Medical University, China

***Correspondence:**
Chi Pui Pang
cppang@cuhk.edu.hk

Specialty section:
This article was submitted to Molecular and Structural Endocrinology, a section of the journal Frontiers in Endocrinology

Received: *18 March 2022*
Accepted: *22 June 2022*
Published: *15 July 2022*

Citation:
Chu KO, Chan KP, Yip YWY, Chu WK, Wang CC and Pang CP (2022) Systemic and Ocular Anti-Inflammatory Mechanisms of Green Tea Extract on Endotoxin-Induced Ocular Inflammation. Front. Endocrinol. 13:899271. doi: 10.3389/fendo.2022.899271

Introduction: Green tea extract (GTE) alleviated ocular inflammations in endotoxin-induced uveitis (EIU) rat model induced by lipopolysaccharide (LPS) but the underlying mechanism is unclear.

Objectives: To investigate the systematic and local mechanisms of the alleviation by untargeted metabolomics using liquid chromatography-tandem mass spectrometry

Methods: Sprague-Dawley rats were divided into control group, LPS treatment group, and LPS treatment group treated with GTE two hours after LPS injection. The eyes were monitored by slip lamp and electroretinography examination after 24 hours. The plasma and retina were collected for metabolomics analysis

Results: In LPS treated rats, the iris showed hyperemia. Plasma prostaglandins, arachidonic acids, corticosteroid metabolites, and bile acid metabolites increased. In the retina, histamine antagonists, corticosteroids, membrane phospholipids, free antioxidants, and sugars also increased but fatty acid metabolites, N-acetylglucosamine-6-sulphate, pyrocatechol, and adipic acid decreased. After GTE treatment, the a- and b- waves of electroretinography increased by 13%. Plasma phosphorylcholine lipids increased but plasma prostaglandin E1, cholanic metabolites, and glutarylglycine decreased. In the retina, tetranor-PGAM, pantothenic derivatives, 2-ethylacylcarinitine, and kynuramine levels decreased but anti-oxidative seleno-peptide level increased. Only phospholipids, fatty acids, and arachidonic acid metabolites in plasma and in the retina had significant correlation ($p < 0.05$, $r > 0.4$ or $r < -0.4$).

Conclusions: The results showed GTE indirectly induced systemic phosphorylcholine lipids to suppress inflammatory responses, hepatic damage, and respiratory mitochondrial stress in EIU rats induced by LPS. Phospholipids may be a therapeutic target of GTE for anterior chamber inflammation

Keywords: green tea extract, ocular inflammation, metabolomics, endotoxin induced uveitis, LCMS (liquid chromatography-mass spectrometry)

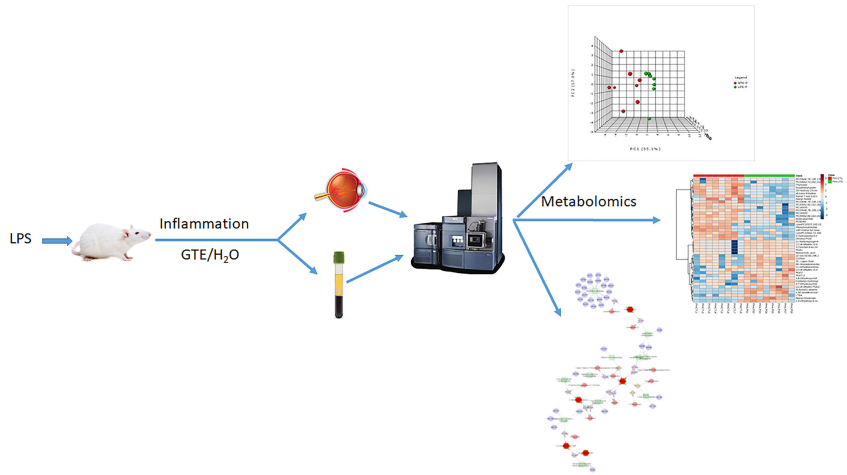

GRAPHICAL ABSTRACT |

INTRODUCTION

Green tea extract (GTE) possesses potent anti-inflammatory and anti-oxidative properties attributed to its biologically active polyphenol constituents, mainly catechins (1). We have shown its anti-inflammatory effects in ocular tissues of rats with lipopolysaccharide (LPS) induced uveitis model (EIU) (2). Uveitis is a complex inflammatory disease that can affect many parts of the eye and lead to severe irritations, visual dysfunction, and even blindness (3, 4). Uveitis can be caused by infectious agents and autoimmunity, but most uveitis patients are idiopathic. Current therapies mainly rely on antibiotics, corticosteroids, antimetabolites, or cytotoxic agents (5). The latter are immunosuppressive and not suitable for many patients. Corticosteroids are effective for acute and chronic treatments of non-infectious ocular inflammation but with possible side effects, including cataract formation, intraocular pressure elevation (6, 7), hypertension, Cushing's syndrome, and osteoporosis (8), especially after long term treatment for chronic and recurrent ocular inflammation. In addition, some uveitis patients do not respond to corticosteroids. GTE catechins have been shown to alleviate ocular inflammations in EIU rats (2, 9) and experimental autoimmune uveoretinitis (EAU) mice (10). Its therapeutic potential is to be explored.

The EIU rat model shows intraocular inflammatory responses at anterior uvea and posterior segments that mimics acute infectious uveitis in human (11–13). Characteristic features of EIU rats include cellular infiltration and intense blood vessel dilation in the iris and the retina. The inflammatory responses had been reported to occur at the 4^{th} hour after LPS injection and reach the peak at the 24^{th} hour (13, 14). Pro-inflammatory mediators, like nitric oxide (NO) and prostaglandin (PGE_2) (15, 16), and intercellular adhesion molecule (ICAM-1) (17), had been found in the inflamed eyes of EIU rats. Pro-inflammatory cytokines tumor necrosis factor-α (TNF–α), interleukin 6 (IL-6), and monocyte chemoattractant protein-1 (MCP-1) were elevated in the anterior chamber. Phosphorylation of nuclear factor-κB (NF-κB) and activation of cluster of differentiation 14 (CD-14) and toll-like receptor 4 (TLR-4) receptors had been detected in the iris and ciliary body (2). In the retina, there were reported increases of TNFα, IL-1β, IL-6, and MMP-9, phosphorylation of NF-κB and signal transducer and activator of transcription 3 (STAT3) in association with 67 kDa laminin receptor (67LR) (9). GTE catechins suppressed the expressions and phosphorylation of these inflammatory proteins, subsequently mediated related metabolic pathways in the cells (18). In this study, we used this model to investigate the underlying mechanisms of how GTE relieve LPS induced inflammation using untargeted metabolomics.

In human endothelial cells with vascular-endothelial-growth factor, after GTE treatment, we found that GTE suppressed cell growth through a wide range of metabolic pathways (19). There was activation of signaling ceramide lipids, antioxidants like ascorbic acid and cysteine, and the energy production vitamin B6 pathway. GTE suppressed nucleotides, the signaling molecule myoinositol, oxidative phosphorylated metabolite succinic acid, and energy production metabolites vitamin B3 and B5. GTE also contributed to homeostatic balance with minimal detrimental pro-oxidative and apoptotic effects. It reportedly protected mouse liver tissues against hepatotoxicity by normalizing blood levels of the energy associated molecules oleoylcarnitine and palmitoylcarnitine, glucose, glutathione, cholic acid, and taurine (19). However, the pharmacodynamic mechanisms of GTE on systemic metabolism and subsequent local anti-inflammation effects on ocular tissues have not been fully elucidated. In this study, we used the metabolomic profiling strategy to investigate the pathological responses involved in the systemic and ocular inflammation induced by LPS in EIU rats and their subsequent suppressions by GTE. We hypothesized that GTE indirectly

alleviated ocular inflammation through systemic rectification rather than directly acting on the ocular tissues.

MATERIALS AND METHODS

Materials

Green tea extract (GTE), Theaphenon E®, kindly provided by Dr. Yukihiko Hara, contained 70% epigallocatechin gallate (EGCG), 5% epigallate catechins (EGC), 4% epicatechin (EC), 0.6% gallocatechin (GC) and had been assessed in our laboratory (20). The optimal dose, 550 mg/kg, for anti-inflammatory effects against the EIU has been verified (21).

Endotoxin-Induced Uveitis and GTE Treatment

All experiments were conducted according to the Association for Research in Vision and Ophthalmology (ARVO) statement on the use of animals. Ethics approval for this study was obtained from the Animal Ethics Committee of the Chinese University of Hong Kong. Female Sprague-Dawley rats (about 250 g, 6–8 weeks old) were obtained from the Laboratory Animal Service Centre of Chinese University of Hong Kong. All animals were housed at 25°C with 12/12 hour light-dark cycles and were allowed to access food and water freely. After overnight fasting and body weights were recorded, EIU was induced by injection of lipopolysaccharide (LPS; *Salmonella typhimurium;* Sigma Chemicals, St. Louis, MO) in sterile saline at 1 mg/kg into a footpad of the rats as previous study (2). In brief, the rats were randomly divided into three groups (n=6): i) control group - footpad injected with saline and oral feeding with water; ii) LPS group - footpad injected with 1 mg/kg LPS and oral feeding with water; iii) GTE group – footpad injected with 1 mg/kg LPS and oral feeding with 550 mg/kg GTE 2 hours later. Twenty-four hours after LPS injection, rats were anesthetized and terminated by taking blood through heart puncture and cervical dislocation. Plasma and retina samples were collected for metabolomics analysis.

Ophthalmic Examinations

Both eyes of the rats were evaluated using a slit lamp as described previously (2). Inflammatory responses including dilation of iris, conjunctival vessels, and iridal hyperemia in the anterior chamber were recorded.

Electroretinography

Three rats in each group were dark-adapted at least 12 hours before electroretinography (ERG). The rats were anesthetized, and pupils were dilated for ERG examination. The amplitude of the b-wave was measured from the trough of the a-wave to the peak of the b-wave in both eyes from each treatment group.

Assays for Phospholipase A2 (PLA2) Activity in Plasma

PLA2 activities in the plasma of rats were assayed by a PLA2 kit (Abcam, Cambridge, UK) according to the manufacturer's instructions.

Plasma and Retina Samples for Metabolomics Studies

The extraction protocols were modified from reported XCMS protocols (22). In brief, blood was withdrawn from heart puncture and centrifuged at 3,000 g for 20 minutes at 4°C. The upper plasma layer was collected and stored at -80°C. For analysis, 100 µL plasma was mixed with 800 µL ice-cold acetonitrile/methanol (1:1), vortexed for 30 seconds, sonicated for 10 minutes in ice, and centrifuged for 15 minutes at 17,000 g at 4°C. The supernatant was vacuum evaporated, the resultant residue dissolved in 50 µL 50% acetonitrile, vortexed, and centrifuged. The reconstituted supernatant was ready for nano-UPLC-MS analysis.

Retina from the sacrificed rats was washed, dried, and snap-frozen by liquid nitrogen for storage at - 80°C. Prior to analysis, it was smashed into powder in liquid nitrogen. The sample molecules were extracted by 80% methanol at -20°C with vortex, sonication in ice, and centrifugation. The supernatant was vacuum evaporated, and the residues dissolved in 50 µL 50% acetonitrile and centrifuged. The reconstituted supernatant was taken for total protein assay (Pierce BCA protein assay kit, Rockford, AZ) and UPLC-MS analysis **(Supplementary Protocols)**.

Liquid Chromatography-Mass Spectrometry Analysis

Hydrophobic analysis was conducted on an ACQUITY nano UPLC M-Class System by reverse-phase separation on a 75 µm × 250 mm × 1.7 µm BEH130 C18 column (Waters, Milford, MA) at 45°C. Hydrophilic analysis was performed on Agilent 1100 micro HPLC system (Santa Clara, CA) and capillary column EX-nano Inertsil CN-3 (GL Sciences, Tokyo, Japan) at 35°C. Metabolites were detected by Micromass Q-Tof Micro mass spectrometry (Waters MS Technologies, Manchester, UK) in both positive and negative ionization modes.

For hydrophobic analysis, 1 µL sample (injection volume adjusted according to the total protein content) was injected at 0.5 µL/min. Mobile phase A was 5% (v/v) acetonitrile in 0.2% acetic acid, and mobile phase B was 95% (v/v) acetonitrile in 0.2% acetic acid. Binary elution gradient was over a duration of 35.5 min: 0 - 1.34 min, 95% A; 1.34 - 15.0 min, 80% A; 15.0 – 18.5 min, 45% A; 18.5 – 20.5 min, 20% A; 20.5 – 30.5 min, 20% A; 30.5 – 32.5 min, 95% A; 32.5 – 35.5 min, 95% A. For hydrophilic analysis, 1 µL sample was injected at 1.5 µL/min. Mobile phase A was 5% (v/v) acetonitrile in 0.2% acetic acid and mobile phase B was 95% (v/v) acetonitrile in 0.2% acetic acid. The gradient elution was 40.0 min: 0 - 5.0 min, 100% B; 5.0 – 15.0 min, 70% B; 15.0 – 18.0 min, 40% B; 18.0 – 21.0 min, 30% B; 21.0 – 24.0 min, 5% B; 24.0 – 32.0 min, 5% B; 32.0 – 33.0 min, 100% B; 33.0 – 40.0 min, 100% B. The procedure was validated according to published studies (23–25) **(Supplementary Protocols)**.

Electrospray (ESI) Mass Spectrometry (MS)

Metabolites were analyzed by positive and negative ionization modes with Nano Lock spray. In positive mode the capillary voltage was 2,800 V, sample cone 35 V, extraction cone 3.0 V, source temperature 130°C, and cone gas rate 80 L/hr. Full scan

was 50 – 1,000 m/z, scan time 1s and inter-scan delay 0.1s. The microchannel plate (MCP) detector was at 2,500 V. Sodium cesium iodide was used for calibration. In negative ESI mode, capillary voltage was -3,500 V, sample cone 35 V, extraction cone 3.0 V, source temperature 120°C, and cone gas rate 80 L/hr. The full scan was 50 – 1,000 m/z, scan time 1s, and interscan delay 0.1s. MCP detector was 2,900 V. All operating parameters were optimized for sensitivity and resolution. Leucine encephalin was used for lock spray calibration. Target analysis by exact mass analysis with target mass ± 0.005 m/z quantified the ionization species of target metabolites and minimized interferences to the validated analysis. The MS/MS profiles of key metabolites were compared with commercially available standards or public databases mainly from XCMS using the above-mentioned LC method with collision energy profile from 20 – 60 eV. Analysis of samples was repeated thrice. The stability of the MS signal intensity over different batches of samples was assessed by selected QC biomarkers from a mixture of control, LPS, and GTE treatment samples for every 12-samples analysis. Stability of QC samples was assessed by the reproducibility (coefficient of variance, CV) of the ion signals **(Supplementary Protocols)**.

Metabolites Investigation

MS data of each sample was processed and compared among the study groups by Markerlynx™ 4.1 (Waters). Metabolites and their adducts were identified by mass (m/z) +/- 10 ppm through the public database METLIN (http://metlin.scripps.edu/) and HMDB (http://www.hmdb.ca/). Identities of metabolites were confirmed by MS/MS fragmentation characteristics from public databases or commercially available standards.

We conducted pathway analysis by METLIN, KEGG (http://www.kegg.com/), Metaboanalyst 3.0 (http://www.metaboanalyst.ca/), IMPaLA (http://impala.molgen.mpg.de/), and Metscape in Cytoscape 3.4. MS data of each sample was processed and compared among the study groups by Markerlynx™ 4.1 (Waters) with ApexTrack peak integration. For extended analysis, S-Plot – P (loadings) was used. The ion counts of each feature were normalized to the total ion intensity. Multivariate analysis and orthogonal partial least square discriminant analysis (OPLS-DA) were conducted. Principle component analysis between groups was performed by Metaboanalyst. Samples were included for analysis if they were within the 95% Hotelling's T2 range, VIP value > 2, R2 > 0.6, and Q2 > 0.5. Markers were selected from the S-Plot above 0.4 of the P (correlation), and $p < 0.05$ by student t-test. Analysis was repeated if fold changes were more than 1.5 or less than 0.75. Fold changes (FC) between control and LPS groups were calculated as the ion count from the control group divided by the ion count from the LPS group. Fold changes between LPS and GTE groups were calculated similarly. For very highly expressed metabolites, > 1,000 fold changes was assigned. If the metabolites were not detected, the fold change would be assigned as < 0.01 folds **(Supplementary Protocols)**.

Statistical Analyses

Fold changes of metabolites from each pair of treatments were compared by independent t-test. Supervision heatmap clustering of metabolites between the control group and LPS group, and between the LPS group and the GTE group, were evaluated by Metaboanalyst using Euclidean and Ward as the clustering parameters. Data were processed by the normalized sum of response, log scale transformation, and Pareto scaling before statistical analysis by Metaboanalyst. Principal component analysis (PCA) by Metaboanalyst was used to differentiate the samples under different treatments. Statistical significance was defined as $p < 0.05$. Averaged parameters were presented as means ± SD.

RESULTS

Clinical Manifestation

Similar to our previous study (2), slit-lamp examination showed inflammatory features in the iris, including hyperemia and edema associated with miosis and fibril formation, which appeared 24 hours after LPS injection but were resolved after GTE ingestion at 2 hours thereafter (**Figures 1A–C**). Clinical scores were increased by LPS induction (0.33 ± 0.52, compared to negative control 3.2 ± 0.41, P < 0.05) and reduced after GTE treatment (2.17 ± 0.41) (P < 0.05). The conductivity of rod photoreceptors and bipolar cells of the retina were not affected by LPS as shown by scotopic ERG (a-wave = 119.1 ± 33.1, b-wave = 443.3.3 ± 98.9, as compared to negative control, a-wave = 115.7 ± 17.3; b-wave = 455.3 ± 75.5), which, however, was slightly increased by 13% (P < 0.05) following GTE treatment (a-wave = 134.4 ± 33.4, b-wave = 521.7 ± 130.5) (**Figure 1D**).

Differentiation of Metabolites in Plasma and Retina After Treatments

Differential patterns of metabolites were found in plasma and retina samples among different treatment groups (**Supplementary Tables 1A, B**). LPS treatment led to decrease in plasma lipids, fatty acids and tyrosine metabolites but increase of arachidonic acid, retinoic acid, corticosteroid, cholestanoic acid, peptides, amino acids, and antioxidants. After GTE treatment, metabolites of lipids, fatty acids, and polyphenol increased while metabolites of arachidonic acid, cholestanoic acid, peptides, and amino acids decreased. In the retina, metabolites of phospholipids, histamine, corticosteroids, and nucleotides decreased but those of vitamins, co-factors, acylcarnitines, and neurotransmitters increased. GTE treatment decreased metabolites of lipids and fatty acids, acylcarnitine, peptides, amino acids, vitamins, co-factors, arachidonic acid, and endogenous antioxidant, but increased those of cyclic nucleotides. Heatmaps showed metabolites related to inflammation, oxidation, signaling, energy suppression, and structural degradation were associated with LPS whereas metabolites related to anti-inflammation, anti-oxidation, signaling activation, energy recovery, and structural molecule synthesis were associated with GTE. Principal component analysis (PCA) showed a clear separation of metabolomic profiles of the samples among different treatments (**Figures 2**, **3**).

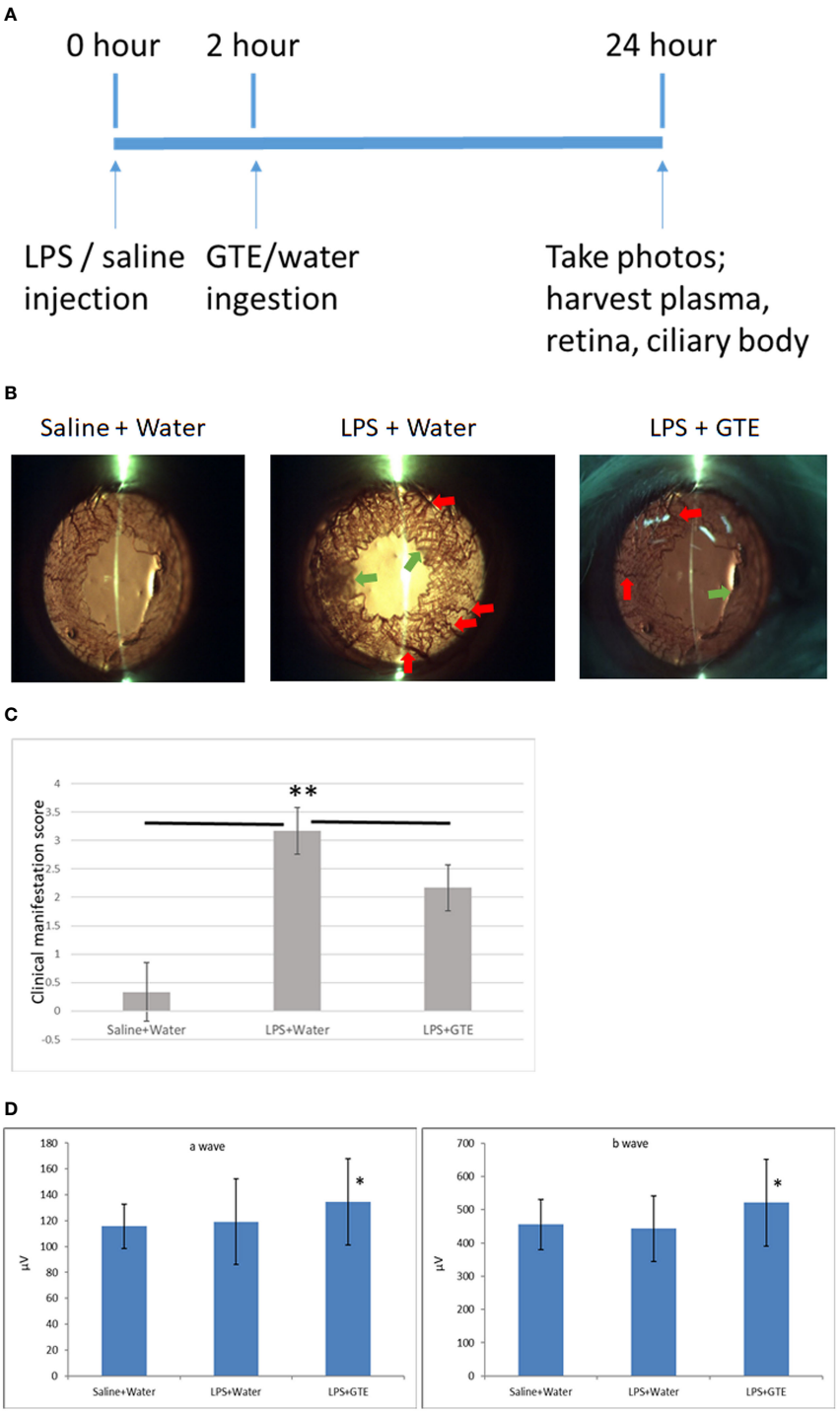

FIGURE 1 | Clinical features of anterior inflammation in the rat eyes. **(A)** Schematic diagram of the experimental procedures. **(B)** Control rats (saline+water ingestion) showed no inflammatory manifestation by slit-lamp examination. Iris of LPS treated EIU rats 24 hours after LPS injection (LPS+water) showed hyperemia (red arrow) and edema (green arrow). EIU rats treated by GTE two hours after LPS injection (LPS+GTE) showed suppression of inflammatory responses. **(C)** Clinical manifestation score of ocular inflammation in normal control rats (saline+water), EIU (LPS+water) rats, and EIU rats treated by GTE (LPS+GTE). n=6 in each group. Error bar indicates standard deviation. **—**: comparison between two groups. ** - $p < 0.05$ comparing with different treatment groups by Mann–Whitney U test. **(D)** Inter-group comparisons of a-wave and b-wave of scotopic ERG amplitudes. Rats were tested 24 hours after LPS injection. The asterisk marked the statistical significance of the comparison between the three groups. Data are also presented as mean ± SD and analyzed by ANOVA test (*$P < 0.05$, n = 3; both eyes from each rat).

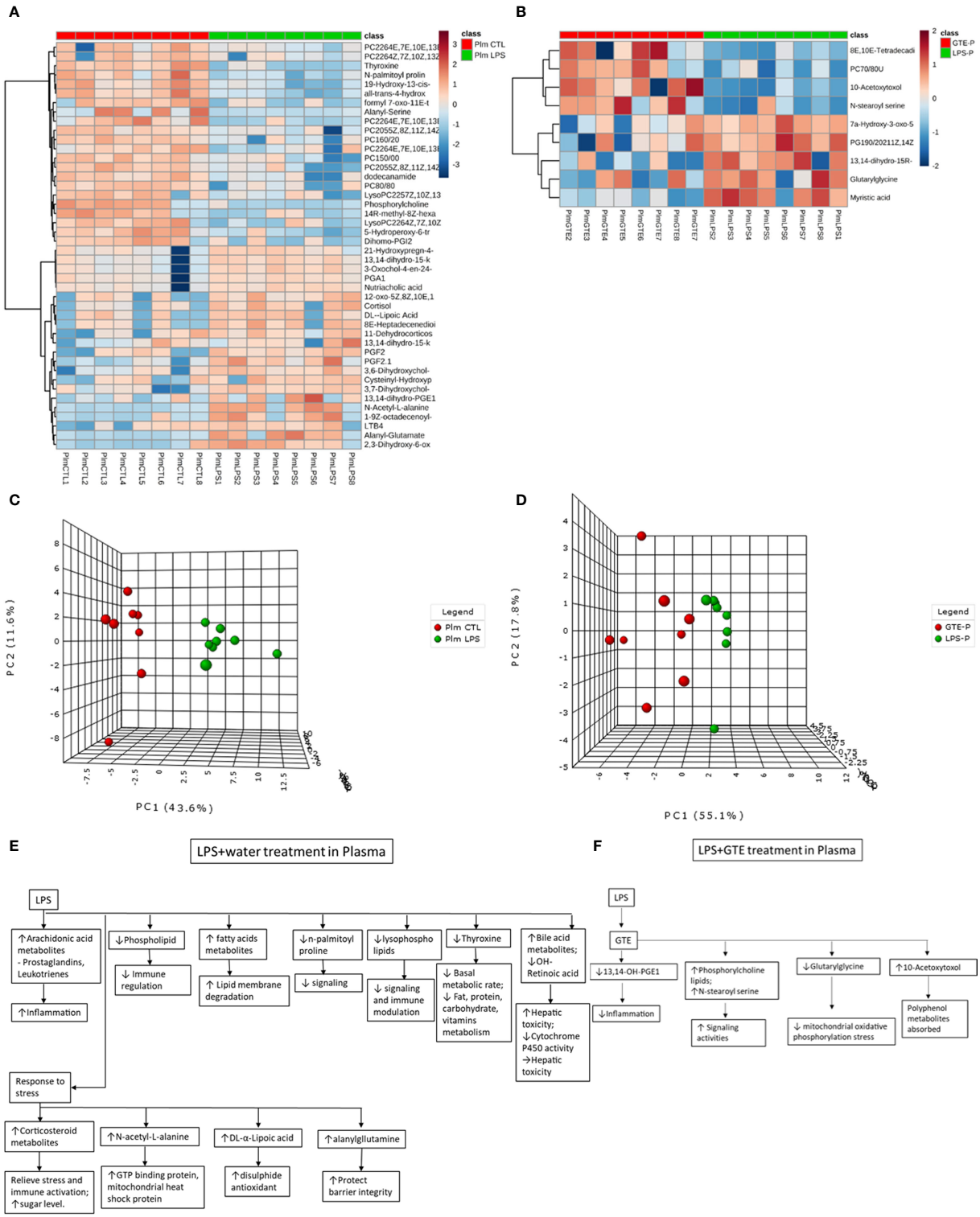

FIGURE 2 | Heatmaps of metabolites showed patterns of differential metabolite profiles between different treatment groups in plasma. **(A)** Between controls and EIU as induced by LPS in the plasma; **(B)** Between EIU induced by LPS and after GTE treatment in the plasma Principal component analysis (PCA) showed **(C)** comparison of controls and EIU induced by LPS, **(D)** comparison of EIU induced by LPS and after GTE treatment samples in plasma. Metabolites and their associated biological activities were shown in **(E)** the plasma of the EIU rats induced by LPS, and **(F)** the plasma of the EIU rats after GTE treatment.

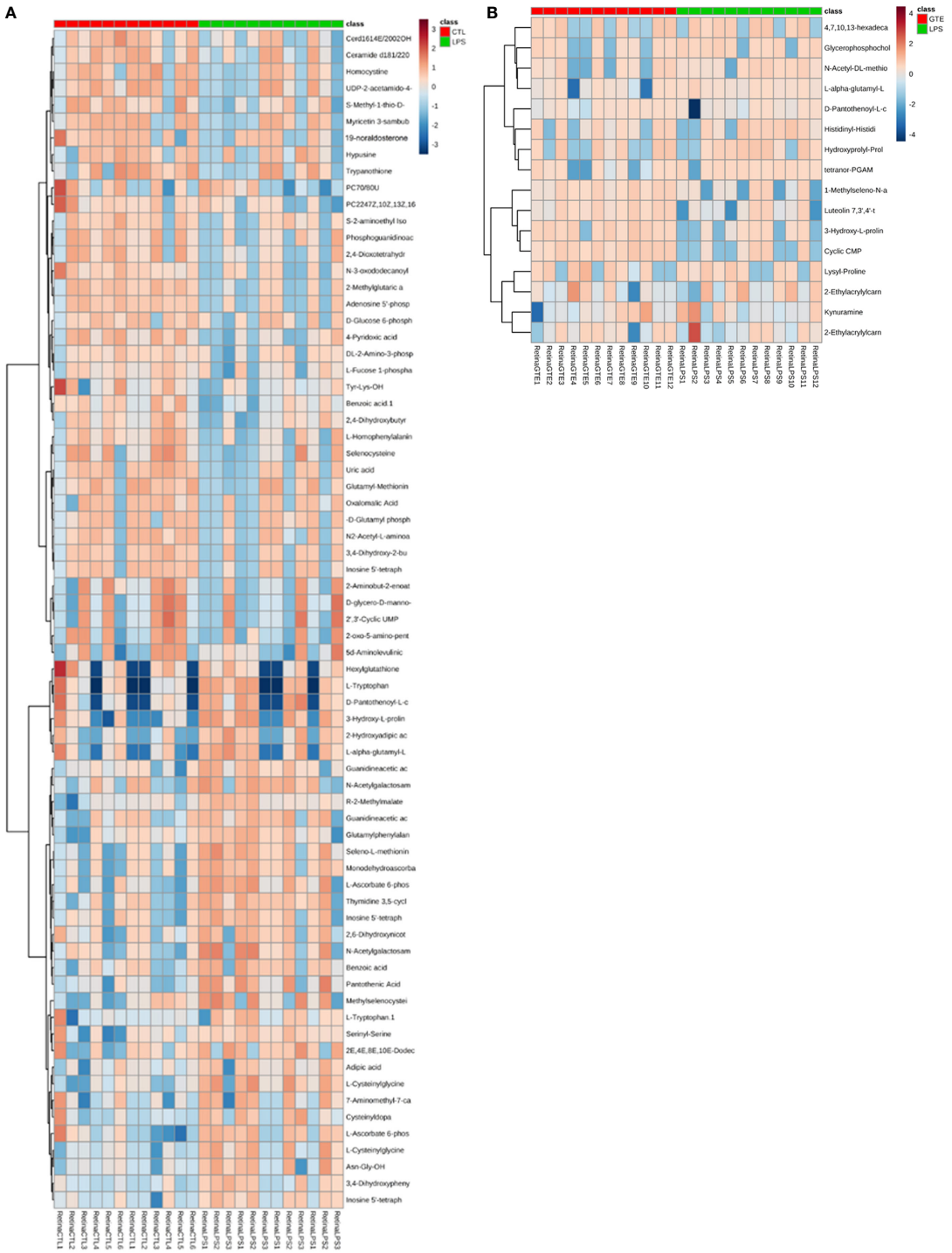

FIGURE 3 | Continued

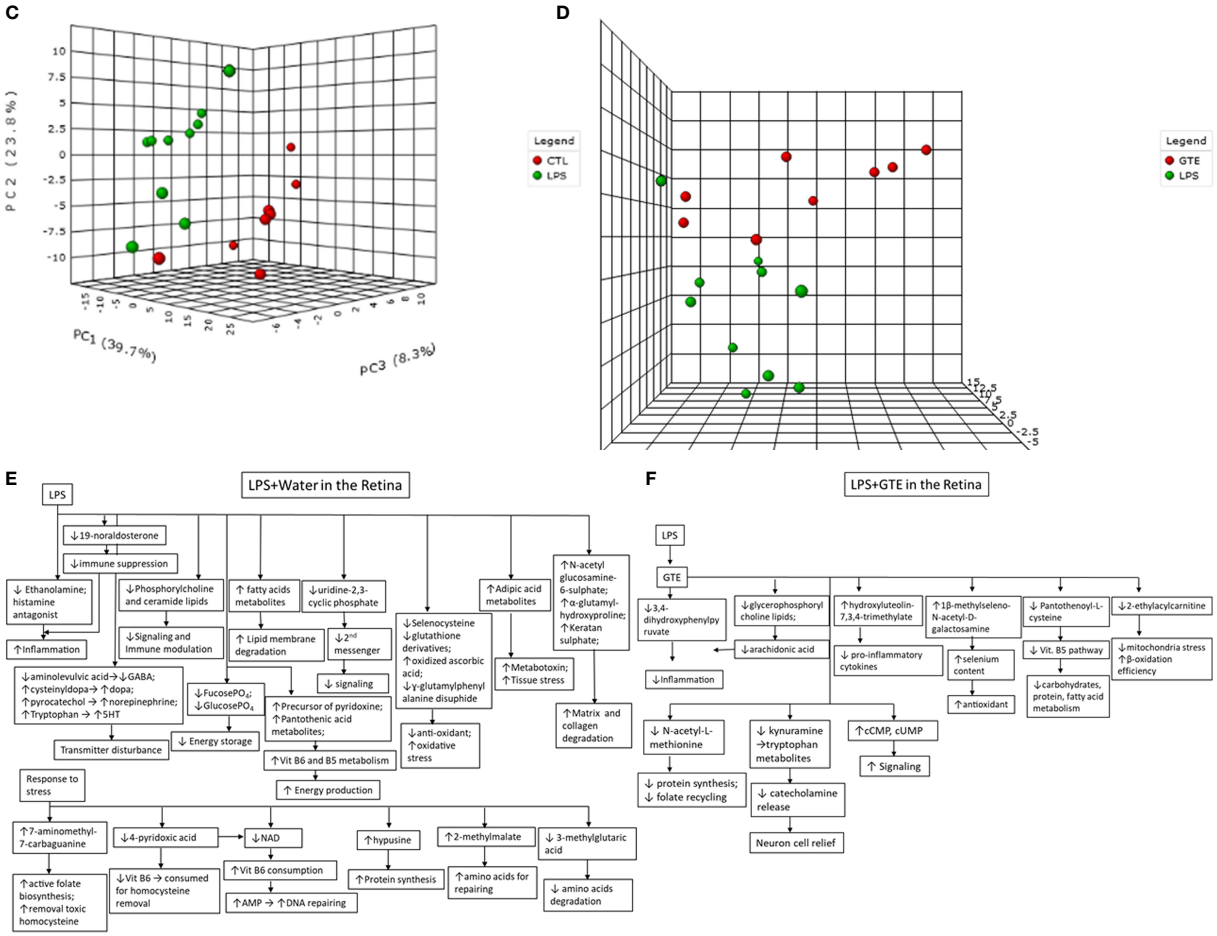

FIGURE 3 | Heatmaps of metabolites showed patterns of differential metabolite profiles between different treatment groups in retina. **(A)** Between controls and EIU as induced by LPS in the retina; **(B)** Between EIU induced by LPS and after GTE treatment in the retina. Principal component analysis (PCA) showed **(C)** comparison of controls and EIU induced by LPS samples in the retina, and **(D)** comparison of EIU induced by LPS induction and after GTE treatment samples in the retina. Metabolites and their associated biological activities were shown in **(E)** the iris ciliary body of the EIU rats after GTE treatment, **(E)** the retina of EIU induced by LPS, and **(F)** the retina of EIU after and GTE treatment.

Pathways Analysis Following LPS and GTE Treatments in Plasma and Retina

Metscape analysis showed that systemic and retinal pathways affected by LPS induction were associated with inflammation, signaling, anti-oxidation, energy production, and biosynthesis. GTE affected systemic and local metabolic pathways involved in inflammation, signaling, energy production, and biosynthesis (**Supplementary Table 2**).

In plasma, pathways activated by LPS were associated with inflammation, such as steroid hormones, prostanoids, and arachidonic acid. Pathways related to signaling such as glycerophospholipid and tyrosine metabolism were depressed. Metabolites related to mitochondrial acitivity, and lipoate metabolism increased. After GTE administration, the systemic pathways associated with arachidonic acid and linoleate metabolism, and fatty acid biosynthesis were depressed while signaling mechanism of glycerophospholipid was activated.

In the retina, LPS induced inflammation-related prostaglandin formation pathway, amino acids metabolism, and vitamin B5 metabolism. LPS modulated energy-related pathways. It depressed fructose, mannose, and vitamin B6 metabolisms but activated vitamin B5-CoA biosynthesis. It depressed signaling related pathway (glycerophospholipid metabolism), anti-oxidation pathway (selenoamino acid metabolism), and nucleotides biosynthesis pathway (pyrimidine metabolism). The pathways activated in the retina following GTE administration were associated with inflammation-modulating signaling pathway (glycosphingolipid biosynthesis) and nucleotide metabolism pathway (pyrimidine metabolism). Inflammation was relieved as shown in the deactivation of prostaglandin formation from arachidonate metabolism, membrane formation (glycerophospholipid biosynthesis), anti-oxidation pathway (methionine and cysteine metabolism), and energy production pathway (vitamin B5 - CoA biosynthesis and fatty acid beta oxidation).

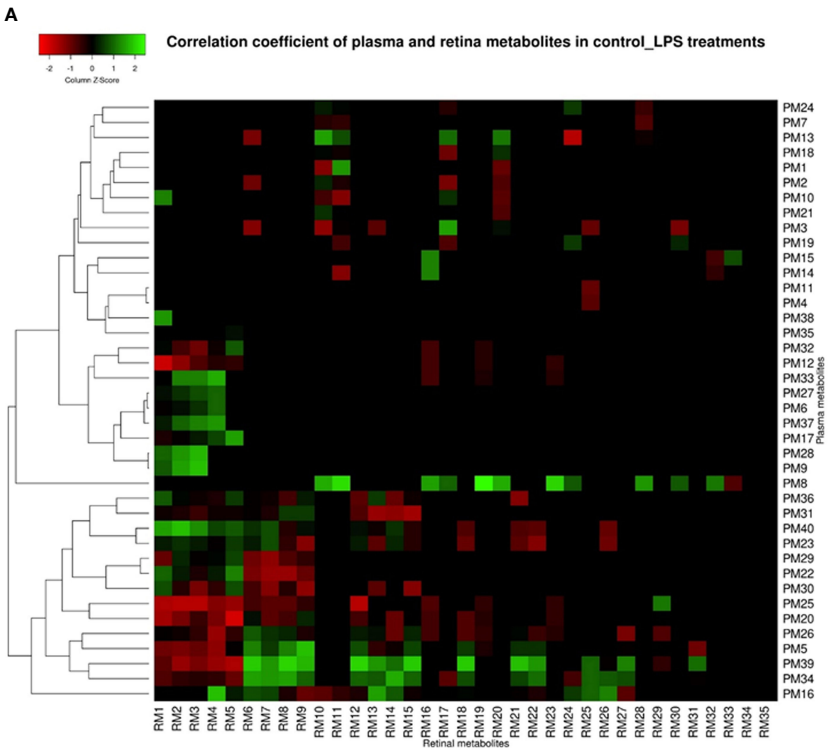

Plasma metabolites	Plasma metabolites symbols	Retina Metabolites	Retinal metabolites symbols
11-Dehydrocorticosterone	PM1	R-2-Aminobut-2-enoate	RM1
12-oxo-5Z,8Z,10E,14Z-eicosatetraenoic acid	PM2	R-2-Methylglutaric acid	RM2
13,14-dihydro-15-keto-PGF1	PM3	R-S-Methyl-1-thio-D-glycerate	RM3
13,14-dihydro-PGE1	PM4	R-R-2-Methylmalate	RM4
14R-methyl-8Z-hexadecenoic acid	**PM5**	R-2-oxo-5-amino-pentanoic acid	RM5
19-Hydroxy-13-cis-retinoic acid	PM6	R-Myricetin 3-sambubioside	RM6
1-9Z-octadecenoyl-2-5Z,8Z,11Z,14Z-eicosatetraenoyl-3-O-alpha-D-glucuronyl-sn-glycerol	PM7	R-Ceramide d181/220	RM7
2,3-Dihydroxy-6-oxo-5-cholan-24-oic Acid	**PM8**	R-Cerd1614E/2002OH	RM8
21-Hydroxypregn-4-ene-3,20-dione hydrogen succinate	PM9	R-Dinor-PGE10	RM9
3,6-Dihydroxycholl-4-en-24-oic Acid	PM10	R-Inosine 5'-tetraphosphate	RM10
3-Oxochol-4-en-24-oic Acid	PM11	R-Thymidine 3,5-cyclic monophosphate	RM11
5-Hydroperoxy-6-trans-8,11,14-cis-eicosatetraenoate 5-HPETE	PM12	R-2,4-Dioxotetrahydropyrimidine D-ribonucleotide	RM12
8E-Heptadecenedioic acid	PM13	R-Hypusine	RM13
Acetyl-L-alanine	PM14	R-D-Glucose 6-phosphate	RM14
Alanyl-Glutamate	PM15	R-Phosphoguanidinoacetate	RM15
Alanyl-Serine	PM16	R-Adipic acid	RM16
all-trans-4-hydroxyretinoic acid	PM17	R-Guanidineacetic acid	RM17
Cortisol	PM18	R-4-Pyridoxic acid	RM18
Cysteinyl-Hydroxyproline	PM19	R-7-Aminomethyl-7-carbaguanine	RM19
Dihomo-PGI2	**PM20**	R-L-Ascorbate 6-phosphate	RM20
DL-Lipoic Acid	PM21	R-S-2-aminoethyl Isothiourea	RM21
dodecanamide	PM22	R-Homocystine	RM22
formyl 7-oxo-11E-tetradecenoate	**PM23**	R-5d-Aminolevulinic Acid	RM23
LTB4	PM24	R-Benzoic acid	RM24
LysoPC22:5Z,10Z,13Z,16Z,19Z	**PM25**	R-Oxalomalic Acid	RM25
LysoPC22:6Z,7Z,10Z,13Z,16Z,19Z	**PM26**	R-L-Fucose 1-phosphate	RM26
N-palmitoyl proline	PM27	R-Uric acid	RM27
Nutriacholic acid	PM28	R-Pantothenic Acid	RM28
PC 15:0/0:0	PM29	R-2,6-Dihydroxynicotinate	RM29
PC 16:0/2:0	**PM30**	R-L-Cysteinylglycine disulfide	RM30
PC 20:5:5Z,8Z,11Z,14Z,17Z/0:0	PM31	R-Selenocysteine	RM31
PC 20:5:5Z,8Z,11Z,14Z,17Z/0:0.1	PM32	R-Seleno-L-methionine	RM32
PC 22:6:4E,7E,10E,13E,16E,19E/0:0U	PM33	R-2E,4E,8E,10E-Dodecatetraenedioic acid	RM33
PC 22:6:4E,7E,10E,13E,16E,19E/0:0U.2	**PM34**	R-Methylselenocysteine Se-oxide	RM34
PC 22:6:4Z,7Z,10Z,13Z,16Z,19Z/0:0	PM35	R-Monodehydroascorbate	RM35
PC 8:0/8:0	PM36		
PGA1	PM37		
PGF2.1	PM38		
Phosphorylcholine	**PM39**		
Thyroxine	**PM40**		

FIGURE 4 | Continued

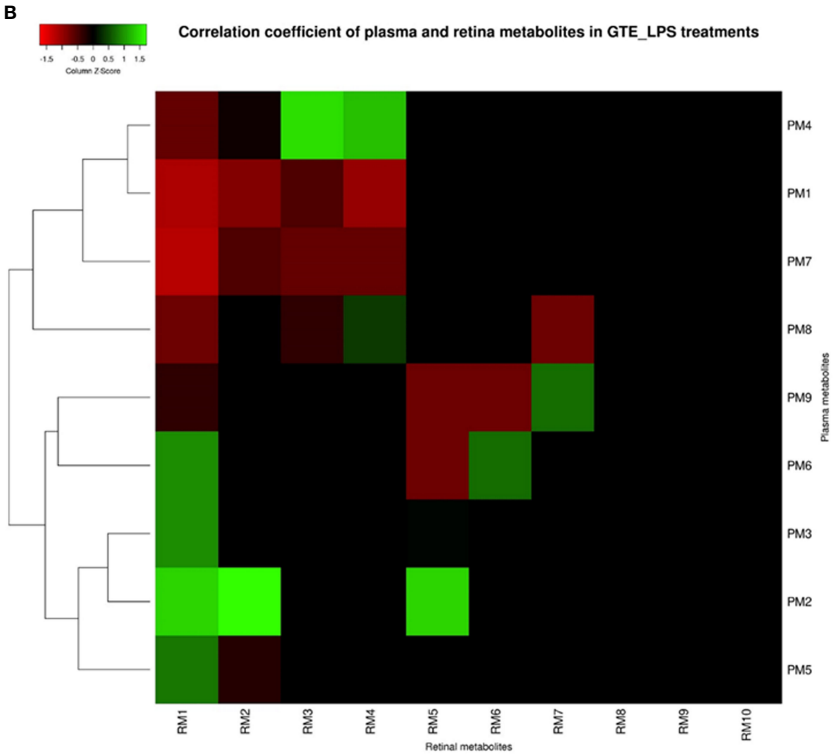

Plasma metabolites	Plasma metabolites symbols	Retina Metabolites	Retinal metabolites symbols
10-Acetoxytoxol	**PM1**	2-Ethylacrylylcarnitine.1	RM1
13,14-dihydro-15R-Prostaglandin E1	**PM2**	Glycerophosphocholine	RM2
7a-Hydroxy-3-oxo-5b-cholanoic acid	PM3	Kynuramine	RM3
8E,10E-Tetradecadienal	**PM4**	2-Ethylacrylylcarnitine	RM4
Glutarylglycine	PM5	4,7,10,13-hexadecatetraenoic acid	RM5
Myristic acid	PM6	Cyclic CMP	RM6
N-stearoyl serine	PM7	D-Pantothenoyl-L-cysteine	RM7
PC 70/80U	**PM8**	1-Methylseleno-N-acetyl-D-galactosamine	RM8
PG190/20211Z,14Z	PM9	L-alpha-glutamyl-L-hydroxyproline	RM9
		tetranor-PGAM	RM10

FIGURE 4 | Heatmap showing the correlation coefficients between systemic metabolites in the plasma associated with metabolites in the retina of EIU rats before and after GTE treatment. The labeled metabolites are the plasma metabolites that gave correlations ($r > 0.5$ or $r < -0.5$; $p < 0.05$) with metabolites in the retina. The heatmaps show the correlation coefficients between systemic metabolites regulation associated with **(A)** metabolites in the retina under LPS induction, and **(B)** metabolites in the retina under GTE treatment. The tables show the labeled metabolites corresponding to the metabolites present in the plasma and the retina. The bold plasma metabolites in the tables indicate that those metabolites give higher correlation coefficients and have wider coverage to the metabolites present in the retina.

Metscape also showed interconnections of pathways of inflammatory mediators, such as prostaglandins, corticosteroids, leukotrienes, arachidonic acids (**Supplementary Figure 1**). Immune-related prostanoids and leukotriene metabolites were elevated whereas the 5-hydroperoxide (5-HPETE), a precursor of leukotriene, was reduced (**Supplementary Figure 2**). LPS also depressed the tyrosine pathway associated with thyroxine biosynthesis (**Supplementary Figure 3**).

Correlation of Metabolites in Plasma With Retina

We correlated the differentially expressed metabolites in the plasma and retina to explore the relationships between metabolites expression in the local ocular tissue and those in circulation. Plasma phospholipids, fatty acid metabolites and bile acid metabolites were highly correlated ($p < 0.05$; $r > 0.4$ or $r < -0.4$) with many metabolites in the retina (**Supplementary Table 3**) (**Figure 4**). After LPS induction, phosphochloline lipid metabolites, PC (22:6 (4E,7E,10E,13E,16E,19E)), lysophosphochloline lipid metabolites, lysoPC (22:6(4Z,7Z,10Z,13Z,16Z,19Z)), and fatty acid metabolite, 14R-methyl-8Z-hexadecenoic acid in the plasma were negatively correlated to 5, 6, 9, and 6 metabolites but were positively correlated to 17, 15, 5, and 13 metabolites in the retina respectively. After GTE treatment, phosphocholine lipid metabolites, PC (7:0/8:0), phospholipid, PG (19:0/20:2(11Z,14Z)) and fatty acid metabolites, N-stearoylserine, in the plasma were negatively correlated to 4, 3, and 4 metabolites but were positively correlated to 0, 1, and 0 metabolite in the retina respectively.

Comparison of PLA2 Activities

Phospholipase A2 (PLA2) hydrolyses the sn-2 position of membrane and plasma glycerophospholipids to release arachidonic acid which is a precursor of eicosanoids such as prostaglandins and leukotrienes for inflammation actions. It also

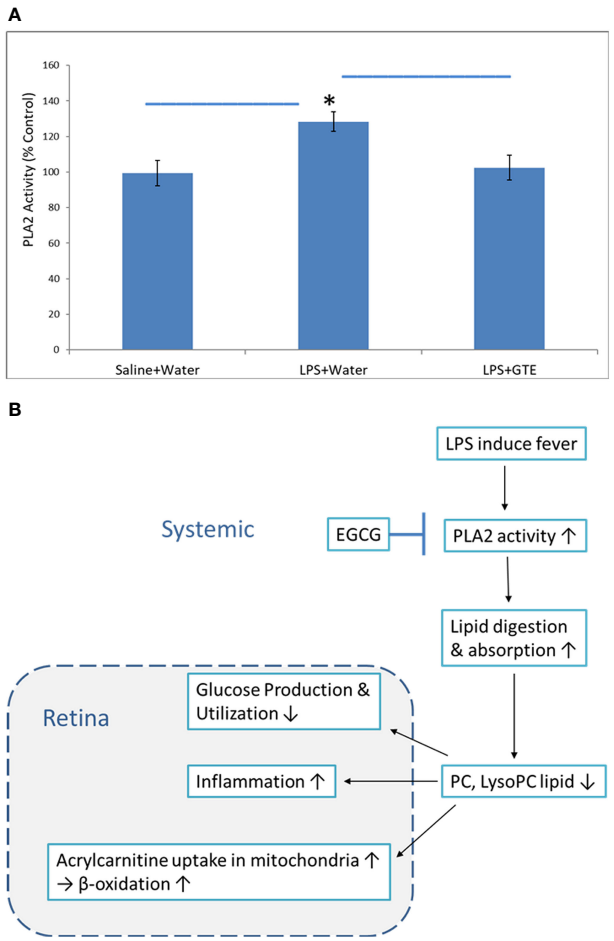

FIGURE 5 | The proposed mechanism of how catechins in GTE inhibit phospholipase A2 (PLA2) activity and alleviate retinal inflammation and metabolic stress. **(A)** The chart shows the relative PLA2 activities in six rat plasma samples of different treatment groups. **(B)** LPS induced fever caused by LPS induced PLA2 activity to increase lipid digestion and subsequently reduce phosphocholine lipids. Catechins inhibited PLA2 activity, increased PC levels, and subsequently inhibited inflammation. *:- a significant difference between groups; error bar:- standard derivation; horizontal bar:- one-way ANOVA comparison between three groups.

produces lipid mediators like lysophospholipids. The relative PLA2 activities in plasma in the LPS group were 128.3 ± 5.5% higher than the negative control and GTE treatment group, 102.5 ± 5.5% ($P < 0.05$) (**Figure 5A**).

DISCUSSION

Inflammation of the iris in our EIU model and the anti-inflammatory effects of GTE treatment were consistent with our previous study (2). In chronic ocular inflammation, neuritis has been reported to detriment neuron conductivity and diminish evoked potential (26). However, in our EIU model of acute ocular inflammation, the conductivity was not affected as shown by ERG in the a- and b-waves. GTE could improve the sensory symptom but not the conductivity of the nerve (27) through anti-oxidation protection (28). In our study, the conductivity of the rod photoreceptors and bipolar cells was improved by GTE treatment (**Figure 1D**), suggesting temporary increase of conductivity by GTE.

Our results showed different systemic and retinal metabolic responses to the LPS induced inflammation and subsequent GTE alleviation. The systemic metabolic responses to LPS included increases in inflammation promoting prostanoids, inflammation resolving corticosteroids, bile acids, endogenous antioxidants, and degraded peptides. There were decreases in structural and signal related lipids and fatty acids, and basal metabolic regulatory hormone thyroid hormone tyrosine. The inflammation was so intensive that 5-hydroperoxide (5-HPETE), a precursor of leukotriene, was exhausted (**Supplementary Figure 2**). The systemic metabolic responses of GTE on LPS induced inflammation included increases in structural and signal related lipids and fatty acids but decreases in inflammation associated prostanoids, bile acids, and degraded peptides. Similarly, the retinal metabolic responses to LPS included increase of energy associated vitamins, co-factors, and metabolites of neurotransmitters but decreases of anti-inflammation related corticosteroids and histamine metabolites, signaling related phospholipids and nucleotide metabolites. The retinal metabolic responses of GTE on LPS induced inflammation included increases in signaling nucleotides metabolites but decreases in structural and signaling related lipid and fatty acid mediators, inflammation associated prostanoids, and energy-related vitamins and co-factors (**Figures 2**, **3**). Taken together, the results suggested that GTE relieved different metabolic and energetic stresses, and resolved structural destruction and toxicity.

Pathway analysis also showed that LPS activated systemic metabolic inflammatory-related pathways, prostaglandin biosynthesis, leukotriene metabolism, and steroid hormone biosynthesis. LPS caused homeostatic responses to release corticosteroids to counter inflammation. In the retina, it activated inflammation pathways, caused protein degradation, and disturbed energy production metabolisms by increased vitamin B5 but decreased vitamin B6, fructose and mannose metabolisms pathways. It also suppressed pathways involving selenoamino acid metabolism to reduce antioxidant capacity and caused oxidative stress. GTE relieved systemic inflammation by suppressing systemic inflammation-related pathways that involved arachidonic acid metabolism and activating cellular signaling glycerophospholipid metabolism. In the retina, it relieved inflammation by activating signaling pathways like the glycosphingolipid biosynthesis pathway and suppressing prostanoid production and glycerophospholipid biosynthesis for membrane signaling (**Supplementary Table 2**).

Significant differentiated metabolite profiles in the plasma were found following LPS induction and after GTE treatment. Phosphorylcholine lipids have anti-inflammatory property and inhibited TNF-α-mediated NF-κB translocation in a dose-dependent manner in Caco-2 cells (29). Classical eicosanoids

from COX mediated metabolites of arachidonic acid and N-acylamides, N-palmitoyl proline, are strongly pro-inflammatory (30). LPS modulates phosphorylcholine lipid, arachidonic acid metabolites, N-palmitoyl proline, thyroxine, and nutriaholic acid, which are associated with inflammation responses (31, 32), basal metabolism, hepatic detriment (33, 34), and signaling (35). Alanylglutamine can reduce infection-induced inflammatory damage, and infection-associated symptoms like dehydration, and inhibits apoptosis due to cellular damage (36). LPS induced homeostatic responses to increase corticosteroids, alanylglutamine, and DL-α-lipoic acid are associated with immune responses (37, 38), mitochondria stress suppression (33), and anti-oxidation recovery (39) (**Figure 2E**) (**Supplementary Table 1A**).

After GTE treatment, it increased phosphorylcholine lipids but lowered free structural lipids, arachidonic acid metabolites, bile acid metabolites, 7alpha-hydroxy-3-oxo-5b-cholanoic acid, and acyl glycine, glutarylglycine, which is associated with mitochondrial fatty acid beta-oxidation as acylglycines, are normally minor metabolites of fatty acids, indicating inflammation was relieved, cellular membrane integrity maintained, hepatic recovered and mitochondria stress relieved (**Figure 2F**) (40). Only polyphenol catabolite, 10-acetoxytoxol, was detected in plasma suggesting extensive metabolism of catechins whose direct anti-inflammatory effects are thus questionable (**Supplementary Table 1B**).

In the retina, LPS lowered the histamine antagonist, ethanolamine and the endogenous antioxidant se-methylselenocysteine but increased the glucocorticoid 19-noraldosterone, the catabolite monodehydroascorbate (41, 42) and tissue damaged associated metabolites, N-acetylglucosamine 6-sulfate and L-alpha-glutamyl-l-hydroxyproline. Homeostatic response increased the absorption of L-ascorbate 6-phosphate, elevated 7-aminomethyl-7-carbaguanine and D-pantothenoyl-L-cysteine (43, 44). But it depleted inflammation mediators, fucose-1-phosphate, and energy sources, D-Glucose-6-phosphate (45), increased membrane signaling lipid metabolites, metabotoxin, adipic acid (46), and increased amino acid precursor, R-2-methylmalate. Neuron activity was compromised as the reduction of neural peptide, N-acetylaspartylglutamic acid, amino acid, aminolevulinic acid, and increasing the melanocytes and neurotransmitters metabolites, cysteinyldopa and pyrocatechol (47, 48). These findings indicate inflammation; oxidative, mitochondrial and retinal stress; and tissue damage have occurred with the activation of energy production and biosynthesis pathways (**Supplementary Tables 1C, D**) (**Figure 3E**).

After GTE treatment, the metabolites profiles in the retina also showed inflammation resolved. GTE reduced the inflammatory prostaglandin metabolite tetranor-PGAM and lowered free glycerophosphocholine level (49). It also decreased the collagen degradant L-alpha-glutamyl-l-hydroxyproline, elevated the selenium antioxidant 1β-methylseleno-N-acetyl-D-galactosamine, decreased antioxidant amino acid metabolites, N-acetyl-L-methionine and energy production associated metabolites, D-pantothenoyl-L-cysteine, and lowered 2-ethylacrylcarnitine and kynuramine. But it increased signaling cyclic CMP (50). L-Carnitine transports fatty acids into the mitochondrial matrix to produce energy. L-carnitine and its esters metabolites increased during oxidative stress (51). Kynuramine is a biogenic amine, which is a major metabolite of melatonin in the brain produced by oxidative and photochemical reactions. Therefore, they can be a biomarker for oxidative stress and inflammation (52). It indicates relief of inflammation and oxidative, mitochondrial, and neuronal stress with recoveries of membrane integrity, cellular activities, and biosynthesis. Presence at a low level of the polyphenol metabolite, 6-hydroxyluteolin-7,3',4'-trimethyl ether, in the retina indicated low bioavailability and extensive metabolism of catechins (**Figure 3F**) (53).

Correlation of the metabolites in the plasma with the retina showed the highest correlated systemic metabolites to retinal metabolites were phosphorylcholine lipids, fatty acids, and arachidonic acid metabolites (**Figure 4**) (**Supplementary Table 3**). The phosphorylcholine lipids involve immune regulation and maintenance of tissue homeostasis. Bioactive endogenous lipids are important mediators in all phases of inflammation involving regulation, fine-tuning, and cessation. While classical eicosanoids are mainly pro-inflammation, some lysoglycerophospholipids and sphingolipids are pro-resolving mediators. Phosphatidylcholine (PC) also showed anti-inflammatory properties against TNF-α induced inflammation in ulcerative colitis (29, 31, 32). LPS caused both ocular and systemic inflammation possibly by suppressing phosphorylcholine lipids production. The systemic levels of phosphatidylcholine and lysophosphatidylcholine were correlated with retinal metabolites. On the other hand, GTE increased systemic phosphatidylcholine and sphingosine metabolite, N-stearoyl serine, were negatively associated with retinal metabolites relating to the malfunction of mitochondria, neuron stress, tissue damage, and inflammation (**Figure 4B**) (54, 55). LPS activated toll-like receptor (TLR-4) expression and induced innate immune response leading to uveitis (56). Phospholipids decreased activation of TLR-4 by competitive interaction with accessory proteins of TLR-4 (57). PLA2 increased lipid digestion and reduced absorption of phosphatidylcholine and lysophosphatidylcholine (58, 59). Catechins inhibited PLA2 and could increase phosphatidylcholine and lysophosphatidylcholine levels and decrease the arachidonic acid (AA), a precursor of eicosanoid metabolites, to release for anti-inflammation (60). In this study, LPS lowered the systemic phosphocholine lipid level and indirectly induced inflammation in the retina. GTE could then inhibit TLR-4 activity indirectly by increasing the systemic phospholipid and sphingosine levels (**Figure 5**).

In our metabolomic study, GTE alone was not used as a control because it affects many metabolic pathways (61). This study aimed to investigate the underlying metabolic mechanisms how GTE can resolve the inflammation induced by LPS, so GTE with LPS served as treatment controls while LPS as a positive control. However, this study is an untargeted metabolomics study. Although we have verified the identity of the metabolites according to the exact mass and fragmentation patterns, we need to do targeted metabolomics to further confirm the identity of each metabolite. Since many metabolites are not commercially available, we cannot perform

a comprehensive targeted metabolomics analysis in this study. Nevertheless, we plan to select a few target phospholipids for further studies and validation.

CONCLUSION

The untargeted metabolomics approach can overview a series of underlying mechanisms of LPS caused inflammation and GTE alleviation simultaneously. It showed LPS induced inflammation involved signaling suppression, oxidative and respiratory stress, and increased energy consumption in the retina. GTE relieved the inflammation was associated with alleviating oxidative, mitochondrial, and neuronal stresses, and energy consumption. GTE may increase systemic phospholipids to alleviate ocular inflammation indirectly rather than act directly with anti-inflammatory effects on the retina tissues. Phospholipids could be a potential therapeutic agent for ocular inflammation.

DATA AVAILABILITY STATEMENT

The original contributions presented in the study are included in the article/**Supplementary Material**. Further inquiries can be directed to the corresponding author.

ETHICS STATEMENT

The animal study was reviewed and approved by the Animal Ethics Committee of the Chinese University of Hong Kong. Written informed consent was obtained from the owners for the participation of their animals in this study.

AUTHOR CONTRIBUTIONS

KOC: conceptualization, methodology, validation, formal analysis, investigation, data curation, writing - original draft, writing - review and editing, visualization, supervision, and project administration; KPC and YY: methodology and investigation; WC: writing - review and editing; CW: review and editing, funding acquisition; CP: writing – review and editing, supervision, resources, and funding acquisition. All authors contributed to the article and approved the submitted version.

FUNDING

The study was funded by Research Grant Council General Research Fund (Project No. 475012 to CCW) and Health and Medical Research Fund (Project No. 12130811 to CPP), Hong Kong.

SUPPLEMENTARY MATERIAL

The Supplementary Material for this article can be found online at: https://www.frontiersin.org/articles/10.3389/fendo.2022.899271/full#supplementary-material

REFERENCES

1. Musial, C, Kuban-Jankowska, A, and Gorska-Ponikowska, M. Beneficial Properties of Green Tea Catechins. *Int J Mol Sci* (2020) 21:1744. doi: 10.3390/ijms21051744
2. Qin, YJ, Chu, KO, Yip, YW, Li, WY, Yang, YP, Chan, KP, et al. Green Tea Extract Treatment Alleviates Ocular Inflammation in a Rat Model of Endotoxin-Induced Uveitis. *PLoS One* (2014) 9:e103995. doi: 10.1371/journal.pone.0103995
3. Durrani, OM, Tehrani, NN, Marr, JE, Moradi, P, Stavrou, P, and Murray, PI. Degree, Duration, and Causes of Visual Loss in Uveitis. *Br J Ophthalmol* (2004) 88:1159–62. doi: 10.1136/bjo.2003.037226
4. Gritz, DC, and Wong, IG. Incidence and Prevalence of Uveitis in Northern California; the Northern California Epidemiology of Uveitis Study. *Ophthalmology* (2004) 111:491–500. doi: 10.1016/j.ophtha.2003.06.014
5. Siddique, SS, Shah, R, Suelves, AM, and Foster, CS. Road to Remission: A Comprehensive Review of Therapy in Uveitis. *Expert Opin Investig Drugs* (2011) 20:1497–515. doi: 10.1517/13543784.2011.617741
6. Pavesio, CE, and Decory, HH. Treatment of Ocular Inflammatory Conditions With Loteprednol Etabonate. *Br J Ophthalmol* (2008) 92(4):455–9. doi: 10.1136/bjo.2007.132621
7. Becker, B, and Mills, DW. Elevated Intraocular Pressure Following Corticosteroid Eye Drops. *JAMA* (1963) 185:884–6. doi: 10.1001/jama.1963.03060110088027
8. Jabs, DA, Rosenbaum, JT, Foster, CS, Holland, GN, Jaffe, GJ, Louie, JS, et al. Guidelines for the Use of Immunosuppressive Drugs in Patients With Ocular Inflammatory Disorders: Recommendations of an Expert Panel. *Am J Ophthalmol* (2000) 130:492–513. doi: 10.1016/s0002-9394(00)00659-0
9. Ren, JL, Yu, QX, Liang, WC, Leung, PY, Ng, TK, Chu, WK, et al. Green Tea Extract Attenuates LPS-Induced Retinal Inflammation in Rats. *Sci Rep* (2018) 8:429. doi: 10.1038/s41598-017-18888-5
10. Li, J, Yip, YWY, Ren, J, Hui, WK, He, JN, Yu, QX, et al. Green Tea Catechins Alleviate Autoimmune Symptoms and Visual Impairment in a Murine Model for Human Chronic Intraocular Inflammation by Inhibiting Th17-Associated Pro-Inflammatory Gene Expression. *Sci Rep* (2019) 9:2301. doi: 10.1038/s41598-019-38868-1
11. Rosenbaum, JT, McDevitt, HO, Guss, RB, and Egbert, PR. Endotoxin-Induced Uveitis in Rats as a Model for Human Disease. *Nature* (1980) 286:611–3. doi: 10.1038/286611a0
12. Howes, ELJr, Aronson, SB, and McKay, DG. Ocular Vascular Permeability. Effect of Systemic Administration of Bacterial Endotoxin. *Arch Ophthalmol* (1970) 84:360–7. doi: 10.1001/archopht.1970.00990040362017
13. Kogiso, M, Tanouchi, Y, Mimura, Y, Nagasawa, H, and Himeno, K. Endotoxin-Induced Uveitis in Mice. 1. Induction of Uveitis and Role of T Lymphocytes. *Jpn J Ophthalmol* (1992) 36:281–90.
14. Bhattacherjee, P, Williams, RN, and Eakins, KE. An Evaluation of Ocular Inflammation Following the Injection of Bacterial Endotoxin Into the Rat Foot Pad. *Invest Ophthalmol Vis Sci* (1983) 24:196–202.
15. Moita, E, Gil-Izquierdo, A, Sousa, C, Ferreres, F, Silva, LR, Valentão, P, et al. Integrated Analysis of COX-2 and iNOS Derived Inflammatory Mediators in LPS-Stimulated RAW Macrophages Pre-Exposed to Echium Plantagineum L. Bee Pollen Extract. *PloS One* (2013) 8:e59131. doi: 10.1371/journal.pone.0059131
16. Kozak, YD, Omri, B, Smith, JR, Naud, MC, Goldenberg, BT, and Crisanti, P. Protein Kinase Cζ (Pkcζ) Regulates Ocular Inflammation and Apoptosis in Endotoxin-Induced Uveitis (EIU). *Am J Pathol* (2007) 170:1241–57. doi: 10.2353/ajpath.2007.060236

17. Ruiz-Moreno, JM, Thillaye, B, and de Kozak, Y. Retino-Choroidal Changes in Endotoxin-Induced Uveitis in the Rat. *Ophthalmic Res* (1992) 24:162–8. doi: 10.1159/000267163
18. Chu, KO, Chan, SO, Pang, CP, and Wang, CC. Pro-Oxidative and Antioxidative Controls and Signaling Modification of Polyphenolic Phytochemicals: Contribution to Health Promotion and Disease Prevention? *J Agric Food Chem* (2014) 62:4026–38. doi: 10.1021/jf500080z
19. Lu, YH, Sun, JC, Katya, P, Yang, X, Greenhaw, J, Salminen, WF, et al. Metabolomics Evaluation of the Effects of Green Tea Extract on Acetaminophen-Induced Hepatotoxicity in Mice. *Food Chem Toxicol* (2013) 62:707–21. doi: 10.1016/j.fct.2013.09.025
20. Chu, KO, Chan, KP, Wang, CC, Chu, CY, Li, WY, Choy, KW, et al. Green Tea Catechins and Their Oxidative Protection in the Rat Eye. *J Agric Food Chem* (2010) 58:1523–34. doi: 10.1021/jf9032602
21. Yang, Y, Qin, YJ, Yip, YW, Chan, KP, Chu, KO, Chu, WK, et al. Green Tea Catechins are Potent Anti-Oxidants That Ameliorate Sodium Iodate-Induced Retinal Degeneration in Rats. *Sci Rep* (2016) 6:29546. doi: 10.1038/srep29546
22. Available at: https://xcmsonline.scripps.edu/landing_page.php?pgcontent=institute.
23. Naz, S, Vallejo, M, García, A, and Barbas, C. Method Validation Strategies Involved in non-Targeted Metabolomics. *J Chromatogr A* (2014) 1353:99–105. doi: 10.1016/j.chroma.2014.04.071
24. Kamleh, MA, Snowden, SG, Grapov, D, Blackburn, GJ, Watson, DG, Xu, N, et al. LC-MS Metabolomics of Psoriasis Patients Reveals Disease Severity-Dependent Increases in Circulating Amino Acids That are Ameliorated by Anti-Tnfα Treatment. *J Proteome Res* (2015) 14:557–66. doi: 10.1021/pr500782g
25. Kenny, LC, Broadhurst, DI, Dunn, W, Brown, M, North, RA, McCowan, L, et al. Robust Early Pregnancy Prediction of Later Preeclampsia Using Metabolomic Biomarkers. *Hypertension* (2010) 56:741–9. doi: 10.1161/HYPERTENSIONAHA.110.157297
26. Atilla, H, Tekeli, O, Ornek, K, Batioglu, F, Elhan, AH, and Eryilmaz, T. Pattern Electroretinography and Visual Evoked Potentials in Optic Nerve Diseases. *J Clin Neurosci* (2006) 13:55–9. doi: 10.1016/j.jocn.2005.02.007
27. Lee, JS, Kim, YT, Jeon, EK, Won, HS, Cho, YS, and Ko, YH. Effect of Green Tea Extracts on Oxaliplatin-Induced Peripheral Neuropathy in Rats. *BMC Complement Altern Med* (2012) 12:124. doi: 10.1186/1472-6882-12-124
28. Mandel, SA, Avramovich-Tirosh, Y, Reznichenko, L, Zheng, H, Weinreb, O, Amit, T, et al. Multifunctional Activities of Green Tea Catechins in Neuroprotection. Modulation of Cell Survival Genes, Iron-Dependent Oxidative Stress and PKC Signaling Pathway. *Neurosignals* (2005) 14:46–60. doi: 10.1159/000085385
29. Treede, I, Braun, A, Sparla, R, Kühnel, M, Giese, T, Turner, JR, et al. Anti-Inflammatory Effects of Phosphatidylcholine. *J Biol Chem* (2007) 282:27155–64. doi: 10.1074/jbc.M704408200
30. Raboune, S, Stuart, JM, Leishman, E, Takacs, SM, Rhodes, B, Basnet, A, et al. Novel Endogenous N-Acyl Amides Activate TRPV1-4 Receptors, BV-2 Microglia, and are Regulated in Brain in an Acute Model of Inflammation. *Front Cell Neurosci* (2014) 8:195. doi: 10.3389/fncel.2014.00195
31. Harnett, W, and Harnett, MM. Phosphorylcholine: Friend or Foe of the Immune System? *Immunol Today* (1999) 20:125–9. doi: 10.1016/s0167-5699(98)01419-4
32. Chiurchiù, V, Leuti, A, and Maccarrone, M. Bioactive Lipids and Chronic Inflammation: Managing the Fire Within. *Front Immunol* (2018) 9:38. doi: 10.3389/fimmu.2018.00038
33. Solmonson, A, and DeBerardinis, RJ. Lipoic Acid Metabolism and Mitochondrial Redox Regulation. *J Biol Chem* (2018) 293:7522–30. doi: 10.1074/jbc.TM117.000259
34. Ross, AC, and Zolfaghari, R. Cytochrome P450s in the Regulation of Cellular Retinoic Acid Metabolism. *Annu Rev Nutr* (2011) 31:65–87. doi: 10.1146/annurev-nutr-072610-145127
35. Bradshaw, HB, and Walker, JM. The Expanding Field of Cannabimimetic and Related Lipid Mediators. *Br J Pharmacol* (2005) 144:459–65. doi: 10.1038/sj.bjp.0706093
36. Warren, CA,. Calabrese, GM, Li, Y, Pawlowski, SW, Figler, RA, Rieger, J, et al. Effects of Adenosine A_2A Receptor Activation and Alanyl-glutamine in Clostridium Difficile Toxin-Induced Ileitis in Rabbits and Cecitis in Mice. *BMC Infect Dis* (2012) 12:13. doi: 10.1186/1471-2334-12-13
37. Taves, MD, Gomez-Sanchez, CE, and Soma, KK. Extra-Adrenal Glucocorticoids and Mineralocorticoids: Evidence for Local Synthesis, Regulation, and Function. *Am J Physiol Endocrinol Metab* (2011) 301:E11–24. doi: 10.1152/ajpendo.00100.2011
38. Mühling, J, Burchert, D, Langefeld, TW, Matejec, R, Harbach, H, Engel, J, et al. Pathways Involved in Alanyl-Glutamine-Induced Changes in Neutrophil Amino- and α-Keto Acid Homeostasis or Immunocompetence. *Amino Acids* (2007) 33:511–24. doi: 10.1007/s00726-006-0395-x
39. Petersen Shay, K, Moreau, RF, Smith, EJ, and Hagen, TM. Is Alpha-Lipoic Acid a Scavenger of Reactive Oxygen Species *In Vivo*? Evidence for its Initiation of Stress Signaling Pathways That Promote Endogenous Antioxidant Capacity. *IUBMB Life* (2008) 60:362–7. doi: 10.1002/iub.40
40. Lewis-Stanislaus, AE, and Li, L. A Method for Comprehensive Analysis of Urinary Acylglycines by Using Ultra-Performance Liquid Chromatography Quadrupole Linear Ion Trap Mass Spectrometry. *J Am Soc Mass Spectrom* (2010) 21:2105–16. doi: 10.1016/j.jasms.2010.09.004
41. Badiou, S, Bellet, H, Lehmann, S, Cristol, JP, and Jaber, S. Elevated Plasma Cysteinylglycine Levels Caused by Cilastatin-Associated Antibiotic Treatment. *Clin Chem Lab Med* (2005) 43:332–4. doi: 10.1515/CCLM.2005.057
42. Orlowski, M, and Wilk, S. Intermediates of the Gamma-Glutamyl Cycle in Mouse Tissues. Influence of Administration of Amino Acids on Pyrrolidone Carboxylate and Gamma-Glutamyl Amino Acids. *Eur J Biochem* (1975) 53:581–90. doi: 10.1111/j.1432-1033.1975.tb04101.x
43. Sengupta, S, Wehbe, C, Majors, AK, Ketterer, ME, DiBello, PM, and Jacobsen, DW. Relative Roles of Albumin and Ceruloplasmin in the Formation of Homocystine, Homocysteine-Cysteine-Mixed Disulfide, and Cystine in Circulation. *J Biol Chem* (2001) 276:46896–904. doi: 10.1074/jbc.M108451200
44. Ostojic, SM, Ostojic, J, Drid, P, and Vranes, M. Guanidinoacetic Acid Versus Creatine for Improved Brain and Muscle Creatine Levels: A Superiority Pilot Trial in Healthy Men. *Appl Physiol Nutr Metab* (2016) 41:1005–7. doi: 10.1139/apnm-2016-0178
45. Osiki, PO, Ojuka, E, and Marmaan, G. An Investigation of the Suitability of Using Octanoylcarnitine Together With Malate as a Substrate Combination for Assessing Beta-Oxidation Using High Resolution Respirometry. *FASEB J* (2016) 30:1015.
46. Liebich, HM, Pickert, A, Stierle, U, and Wöll, J. Gas Chromatography-Mass Spectrometry of Saturated and Unsaturated Dicarboxylic Acids in Urine. *J Chromatogr* (1980) 199:181–9. doi: 10.1016/s0021-9673(01)91371-8
47. Richard, DM, Dawes, MA, Mathias, CW, Acheson, A, Hill-Kapturczak, N, and Dougherty, DM. L-Tryptophan: Basic Metabolic Functions, Behavioral Research and Therapeutic Indications. *Int J Tryptophan Res* (2009) 2:45–60. doi: 10.4137/ijtr.s2129
48. Gosain, A, Jones, SB, Shankar, R, Gamelli, RL, and DiPietro, LA. Norepinephrine Modulates the Inflammatory and Proliferative Phases of Wound Healing. *J Trauma* (2006) 60:736–44. doi: 10.1097/01.ta.0000196802.91829.cc
49. Glynn, P. Neuronal Phospholipid Deacylation is Essential for Axonal and Synaptic Integrity. *Biochim Biophys Acta* (2013) 1831:633–41. doi: 10.1016/j.bbalip.2012.07.023
50. Seifert, R, Burhenne, H, Reinecke, D, Sandner, P, Pich, A, Schwede, F, et al. Cyclic CMP and Cyclic UMP: New (Old) Second Messengers. *BMC Pharmacol* (2011) 11(Suppl 1):O34. doi: 10.1186/1471-2210-11-S1-O34
51. Pekala, J, Patkowska-Sokoła, B, Bodkowski, R, Jamroz, D, Nowakowski, P, Lochyński, S, et al. L-Carnitine–Metabolic Functions and Meaning in Humans Life. *Curr Drug Metab* (2011) 12:667–78. doi: 10.2174/138920011796504536
52. Hardeland, R, Tan, DX, and Reiter, RJ. Kynuramines, Metabolites of Melatonin and Other Indoles: The Resurrection of an Almost Forgotten Class of Biogenic Amines. *J Pineal Res* (2009) 47:109–26. doi: 10.1111/j.1600-079X.2009.00701.x
53. Hytti, M, Piippo, N, Korhonen, E, Honkakoski, P, Kaarniranta, K, and Kauppinen, A. Fisetin and Luteolin Protect Human Retinal Pigment Epithelial Cells From Oxidative Stress-Induced Cell Death and Regulate Inflammation. *Sci Rep* (2015) 5:17645. doi: 10.1038/srep17645
54. Kang, HW, Wei, J, and Cohen, DE. Regulation of Lipid and Glucose Metabolism by Phosphatidylcholine Transfer Protein. *Trends Endocrinol Metab* (2010) 21:449–56. doi: 10.1016/j.tem.2010.02.001

55. Bretscher, P, Egger, J, Shamshiev, A, Trötzmüller, M, Köfeler, H, Carreira, EM, et al. Phospholipid Oxidation Generates Potent Anti-Inflammatory Lipid Mediators That Mimic Structurally Related Pro-Resolving Eicosanoids by Activating Nrf2. *EMBO Mol Med* (2015) 7:593–607. doi: 10.15252/emmm.201404702
56. Chang, JH, McCluskey, PJ, and Wakefield, D. Toll-Like Receptors in Ocular Immunity and the Immunopathogenesis of Inflammatory Eye Disease. *Br J Ophthalmol* (2006) 90:103–8. doi: 10.1136/bjo.2005.072686
57. Erridge, C, Kennedy, S, Spickett, CM, and Webb, DJ. Oxidized Phospholipid Inhibition of Toll-Like Receptor (TLR) Signaling Is Restricted to TLR2 and TLR4. *J Biol Chem* (2008) 283:24748–59. doi: 10.1074/jbc.M800352200
58. Jeewandara, C, Gomes, L, Udari, S, Paranavitane, SA, Shyamali, NL, Ogg, GS, et al. Secretory Phospholipase A2 in the Pathogenesis of Acute Dengue Infection. *Immun Inflamm Dis* (2016) 5:7–15. doi: 10.1002/iid3.135
59. Cunningham, TJ, Yao, L, Oetinger, M, Cort, L, Blankenhorn, EP, and Greenstein, JI. Secreted Phospholipase A2 Activity in Experimental Autoimmune Encephalomyelitis and Multiple Sclerosis. *J Neuroinflammation* (2006) 3:26. doi: 10.1186/1742-2094-3-26
60. Wang, S, Noh, SK, and Koo, SI. Green Tea Catechins Inhibit Pancreatic Phospholipase A(2) and Intestinal Absorption of Lipids in Ovariectomized Rats. *J Nutr Biochem* (2006) 17:492–8. doi: 10.1016/j.jnutbio.2006.03.004
61. Sasaki, GY, Li, J, Cichon, MJ, Kopec, RE, and Bruno, RS. Catechin-Rich Green Tea Extract and the Loss-Of-TLR4 Signaling Differentially Alter the Hepatic Metabolome in Mice With Nonalcoholic Steatohepatitis. *Mol Nutr Food Res* (2021) 65:e2000998. doi: 10.1002/mnfr.202000998

Conflict of Interest: The authors declare that the research was conducted in the absence of any commercial or financial relationships that could be construed as a potential conflict of interest.

Publisher's Note: All claims expressed in this article are solely those of the authors and do not necessarily represent those of their affiliated organizations, or those of the publisher, the editors and the reviewers. Any product that may be evaluated in this article, or claim that may be made by its manufacturer, is not guaranteed or endorsed by the publisher.

frontiers | Frontiers in Endocrinology

ORIGINAL RESEARCH
published: 19 July 2022
doi: 10.3389/fendo.2022.946327

Differentially Regulated Apolipoproteins and Lipid Profiles as Novel Biomarkers for Polypoidal Choroidal Vasculopathy and Neovascular Age-Related Macular Degeneration

Xinyuan Zhang[1,2*†], *Bingjie Qiu*[1,2†], *Zhizhong Gong*[3], *Xiaosi Chen*[1,2], *Yanhong Wang*[4] *and Yao Nie*[1,2]

[1] Beijing Tongren Eye Center, Beijing Tongren Hospital, Capital Medical University, Beijing, China, [2] Beijing Retinal and Choroidal Vascular Disorders Study Group, Beijing, China, [3] Division of Medical Affairs, Beijing Hospital of Traditional Chinese Medicine, Capital Medical University, Beijing, China, [4] Department of Epidemiology and Biostatistics, Institute of Basic Medical Sciences Chinese Academy of Medical Sciences & School of Basic Medicine Peking Union Medical College, Beijing, China

Lipid dyshomeostasis has been implicated in the pathogenesis of various retinal and choroidal vascular diseases. This study aims to investigate whether apolipoprotein (apo) mediated differential regulation of lipid metabolism contributes to the phenotypes of polypoidal choroidal vasculopathy (PCV) and neovascular age-related macular degeneration (nAMD). This study involved 148 subjects including 53 patients with PCV, 44 patients with nAMD, and 51 age-, sex-matched subjects with normal fundus controls. Routine blood biochemistry profile was evaluated. Apolipoproteins was estimated by Luminex technology. After controlling for age, gender, body mass index, duration of hypertension and type 2 diabetes mellitus, apoB/non-high density lipoprotein cholesterol (HDL-C) (p=0.015) was an independent risk factor for nAMD, apoB was an independent risk factor for PCV(p=0.011), compared with control. Low-density lipoprotein cholesterol (LDL-C) was significantly higher in patients with PCV when compared with nAMD (p=0.037). Furthermore, apoB/non-HDL, LDL-C, triglycerides and were significantly correlated with the pathogenesis of subgroups of PCV and nAMD. We concluded that lipid profiles and apos are differential regulated in PCV, nAMD and their subtypes, indicating different pathogenicity contributed to the different phenotypes of PCV and nAMD. Non-pachy PCV shares pathological similarities with nAMD, which is highly correlated with age-related atherosclerosis.

Keywords: polypoidal choroidal vasculopathy, neovascular age-related macular degeneration, serum lipid profiles, apolipoproteins, regulatory mechanisms

OPEN ACCESS

Edited by:
Lvzhen Huang,
Peking University People's Hospital, China

Reviewed by:
Iat Fan Lai,
Kiang Wu Hospital, Macau, Macao SAR, China
Jia-Horung Hung,
National Cheng Kung University Hospital, Taiwan
Xiaomeng Wang,
Duke-NUS Medical School, Singapore

***Correspondence:**
Xinyuan Zhang
mmzxy2010@163.com

†*These authors share first authorship*

Specialty section:
This article was submitted to Molecular and Structural Endocrinology, a section of the journal Frontiers in Endocrinology

Received: *17 May 2022*
Accepted: *03 June 2022*
Published: *19 July 2022*

Citation:
Zhang X, Qiu B, Gong Z, Chen X, Wang Y and Nie Y (2022) Differentially Regulated Apolipoproteins and Lipid Profiles as Novel Biomarkers for Polypoidal Choroidal Vasculopathy and Neovascular Age-Related Macular Degeneration. Front. Endocrinol. 13:946327. doi: 10.3389/fendo.2022.946327

INTRODUCTION

Age-related macular degeneration (AMD) is a major and irreversible blindness in elderly people worldwide (1, 2). Polypoidal choroidal vasculopathy (PCV), which is considered a distinct subtype of neovascular AMD (nAMD), is more prevalent in Asia population than Caucasians although it was first reported by Dr. Yannuzzi in US in the 1990s (3, 4). Both PCV and nAMD are multifactorial disorders and share a variety of characteristics in phenotype, risk factors, natural history, and treatment strategies (5). Recently, several genetic and epigenetic studies raised the hypothesis that PCV is a genetic disorder, AMD-related gene polymorphisms such as *ARMS2* A69S and *CFH* Y402H (6) have been found associated with PCV. On the other hand, the disparity in response to intravitreal anti-VEGF drugs between nAMD and PCV has also received extensive attention. Although the natural history, clinical features, pathological and genetic correlation of the two diseases has been intensively studied (5, 7–9), the pathogenic similarities and differences between PCV and nAMD remain largely unknown.

Dysregulated lipid metabolism has been implicated in the pathogenesis of PCV and nAMD. Lipoproteins are soluble lipid protein complexes that are formed by the interactions between apolipoproteins (apos, amphipathic proteins) and lipids (10). Abnormal expression of genes of lipid metabolism and the reverse cholesterol transport (RCT) pathway, such as *Cholesterol Ester Transfer Protein (CETP), Hepatic Lipase (LIPC), ATP-binding Cassette Transporter A1 (ABCA1)* and *Apolipoprotein E (APOE)*, has been reported in patients with PCV and nAMD (11–13). Furthermore, dysregulated lipoproteins [triglycerides (TG), total cholesterol (TC), high-density lipoprotein- cholesterol (HDL-C) and low-density lipoprotein (LDL-C)] and apolipoproteins have been reported in both PCV and nAMD (12, 14, 15); however, results from existing studies are controversial and the connections remain elusive (15, 16).

The differential regulation mechanism and the interactions between apos and lipid profiles remain uncertain. Our previous studies have shown that abnormal plasma levels of apolipoproteins and lipid profiles are correlated with variety of retinal vascular disorders including diabetic retinopathy (17–19). It is interesting to determine if apolipoprotein-mediated differential regulation of lipid metabolism is a pathological cause of the clinical phenotypes of nAMD and PCV. In this study, we aim to determine the differential serum levels of lipoproteins, apoproteins and their ratios, and to determine their associations with the pathogenesis of PCV and nAMD.

Abbreviations: ABCA1, ATP-binding cassette transporter A1; Apo, apolipoproteins; ApoA, apolipoprotein A; ApoB, apolipoprotein B; ApoC, apolipoprotein C; ApoE, apolipoprotein E; AUC, area under curve; BCVA, best-corrected visual acuity; BMI, body mass index; CETP, cholesterol ester transfer protein; HBP, hypertension; HDL-C, high-density lipoprotein; ICGA, indocyanine green angiography; IQR, interquartile range; LDL-C, low-density lipoprotein; LIPC, hepatic lipase; Lpa, lipoprotein(a); LR, likelihood ratio; nAMD, neovascular age-related macular degeneration; Non-pachy nAMD, nAMD with non-pachy choroid; Non-pachy PCV, PCV with non-pachy choroid; OCT, optical coherence tomography; OR, Odd ratio; Pachy-nAMD, nAMD with pachy-choroid; Pachy-PCV, PCV with pachy-choroid; PCV, Polypoidal choroidal vasculopathy; PED, pigment epithelium detachment; RCT: reverse cholesterol transport pathway; ROC, receiver operating characteristic; SFCT, Subfoveal choroidal thickness; TC, total cholesterol; TG, Triglycerides.

MATERIALS AND METHODS

Study Subjects

The study subjects were selected from our Retinal and Choroidal Study Cohort (RCSC), a prospective cohort from year of 2016 to 2022 in Beijing Tongren Eye Center. This cohort comprises patients with PCV, nAMD, pachychoroid pigment epitheliopathy, pachychoroid neovasculopathy, focal choroidal excavation, peripapillary pachychoroid syndrome pachydrusen and age-, sex-, duration of the systemic disorders (hypertension and diabetes mellitus) matched controlled subjects (with normal fundus in both eyes). This study was approved by the institutional review board of Beijing Tongren Hospital and adhered to the tenets of the Declaration of Helsinki. All participants signed informed consent form approved by the Ethics Committee of Beijing Tongren Hospital, Capital Medical University before participation.

This nested case-control study compromised 148 subjects, including 53 patients with PCV, 44 patients with nAMD and 51 age-, sex- matched healthy controls from RCSC as prescribed above.

The inclusion criteria were: 1) naïve PCV and nAMD not treated with anti-vascular endothelial growth factor (VEGF) at least within 1 year 2) No history of lipid-lowering medications. PCV was diagnosed by the fundus examination, fundus color photography, Swept Source optical coherent tomography (SS-OCT) and further confirmed by indocyanine green angiography (ICGA) according to EVEREST study report 2, modified EVEREST criteria (19–21) and the 2020 Asia-pacific eye image association PCV expert consensus of the working group (22). nAMD was diagnosed according to the "Expert consensus on macular degeneration" published in 2019 by Spaide et al. (23).

Exclusion criteria included those with 1) complicated with other fundus diseases such as macular hole, diabetic retinopathy, metastatic carcinoma, melanoma and others 2) history of serious systemic diseases including stroke and myocardial infarction within 6 months or not be able to tolerate eye examination 4) patients with history of metabolic disorders or on lipid lowering therapy. 5) subjects with one eye diagnosed with PCV and the other eye diagnosed with nAMD were also excluded.

Normal fundus control was defined as: 1) normal fundus in both eyes were evaluated by fundus ophthalmoscopy and OCT configuration 2) history of serious systemic diseases including stroke and myocardial infarction within 6 months or not be able to tolerate eye examination 3) patients with history of metabolic disorders or on lipid lowering therapy was excluded 4) subjects (with normal fundus in both eyes) with other systemic disorders were matched with the study groups when enrolled.

Subgroup Grouping Criteria

The enrolled patients with PCV and nAMD were further categorized to the pachy-PCV/nAMD group or the non-pachy nAMD group respectively, according to the likelihood ratio test

results determined in the same large cohort as we described previously (24). After controlling for age and diopter, the diagnostic cut off value range of pachy-choroid among 20-29 years old was 320-330 μm [likelihood ratio (LR): 1.17]; among 40-59 years old was 330-340μm (LR: 1.07); among 60 to 79 years old was 250-275 μm (LR: 1.07) and ≥ 80 years old was 200-225 μm (LR: 1.00).

Eye Examination

The best-corrected visual acuity (BCVA), slit-lamp microscopic examination (SL-IE Slit Lamp Microscope, Topcon Co., Ltd, Tokyo, Japan), non-contact intraocular pressure (TX20 Automatic Non-contact Tonometer, Canon Co., Ltd, Tokyo, Japan), fundus photography (CR-1 non-mydriatic Fundus Camera, Canon Co., Ltd), OCT, fluorescent angiography and indocyanine green angiography (ICGA) were performed for all the participants. nAMD and PCV were diagnosed by OCT and indocyanine green angiography (ICGA) according to EVEREST study report 2, modified EVEREST criteria (20, 21) and the 2020 Asia-pacific eye image association PCV expert consensus of the working group (22).

Lipoprotein Profiling and Routine Biochemical Examination

All participants underwent a standardized assessment of other risk factors including age, gender, duration of diabetes, duration of hypertension (HBP) and body mass index (BMI). The serum levels of TC, TG, LDL-C and HDL-C were tested by routine biochemical examination.

50 μL of serum was utilized to determine the level of apolipoproteins (A-I, A-II, B, C-II, C-III, E) determined by Luminex technology (Luminex 200^{TM} liquid chip detector, Millipore, Boston, Massachusetts, USA), according to the manufacturer's instructions.

Non-HDL-C, LDL/HDL, (TC-HDL)/HD, log (TG/HDL), apoA-I/apoA-II, apoB/non-HDL-C, apoB/apoA-I, apoC-III/apoC-II/and apo E/apoC-II ratios were also calculated.

Determination of the Cutoff Value for apoA-I/apoA-II, apoB/non-HDL-C, apoB/apoA-I, apoC-III/apoC-II/and apoE/apoC-II Ratios by Receiver Operating Characteristic Curve

The cut off values for the ratios of apoA-I/apoA-II, apoB/non-HDL-C, apoB/apoA-I, ApoC-III/apoC-II, apo E/apoC-II, LDL/HDL, (TC- HDL)/HDL and log (TG/HDL) were determined by ROC curve. The indicators with high sensitivity and specificity (with maximum Youden index) were selected as the cut off values on ROC curve. The control group as stated above in 2.1. The cut off value of the apoB/non-HDL-C ratio was 0.43 [Area under curve (AUC): 0.62, sensitivity= 0.68, specificity=0.60], the apoB/apoA-I ratio was 1.77 (AUC: 0.544, sensitivity = 0.16, specificity= 0.94) in patients with PCV, the cut off value for the apoB/non-HDL-C ratio was 0.45 (AUC:0.71, sensitivity = 0.78, specificity = 0.63) in patients with nAMD. The ratio values (apoA-I/apoA-II, ApoC-III/apoC-II and apo E/apoC-II) with lower sensitivity (AUC< 0.50, sensitivity and specificity <0.5) were not considered in this study.

Sample Size Determination

Sample size was calculated by the Power Analysis and Sample Size software (PASS 2022, NCSS LLC, Utah, USA) based on our pilot study result. According to the pilot study results, the mean value of LDL-C (which required maximum numbers among all the biochemical parameters) in the study group was 3.32 ± 0.79, in the control group was 3.08 ± 0.87, the minimum number per arm (sample size) was 36 subjects to detect the difference between the four groups with the designed power (1- beta= 90%) at 95% confidence level (alpha=0.05) as we previously described [32]. We increased the sample size to above 40 to in each group considering the variability (even in normal controls) of apos.

Statistical Analysis

SPSS software (SPSS, Inc. 25.0, Chicago, IL, USA) was utilized for the statistical analysis. Baseline parameters including the age and gender of participants, duration of diabetes and HBP, BMI, TG, TC, HDL-C, LDL-C, the serum levels of apolipoproteins, LDL/HDL, (TC- HDL)/HDL, log (TG/HDL), the ApoB/ApoA-I ratio and the ApoB/Non-HDL ratio were described by means ± standard deviation (mean ± SD). One-way analysis of variance (ANOVA) or the Kruskal–Wallis test was applied according to the data distribution for the group comparisons. ANOVA or the univariate logistic regression was performed to assess the association between the serum levels of lipids, apolipoproteins and the ratios of lipoproteins and apolipoproteins between different groups. Multivariate logistic regression models were applied to evaluate the effects of serum lipids or apolipoproteins among PCV, nAMD and normal control groups. The Odds ratio for group comparison was analyzed using the normal control as the reference, OR > 1 means the variable is an independent risk factor for the study group, OR < 1 means the variable is an independent protective factor for the disease. When the disease sub-group was used as the reference, OR > 1 means that higher level of the independent variable was found in the study group, whereas an OR < 1 means the higher level of the independent variable was in the reference group (25). Statistical significance was defined as $p<0.05$.

RESULTS

Baseline Demographic and Clinical Characteristics

A total of 148 subjects (84 males and 64 females, aged 51-94 years old) including 53 patients with PCV (aged 54-81 yrs, 67.49 ± 7.67 yrs), 44 patients with nAMD (aged 51-94 yrs, 71.30 ± 9.46 yrs) and age-, gender-, duration of hypertension and type 2 diabetes mellitus matched 51 subjects with normal fundus in both eyes (aged 51-78 yrs, 66.04 ± 7.91 yrs) were recruited from the outpatient clinic of Beijing Tongren Hospital from September 2016 to September 2021 (**Table 1**).

TABLE 1 | Baseline demographic characteristics and biochemical parameters in subjects with PCV, nAMD and control.

	Control (*N* = 51)	PCV (*N* = 53)	nAMD (*N* = 44)	F/χ^2	*P* value
Age, years (mean ± SD)	66.04 ± 7.91	67.49 ± 7.67	71.30 ± 9.46	5.44[b]	0.066
Gender, female(N) (%)	26(50.98)	23(43.40)	15(34.09)	2.75[c]	0.253
Duration of Hypertension (mean ± SD)	4.36 ± 9.40	4.82 ± 9.17	8.08 ± 12.43	3.91[b]	0.141
Duration of DM (mean ± SD)	0.03 ± 0.16	2.13 ± 5.27	2.19 ± 6.31	5.88[b]	0.053
BMI (mean ± SD)	23.82 ± 3.38	24.45 ± 3.22	24.68 ± 2.43	0.95[a]	0.390
TG, mmol/L (mean ± SD)	1.42 ± 0.66	1.26 ± 0.52	1.22 ± 0.64	3.09[b]	0.213
TC, mmol/L (mean ± SD)	5.10 ± 0.99	5.16 ± 0.96	4.60 ± 1.27	3.59[a]	0.030*
LDL-C, mmol/L (mean ± SD)	3.09 ± 0.86	3.33 ± 0.87	2.81 ± 0.96	3.52[a]	0.032*
HDL-C, mmol/L (mean ± SD)	1.37 ± 0.38	1.32 ± 0.31	1.25 ± 0.33	1.35[a]	0.262
LDL/HDL (mean ± SD)	2.40 ± 0.85	2.66 ± 0.95	2.32 ± 0.84	2.70[b]	0.259
(TC- HDL)/HDL (mean ± SD)	2.94 ± 1.07	3.08 ± 1.08	2.78 ± 1.03	1.13[a]	0.325
log (TG/HDL) (mean ± SD)	-0.01 ± 0.29	-0.04 ± 0.21	-0.04 ± 0.25	0.21[a]	0.815
apo A-I, mg/ml (mean ± SD)	0.61 ± 0.15	0.64 ± 0.20	0.63 ± 0.15	0.96[b]	0.618
apo C-III, mg/ml (mean ± SD)	0.28 ± 0.11	0.28 ± 0.13	0.27 ± 0.14	0.31[b]	0.857
apo E, mg/ml (mean ± SD)	0.03 ± 0.01	0.03 ± 0.01	0.03 ± 0.01	0.10[b]	0.952
apo A-II, mg/ml (mean ± SD)	0.41 ± 0.08	0.43 ± 0.12	0.42 ± 0.09	0.99[a]	0.373
apo B, mg/ml (mean ± SD)	1.51 ± 0.39	1.72 ± 0.47	1.56 ± 0.56	2.40[a]	0.095
apo C-II, mg/ml (mean ± SD)	0.14 ± 0.06	0.14 ± 0.07	0.13 ± 0.07	0.40[b]	0.820
apo B/non-HDL-C (mean ± SD)	0.41 ± 0.09	0.45 ± 0.11	0.51 ± 0.15	13.05[b]	0.001*
apo B/apo AI(mean ± SD)	2.62 ± 1.00	2.82 ± 1.15	2.58 ± 0.83	0.51[b]	0.774
non-HDL-C, mmol/L (mean ± SD)	3.74 ± 0.96	3.84 ± 0.93	3.35 ± 1.10	3.07[a]	0.049*

**Statistically significant: p ≤ 0.05. Mean ± SD was showed in the Table . According to the type of data and the data distribution, [a] one-way ANOVA analysis, Post-hoc Bonferroni's statistic. [b] Kruskal–Wallis. [c] Chi-square test were applied.*

SD, standard deviation; DM, diabetes milletus; BMI, body mass index; TG, triglycerides; TC, total cholesterol; LDL-C, low-density lipoprotein cholesterol; HDL-C, high density lipoproteincholesterol;apo, apolipoprotein; PCV, polypoidal choroidal vasculopathy; nAMD, neovascular age-related macular degeneration; N, normal fundus control.

There were no statistically significant differences in age or gender between the PCV, nAMD and control groups (p_{age}=0.066, p_{gender}=0.253). No statistically significance difference was found in the duration of DM, HBP and BMI among the PCV, nAMD and healthy control groups ($p_{duration\ of\ DM}$ =0.053, $p_{duration\ of\ HBP}$ =0.141, p_{BMI} =0.390). Furthermore, serum level of TC, LDL, apoB/non-HDL, non-HDL-C was significant differences among the three groups (p_{TC}=0.030, $p_{LDL\text{-}C}$=0.032, $p_{apoB/non\text{-}HDL\text{-}C}$=0.001, $p_{non\text{-}HDL\text{-}C}$=0.049) by one-way ANOVA analysis or Kruskal–Wallis test (**Table 1**).

Comparison of the PCV Group and nAMD Group by Univariate Logistic Regression Analysis

Univariate logistic regression model showed that in comparison with healthy controls, apoB was an independent risk factors for PCV with statistical difference (OR 3.31, 95% CI 1.23-8.92, *p*=0.018) (**Table 2**).

Compared with healthy controls, univariate logistic regression analysis showed that age (OR=1.10, 95%CI 1.04-1.16, *p*=0.001), apo-B/non-HDL-C (per 0.1) were independent risk factors for nAMD (OR=2.08, 95% CI 1.35-3.21, *p*=0.001). Interestingly, TC was found to have a protective effect for patients with nAMD with statistical significance (OR=0.67, 95% CI 0.46-0.98, *p*=0.036) (**Table 2**).

In comparison with nAMD, univariable logistic regression analysis showed that the serum levels of TC, LDL-C and non-HDL-C were significantly higher and associated with increased risk for PCV (OR_{TC}= 0.65, 95% CI 0.44-0.95, *p*=0.027, $OR_{LDL\text{-}C}$ =0.55, 95% CI 0.34-0.89, *p*=0.015, $OR_{non\text{-}HDL\text{-}C}$ 0.62 95% CI 0.40-0.95, *p*=0.027, respectively). In addition, age was significantly older in patients with nAMD patients compared with that with PCV patients (OR=1.07, 95% CI 1.01-1.13, *p*=0.015) and apo-B/non-HDL-C (per 0.1) were independent risk factors for nAMD compared to PCV patients (OR=1.50, 95% CI 1.08-2.08, *p*=0.016) (**Table 2**).

Comparisons of the Subgroups of PCV and nAMD by Univariable Logistic Regression Analysis

To further explore the correlations of the serum levels of apolipoproteins and lipid profiles with PCV and nAMD, patients with PCV and nAMD were sub-grouped to pachy (eyes with pachychoroid) and non-pachy groups according to the criteria as we described previously. Serum levels of TG were significantly lower in the pachy-PCV patients when compared with healthy controls (OR_{TG} 0.21, 95% CI 0.06-0.80, *p*=0.022). The univariate logistic regression analysis indicated that serum levels of apoA-II (per 0.1mg/dl) and Apo-B were significantly higher in patients with non-pachy PCV ($OR_{apoA\text{-}II}$ 1.76, 95% CI 1.08-2.86, *p*=0.024; $OR_{Apo\text{-}B}$ 5.74, 95% CI 1.72-19.12, *p*=0.004 respectively) (**Table 3**).

The serum levels of TG, apoA-I (per 0.1mg/dl) and apoA-II (per 0.1mg/dl) were significantly higher in non-pachy PCV than those in pachy-PCV (OR_{TG} 6.52, 95% CI 1.29-32.97, *p*=0.023; $OR_{apoA\text{-}I}$1.41, 95% CI 1.01-1.98, *p*=0.044; $OR_{apoA\text{-}II}$ 1.88, 95% CI 1.02-3.44, *p*=0.043, respectively) (**Table 3**).

Compared to the healthy control group, the level of TG, TC, LDL-C and non-HDL-C were significantly lower in the pachy-nAMD group (OR_{TG} 0.10, 95% CI 0.02-0.61, *p*=0.013; OR_{TC} 0.38, 95% CI 0.18-0.81, *p*=0.012; $OR_{LDL\text{-}C}$ 0.40, 95% CI 0.17-0.97, *p*=0.044; $OR_{non\text{-}HDL\text{-}C}$ 0.35, 95% CI 0.15-0.82, *p*=0.015, respectively). Additionally, the apo-B/non-HDL-C ratio (per 0.1)

TABLE 2 | Comparisons of the variables between PCV, nAMD and control groups by univariate logistic regression analysis.

(a) PCV vs. N‡	Factor	OR	95% CI	*p* value
	Gender, ref: male	1.31	(0.60, 2.85)	0.493
	Age	1.03	(0.98, 1.08)	0.310
	BMI	1.07	(0.94, 1.23)	0.300
	Duration of hypertension	1.01	(0.96, 1.05)	0.760
	Duration of DM	1.80	(0.64, 5.01)	0.264
	TG	0.63	(0.32, 1.24)	0.180
	TC	1.03	(0.69, 1.53)	0.894
	LDL-C	1.32	(0.84, 2.08)	0.228
	HDL-C	0.59	(0.19, 1.84)	0.362
	LDL/HDL	1.38	(0.88, 2.16)	0.156
	(TC- HDL)/HDL	1.17	(0.81, 1.68)	0.408
	log (TG/HDL), per 0.1	0.96	(0.82, 1.12)	0.607
	apo A-I, per 0.1	1.11	(0.89, 1.39)	0.354
	apo C-III, per 0.1	1.06	(0.77, 1.47)	0.717
	apo E, per 0.01	1.07	(0.76, 1.51)	0.711
	apo A-II, per 0.1	1.31	(0.88, 1.95)	0.182
	apo B	3.31	(1.23, 8.92)	0.018
	apo C-II, per 0.1	1.08	(0.60, 1.97)	0.794
	apo B/non-HDL-C, per 0.1	1.17	(0.83, 1.63)	0.368
	apo B/apo AI	1.21	(0.83, 1.76)	0.315
	non-HDL-C	1.11	(0.73, 1.68)	0.632
(b) nAMD vs. N‡	**Factor**	**OR**	**95% CI**	***p* value**
	Gender, ref: male	1.87	(0.81, 4.32)	0.142
	Age	1.10	(1.04, 1.16)	0.001
	BMI	1.08	(0.94, 1.25)	0.260
	Duration of hypertension	1.04	(1.00, 1.08)	0.088
	Duration of DM	1.78	(0.64, 4.96)	0.273
	TG	0.61	(0.32, 1.18)	0.141
	TC	0.67	(0.46, 0.98)	0.036
	LDL-C	0.70	(0.44, 1.12)	0.137
	HDL-C	0.39	(0.11, 1.30)	0.124
	LDL/HDL	0.89	(0.55, 1.44)	0.627
	(TC- HDL)/HDL	0.87	(0.59, 1.29)	0.483
	log (TG/HDL), per 0.1	0.96	(0.83, 1.12)	0.597
	apo A-I, per 0.1	1.13	(0.86, 1.49)	0.387
	apo C-III, per 0.1	1.01	(0.74, 1.37)	0.962
	apo E, per 0.01	1.10	(0.81, 1.50)	0.529
	apo A-II, per 0.1	1.09	(0.71, 1.68)	0.699
	apo B	1.76	(0.78, 3.94)	0.172
	apo C-II, per 0.1	0.97	(0.49, 1.89)	0.918
	apo B/non-HDL-C, per 0.1	2.08	(1.35, 3.21)	0.001
	apo B/apo A-I	0.96	(0.61, 1.50)	0.843
	non-HDL-C	0.68	(0.45, 1.03)	0.071
(c) nAMD vs. PCV‡	**Factor**	**OR**	**95% CI**	***p* value**
	Gender, ref: male	1.43	(0.62, 3.29)	0.404
	Age	1.07	(1.01, 1.13)	0.015
	BMI	1.01	(0.87, 1.18)	0.883
	Duration of hypertension	1.03	(0.99, 1.08)	0.143
	Duration of DM	0.99	(0.92, 1.06)	0.763
	TG	0.88	(0.43, 1.79)	0.727
	TC	0.65	(0.44, 0.95)	0.027
	LDL-C	0.55	(0.34, 0.89)	0.015
	HDL-C	0.60	(0.17, 2.11)	0.422
	LDL/HDL	0.64	(0.40, 1.04)	0.074
	(TC- HDL)/HDL	0.74	(0.50, 1.10)	0.139
	log (TG/HDL), per 0.1	0.99	(0.83, 1.19)	0.929
	apo A-I, per 0.1	0.98	(0.78, 1.24)	0.888
	apo C-III, per 0.1	0.97	(0.73, 1.28)	0.810
	apo E, per 0.01	1.05	(0.78, 1.41)	0.740
	apo A-II, per 0.1	0.86	(0.60, 1.24)	0.417
	apo B	0.83	(0.40, 1.73)	0.617

(Continued)

TABLE 2 | Continued

(a) PCV vs. N‡	Factor	OR	95% CI	*p* value
	apo C-II, per 0.1	0.91	(0.50, 1.64)	0.751
	apo B/non-HDL-C, per 0.1	1.50	(1.08, 2.08)	0.016
	apo B/apo A-I	0.77	(0.50, 1.19)	0.238
	non-HDL-C-C	0.62	(0.40, 0.95)	0.027

**Statistically significant: $p \leq 0.05$. ‡ represents for the reference group.*

ref: reference; OR, Odd ratio; CI, confidence interval; BMI, body mass index; DM, diabetic retinopathy; TG, triglycerides; TC, total cholesterol; LDL-C, low-density lipoprotein cholesterol; HDL-C, high density lipoprotein-cholesterol; apo, apolipoprotein; PCV, polypoidal choroidal vasculopathy; nAMD, neovascular age-related macular degeneration; N, normal fundus control.

TABLE 3 | Comparisons of the variables between the sub-groups (pachy and non-pachy) of PCV and control group by univariate logistic regression analysis.

(c) pachy-PCV vs. N‡	Factor	OR	95% CI	*p* value
	Gender, ref: male	0.56	(0.19, 1.66)	0.295
	Age	0.99	(0.92, 1.06)	0.702
	BMI	1.09	(0.92, 1.28)	0.326
	Duration of hypertension	0.99	(0.93, 1.06)	0.74
	Duration of DM	2.01	(0.58, 6.94)	0.27
	TG	0.21	(0.06, 0.80)	0.022
	TC	0.94	(0.53, 1.69)	0.84
	LDL-C	1.35	(0.71, 2.56)	0.358
	HDL-C	0.37	(0.06, 2.23)	0.28
	LDL/HDL	1.53	(0.83, 2.81)	0.175
	(TC- HDL)/HDL	1.20	(0.72, 2.00)	0.48
	log (TG/HDL), per 0.1	0.88	(0.72, 1.09)	0.254
	apo A-I, per 0.1	0.98	(0.95, 1.02)	0.323
	apo C-III, per 0.1	0.71	(0.42, 1.19)	0.197
	apo E, per 0.01	0.82	(0.49, 1.38)	0.453
	apo A-II, per 0.1	0.78	(0.43, 1.42)	0.412
	apo B	1.44	(0.39, 5.30)	0.579
	apo C-II, per 0.1	0.64	(0.25, 1.65)	0.354
	apo B/non-HDL-C, per 0.1	0.79	(0.47, 1.31)	0.354
	apo B/apo A-I	1.42	(0.87, 2.33)	0.161
	non-HDL-C	1.06	(0.59, 1.92)	0.835
(b) non-pachy PCV vs. N‡	**Factor**	**OR**	**95% CI**	***p* value**
	Gender, ref: male	0.86	(0.36, 2.04)	0.723
	Age	1.05	(0.99, 1.11)	0.128
	BMI	1.04	(0.90, 1.21)	0.566
	Duration of hypertension	1.01	(0.97, 1.06)	0.58
	Duration of DM	1.97	(0.51, 7.61)	0.326
	TG	0.93	(0.46, 1.89)	0.837
	TC	1.07	(0.70, 1.63)	0.769
	LDL-C	1.30	(0.80, 2.13)	0.295
	HDL-C	0.73	(0.22, 2.45)	0.612
	LDL/HDL	1.31	(0.80, 2.16)	0.281
	(TC- HDL)/HDL	1.15	(0.77, 1.71)	0.506
	log (TG/HDL), per 0.1	1.01	(0.86, 1.19)	0.924
	apo A-I, per 0.1	1.32	(0.99, 1.74)	0.055
	apo C-III, per 0.1	1.31	(0.89, 1.93)	0.17
	apo E, per 0.01	1.22	(0.83, 1.80)	0.319
	apo A-II, per 0.1	1.76	(1.08, 2.86)	0.024
	apo B	5.74	(1.72, 19.12)	0.004
	apo C-II, per 0.1	1.40	(0.70, 2.79)	0.336
	apo B/non-HDL-C, per 0.1	1.50	(0.98, 2.30)	0.064
	apo B/apo A-I	1.10	(0.72, 1.67)	0.657
	non-HDL-C	1.12	(0.72, 1.76)	0.615
(c) non-pachy PCV vs. pachy-PCV‡	**Factor**	**OR**	**95% CI**	***p* value**
	Gender, ref: male	1.52	(0.48, 4.81)	0.473
	Age	1.06	(0.99, 1.15)	0.117

(Continued)

TABLE 3 | Continued

(c) pachy-PCV vs. N‡	Factor	OR	95% CI	*p* value
	BMI	0.95	(0.79, 1.15)	0.600
	Duration of hypertension	1.03	(0.96, 1.10)	0.456
	Duration of DM	0.93	(0.84, 1.03)	0.144
	TG	6.52	(1.29, 32.97)	0.023
	TC	1.14	(0.62, 2.08)	0.675
	LDL-C	1.00	(0.52, 1.90)	0.987
	HDL-C	1.91	(0.30, 12.36)	0.498
	LDL/HDL	0.87	(0.48, 1.60)	0.659
	(TC- HDL)/HDL	0.96	(0.57, 1.63)	0.889
	log (TG/HDL), per 0.1	1.23	(0.93, 1.63)	0.155
	apo A-I, per 0.1	1.41	(1.01, 1.98)	0.044
	apo C-III, per 0.1	0.99	(0.76, 1.30)	0.964
	apo E, per 0.01	1.46	(0.84, 2.52)	0.176
	apo A-II, per 0.1	1.88	(1.02, 3.44)	0.043
	apo B	0.28	(0.07, 1.20)	0.086
	apo C-II, per 0.1	1.88	(0.76, 4.66)	0.171
	apo B/non-HDL-C, per 0.1	1.52	(0.95, 2.43)	0.082
	apo B/apo A-I	0.79	(0.48, 1.30)	0.361
	non-HDL-C	1.07	(0.57, 2.00)	0.836

**Statistically significant: $p \leq 0.05$. ‡ represents for the reference group.*

ref, reference; OR, Odd ratio; CI, confidence interval; BMI, body mass index; DM, diabetic retinopathy; TG, triglycerides; TC, total cholesterol; LDL-C, low-density lipoprotein cholesterol; HDL-C, high density lipoprotein-cholesterol; apo, apolipoprotein; Pachy-PCV, polypoidal choroidal vasculopathy with pachy-choroid; Non-pachy PCV, polypoidal choroidal vasculopathy with non-pachy choroid; N, normal fundus control.

was significantly higher in the pachy-nAMD group than that in the healthy control group (OR $_{\text{apo-B/non-HDL-C}}$ 2.25, 95% CI 1.21-4.19, p=0.011) (**Table 4**). Age and apo-B/non-HDL-C ratio (per 0.1) were also significantly higher in the non-pachy nAMD group than that in the healthy control group (OR $_{\text{age}}$ 1.09, 95% CI 1.03-1.16, p=0.004; OR $_{\text{apo-B/non-HDL-C}}$ 2.06, 95% CI 1.29-3.27, p=0.002, respectively) (**Table 4**). In comparison with the pachy-nAMD group, TG was significantly higher in the non-pachy nAMD group (OR $_{\text{TG}}$ 8.85, 95% CI 1.22-64.32, p=0.031) (**Table 4**).

Comparisons in the Lipid Profiles and Apolipoproteins Between PCV and nAMD by Multivariable Logistic Regression Analysis

After adjusting for age, gender, BMI and duration of HBP, the results suggested that apo-B was an independent risk factors for PCV when compared to normal control (OR $_{\text{Apo-B}}$ 4.06, 95% CI 1.38-11.96, p=0.011) (**Table 5**). The analysis also showed that the apo-B/non-HDL-C ratio (per 0.1) was an independent risk factor for nAMD, which is consistent with the univariate logistic analysis (OR 1.80, 95% CI 1.12-2.90, p=0.015) (**Table 5**).

The results indicated that age is a risk factor specifically for nAMD compared with PCV (OR $_{\text{age}}$ 1.07, 95% CI 1.01-1.14, p=0.033) (**Table 5**).

Comparisons in the Lipid Profiles and Apolipoproteins Between Subgroups of PCV and nAMD by Multivariable Logistic Regression Analysis

To identify specific lipid metabolic dysfunction biomarkers, after adjusting for age, gender, BMI and duration of HBP, we compared nAMD and PCV, pachy and non-pachy PCV and nAMD by multivariate logistic regression analysis.

LDL-C was found to be a specific risk factor for patients with pachy-PCV, whereas lower level of TG was found in non-pachy PCV patients (OR $_{\text{LDL-C}}$ 3.44, 95% CI 1.13-10.47, p=0.030; OR $_{\text{TG}}$ 0.04, 95% CI 0.00-0.37, p=0.005, respectively) (**Table 6**). Furthermore, significantly increased levels of apoA-II (per 0.1mg/dl) and apoB were associated with increased risk of non-pachy PCV (OR OR apoA-II 1.94, 95% CI 1.03-3.68, p=0.042; OR aopB 6.20, 95% CI 1.37-28.02, p=0.018, respectively) (**Table 6**). In addition, higher level of apo-B/non-HDL-C (per 0.1) was associated with higher risk for non-pachy PCV in comparison with pachy-PCV (OR $_{\text{apo-B/non-HDL-C}}$ 2.64, 95% CI 1.05-6.59, p=0.038) (**Table 6**).

Compared with healthy controls, age and the apo-B/non-HDL-C ratio (per 0.1) were strong risk factors for pachy-nAMD (OR $_{\text{age}}$ 1.22, 95% CI 1.01-1.47, p=0.036; OR $_{\text{apo-B/non-HDL-C}}$ 2.78, 95% CI 1.16-6.68, p=0.022, respectively) (**Table 7**). The apo-B/non-HDL-C ratio (per 0.1) was specific risk factor for non-pachy nAMD (OR $_{\text{apo-B/non-HDL-C}}$ 1.76, 95% CI 1.08-2.87, p=0.023) (**Table 7**). The serum levels of apoproteins showed no differences between pachy-nAMD and non-pachy nAMD patients (**Table 7**).

DISCUSSION

In this study, we found that the apoB/non-HDL-C ratio was an independent risk factor for nAMD, whereas apoB was an independent risk factor for PCV. In addition, age was a specific risk factor for nAMD compared with PCV. In the subgroup analysis for PCV and nAMD, it was found that apoB/non-HDL was an independent risk factor for both pachy- and non-pachy nAMD compared with control. apoB/non-HDL-C was also an independent risk factor for non-pachy PCV, indicating that non-pachy PCV shares pathological

TABLE 4 | Comparisons of the variables between the sub-groups (pachy- and nonpachy-) of nAMD and control groups by univariate logistic regression analysis.

(c) pachy-nAMD vs. N‡	Factor	OR	95% CI	*p* value
	Gender, ref: male	0.18	(0.04, 0.87)	0.033
	Age	1.04	(0.96, 1.13)	0.327
	BMI	1.15	(0.94, 1.41)	0.169
	Duration of hypertension	1.01	(0.94, 1.08)	0.830
	Duration of DM	1.73	(0.61, 4.85)	0.300
	TG	0.10	(0.02, 0.61)	0.013
	TC	0.38	(0.18, 0.81)	0.012
	LDL-C	0.40	(0.17, 0.97)	0.044
	HDL-C	0.50	(0.08, 3.04)	0.451
	LDL/HDL	0.67	(0.31, 1.46)	0.314
	(TC- HDL)/HDL	0.66	(0.35, 1.25)	0.204
	log (TG/HDL), per 0.1	0.81	(0.64, 1.04)	0.099
	apo A-I, per 0.1	1.14	(0.73, 1.79)	0.562
	apo C-III, per 0.1	0.93	(0.54, 1.61)	0.805
	apo E, per 0.01	1.17	(0.72, 1.92)	0.524
	apo A-II, per 0.1	0.63	(0.33, 1.20)	0.16
	apo B	0.96	(0.19, 4.79)	0.964
	apo C-II, per 0.1	0.87	(0.29, 2.58)	0.794
	apo B/non-HDL-C, per 0.1	2.25	(1.21, 4.19)	0.011
	apo B/apo A-I	0.71	(0.31, 1.60)	0.405
	non-HDL-C, per 0.1	0.35	(0.15, 0.82)	0.015
(b) non-pachy nAMD vs. N‡	**Factor**	**OR**	**95% CI**	***p* value**
	Gender, ref:male	0.69	(0.28, 1.71)	0.427
	Age	1.09	(1.03, 1.16)	0.004
	BMI	1.07	(0.91, 1.25)	0.426
	Duration of hypertension	1.04	(1.00, 1.08)	0.079
	Duration of DM	1.89	(0.36, 9.98)	0.455
	TG	0.87	(0.44, 1.72)	0.686
	TC	0.76	(0.51, 1.13)	0.176
	LDL-C	0.82	(0.50, 1.34)	0.425
	HDL-C	0.35	(0.09, 1.37)	0.129
	LDL/HDL	0.99	(0.58, 1.69)	0.968
	(TC- HDL)/HDL	0.97	(0.63, 1.49)	0.879
	log (TG/HDL), per 0.1	1.03	(0.87, 1.21)	0.763
	apo A-I, per 0.1	1.12	(0.84, 1.50)	0.445
	apo C-III, per 0.1	1.04	(0.73, 1.48)	0.851
	apo E, per 0.01	1.10	(0.77, 1.57)	0.615
	apo A-II, per 0.1	1.47	(0.85, 2.53)	0.168
	apo B	0.48	(0.20, 1.16)	0.102
	apo C-II, per 0.1	1.01	(0.46, 2.18)	0.991
	apo B/non-HDL-C, per 0.1	2.06	(1.29, 3.27)	0.002
	apo B/apo A-I	1.05	(0.65, 1.68)	0.849
	non-HDL-C	0.81	(0.52, 1.25)	0.332
(c) non-pachy nAMD vs. pachy-nAMD‡	**Factor**	**OR**	**95% CI**	***p* value**
	Gender, ref: male	3.97	(0.75, 21.04)	0.105
	Age	1.05	(0.97, 1.14)	0.203
	BMI	0.85	(0.63, 1.14)	0.280
	Duration of hypertension	1.04	(0.96, 1.12)	0.342
	Duration of DM	1.01	(0.90, 1.13)	0.904
	TG	8.85	(1.22, 64.32)	0.031
	TC	1.38	(0.80, 2.39)	0.242
	LDL-C	1.54	(0.75, 3.17)	0.236
	HDL-C	0.67	(0.09, 4.90)	0.697
	LDL/HDL	1.49	(0.65, 3.42)	0.352
	(TC- HDL)/HDL	1.51	(0.74, 3.09)	0.256
	log (TG/HDL), per 0.1	1.38	(0.99, 1.91)	0.057
	apo A-I, per 0.1	0.99	(0.62, 1.58)	0.977
	apo C-III, per 0.1	1.06	(0.69, 1.65)	0.783
	apo E, per 0.01	0.96	(0.63, 1.46)	0.833
	apo A-II, per 0.1	1.91	(0.91, 4.00)	0.088
	apo B	0.59	(0.18, 1.95)	0.391

(Continued)

TABLE 4 | Continued

(c) pachy-nAMD vs. N‡	Factor	OR	95% CI	*p* value
	apo C-II, per 0.1	1.13	(0.40, 3.18)	0.821
	apo B/non-HDL-C, per 0.1	0.84	(0.53, 1.31)	0.434
	apo B/apo A-I	1.68	(0.62, 4.54)	0.304
	non-HDL-C	1.62	(0.85, 3.08)	0.146

**Statistically significant: $p \leq 0.05$. ‡ represents for the reference group.*

ref, reference; OR, Odd ratio; CI, confidence interval; BMI, body mass index; DM, diabetic retinopathy; TG, triglycerides; TC, total cholesterol; LDL-C, low-density lipoprotein cholesterol; HDL-C, high density lipoprotein-cholesterol; apo, apolipoprotein; Pachy-nAMD, Neovascular age-related macular degeneration with pachy-choroid; Non-pachy nAMD, Neovascular age-related macular degeneration with non-pachy choroid.

TABLE 5 | Comparisons in the lipid profiles and apolipoproteins between PCV, nAMD and control by multivariable logistic regression analysis.

(a) PCV vs. N‡	Factor	OR	95% CI	*p* value
	Gender, ref: male	0.90	(0.37, 2.19)	0.816
	Age	1.00	(0.94, 1.06)	0.991
	BMI	1.03	(0.90, 1.18)	0.68
	Duration of hypertension	1.02	(0.97, 1.06)	0.496
	apo B	4.06	(1.38, 11.96)	0.011
(b) nAMD vs. N‡	**Factor**	**OR**	**95% CI**	***p* value**
	Gender, ref: male	0.88	(0.29, 2.65)	0.823
	Age	1.08	(1.01, 1.15)	0.029
	BMI	1.07	(0.89, 1.28)	0.480
	Duration of hypertension	1.00	(0.95, 1.05)	0.962
	apo B/non-HDL-C, per 0.1	1.80	(1.12, 2.90)	0.015
	TC	0.95	(0.58, 1.56)	0.840
(c) nAMD vs. PCV‡	**Factor**	**OR**	**95% CI**	***p* value**
	Gender, ref: male	0.53	(0.19, 1.44)	0.213
	Age	1.07	(1.01, 1.14)	0.033
	BMI	1.03	(0.86, 1.23)	0.777
	Duration of hypertension	1.01	(0.97, 1.07)	0.562
	apo B/non-HDL-C, per 0.1	1.35	(0.93, 1.97)	0.112
	Factor	OR	95% CI	*p* value
	Gender, ref: male	0.58	(0.21, 1.59)	0.287
	Age	1.06	(1.00, 1.13)	0.061
	BMI	1.03	(0.87, 1.23)	0.704
	Duration of hypertension	1.01	(0.97, 1.06)	0.664
	non-HDL-C	0.60	(0.35, 1.03)	0.062

**Statistically significant: $p \leq 0.05$. ‡ represents for the reference group.*

ref, reference; OR, Odd ratio; CI, confidence interval; BMI, body mass index; DM, diabetic retinopathy; TG, triglycerides; TC, total cholesterol; LDL-C, low-density lipoprotein cholesterol; HDL-C, high density lipoprotein-cholesterol; apo, apolipoprotein; PCV, polypoidal choroidal vasculopathy; nAMD, neovascular age-related macular degeneration.

similarities with nAMD. LDL-C was an independent risk factor for pachy-PCV. These results above indicated differential regulated lipid profiles and apolipoproteins contributed to the phenotypes of PCV and nAMD.

Increasing evidence indicates that dysfunction of lipid metabolism plays a vital role in the pathogenesis of PCV and nAMD. The reverse cholesterol transport pathway regulated by *ABCA1* gene has been implicated in the development of choroidal neovascularization (26) and basal laminal deposits in mice on high-fat diets (27, 28). Genetic studies demonstrated that genetic variants associated with high-density lipoprotein (HDL) pathway, such as *LIPC*, *CETP* and *APOE*, are associated with the pathogenesis of nAMD or PCV (12, 29).

In this study, we determined the differential levels of apolipoproteins in plasma, lipid profiles and their ratios, and reported the associations of apolipoprotein-mediated lipoproteins formation with PCV and nAMD. ApoB, especially apoB-100 is involved in lipid metabolism and is the main component of lipoproteins. ApoB provides structural integrity to lipoproteins and shields the water-repellent lipids at its center. Compared with LDL-C, apoB level has been shown to be a better indicator for cardiovascular disease (30). In this study, we found that apoB and LDL-C were independent risk factors for PCV, indicating PCV is a lipid dysfunction associated disease.

As we reported previously (31), the ratios of apolipoproteins or lipoproteins reflect two or three parameters respectively, and serve as better indicators to mirror the metabolic and clinical interactions between lipid fractions. In the current study, we have showed that apoB/non-HDL-C was an independent risk factor for nAMD, pachy-nAMD, non-pachy nAMD, and non-pachy PCV, after adjusting for age, sex, duration of hypertension, BMI, and lipoproteins by multivariable logistic analysis. ApoB-100 binds

TABLE 6 | Comparisons in the lipid profiles and apolipoproteins between the subgroups of PCV (pachy- and nonpachy-) and control by multivariable logistic regression analysis.

(a) pachy-PCV vs. N‡	Factor	OR	95% CI	*p* value
	Gender, ref: male	0.49	(0.10, 2.47)	0.387
	Age	0.92	(0.82, 1.03)	0.13
	BMI	1.15	(0.91, 1.44)	0.238
	Duration of hypertension	1.00	(0.93, 1.09)	0.939
	TG	0.04	(0.00, 0.37)	0.005
	LDL-C	3.44	(1.13, 10.47)	0.030
	apo B/non-HDL-C, per 0.1	1.92	(0.78, 4.74)	0.159
(b) non-pachy PCV vs. N‡	**Factor**	**OR**	**95% CI**	***p* value**
	Gender, ref: male	0.74	(0.24, 2.34)	0.609
	Age	1.01	(0.94, 1.09)	0.701
	BMI	0.94	(0.78, 1.14)	0.519
	Duration of hypertension	1.03	(0.98, 1.09)	0.222
	apo A-II, per 0.1	1.94	(1.03, 3.68)	0.042
	apo B	6.20	(1.37, 28.02)	0.018
(c) non-pachy PCV vs. pachy-PCV‡	**Factor**	**OR**	**95% CI**	***p* value**
	Genfer, ref:male	1.59	(0.39, 6.41)	0.518
	Age	1.07	(0.97, 1.18)	0.155
	BMI	1.02	(0.82, 1.26)	0.882
	Duration of hypertension	1.01	(0.94, 1.10)	0.715
	apo B/non-HDL-C, per 0.1	2.64	(1.05, 6.59)	0.038
	apo C-III, per 0.1	0.92	(0.66, 1.28)	0.611

**Statistically significant: $p \leq 0.05$. ‡ represents for the reference group.*

ref, reference; OR, Odd ratio; CI, confidence interval; BMI, body mass index; DM, diabetic retinopathy; TG, triglycerides; TC, total cholesterol; LDL-C, low-density lipoprotein cholesterol; HDL-C, high density lipoprotein-cholesterol; apo, apolipoprotein; Pachy-PCV, polypoidal choroidal vasculopathy with pachy-choroid; Non-pachy PCV, polypoidal choroidal vasculopathy with non-pachy choroid.

one VLDL, LDL and lipoprotein (a) (Lpa) to form the lipoprotein particle. Each apoB can only bind one atherosclerotic lipoprotein particle (VLDL, LDL-C, Lpa), thus the serum level of apoB represents the level of atherosclerotic lipoprotein particles. However, the quality of cholesterol carried by apoB varied greatly due to the cholesterol LDL particles (rich or deplete LDL particles) (30). On the other hand, non-HDL-C is the arithmetic sum of cholesterol in VLDL and LDL particles, equivalent to all atherosclerotic cholesterol in lipoproteins (30). ApoB and non-HDL-C have mirror effects on each other, because apoB represents all the atherogenic particles and non-HDL-C represents all the atherogenic cholesterol. Higher level of apoB/non-HDL-C implies that there are more cholesterol-deplete atherosclerotic lipoprotein particles, lower ratio of apoB/non-HDL-C indicated there are more cholesterol-rich atherosclerotic lipoprotein particles. The INTERHEART study have shown that the risk of cardiovascular disease was lower when serum level of apoB was less than non-HDL-C (cholesterol-rich in ApoB particles) (25). Other studies showed that the cholesterol-deplete apoB is also associated with obesity, blood glucose disorders and cardiovascular diseases. We therefore hypothesized that atherosclerosis caused by cholesterol deficiency may play a role in the pathogenesis of pachy-nAMD, non-pachy nAMD, and non-pachy PCV, indicating that non-pachy PCV shares pathological similarities with nAMD, which is highly correlated with age-related atherosclerosis.

We found that apoB/non-HDL-C was a distinct biomarker for nAMD and non-pachy PCV, indicating that 1) non-pachy PCV may share pathological similarity with nAMD 2)nAMD and non-PCV closely correlated with age-related atherosclerosis. A biomarker was defined as a "characteristic that is objectively measured and evaluated as an indication of normal biological processes, pathogenic processes, or pharmacologic responses to a therapeutic intervention" by the Biomarker Definition Working Group, supported by the U.S. National Institute of Health (32). A biomarker can be diagnostic, monitoring, safety, and susceptibility/risk biomarkers based on its main clinical applications (33). Serum cytokines including IL-1α, IL-1β, IL-4, IL-5, IL-10, IL-13, and IL-17 were found in patients with AMD, supporting that inflammation contributes to the pathogenesis of AMD. Furthermore, IK-17 and TNF-α are indicators for good responder to anti-VEGF therapy in patients with AMD (34). Serum lipid profile (forty-one discriminating metabolites) identified by mass spectrometry, especially the distinct lipid metabolism activating factor was found to be a distinct indicator for PCV (11). Differently expressed mRNAs including ENSG00000249572, miRNA has-miR-20a-5p in peripheral blood mononuclear cells found were to be predictors for good and poor responders to anti-VEGF therapy in patients with nAMD (35). Furthermore, OCT and OCT angiography characteristics have been used as biomarkers for diagnosis and treatment on PCV and nAMD (36). The height of the pigment epithelium detachment (PED) and reflectivity of the content of the PED may predict polypoidal lesions closure (36). Re-examining the baseline scans for an inverted U-shaped elevation in anti-VEGF resistant cases was helpful for detecting polypoidal lesions closure (33). These cellular, molecular and imaging biomarkers have not only deepened our understanding the pathogenesis of PCV and nAMD, but also provide insight to find novel therapeutic targets.

TABLE 7 | Comparisons in the lipid profiles and apolipoproteins between the subgroups of nAMD (pachy- and nonpachy-) and control by multivariable logistic regression analysis.

(a) pachy nAMD vs. N‡	Factor	OR	95% CI	*p* value
	Gender, ref: male	0.35	(0.04, 3.43)	0.366
	Age	1.22	(1.01, 1.47)	0.036
	BMI	1.36	(0.92, 2.02)	0.121
	Duration of hypertension	0.94	(0.84, 1.06)	0.315
	apo B/non-HDL-C, per 0.1	2.78	(1.16, 6.68)	0.022
(b) pachy-pachy nAMD vs. N‡	**Factor**	**OR**	**95% CI**	***p* value**
	Gender, ref: male	0.93	(0.29, 2.95)	0.904
	Age	1.06	(0.98, 1.13)	0.137
	BMI	1.02	(0.83, 1.25)	0.861
	Duration of hypertension	1.02	(0.97, 1.07)	0.536
	apo B/non-HDL-C, per 0.1	1.76	(1.08, 2.87)	0.023
(c) non-pachy nAMD vs. pachy-nAMD‡	**Factor**	**OR**	**95% CI**	***p* value**
	Gender, ref: male	2.19	(0.29, 16.59)	0.449
	Age	0.96	(0.86, 1.07)	0.425
	BMI	0.74	(0.50, 1.10)	0.133
	Duration of hypertension	1.09	(0.98, 1.21)	0.113
	apo B/non-HDL-C, per 0.1	0.71	(0.41, 1.24)	0.232
	Factor	**OR**	**95% CI**	***p* value**
	Gender, ref: male	2.21	(0.289, 16.9)	0.444
	Age	0.96	(0.86, 1.07)	0.42
	BMI	0.73	(0.49, 1.09)	0.126
	Duration of hypertension	1.09	(0.98, 1.20)	0.113
	LDL/HDL	0.85	(0.32, 2.28)	0.745
	apo B/non-HDL-C, per 0.1	0.72	(0.41, 1.24)	0.231
	Factor	**OR**	**95% CI**	***p* value**
	Gender, ref: male	2.20	(0.29, 16.75)	0.447
	Age	0.96	(0.86, 1.07)	0.416
	BMI	0.74	(0.49, 1.10)	0.132
	Duration of hypertension	1.09	(0.98, 1.21)	0.11
	(TC- HDL)/HDL	0.92	(0.40, 2.11)	0.843
	apo B/non-HDL-C, per 0.1	0.72	(0.41, 1.24)	0.232
	Factor	OR	95% CI	*p* value
	Gender, ref: male	1.89	(0.24, 14.97)	0.545
	Age	0.99	(0.88, 1.11)	0.816
	BMI	0.73	(0.49, 1.10)	0.129
	Duration of hypertension	1.10	(0.97, 1.24)	0.136
	log (TG/HDL), per 0.1	36.17	(0.10, 13544.76)	0.235
	apo B/non-HDL-C, per 0.1	0.58	(0.27, 1.24)	0.163

**Statistically significant: $p \leq 0.05$. ‡ represents for the reference group.*

ref, reference; OR, Odd ratio; CI, confidence interval; BMI, body mass index; DM, diabetic retinopathy; TG, triglycerides; TC, total cholesterol; LDL-C, low-density lipoprotein cholesterol; HDL-C, high density lipoprotein-cholesterol; apo, apolipoprotein; Pachy-nAMD, Neovascular age-related macular degeneration with pachy-choroid; Non-pachy nAMD, Neovascular agerelated macular degeneration with non-pachy choroid.

As another risk factor for atherosclerosis, TG was found to play a significant protective role in pachy-PCV, which was supported by a meta-analysis (included 9 studies). The results showed that increased TG level of 1 mmol/L would significantly reduce the risk of AMD (relative risk, 0.91; 95% CI, 0.87 to 0.94; $I^2 = 2.6\%$; $p = 0.42$) (37). Several other studies also reported that lower TG level in AMD patients (in comparison with normal control), representing a reverse association between TG and cardiovascular diseases (16, 38).TGs are main from of lipid ester and the main constituent of body fat, containing glycerol and three fatty acids. The underlying mechanism of its protective effects on AMD or PCV merits further *in vivo* or *in vitro* studies.

A limitation of this study is that it was a nested case-control study with relatively small sample size. Therefore, further longitudinal follow-up studies of large cohorts are warranted to gain insight into the underlying pathological mechanisms and the causal relationship between apos and PCV/nAMD. Furthermore, as this study only included the subjects without lipid lowering therapy, the subjects with severe hyperglycemia may also be excluded, this group of patients may have distinct phenotype of nAMD or PCV, it is interesting to investigate the correlations between the plasma lipid biomarkers for these patients. Furthermore, although we have demonstrated the difference of the dysregulated apolipoproteins and lipid profile in PCV and nAMD, the present study should also merit consideration in interpreting the findings, which need to be further validated with well-designed, prospective, large cohort clinical studies. Nevertheless, this study provides a basis for future studies in PCV and nAMD subtypes on molecular mechanisms related to lipid metabolism.

In summary, to our knowledge, this is the first study to investigate the associations between the dysfunction of lipid metabolism and the phenotypes of PCV, nAMD, pachy- and non-pachy PCV and nAMD. Our results indicated that different regulatory mechanisms of lipid metabolism are associated with distinct phenotypes of PCV and nAMD. Differentially regulated apolipoproteins and lipid profiles could be used as novel biomarkers for PCV and nAMD.

DATA AVAILABILITY STATEMENT

The original contributions presented in the study are included in the article/supplementary material. Further inquiries can be directed to the corresponding authors.

ETHICS STATEMENT

The studies involving human participants were reviewed and approved by Ethics Committee of Beijing Tongren Hospital, Capital Medical University. The patients/participants provided their written informed consent to participate in this study.

AUTHOR CONTRIBUTIONS

Conceptualization, XZ; methodology, XZ and BQ; formal analysis, XZ and BQ; investigation, XZ and BQ; Statistical analysis: XZ, BQ, ZG, YW. writing—review and editing, XZ and BQ; funding acquisition, XZ subjects enrolment: BQ; YN; XC. All authors contributed to the article and approved the submitted version.

FUNDING

This work was supported by the National Natural Science Foundation of China [Grant 81570850 and 82070988] and the Ministry of Science and Technology Foundation of China [Grant 2016YFC1305604].

ACKNOWLEDGMENTS

This work is supported by the National Natural Science Foundation of China [Grant 81570850 and 82070988] and the Ministry of Science and Technology Foundation of China [Grant 2016YFC1305604].

REFERENCES

1. Wong WL, Su X, Li X, Cheung CM, Klein R, Cheng CY, et al. Global Prevalence of Age-Related Macular Degeneration and Disease Burden Projection for 2020 and 2040: A Systematic Review and Meta-Analysis. *Lancet Global Health* (2014) 2:e106–16. doi: 10.1016/s2214-109x(13)70145-1
2. Resnikoff S, Pascolini D, Etya'ale D, Kocur I, Pararajasegaram R, Pokharel GP, et al. Global Data on Visual Impairment in the Year 2002. *Bull World Health Organ* (2004) 82:844–51.
3. Lim LS, Mitchell P, Seddon JM, Holz FG, Wong TY. Age-Related Macular Degeneration. *Lancet* (2012) 379:1728–38. doi: 10.1016/s0140-6736(12)60282-7
4. Chen P-J, Chen S-N. Clinical Characteristics of Exudative Age-Related Macular Degeneration in Taiwan. *Taiwan J Ophthalmol* (2012) 2:127–30. doi: 10.1016/j.tjo.2012.10.002
5. Wong CW, Yanagi Y, Lee WK, Ogura Y, Yeo I, Wong TY, et al. Age-Related Macular Degeneration and Polypoidal Choroidal Vasculopathy in Asians. *Prog Retin Eye Res* (2016) 53:107–39. doi: 10.1016/j.preteyeres.2016.04.002
6. Zhang X, Sivaprasad S. Drusen and Pachydrusen: The Definition, Pathogenesis, and Clinical Significance. *Eye (London England)* (2021) 35:121–33. doi: 10.1038/s41433-020-01265-4
7. Tso MOM, Suarez MJ, Eberhart CG. Pathologic Study of Early Manifestations of Polypoidal Choroidal Vasculopathy and Pathogenesis of Choroidal Neo-Vascularization. *Am J Ophthalmol Case Rep* (2018) 11:176–80. doi: 10.1016/j.ajoc.2017.10.012
8. Yannuzzi LA, Ciardella A, Spaide RF, Rabb M, Freund KB, Orlock DA. The Expanding Clinical Spectrum of Idiopathic Polypoidal Choroidal Vasculopathy. *Arch Ophthalmol (Chicago Ill 1960)* (1997) 62: 478–85, 115. doi: 10.1001/archopht.1997.01100150480005
9. Yanagisawa S, Kondo N, Miki A, Matsumiya W, Kusuhara S, Tsukahara Y, et al. Difference Between Age-Related Macular Degeneration and Polypoidal Choroidal Vasculopathy in the Hereditary Contribution of the A69S Variant of the Age-Related Maculopathy Susceptibility 2 Gene (ARMS2). *Mol Vision* (2011) 17:3574–82.
10. Ding M, Rexrode KM. A Review of Lipidomics of Cardiovascular Disease Highlights the Importance of Isolating Lipoproteins. *Metabolites* (2020) 10:163. doi: 10.3390/metabo10040163
11. Li M, Zhang X, Liao N, Ye B, Peng Y, Ji Y, et al. Analysis of the Serum Lipid Profile in Polypoidal Choroidal Vasculopathy. *Sci Rep* (2016) 6:38342. doi: 10.1038/srep38342
12. Xu N, Xu H, Zhao M, Xu Y, Huang L. Associations of Systemic, Serum Lipid and Lipoprotein Metabolic Pathway Gene Variations With Polypoidal Choroidal Vasculopathy in China. *PloS One* (2019) 14:e0226763. doi: 10.1371/journal.pone.0226763
13. Klaver CC, Kliffen M, van Duijn CM, Hofman A, Cruts M, Grobbee DE, et al. Genetic Association of Apolipoprotein E With Age-Related Macular Degeneration. *Am J Hum Genet* (1998) 63:200–6. doi: 10.1086/301901
14. Nowak M, Swietochowska E, Marek B, Szapska B, Wielkoszynski T, Kos-Kudla B, et al. Changes in Lipid Metabolism in Women With Age-Related Macular Degeneration. *Clin Exp Med* (2005) 4:183–7. doi: 10.1007/s10238-004-0054-z
15. Han X, Ong JS, Hewitt AW, Gharahkhani P, MacGregor S. The Effects of Eight Serum Lipid Biomarkers on Age-Related Macular Degeneration Risk: A Mendelian Randomization Study. *Int J Epidemiol* (2021) 50:325–36. doi: 10.1093/ije/dyaa178
16. Kersten E, Paun CC, Schellevis RL, Hoyng CB, Delcourt C, Lengyel I, et al. Systemic and Ocular Fluid Compounds as Potential Biomarkers in Age-Related Macular Degeneration. *Survey Ophthalmol* (2018) 63:9–39. doi: 10.1016/j.survophthal.2017.05.003
17. Zhang X, Qiu B, Wang Q, Sivaprasad S, Wang Y, Zhao L, et al. Dysregulated Serum Lipid Metabolism Promotes the Occurrence and Development of Diabetic Retinopathy Associated With Upregulated Circulating Levels of VEGF-A, VEGF-D, and PlGF. *Front Med* (2021) 8:779413. doi: 10.3389/fmed.2021.779413
18. Zhang X, Wang K, Zhu L, Wang Q. Reverse Cholesterol Transport Pathway and Cholesterol Efflux in Diabetic Retinopathy. *J Diabetes Res* (2021) 2021:8746114. doi: 10.1155/2021/8746114
19. Wang K, Zhang X, Nie Y. Effects of Dyslipidemia on Retinal Micro-Vasculopathy and Retinal Neuron Degeneration in Patients With Diabetic. *Chin J Of Ophthalmologic Med (Electronic Edition)* (2020) 10:212–28. doi: 10.3877/cma.j.issn.2095-2007.2020.04.004
20. Tan CS, Ngo WK, Chen JP, Tan NW, Lim THGroup ES. EVEREST Study Report 2: Imaging and Grading Protocol, and Baseline Characteristics of a Randomised Controlled Trial of Polypoidal Choroidal Vasculopathy. *Br J Ophthalmol* (2015) 99:624–8. doi: 10.1136/bjophthalmol-2014-305674

21. Cheung CMG, Laude A, Wong W, Mathur R, Chan CM, Wong E, et al. Improved Specificity of Polypoidal Choroidal Vasculopathy Diagnosis Using a Modified Everest Criteria. *Retina-the J Retinal Vitreous Dis* (2015) 35:1375–80. doi: 10.1097/iae.0000000000000482
22. Cheung CMG, Lai TYY, Teo K, Ruamviboonsuk P, Chen SJ, Kim JE, et al. Polypoidal Choroidal Vasculopathy: Consensus Nomenclature and Non-Indocyanine Green Angiograph Diagnostic Criteria From the Asia-Pacific Ocular Imaging Society PCV Workgroup. *Ophthalmology* (2021) 128:443–52. doi: 10.1016/j.ophtha.2020.08.006
23. Spaide RF, Jaffe GJ, Sarraf D, Freund KB, Sadda SR, Staurenghi G, et al. Consensus Nomenclature for Reporting Neovascular Age-Related Macular Degeneration Data: Consensus on Neovascular Age-Related Macular Degeneration Nomenclature Study Group. *Ophthalmology* (2020) 127:616–36. doi: 10.1016/j.ophtha.2019.11.004
24. Zhang X, Qiu B, Wang Y, Li Z, Zeng Y, Chen X, et al. Distribution Characteristics of Choroidal Thickness in Normal Population and the Diagnostic Cut Off Value of Pachychoroid. *Chin J Exp Ophthalmol* (2022) 40:548–55. doi: 10.3760/cma.j.cn115989-20220401-00127
25. Sniderman AD, Islam S, Yusuf S, McQueen MJ. Discordance Analysis of Apolipoprotein B and non-High Density Lipoprotein Cholesterol as Markers of Cardiovascular Risk in the INTERHEART Study. *Atherosclerosis* (2012) 225:444–9. doi: 10.1016/j.atherosclerosis.2012.08.039
26. Sene A, Khan AA, Cox D, Nakamura RE, Santeford A, Kim BM, et al. Impaired Cholesterol Efflux in Senescent Macrophages Promotes Age-Related Macular Degeneration. *Cell Metab* (2013) 17:549–61. doi: 10.1016/j.cmet.2013.03.009
27. Dithmar S, Sharara NA, Curcio CA, Le NA, Zhang Y, Brown S, et al. Murine High-Fat Diet and Laser Photochemical Model of Basal Deposits in Bruch Membrane. *Arch Ophthalmol (Chicago Ill 1960)* (2001) 119:1643–9. doi: 10.1001/archopht.119.11.1643
28. Sallo FB, Bereczki E, Csont T, Luthert PJ, Munro P, Ferdinandy P, et al. Bruch's Membrane Changes in Transgenic Mice Overexpressing the Human Biglycan and Apolipoprotein B-100 Genes. *Exp Eye Res* (2009) 89:178–86. doi: 10.1016/j.exer.2009.03.006
29. Liu K, Chen LJ, Lai TY, Tam PO, Ho M, Chiang SW, et al. Genes in the High-Density Lipoprotein Metabolic Pathway in Age-Related Macular Degeneration and Polypoidal Choroidal Vasculopathy. *Ophthalmology* (2014) 121:911–6. doi: 10.1016/j.ophtha.2013.10.042
30. de Nijs T, Sniderman A, de Graaf J. ApoB Versus Non-HDL-Cholesterol: Diagnosis and Cardiovascular Risk Management. *Crit Rev Clin Lab Sci* (2013) 50:163–71. doi: 10.3109/10408363.2013.847897
31. Nie Y, Chen X, Zhang X, Gong H, Zhu M, Qiu B, et al. Plasma Apolipoproteins and Their Ratios as Novel Biomarkers for Type 2 Diabetes Mellitus and Diabetic Retinopathy. *Front Endocrinol* (2022).
32. Group. BDW. Biomarkers and Surrogate Endpoints: Preferred Definitions and Conceptual Framework. *Clin Pharmacol Ther* (2001) 69:89–95. doi: 10.1067/mcp.2001.113989
33. García-Gutiérrez MS, Navarrete F, Sala F, Gasparyan A, Austrich-Olivares A, Manzanares J. Biomarkers in Psychiatry: Concept, Definition, Types and Relevance to the Clinical Reality. *Front Psychiatry* (2020) 11:432. doi: 10.3389/fpsyt.2020.00432
34. Nassar K, Grisanti S, Elfar E, Lüke J, Lüke M, Grisanti S. Serum Cytokines as Biomarkers for Age-Related Macular Degeneration. *Graefe's Arch Clin Exp Ophthalmol = Albrecht von Graefes Archiv fur klinische und experimentelle Ophthalmologie* (2015) 253:699–704. doi: 10.1007/s00417-014-2738-8
35. Oca AI, Pérez-Sala Á, Pariente A, Ochoa R, Velilla S, Peláez R, et al. Predictive Biomarkers of Age-Related Macular Degeneration Response to Anti-VEGF Treatment. *J Pers Med* (2021) 11(12):1329. doi: 10.3390/jpm11121329
36. Fenner BJ, Cheung CMG, Sim SS, Lee WK, Staurenghi G, Lai TYY, et al. Evolving Treatment Paradigms for PCV. *Eye (London England)* (2022) 36:257–65. doi: 10.1038/s41433-021-01688-7
37. Wang Y, Wang M, Zhang X, Zhang Q, Nie J, Zhang M, et al. The Association Between the Lipids Levels in Blood and Risk of Age-Related Macular Degeneration. *Nutrients* (2016) 8:663. doi: 10.3390/nu8100663
38. van Leeuwen EM, Emri E, Merle BMJ, Colijn JM, Kersten E, Cougnard-Gregoire A, et al. A New Perspective on Lipid Research in Age-Related Macular Degeneration. *Prog retinal eye Res* (2018) 67:56–86. doi: 10.1016/j.preteyeres.2018.04.006

Conflict of Interest: The authors declare that the research was conducted in the absence of any commercial or financial relationships that could be construed as a potential conflict of interest.

frontiers | Frontiers in Endocrinology

ORIGINAL RESEARCH
published: 22 July 2022
doi: 10.3389/fendo.2022.895186

Alterations in Spontaneous Neuronal Activity and Microvascular Density of the Optic Nerve Head in Active Thyroid-Associated Ophthalmopathy

Pingyi Zhu[1,2†], Zihui Liu[3†], Yi Lu[2], Yu Wang[2], Danbin Zhang[4], Pinghui Zhao[2], Lulu Lin[2], Nimo Mohamed Hussein[2], Xiaozheng Liu[2,5], Zhihan Yan[2], Guanghui Bai[2,6] and Yunhai Tu[1,3*]*

[1] Wenzhou Medical University, Wenzhou, China, [2] Department of Radiology, The Second Affiliated Hospital and Yuying Children's Hospital of Wenzhou Medical University, Wenzhou, China, [3] Department of Orbital and Oculoplastic Surgery, The Eye Hospital of Wenzhou Medical University, Wenzhou, China, [4] Department of Radiology, The First Affiliated Hospital, Zhejiang University School of Medicine, Hangzhou, China, [5] China-USA Neuroimaging Research Institute, The Second Affiliated Hospital and Yuying Children's Hospital of Wenzhou Medical University, Wenzhou, China, [6] Wenzhou Key Laboratory of Basic Science and Translational Research of Radiation Oncology, Wenzhou, China

Purpose: To investigate changes in local spontaneous brain activity in patients with active thyroid-associated ophthalmopathy (TAO) and explore the relationship between such alterations and microvascular indices.

Methods: Thirty-six active TAO patients with active phase and 39 healthy controls (HCs) were enrolled in this study. All participants underwent resting-state functional magnetic resonance imaging (rs-fMRI), neuropsychological tests, and ophthalmological examinations. The rs-fMRI-based fractional low-frequency fluctuation amplitude (fALFF) analysis methods were used to assess spontaneous brain activity in both groups. The structure (peripapillary retinal nerve fiber layer, pRNFL) and microvascular indices (the optic nerve head (ONH) whole image vessel density, ONH-wiVD, and peripapillary vessel density) were analyzed through optical coherence tomographic angiography imaging. The relationship between abnormal spontaneous brain activity and ophthalmological indices was analyzed using the Spearman's rank correlation analysis.

Results: Compared with HCs, active TAO patients had increased fALFF in the right inferior temporal gyrus (R.ITG) and left posterior cingulate gyrus (L.PCC), but decreased fALFF in the right calcarine (R.CAL). The fALFF values in L.PCC were positively correlated

OPEN ACCESS

Edited by:
Jing Li,
Capital Normal University, China

Reviewed by:
Yong Tao,
Capital Medical University, China
Lian Zhao,
National Eye Institute (NIH), United States

***Correspondence:**
Guanghui Bai
bghu79@126.com
Yunhai Tu
23200469@qq.com

[†]These authors have contributed equally to this work

Specialty section:
This article was submitted to Molecular and Structural Endocrinology, a section of the journal Frontiers in Endocrinology

Received: 13 March 2022
Accepted: 02 May 2022
Published: 22 July 2022

Citation:
Zhu P, Liu Z, Lu Y, Wang Y, Zhang D, Zhao P, Lin L, Hussein NM, Liu X, Yan Z, Bai G and Tu Y (2022) Alterations in Spontaneous Neuronal Activity and Microvascular Density of the Optic Nerve Head in Active Thyroid-Associated Ophthalmopathy. Front. Endocrinol. 13:895186. doi: 10.3389/fendo.2022.895186

with peripapillary vessel density, whereas fALFF values in R.CAL were negatively related to peripapillary vessel density.

Conclusions: This study demonstrates that changes in spontaneous brain activity of active TAO are accompanied by peripapillary microvascular variations. These results provide insights into the pathophysiological mechanisms of active TAO. In addition, the combination of fALFF values and peripapillary vessel density may be served as important references for better clinical decision making.

Keywords: active thyroid-associated ophthalmopathy, fractional low-frequency fluctuation amplitude, fMRI, resting state, optical coherence tomography angiography

INTRODUCTION

Thyroid-associated ophthalmopathy (TAO), commonly known as Graves' ophthalmopathy or thyroid eye disease, is an organ-specific, progressive autoimmune inflammatory disease affecting the orbital. TAO is the commonest autoimmune orbital illness in adults (1, 2) and often involves both orbits, with an asymmetrical appearance (3, 4). The most common ophthalmic consequences in TAO patients are periorbital edema, upper eyelid retraction, diplopia, exophthalmos, dysfunctional eye movement, and impaired visual function (5–9).

TAO may cause permanent visual loss as well as significant facial disfigurement, significantly reducing the patient's quality of life through restricted daily activity, social dysfunction, and diminished confidence (10, 11). Past studies have shown that TAO impairs the visual pathway and can harm cognitive processes (2–4, 10, 12, 13). Thus, there is an urgent need for a better understanding of the neuropathological mechanisms underlying TAO. Moreover, it is crucial to detect TAO early and prevent associated neuropsychic dysfunctions through prompt treatment, including anti-inflammatory therapy or decompression surgery.

The amplitude of low-frequency fluctuations (ALFF) produced by resting-state functional magnetic resonance imaging (rs-fMRI) is considered to be a direct indicator of the level of spontaneous brain activity (14, 15). ALFF has been extensively used in individuals with a range of ocular or metabolic illnesses, including glaucoma (16), neuromyelitis optica-spectrum disorders (17) and type 2 diabetes (18). However, ALFF is prone to artifacts generated by physiological noise (19). Fractional ALFF (fALFF) is another extensively used technique for determining the contribution of low-frequency oscillations to the overall frequency range (19) and it may be more sensitive than ALFF in detecting regional brain abnormalities since it is less prone to physiological noise artifacts (19). Moreover, fALFF based on rs-fMRI is considered one of the most reliable and reproducible fMRI parameters for assessing the brain's physiological state (14, 15). However, few studies have investigated the value of fALFF in active TAO patients.

Optical coherence tomographic angiography (OCTA) is a novel angiographic technique based on optical coherence tomography (OCT) and can generate 3-dimensional microcirculation vascular maps and better displays of superficial and deep capillary layers of the retina without intravenous injection of a contrast agent. OCTA also generates quantitative data on retinal and choroidal vessels (20). Because it is safer, faster, and non-invasive, OCTA is widely used to diagnose and monitor retinal microvascular pathology in various diseases, including diabetic retinopathy, macular edema, and TAO (21, 22). Ophthalmological parameters, including microvascular detail and parapapillary retinal nerve fiber layer (pRNFL) thickness, can reflect the activity and severity of TAO (1, 23). Therefore, it is worth exploring whether ophthalmological parameters using OCTA correlate with altered fALFF values.

Here, we evaluated changes in local spontaneous brain activity of active TAO cases using fALFF, which can provide a more in-depth assessment of brain dysfunction. We also investigated whether fALFF values from aberrant brain regions correlate to the thickness of pRNFL and the vessels density of ONH, and offer insight into neuropathological mechanisms underlying active TAO.

METHODS

Patients

This study involved patients with active TAO who were admitted to the Eye Hospital of Wenzhou Medical University, Zhejiang Province, China, from September 2019 to July 2021. All participants met the criteria of the European Thyroid Association/European Group (24). Active TAO was indicated by a 7-point clinical activity score (*CAS*) of ≥3 as described previous (25). The healthy controls (HCs) group was made of 39 healthy individuals recruited from community or the health care facility and matched with the TAO group for age, sex, and years of education by using the propensity score-matching (PSM) analysis (1:1 ratio, with nearest-neighbor matching or caliper width of 0.1 of the standard deviation of the logit). Based on Edinburgh Handedness Inventory, all participants were right-handed (26). Exclusion criteria were: (1) symptoms of other ocular diseases, e.g., strabismus, amblyopia, cataracts, and glaucoma; (2) history of eye surgery; (3) history of psychiatric or neurologic illness, e.g., depression and bipolar disorder; (4) alcohol or drug addiction; (5) brain structural abnormalities, e.g., tumors, trauma, and infection; (6) ineligibility for MRI scanning,

e.g., due to implanted metal devices or cardiac pacemaker; (7) low image quality, e.g., motion artifacts, image distortion, which would affect the accuracy of fMRI analysis.

All participants underwent ophthalmological examination, neuropsychological tests, and MRI scanning within a week. Neuropsychological tests included the Beck Depression Inventory-II (BDI-II) (27) and Insomnia Severity Index (ISI) (28). Records on the participants' general medical history and ophthalmology history were retrieved. Participants in the patients group were asked about the courses of hyperthyroidism and TAO. A total of 36 patients with active TAO (17 females and 19 males) and 39 HCs (21 females and 18 males) were finally enrolled into the study. The enrollment flowchart has been presented in the **Supplementary Figure 1**.

Ethical approval for the study was granted by the research ethics committee of the Eye Hospital of Wenzhou Medical University(2020-142-K-127). This study complied with the Declaration of Helsinki guidelines. All study participants gave written informed consent.

MRI Acquisition

MRI examination was done using a 3.0 Tesla scanner (GE Healthcare's Discovery 750, USA) equipped with a 32-channel phase array head coil. The MRI room was completely dark during the tests. Participants were instructed to maintain a steady position, and kept eyes closed while awake. To protect the auditory system, participants were asked to wear noise-canceling earplugs. A sponge pad was used to minimize head movement. Before rs-fMRI scanning, routine head MRI scans, including T1, T2, T2Flair, and diffusion-weighted images, were obtained and analyzed by an expert radiologist to rule out structural brain abnormalities. High-resolution volumetric 3-D T1-weighted imaging data were acquired on a 3D BRAVO sequence in the sagittal orientation using the following parameters: slices = 188, field of view (FOV) = 256mm×256mm, matrix size = 256×256, slice thickness = 1mm, repetition time (TR) = 7.7ms, echo time (TE) = 3.4ms, flip angle (FA) = 9°, no gap. rs-fMRI images were acquired for the whole brain in an axial orientation with a gradient echo planar imaging sequence using the following parameters: slices = 54, FOV = 216mm×216mm, TE = 30ms, TR = 2500ms, flip angle (FA) = 90°, matrix size = 72×72, slice thickness = 3mm, no gap.

MRI Data Preprocessing

rs-fMRI data preprocessing was done using Data Processing Assistant for Resting-State fMRI Advance (DPARSFA, http://www.restfmri.net), a software package based on statistical parametric mapping (SPM8, http://www.fil.ion.ucl.ac.uk/spm). The first 10 volumes were eliminated in order to reduce the environmental noise and to achieve a constant level of magnetization. Remaining volumes were then corrected for slice timing and head motion (head translation or rotation by 3mm in 3 directions or axes). To minimize confusing signals, regression analysis was used (the white matter, cerebral-spinal fluid, and Friston 24 head motion parameters). Images were then normalized in the standard Montreal Neurological Institute (MNI) space using a resampling resolution of $3\times3\times3mm^3$ and spatially smoothed with a 6mm full width at half maximum (FWHM) kernel.

fALFF Analysis

The fALFF were examined using the DPARSFA software based on the preprocessed data. To acquire a power spectrum, preprocessed time series were transformed into the frequency domain using the fast Fourier transform (FFT) (29). The square root of each frequency of the power spectrum was calculated and the average square root of the spectrum in the range of 0.01-0.08 Hz for each voxel analyzed as ALFF (29). To eliminate interference from respiratory and cardiac signals, ALFF values were divided by the sum of the amplitudes across the entire frequency band to get the fALFF (19).

Ophthalmological Examinations

Each individual underwent complete ophthalmological examinations, which included axial length (AL), intraocular pressure, slit lamp examination, best-corrected visual acuity (BCVA), and standard automated perimetry using the 30-2 program of the Humphrey Visual Field Analyser (Carl Zeiss Meditec, Dublin, CA, USA), peripapillary retinal nerve fibre layer (pRNFL) thickness using the SD-Optical Coherent Tomography (RTVue XR Avanti, Optovue Inc. Fremont, CA. USA), and vascular density calculated using the manufacturer's angiometric software (**Figure 1**). The ONH scanning region was classified into 2 parts using an ONH grid, including whole image and peripapillary fields. The default quantified vascular layer is superficial retinal layers which extend from the inner layer membrane to the retinal nerve fiber layer posterior boundary. Vascular density was defined as area of pixels occupied by retinal vessels divided by total area of the whole image. To rule out eye disorders, all patients and HCs were checked by an ophthalmologist with 8 years of experience in active TAO treatment. Although both eyes were eligible for investigation, final analysis involved only data from the right eye.

Statistical Analysis

Two-sample t-test was done using the REST software to compare fALFF differences between active TAO and the HCs, with age and sex as nuisance covariates. AlphaSim multiple comparison correction was done using 3dClustSim on AFNI (Analysis of Functional NeuroImages software) software (http://afni.nimh.nih.gov). The significance threshold was set at uncorrected $p<0.005$, with a voxel number >25, corresponding to corrected $p<0.05$.

The Kolmogorov-Smirnov test was used to normalize continuous variables. The Mann-Whitney U test was used to compare non-normally distributed variables. Normally distributed data were compared using an independent-samples t-test. Differences between two groups of categorical variables were compared using Chi-squared testing. Association between fALFF values and ophthalmological data from active TAO cases was assessed using Spearman's rank correlation analysis. Statistical analyses were done on SPSS version 22 (IBM) and

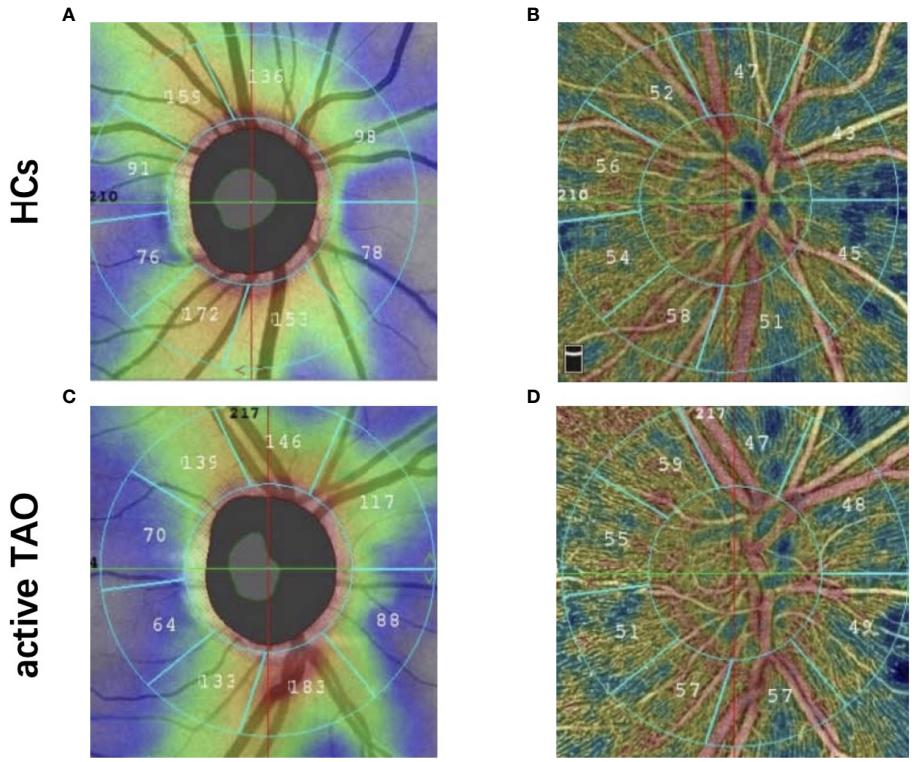

FIGURE 1 | Representative OCT-A image between two groups. Peripapillary retinal nerve fiber layer thickness image in healthy eye **(A)** and active TAO **(B)** eyes. Optic nerve head whole image vessel density and peripapillary vessel density map in healthy eye **(C)** and active TAO **(D)** eyes.

Prism version 7 (GraphPad). P<0.05 was considered statistically significant.

RESULTS

Demographic and Ophthalmological Characteristics Between Active TAO and HCs

The participants' demographic and ophthalmological features are shown on **Table 1**. The active TAO and HC groups did not differ significantly with regards to age, education level, gender, and pRNFL thickness (p>0.05). No notable differences were observed in the BDI-II and ISI (p>0.05) between active TAO and HCs group. Relative to the HCs group, the active TAO group had a significantly lower BCVA (p<0.001) and onh-wiVD (p<0.05). Additionally, relative to HCs, active TAO patients exhibited significantly higher vessel density in the peripapillary (p<0.001) and IOP (p<0.001).

Differences of fALFF Values Between Active TAO and HCs

Compared to HCs, active TAO patients exhibited increased fALFF in the right inferior temporal gyrus (R.ITG) and left posterior cingulate gyrus (L.PCC), and reduced fALFF in the right calcarine (R.CAL, **Table 2**; **Figures 2**–**4**).

TABLE 1 | Demographic and ophthalmological characteristics between active TAO and HCs group.

Characteristics	active TAO (n=36)	HCs (n=39)	*P*-value
	N (%) or $\bar{x}$ ± s or M (P_{25}, P_{75})		
Demographic			
Age (years)	46.6 ± 11.6	47.1 ± 11.3	0.875[c]
Gender			0.566[b]
-male	19 (52.8)	18 (46.2)	
-female	17 (47.2)	21 (53.8)	
With a history of			
-smoking	5 (13.9)	4 (10.3)	0.629[b]
-alcohol drinking	5 (13.9)	5 (12.8)	0.892[b]
-hypertension	5 (13.9)	6 (15.4)	0.855[b]
-diabetes mellitus	1 (0.1)	2 (0.1)	0.604[b]
Ophthalmological			
BCVA	1.0 (0.85-1.0)	1.2 (1.0-1.2)	**<0.001***[b]
AL, mm	23.0 (21.0-24.5)	23. 2(22.7-24.5)	0.213[a]
IOP, mmHg	17.6 (12.7-21.5)	12.6 (10.9-14.2)	**<0.001***[a]
pRNFL thickness (um)	114.4 ± 14.5	114.9 ± 11.9	0.869[c]
vessel density (%)			
-ONH-wiVD	56.7 (54.3-57.6)	58.6 (56.1-59.3)	**0.042***[a]
-Peripapillary	58.2 ± 3.1	52.8 ± 3.0	**<0.001***[c]

[a]*p value with Mann–Whitney test.*
[b]*p value with Chi-square test.*
[c]*p value with independent-samples t-test.*
**Significant at p < 0.05.*
TAO, Thyroid-Associated Ophthalmopathy; HCs, healthy controls; BCVA, Best-corrected visual acuity; AL, axial length; IOP, intraocular pressure; pRNFL, peripapillary retinal nerve fiber layer; ONH-wiVD, optic nerve head whole image vessel density.

TABLE 2 | Brain regions with significant differences of fALFF in subjects with active TAO compared to HCs.

Brain regions	Cluster size	T values	MNI coordinates		
			X	y	z
TAO>HCs					
R.ITG	33	3.4880	51	-9	-33
L.PCC	27	4.1549	-9	-42	27
TAO<HCs					
R.CAL	29	-3.4305	12	-96	-6

fALFF, fractional Amplitude of Low Frequency Fluctuation; TAO, thyroid-associated ophthalmopathy; HCs, healthy controls; MNI, Montreal Neurological Institute; R.ITG, right inferior temporal gyrus; L.PCC, left posterior cingulate gyrus; R.CAL, right calcarine.

Correlations Between fALFF Values and Ocular Variations

In active TAO group, fALFF values in L.PCC positively correlated with peripapillary vessel density (r=0.354, p=0.002, **Figure 5**). fALFF values in R.CAL negatively correlated with peripapillary vessel density (r=-0.249, p=0.031, **Figure 6**). However, there was no significant correlation between altered fALFF values and ONH-wiVD or pRNFL thickness (p>0.05). In HC group, there was no significant correlation between abnormal fALFF values and ocular variation (p>0.05).

DISCUSSION

Although TAO impairment is well documented at the optic nerve and retinal microvascular levels, it is poorly understood at the whole brain activity level. Our data indicate that active TAO patients exhibit significant alternation in spontaneous neural activity in brain regions mainly associated with visual and visual-related functions. Furthermore, fALFF values in abnormal brain regions significantly correlated with peripapillary microvascular impairment. To the best of our knowledge, this is the first study that provided novel insights into regional abnormalities in fALFF utilizing rs-fMRI processing technique, detecting the correlations between altered spontaneous neuronal activity across the entire brain and peripapillary microvascular variations in patients with active TAO, and developing a neuroimaging biomarker for assessing the disease severity and activity.

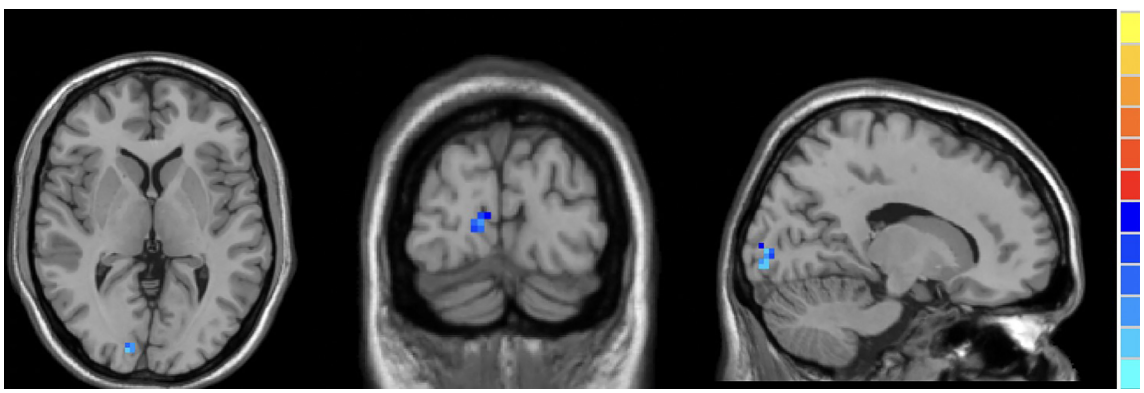

FIGURE 2 | In comparison with HCs, active TAO patients showed decreased fALFF in the right calcarine.

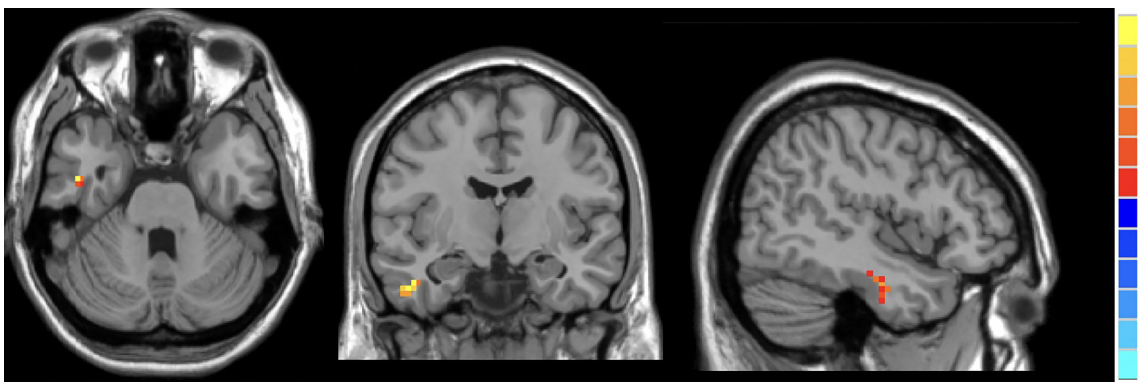

FIGURE 3 | In comparison with HCs, active TAO patients showed increased fALFF in the right inferior temporal gyrus.

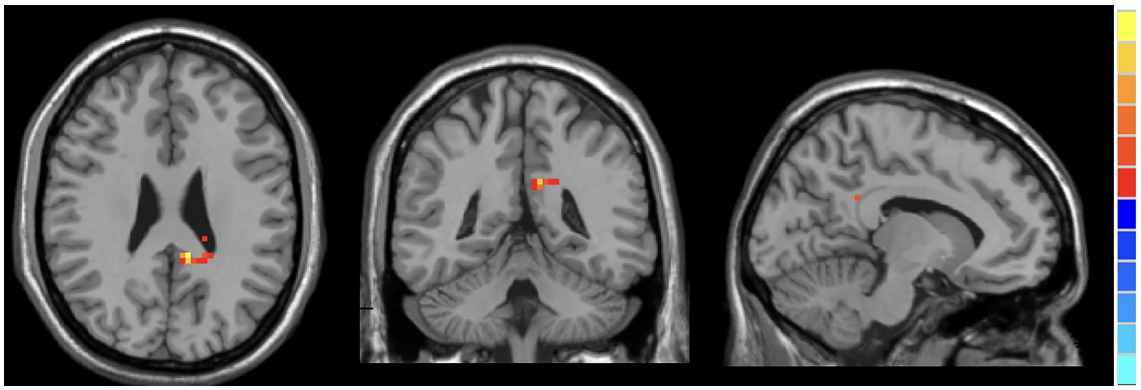

FIGURE 4 | In comparison with HCs, active TAO patients showed increased fALFF in the left posterior cingulate gyrus.

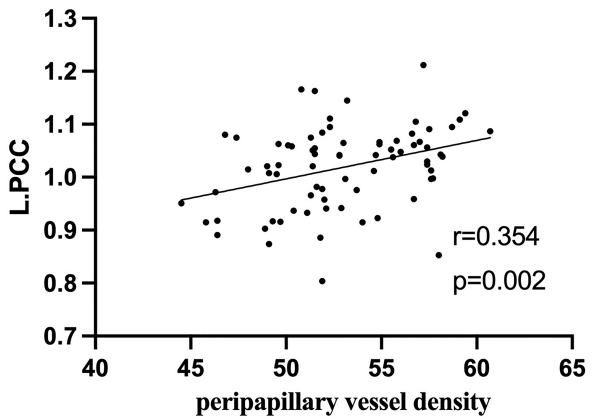

FIGURE 5 | In active TAO group, the fALFF values in L.PCC were positively correlated with peripapillary vessel density (r = 0.354, p = 0.002).

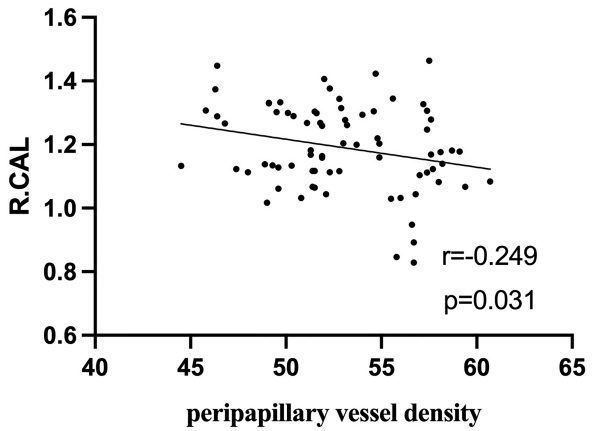

FIGURE 6 | In active TAO group, the fALFF values in R.CAL were negatively correlated with peripapillary vessel density (r = -0.249, p = 0.031).

In this study, we demonstrated that patients with active TAO presented increased peripapillary vessel density compared with the healthy controls. According to existing literatures, acute inflammation may be the main reason, which increases orbital arterial blood flow velocities (30, 31). Consistently, Lei Ye et all (22) also observed that TAO patients had increased retinal microvascular density. However, Jian H et all (32) didn't find a significant difference in peripapillary vessel density between the active non-dysthyroid optic neuropathy (DON) TAO patients and the normal control group, while TAO patients with DON had a significant decreased peripapillary vessel density in comparison to other patients. Researchers postulated that this phenomenon was the consequence of increased venous pressure and choroidal vessel resistance due to elevated intra-orbital pressure. From our prospective, the inconsistent results across studies may be attributed to the differences in severity and activity of the disease.

Relative to HCs, active TAO patients exhibited lower spontaneous neuronal activity in the R.CAL located in the occipital lobe, which is consistent with previous findings (2, 10, 12). The occipital lobe is primarily involved in visual formation and functional visual perception processes (33), and it is where visual information is integrated with information from sensory systems, including the auditory system (34). CAL is regarded to be the primary visual cortex since it receives direct visual input from the eyes *via* thalamic relays (34). Additionally, CAL is included in the Brodmann's region 17(BA17). Previous findings show that cortical visual stimulus generators induce steady-state responses specific to occipital areas *via* visual stimulus streams (35). More specialized, centers of gravity were located in BA17 (35), which revealed that BA17 is crucial for basic visual processing. BA17 receives visual signals from the lateral geniculate nucleus and transmits them to the secondary visual cortex (36). A similar finding revealed that BA17 is important in fundamental visual processing, including visual orientation, spatial frequency, and color perception (16). Our findings of decreased spontaneous neural activity in the R.CAL imply impairment of visual information processing in patients with active TAO, which is consistent with previous findings (16).

Our analyses also revealed increased spontaneous brain activity in R.ITG, which is located in the temporal lobe. Temporal lobe regions are critical for visual information processing and receive substantial inputs from the visual cortex for visual object recognition and spatial localization (34). Moreover, the ITG is considered to be the final location of the ventral cortical visual system, which serves as a link between auditory and visual processing, perception, and memory (37). Notably, ITG is involved in high cognitive functions including emotional regulation (38) and social cognition (39, 40). Previous studies on TAO patients indicate a clear tendency toward anxiety and depression (2, 10). Thus, increased spontaneous neural activity in R.ITG may underlie the dysfunctional visual and emotional regulation in patients with active TAO, contributing to emotional lability, cognitive dysfunction, and increased prevalence of suicidal tendencies.

Here, we find that compared to HCs, active TAO patients exhibited higher L.PCC fALFF values. PCC and ITG form a pivotal hub of the default mode network (DMN) (41, 42). The DMN is involved in the maintenance of baseline brain activities associated with spontaneous cognition, self-awareness, monitoring of the external environment and interactive modulation between internal mind activities and external tasks, which are critical for cognitive performance (42–44). Abnormal spontaneous activities in numerous DMN brain regions is observed in patients with endocrine diseases, such as painful diabetic neuropathy (18), who also demonstrate clear proclivity for anxiety and depression. Accordingly, we could deduce that abnormal spontaneous neuronal activities in the DMN brain regions of patients with active TAO may contribute to cognition dysfunction. Furthermore, active TAO patients are more inclined to irritability and anxiety (45), which may be associated with DMN dysfunction.

ONH vessel density and pRNFL thickness are measured by OCT-A and are useful in identifying TAO patients with DON, the most common vision-threatening condition in TAO and damaged optic nerves (23). It is reported that retinal nerve fiber layer thickness correlates with vascular density and the disease activity of TAO (1). Past studies show that altered fALFF in specific brain regions (left cuneus, bilateral superior frontal gyrus) correlates with RNFL thickness in patients with primary angle-closure glaucoma, suggesting that these finding are conducive to assessing the disease severity (16). A similar finding indicated that functional connectivity density correlates with pRNFL thickness in patients with neuromyelitis opticaspectrum disorders (17). However, to our knowledge, the correlation between fALFF and pRNFL thickness or ONH vascular density in active TAO patients has not been previously investigated. In this study, correlation analysis revealed that the fALFF value of L.PCC positively correlated with peripapillary vessel density. Moreover, we found negative correlation between fALFF values in R.CAL with peripapillary vessel density. These results indicate that combining fALFF values from these brain regions with vessel density in the peripapillary may indicate disease severity in active TAO patients, as well as their involvement in DON.

Several limitations of current research should be recognized. First, neuropsychological tests in our study only included BDI-II and ISI. Future research should include more detailed and comprehensive neuropsychological tests to further confirm association between spontaneous brain activity with cognitive changes. Secondly, our sample size was relatively small. Further studies with a larger sample size could strengthen the statistical power and verify these results. Thirdly, the study was a cross-sectional design. Therefore, a longitudinal follow-up of these subjects may provide more information and reinforce the present interpretation.

CONCLUSION

In summary, our results show that active TAO patients exhibit significant alternations of spontaneous neural activity in brain regions associated with visual and visual-related functions. Additionally, fALFF values in abnormal brain regions significantly correlated with peripapillary microvascular impairment. These abnormalities may provide a clue to reveal neuropathological mechanisms of active TAO. The fALFF results from certain brain regions together with peripapillary vessel density may be served as important references for better clinical decision making.

DATA AVAILABILITY STATEMENT

The raw data supporting the conclusions of this article will be made available by the authors, without undue reservation.

ETHICS STATEMENT

The studies involving human participants were reviewed and approved by the research ethics committee of the Eye Hospital of Wenzhou Medical University. The patients/participants provided their written informed consent to participate in this study.

AUTHOR CONTRIBUTIONS

All the authors included in this paper fulfil the criteria of authorship. GB and YT designed the study and had full access to all data in this study. PYZ, ZL, YL and YW enrolled the participants. DZ, PHZ and LL collated all the preoperative and postoperative data. XZL processed the data. PYZ drafted the manuscript. NH, ZY, GB and YT reviewed and edited the manuscript. All authors read and approved the manuscript.

FUNDING

This research was supported by the National Natural Science Foundation of China (Grant Nos.81771914, 82071902, 82071993), Natural Science Foundation of Zhejiang Province (nos. LY19H180003) and Wenzhou Science and Technology Bureau in China (No. Y20180112).

SUPPLEMENTARY MATERIAL

The Supplementary Material for this article can be found online at: https://www.frontiersin.org/articles/10.3389/fendo.2022.895186/full#supplementary-material

Supplementary Figure 1 | Flowchart of patient enrollment.

REFERENCES

1. Yu L, Jiao Q, Cheng Y, Zhu Y, Lin Z, Shen X. Evaluation of Retinal and Choroidal Variations in Thyroid-Associated Ophthalmopathy Using Optical Coherence Tomography Angiography. *BMC Ophthalmol* (2020) 20:421. doi: 10.1186/s12886-020-01692-7
2. Chen W, Wu Q, Chen L, Zhou J, Chen HH, Xu XQ, et al. Aberrant Brain Voxel-Wise Resting State fMRI in Patients With Thyroid-Associated Ophthalmopathy. *J Neuroimaging* (2021) 31:773–83. doi: 10.1111/jon.12858
3. Blum Meirovitch S, Leibovitch I, Kesler A, Varssano D, Rosenblatt A, Neudorfer M. Retina and Nerve Fiber Layer Thickness in Eyes With Thyroid-Associated Ophthalmopathy. *Isr Med Assoc J* (2017) 19:277–81.
4. Smith TJ, Janssen J. Insulin-Like Growth Factor-I Receptor and Thyroid-Associated Ophthalmopathy. *Endocr Rev* (2019) 40:236–67. doi: 10.1210/er.2018-00066
5. Bahn RS. Graves' Ophthalmopathy. *N Engl J Med* (2010) 362:726–38. doi: 10.1056/NEJMra0905750
6. Maheshwari R, Weis E. Thyroid Associated Orbitopathy. *Indian J Ophthalmol* (2012) 60:87–93. doi: 10.4103/0301-4738.94048
7. Iyer S, Bahn R. Immunopathogenesis of Graves' Ophthalmopathy: The Role of the TSH Receptor. *Best Pract Res Clin Endocrinol Metab* (2012) 26:281–9. doi: 10.1016/j.beem.2011.10.003
8. McAlinden C. An Overview of Thyroid Eye Disease. *Eye Vis (Lond)* (2014) 1:9. doi: 10.1186/s40662-014-0009-8
9. Victores AJ, Takashima M. Thyroid Eye Disease: Optic Neuropathy and Orbital Decompression. *Int Ophthalmol Clin* (2016) 56:69–79. doi: 10.1097/IIO.0000000000000101
10. Chen W, Wu Q, Chen L, Zhou J, Chen HH, Xu XQ, et al. Disrupted Spontaneous Neural Activity in Patients With Thyroid-Associated Ophthalmopathy: A Resting-State fMRI Study Using Amplitude of Low-Frequency Fluctuation. *Front Hum Neurosci* (2021) 15:676967. doi: 10.3389/fnhum.2021.676967
11. Sen E, Berker D, Elgin U, Tutuncu Y, Ozturk F, Guler S. Comparison of Optic Disc Topography in the Cases With Graves Disease and Healthy Controls. *J Glaucoma* (2012) 21:586–9. doi: 10.1097/IJG.0b013e31822e8c4f
12. Qi CX, Wen Z, Huang X. Spontaneous Brain Activity Alterations in Thyroid-Associated Ophthalmopathy Patients Using Amplitude of Low-Frequency Fluctuation: A Resting-State fMRI Study. *Neuroreport* (2021) 32:1416–22. doi: 10.1097/WNR.0000000000001745
13. Yu B, Gong C, Ji YF, Xia Y, Tu YH, Wu WC. Predictive Parameters on CT Scan for Dysthyroid Optic Neuropathy. *Int J Ophthalmol* (2020) 13:1266–71. doi: 10.18240/ijo.2020.08.13
14. Yang H, Long XY, Yang Y, Yan H, Zhu CZ, Zhou XP, et al. Amplitude of Low Frequency Fluctuation Within Visual Areas Revealed by Resting-State Functional MRI. *Neuroimage* (2007) 36:144–52. doi: 10.1016/j.neuroimage.2007.01.054
15. Zuo XN, Di Martino A, Kelly C, Shehzad ZE, Gee DG, Klein DF, et al. The Oscillating Brain: Complex and Reliable. *Neuroimage* (2010) 49:1432–45. doi: 10.1016/j.neuroimage.2009.09.037
16. Wang R, Tang Z, Liu T, Sun X, Wu L, Xiao Z. Altered Spontaneous Neuronal Activity and Functional Connectivity Pattern in Primary Angle-Closure Glaucoma: A Resting-State fMRI Study. *Neurol Sci* (2021) 42:243–51. doi: 10.1007/s10072-020-04577-1
17. Wang Y, Kwapong WR, Tu Y, Xia Y, Tang J, Miao H, et al. Altered Resting-State Functional Connectivity Density in Patients With Neuromyelitis Optica-Spectrum Disorders. *Mult Scler Relat Disord* (2020) 43:102187. doi: 10.1016/j.msard.2020.102187
18. Zhang Q, Zhang P, Yan R, Xu X, Mao C, Liu X, et al. A Single-Blinded Trial Using Resting-State Functional Magnetic Resonance Imaging of Brain Activity in Patients With Type 2 Diabetes and Painful Neuropathy. *Diabetes Ther* (2019) 10:135–47. doi: 10.1007/s13300-018-0534-x
19. Zou QH, Zhu CZ, Yang Y, Zuo XN, Long XY, Cao QJ, et al. An Improved Approach to Detection of Amplitude of Low-Frequency Fluctuation (ALFF) for Resting-State fMRI: Fractional ALFF. *J Neurosci Methods* (2008) 172:137–41. doi: 10.1016/j.jneumeth.2008.04.012
20. Salz DA, de Carlo TE, Adhi M, Moult E, Choi W, Baumal CR, et al. Select Features of Diabetic Retinopathy on Swept-Source Optical Coherence Tomographic Angiography Compared With Fluorescein Angiography and Normal Eyes. *JAMA Ophthalmol* (2016) 134:644–50. doi: 10.1001/jamaophthalmol.2016.0600
21. Durbin MK, An L, Shemonski ND, Soares M, Santos T, Lopes M, et al. Quantification of Retinal Microvascular Density in Optical Coherence Tomographic Angiography Images in Diabetic Retinopathy. *JAMA Ophthalmol* (2017) 135:370–6. doi: 10.1001/jamaophthalmol.2017.0080
22. Ye L, Zhou SS, Yang WL, Bao J, Jiang N, Min YL, et al. Retinal Microvasculature Alteration in Active Thyroid-Associated Ophthalmopathy. *Endocr Pract* (2018) 24:658–67. doi: 10.4158/EP-2017-0229
23. Zhang T, Xiao W, Ye H, Chen R, Mao Y, Yang H. Peripapillary and Macular Vessel Density in Dysthyroid Optic Neuropathy: An Optical Coherence Tomography Angiography Study. *Invest Ophthalmol Vis Sci* (2019) 60:1863–9. doi: 10.1167/iovs.18-25941
24. Bartley GB. The Differential Diagnosis and Classification of Eyelid Retraction. *Ophthalmology* (1996) 103:168–76. doi: 10.1016/S0161-6420(96)30744-6
25. Bartalena L, Baldeschi L, Boboridis K, Eckstein A, Kahaly GJ, Marcocci C, et al. The 2016 European Thyroid Association/European Group on Graves' Orbitopathy Guidelines for the Management of Graves' Orbitopathy. *Eur Thyroid J* (2016) 5:9–26. doi: 10.1159/000443828
26. Espirito-Santo H, Pires CF, Garcia IQ, Daniel F, Silva AG, Fazio RL. Preliminary Validation of the Portuguese Edinburgh Handedness Inventory in an Adult Sample. *Appl Neuropsychol Adult* (2017) 24:275–87. doi: 10.1080/23279095.2017.1290636
27. Lehmicke N, Hicks RA. Relationship of Response-Set Differences on Beck Depression Inventory Scores of Undergraduate Students. *Psychol Rep* (1995) 76:15–21. doi: 10.2466/pr0.1995.76.1.15
28. Sadeghniiat-Haghighi K, Montazeri A, Khajeh-Mehrizi A, Nedjat S, Aminian O. The Insomnia Severity Index: Cross-Cultural Adaptation and Psychometric Evaluation of a Persian Version. *Qual Life Res* (2014) 23:533–7. doi: 10.1007/s11136-013-0489-3
29. Zang YF, He Y, Zhu CZ, Cao QJ, Sui MQ, Liang M, et al. Altered Baseline Brain Activity in Children With ADHD Revealed by Resting-State Functional MRI. *Brain Dev* (2007) 29:83–91. doi: 10.1016/j.braindev.2006.07.002
30. Alp MN, Ozgen A, Can I, Cakar P, Gunalp I. Colour Doppler Imaging of the Orbital Vasculature in Graves' Disease With Computed Tomographic Correlation. *Br J Ophthalmol* (2000) 84:1027–30. doi: 10.1136/bjo.84.9.1027
31. Perri P, Campa C, Costagliola C, Incorvaia C, D'Angelo S, Sebastiani A. Increased Retinal Blood Flow in Patients With Active Graves' Ophthalmopathy. *Curr Eye Res* (2007) 32:985–90. doi: 10.1080/02713680701689773
32. Jian H, Wang Y, Ou L, He W. Altered Peripapillary Vessel Density and Nerve Fiber Layer Thickness in Thyroid-Associated Ophthalmopathy Using Optical Coherence Tomography Angiography. *Int Ophthalmol* (2021) 42(3)855–62. doi: 10.1007/s10792-021-02051-1
33. Yu HL, Liu WB, Wang T, Huang PY, Jie LY, Sun JZ, et al. Difference in Resting-State Fractional Amplitude of Low-Frequency Fluctuation Between Bipolar Depression and Unipolar Depression Patients. *Eur Rev Med Pharmacol Sci* (2017) 21:1541–50.

34. Lu L, Li Q, Zhang L, Tang S, Yang X, Liu L, et al. Altered Cortical Morphology of Visual Cortex in Adults With Monocular Amblyopia. *J Magn Reson Imaging* (2019) 50:1405–12. doi: 10.1002/jmri.26708
35. Keitel C, Maess B, Schröger E, Müller MM. Early Visual and Auditory Processing Rely on Modality-Specific Attentional Resources. *Neuroimage* (2013) 70:240–9. doi: 10.1016/j.neuroimage.2012.12.046
36. Wang J, Li T, Zhou P, Wang N, Xian J, He H. Altered Functional Connectivity Within and Between the Default Model Network and the Visual Network in Primary Open-Angle Glaucoma: A Resting-State fMRI Study. *Brain Imaging Behav* (2017) 11:1154–63. doi: 10.1007/s11682-016-9597-3
37. Chen Z, Chen X, Liu M, Ma L, Yu S. Volume of Hypothalamus as a Diagnostic Biomarker of Chronic Migraine. *Front Neurol* (2019) 10:606. doi: 10.3389/fneur.2019.00606
38. Lin YH, Young IM, Conner AK, Glenn CA, Chakraborty AR, Nix CE, et al. Anatomy and White Matter Connections of the Inferior Temporal Gyrus. *World Neurosurg* (2020) 143:e656–66. doi: 10.1016/j.wneu.2020.08.058
39. Ruby P, Decety J. How Would You Feel Versus How do You Think She Would Feel? A Neuroimaging Study of Perspective-Taking With Social Emotions. *J Cognit Neurosci* (2004) 16:988–99. doi: 10.1162/0898929041502661
40. Pelphrey KA, Viola RJ, McCarthy G. When Strangers Pass: Processing of Mutual and Averted Social Gaze in the Superior Temporal Sulcus. *Psychol Sci* (2004) 15:598–603. doi: 10.1111/j.0956-7976.2004.00726.x
41. Raichle ME. The Brain's Default Mode Network. *Annu Rev Neurosci* (2015) 38:433–47. doi: 10.1146/annurev-neuro-071013-014030
42. Yu Y, Chen L, Wang Q, Hu L, Ding Q, Jia X, et al. Altered Amplitude of Low-Frequency Fluctuations in Inactive Patients With Nonneuropsychiatric Systemic Lupus Erythematosus. *Neural Plast* (2019) 2019:9408612. doi: 10.1155/2019/9408612
43. Qi R, Zhang L, Wu S, Zhong J, Zhang Z, Zhong Y, et al. Altered Resting-State Brain Activity at Functional MR Imaging During the Progression of Hepatic Encephalopathy. *Radiology* (2012) 264:187–95. doi: 10.1148/radiol.12111429
44. Gong J, Chen G, Jia Y, Zhong S, Zhao L, Luo X, et al. Disrupted Functional Connectivity Within the Default Mode Network and Salience Network in Unmedicated Bipolar II Disorder. *Progr Neuro-Psychopharmacol Biol Psych* (2019) 88:11–8. doi: 10.1016/j.pnpbp.2018.06.012
45. Kahaly GJ. Management of Graves Thyroidal and Extrathyroidal Disease: An Update. *J Clin Endocrinol Metab* (2020) 105:3704–20. doi: 10.1210/clinem/dgaa646

Conflict of Interest: The authors declare that the research was conducted in the absence of any commercial or financial relationships that could be construed as a potential conflict of interest.

frontiers | Frontiers in Endocrinology

TYPE Original Research
PUBLISHED 27 July 2022
DOI 10.3389/fendo.2022.938952

OPEN ACCESS

EDITED BY
Lian Zhao,
National Eye Institute (NIH),
United States

REVIEWED BY
Huan Chen,
Peking Union Medical College Hospital (CAMS), China
Xuan Liu,
Tsinghua University, China

*CORRESPONDENCE
Yongzhen Bao
drbaoyz@sina.com

†These authors have contributed equally to this work and share first authorship

SPECIALTY SECTION
This article was submitted to Molecular and Structural Endocrinology, a section of the journal Frontiers in Endocrinology

RECEIVED 08 May 2022
ACCEPTED 31 May 2022
PUBLISHED 27 July 2022

CITATION
Li X, Qin J, Cao X, Ren Z, Cui T and Bao Y (2022) The different structure-function correlation as measured by OCT and octopus perimetry cluster analysis in intracranial tumor and glaucoma patients.
Front. Endocrinol. 13:938952.
doi: 10.3389/fendo.2022.938952

The different structure-function correlation as measured by OCT and octopus perimetry cluster analysis in intracranial tumor and glaucoma patients

Xiaochun Li[1,2†], Jiayin Qin[1,2†], Xiaoguang Cao[1†], Zeqin Ren[1], Ting Cui[2] and Yongzhen Bao[1*]

[1]Department of Ophthalmology, Peking University People's Hospital, Eye Diseases and Optometry Institute, Beijing Key Laboratory of Diagnosis and Therapy of Retinal and Choroid Diseases, College of Optometry, Peking University Health Science Center, Beijing, China, [2]Department of Ophthalmology, Peking University International Hospital, Beijing, China

Background: To explore the correlation between visual field (VF) defect values and retinal nerve fiber layer (RNFL) thickness for intracranial tumor and glaucoma patients.

Methods: Retrospective analysis is performed for the intracranial and glaucoma patients, whose VF defect values were measured with Octopus perimeter cluster analysis, RNFL thickness, ganglion cell layer (GCL) thickness, and optic disk parameters measured with swept-source OCT. The differences between VF and RNFL (including the data of optic disc) are calculated. The correlation between VF defect values and RNFL and GCL thickness are explored.

Results: In total 43 eyes of 29 patients with intracranial tumor and 31 eyes of 19 patients with glaucoma were enrolled. The thickness of RNFL not only for the whole (360°), but also for the four quadrants was thinner in the glaucoma group than those of the intracranial tumor group ($p<0.05$), and similar to the thickness of GCL without significance (p>). There is no significant difference in VF for those two groups except glaucoma having lower sLV ($p<0.05$). A stronger correlation for mean deviations (MD)s of VF ten clusters and RNFL thickness of OCT twelve sectors is found in the glaucoma patients, but few in the intracranial tumor patients. Logistic regression also shows the loss of RNFL or increasing of vertical CDR and cup volume tending to the diagnosis of glaucoma and the irregular VF damage is inclined to the diagnosis of intracranial tumor.

Conclusions: Intracranial tumor has a weak correlation between the RNFL thickness and Octopus VF MD, compared with that of glaucoma. OCT and Octopus VF might provide more helpful information for the differential diagnosis of intracranial tumor and glaucoma.

KEYWORDS

visual field, retinal nerve fiber layer, intracranial tumor, glaucoma, correlation

Background

It is well-known that intracranial tumors can cause visual field (VF) damage when affecting the visual pathway. Also due to the retrograde degeneration, the compression of intracranial tumors can lead to the damage of ganglion cell axons, following the thinning of the retinal nerve fiber layer (RNFL) (1). Similar manifestations and conditions are also found in glaucoma eyes. With the variability of RNFL and VF manifestations, intracranial tumors are sometimes misdiagnosed as other diseases, such as glaucoma (2). A study showed that 6.5% of patients diagnosed with normal-tension glaucoma had clinically relevant compression of the anterior visual pathway (3). However, for intracranial tumors, early diagnosis is important to improve the possibilities of treatment and to reduce mortality (4). We strive to find an indicator to distinguish diagnoses between intracranial tumor and glaucoma.

Octopus perimeter (OP) is one of the most commonly used perimeters for assessing glaucoma and many neurological disorders. Cluster analysis is a special visual field analysis program conducted by OP, and divides OP into 10 clusters according to the distribution of RNFL. The built-in program automatically calculates the arithmetic mean value of mean deviation (MD) in each cluster. The cluster analysis can identify regional visual field defects while there is a small increase in MD. Some studies had explored the relationship between VF and RNFL in intracranial tumor and glaucoma patients (5–7) _ENREF_5. However, few were conducted with Octopus perimeter cluster analysis (8).

Our study is trying to analyze the structure-function correlation between the intracranial tumor and glaucoma patients, which was based on the OP ten clusters analysis and Topcon OCT twelve sectors RNFL thickness. Correlation analysis was performed to associate these VF clusters MD with RNFL sectors thickness measurements, and we try to find the difference in that correlation in the intracranial tumor and glaucoma patients.

Methods

Recruitment of patients, and inclusion and exclusion criteria

This retrospective study is conducted in the Peking University International Hospital, Beijing, China. The study is approved by the local ethical review board in accordance with the Declaration of Helsinki, and all patients provided informed consent.

Nineteen patients with glaucoma, and 29 patients with intracranial tumor, October 2018 to December 2020, are retrospectively enrolled in this study. For glaucoma patients, the inclusion criteria are diagnosed with the primary open-angle or angle-closed glaucoma, and BCVA is better or equal to 20/200. And the exclusion criteria are the acute phase of angle-closure glaucoma, high myopia (<-6.0D), the previous intraocular surgery, or any ocular diseases, which could induce the change of VF or RNFL, such as ocular trauma, corneal degeneration and dystrophy, optic nerve disease, macular or retinal disease. For the patients with intracranial tumor, the inclusion criterion is diagnosed with a pre-operative intracranial tumor, and BCVA is better or equal to 20/200. And the exclusion criteria are high myopia, previous intraocular surgery, or any ocular diseases, which could induce the change of VF or RNFL, such as glaucoma, ocular trauma, corneal degeneration, and dystrophy, optic nerve disease, macular or retinal disease.

Clinical observations

Clinical history and routine clinical examination were performed by slit-lamp microscopy, indirect ophthalmoscopy, uncorrected (UCVA), and best-corrected visual acuity (BCVA) logMAR were tested, besides intraocular pressure (IOP), VF and RNFL. IOP was measured by noncontact tonometer (Canon TX-10/TX-F, Tokyo, Japan), slit lamp examination (Topcon SL-1E, Tokyo, Japan), and fundus examination (90 Dioptre, Volk Optical, Mentor, OH) with an undilated pupil. All tests were performed in the outpatient eye clinic.

VF measurement

VF was tested with Octopus 900 perimeter (Haag-Streit AG, formerly Interzeag AG, Schlieren, Switzerland). The program of White-on-White TOP strategy with 4/1000 asb III 100ms, and Octopus G Standard distribution of points was performed for those included patients. The acceptable criterion of a reproducible test is both a false-positive and false-negative response rate of less than 15%. The manufacturer-provided ten visual field clusters were used (Figure 1), and set as VF01-VF10, with calculated MD values. The clusters of the left eyes were mirrored and numbered as those of the right eyes, to ensure uniform handling of all data.

RNFL measurement

Peripapillary RNFL thickness was measured at the same time without dilating the pupil, using DRI OCT Trion (Topcon Corp., Tokyo, Japan). RNFL measurements were categorized by clock hours, and labeled such that left eye sectors mirrored right eye sectors (Figure 1), set as Clock 1-12. Ganglion cell layer (GCL) thickness also could be read from the reports, and categorized as the rules of RNFL.

Statistical analysis

The Kolmogorov–Smirnov test was used to verify the normality of data distribution. For quantitative comparisons between groups, we used the Student *t-test* for independent samples in parametric

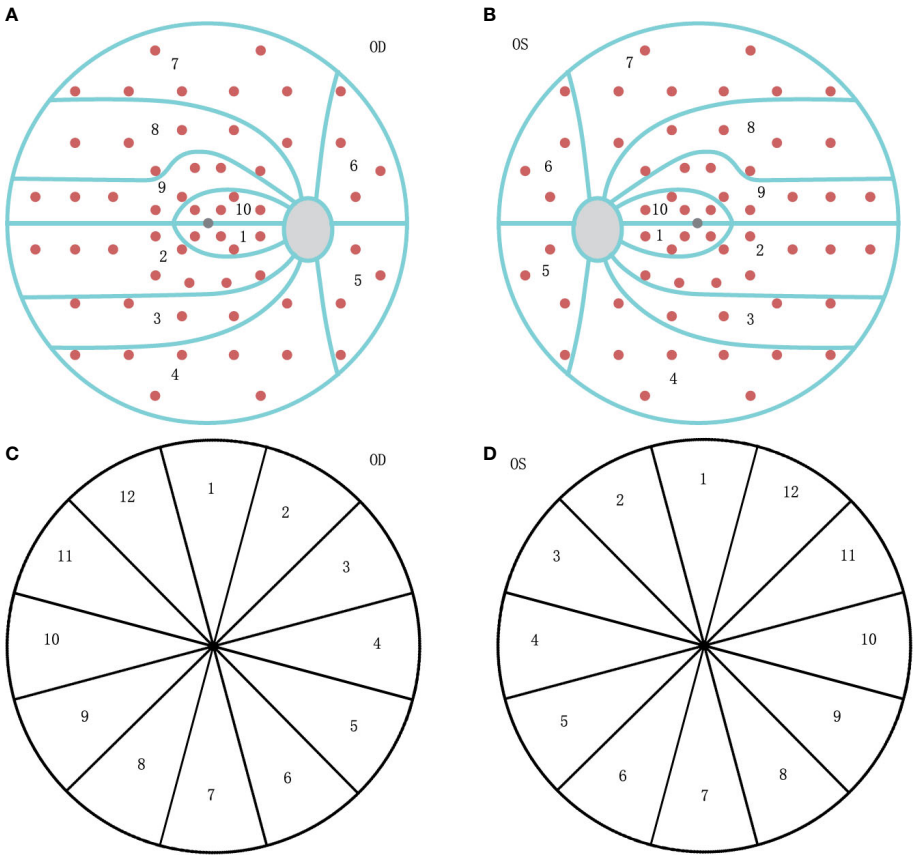

FIGURE 1
The diagram of visual field (VF) clusters and retinal nerve fiber layer (RNFL) clock-hour sector map. **(A)** The ten clusters are numbered 01 to 10 on the VF graph for the right eye (OD). **(B)** The ten clusters are numbered as 01 to 10 on the VF graph for the left eye (OS), mirrored as OD. **(C)** The clockwise number of twelve RNFL sectors on the OCT graph for the right eye (OD). **(D)** The counter-clockwise number of twelve RNFL sectors on the OCT graph for the left eye (OS), mirrored as OD.

variables and the independent Mann-Whitney U test for the non-parametric variables. Pearson correlation coefficients were calculated to assess the relationship between variables. Binary logistic regression is calculated to assess the influence of VF and RNFL changes on the diagnosis of glaucoma or intracranial tumor. Statistical analyses were performed using SPSS statistical software for Windows (version 20.0, IBM-SPSS, Chicago, IL). The level of statistical significance was set at $p<0.05$.

Results

Included patients are divided into two groups, intracranial tumor and glaucoma, due to their diagnosis. The intracranial tumor group contained 43 eyes of 29 patients (11 with pituitary adenoma, eight with meningioma, two with craniopharyngioma, three with glioma, one with ependymoma, one with metastatic tumor, one with cerebellar hemangioblastoma, one with cavernous hemangioma, and one with inflammatory pseudotumor). Of these 29 patients, at least 17 had tumors located near the optic chiasma, and at least 22 had tumors around and compressed the visual pathway directly. The tumor size of 21 patients was collected, with diameters from 12mm to 60mm. And the location of these intracranial tumors is the post-lateral geniculate body for 13 patients. The Glaucoma group contained 31 eyes of 19 patients (12 with primary open-angle glaucoma, and seven with primary angle-closed glaucoma). The mean ages of glaucoma and intracranial tumor groups are 56.21 ± 14.90 and 51.97 ± 14.11 years ($p=0.326$). The female ratios of glaucoma and intracranial tumor groups are no significant difference (9/10 and 18/11, $p=0.315$). IOP of the glaucoma eye was range 12.5 to 25.4 mmHg (17.50 ± 3.67mmHg), higher than that of the eyes with intracranial tumor was range 9.7 to 18.7 mmHg (13.79 ± 2.60mmHg) ($p<0.01$). All included patients, both intracranial tumor and glaucoma groups, had defects in their visual field. However, some of the included patients had suffered damage to RNFL thickness.

As the results of RNFL measured by TOPCON OCT in Table 1, the thickness of RNFL not only for the whole (360°)

but also for the superior, inferior, nasal, and temporal quadrants are thinner in the glaucoma group than those of the intracranial tumor group ($p<0.05$). The thickness of temporal GCL is thinner in the glaucoma group than that of the intracranial tumor group without significance ($p>0.05$). The thickness of GCL for the whole and in the other quadrants of the glaucoma group has no significant difference from those of the intracranial tumor group ($p>0.05$). Moreover, the rim area, disc area, linear CDR, vertical CDR, and cup volume of optic disc measured by OCT all have significant differences for the two groups ($p<0.05$).

On the contrary, the results (global MD, MS) of VF measured with Octopus perimeter (Table 1), for the glaucoma group, have no statistically significant difference ($p>0.05$) from those of the intracranial tumor group. However, the sLV of VF for the glaucoma group is lower than that of the intracranial tumor group ($p<0.05$).

For the glaucoma group, the correlation coefficient between VF cluster MD and RNFL sector thickness is shown in Table 2, the clusters of VF and sectors of RNFL are set in Figure 1. And the strong correlations (value more than 0.45) could be observed in Figure 2. There were few correlations between the temporal VF of physiological blind spots and RNFL. The nasal VF of the physiological blind spot, that is, the binocular overlapping area of the human front, is significantly correlated with RNFL. As shown in Table 3, few correlations were observed between VF cluster MD and RNFL sector thickness for the intracranial tumor group, the figure of correlation is not drawn.

As the binary logistic regression, the thickness of RNFL and the damage of VF are included (Table 4). It shows the loss of RNFL tending to the diagnosis of glaucoma, which might be a weak factor as the value is around one. The vertical CDR and cup volume might be a stronger factor, with higher values tending to the diagnosis of glaucoma and lower tending to the diagnosis of intracranial tumor. And the irregular damage of VF is inclined to the diagnosis of intracranial tumor.

Discussion

Visual field and OCT are the two most commonly used clinical examination methods for nerve injury disorders, such as glaucoma and intracranial tumor. The cluster analysis program in Octopus perimeter, which is designed according to the distribution of RNFL, can sensitively detect regional dysfunction when there are minimal visual field abnormalities. Perdicchi et al's study showed within normal VF and abnormal ganglion cell complex (GCC) eyes of hypertension or early-stage glaucoma, all of the eyes showed abnormal results with cluster analysis (8). Some studies had shown the correlation between the structure and function in glaucoma patients with Humphrey or Octopus perimeter and OCT (9–11) _ENREF_9. Generally, these studies all found a topographic correlation in VF and OCT. But few studies have explored the topographic correlation in intracranial tumor patients with Octopus perimeter and OCT, fewer are in cluster analysis.

TABLE 1 Data of VF and RNFL for the glaucoma and intracranial tumor groups.

Groups	Glaucoma	Intracranial tumor
N (eyes)	31	43
RNFL (360°) (μm)**	80.10±22.13	113.58±33.78
Superior quadrant of RNFL (μm)**	100.55±28.90	145.28±48.67
Inferior quadrant of RNFL (μm)**	92.32±39.34	150.12±43.98
Nasal quadrant of RNFL (μm)**	60.08±17.80	81.14±31.27
Temporal quadrant of RNFL (μm)*	66.65±19.63	78.21±23.16
GCL (360°) (μm)	39.00±6.58	39.27±5.28
Superior quadrant of GCL (μm)	36.85±8.96	37.08±7.40
Inferior quadrant of GCL (μm)	34.10±6.95	33.70±5.35
Nasal quadrant of GCL (μm)	39.46±9.48	38.10±6.23
Temporal quadrant of GCL (μm)	45.55±11.65	48.21±6.59
Rim area (μm^2)**	0.67±0.41	1.59±0.90
Disc area (μm^2) *	1.98±0.37	7.34±33.37
Linear CDR**	0.78±0.21	0.51±0.23
Vertical CDR**	0.79±0.22	0.49±0.23
Cup volume (μm^3)**	0.41±0.29	0.12±0.14
MD of VF (dB)	17.77±7.40	16.89±5.40
MS of VF (dB)	10.02±7.12	10.97±5.35
sLV of VF (dB) *	4.80±2.29	6.15±2.56

Visual field (VF); Retinal nerve fiber layer (RNFL); Ganglion cell layer (GCL); Square root of loss variance (sLV); *$p<0.05$; **$p<0.01$.

TABLE 2 The correlation coefficient of VF and RNFL for the glaucoma group.

	Clock01	Clock02	Clock03	Clock04	Clock05	Clock06	Clock07	Clock08	Clock09	Clock10	Clock11	Clock12
VF01	-0.507**	-0.399*	-0.298	-0.045	-0.072	-0.368*	-0.335	-0.241	-0.550**	-0.403*	-0.520**	-0.392*
VF02	-0.537**	-0.521**	-0.367*	-0.122	-0.275	-0.516**	-0.434*	-0.337	-0.448*	-0.380*	-0.446*	-0.610**
VF03	-0.565**	-0.541**	-0.405*	-0.198	-0.271	-0.463**	-0.370*	-0.268	-0.331	-0.288	-0.301	-0.589**
VF04	-0.622**	-0.548**	-0.404*	-0.193	-0.185	-0.409*	-0.249	-0.196	-0.355*	-0.251	-0.232	-0.434*
VF05	-0.533**	-0.433*	-0.311	-0.135	-0.052	-0.215	-0.128	-0.172	-0.295	-0.177	-0.124	-0.225
VF06	-0.537**	-0.553**	-0.375*	-0.178	-0.163	-0.457**	-0.314	-0.346	-0.419*	-0.300	-0.320	-0.402*
VF07	-0.636**	-0.711**	-0.528**	-0.203	-0.316	-0.575**	-0.544**	-0.484**	-0.498**	-0.310	-0.366*	-0.463**
VF08	-0.644**	-0.670**	-0.477**	-0.136	-0.250	-0.551**	-0.596**	-0.559**	-0.632**	-0.398*	-0.408*	-0.494**
VF09	-0.600**	-0.639**	-0.406*	-0.113	-0.213	-0.530**	-0.643**	-0.647**	-0.692**	-0.461**	-0.463**	-0.500**
VF10	-0.513**	-0.524**	-0.117	0.042	-0.079	-0.403*	-0.549**	-0.530**	-0.754**	-0.517**	-0.439*	-0.426*

Visual field (VF); Retinal nerve fiber layer (RNFL); Square root of loss variance (sLV).
The clusters of VF and category of RNFL are set in Figure 1 *p<0.05; **p<0.01.

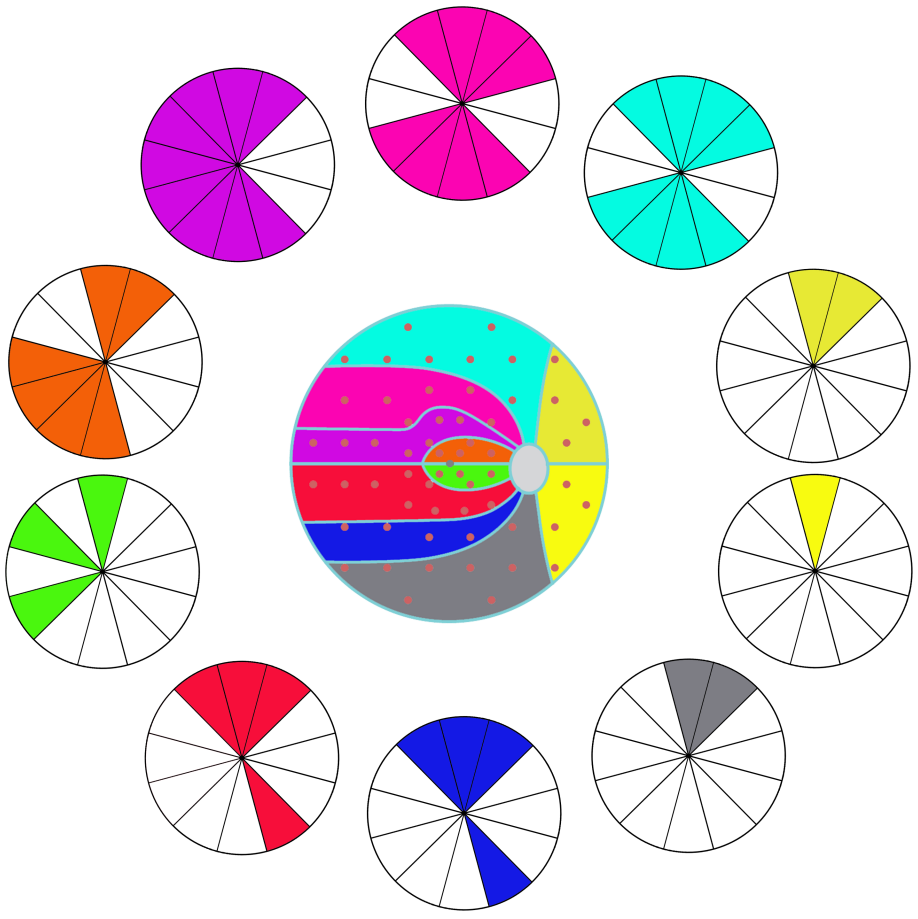

FIGURE 2
The correlation between visual field (VF) clusters and retinal nerve fiber layer (RNFL) clock-hour sectors. The same color indicates the correlation (coefficient value more than 0.45, Pearson's Correlation Analysis) between VF clusters and RNFL sectors.

TABLE 3 The correlation coefficient of VF and RNFL for the intracranial group.

	Clock01	Clock02	Clock03	Clock04	Clock05	Clock06	Clock07	Clock08	Clock09	Clock10	Clock11	Clock12
VF01	-0.128	-0.196	-0.099	0.001	0.103	0.025	0.326*	-0.190	-0.189	-0.211	-0.110	-0.096
VF02	-0.118	-0.117	-0.073	0.002	0.202	0.106	0.167	-0.048	-0.012	0.027	0.018	-0.071
VF03	-0.143	-0.201	-0.089	-0.043	0.154	0.059	0.161	0.017	0.043	0.040	0.038	-0.023
VF04	-0.110	-0.231	-0.079	0.000	0.189	0.072	0.270	-0.018	-0.071	-0.098	-0.056	-0.032
VF05	-0.206	-0.302*	-0.164	-0.081	0.163	-0.007	0.228	-0.207	-0.254	-0.215	-0.197	-0.169
VF06	-0.160	-0.258	-0.100	-0.051	0.029	-0.044	0.221	-0.217	-0.374*	-0.336*	-0.159	-0.110
VF07	-0.086	-0.225	-0.083	-0.081	0.109	-0.030	0.262	-0.090	-0.319*	-0.267	-0.143	-0.088
VF08	-0.007	-0.077	-0.064	0.012	0.205	0.051	0.380*	0.004	-0.184	-0.091	0.016	0.007
VF09	-0.091	-0.015	0.016	0.130	0.296	0.138	0.322*	-0.043	-0.072	0.023	0.039	-0.067
VF10	-0.187	-0.277	-0.149	-0.126	-0.070	-0.200	0.330*	-0.383*	-0.494**	-0.468**	-0.335*	-0.267

Visual field (VF); Retinal nerve fiber layer (RNFL); Square root of loss variance (sLV).
The clusters of VF and category of RNFL are set in Figure 1 *p<0.05; **p<0.01.

TABLE 4 The influence of VF and RNFL on the diagnosis with the binary logistic regression.

	B	Wald	Sig.	Exp (B)OR	95% C.I. of EXP(B)/OR	
					lower	upper
Thickness of RNFL	0.092	5.935	0.015	1.096	1.018	1.180
Vertical CDR	-16.254	3.919	0.048	0.000	0.000	0.850
Cup volume	-8.072	4.000	0.046	0.000	0.000	0.851
sLV of VF	0.680	5.279	0.022	1.975	1.105	3.528

Visual field (VF); Retinal nerve fiber layer (RNFL); squareroot loss variance (sLV); Ganglion cell layer (GCL); odds ratio (OR).

Our study shows a relative weak correlation between the MD of OP clusters with the thickness of RNFL in seven of ten OP clusters in those intracranial tumor patients (cluser1, 5, 6-10), most correlation coefficient absolute value is less than 0.45. While in the glaucoma patients, with each OP cluster, we find moderate correlations in more than one RNFL sector, which is similar to other studies (8, 11, 12) _ENREF_11. Also, the map (Figure 2) shows the topographic structure-function relationship in glaucoma. Previous studies also showed a moderate association between RNFL thickness in each sector with VF region either in Octopus or Humphrey perimetry in glaucoma patients (9–11), a structure-function map which is similar to ours was created. This result is highly consistent with the principle of human eye imaging. In the other words, the VF defect of a certain area can correspond to the thinning RNFL of the corresponding part. And the thinning of RNFL in a certain part can also correspond to VF damage in the corresponding area.

Our study shows a significantly lower vertical CDR and cup volume of the intracranial tumor group than those of the glaucoma group. This finding is quite consistent with the clinic feature of those two diseases. The visual field defect is due to the atrophy of intraocular nerve tissue in glaucoma eyes. The appearance of intraocular nerve tissue atrophy is the loss of rim area and an increase in the value of vertical CDR and cup volume. On the contrary, for intracranial tumor patients, the visual field defect usually is the result of central nervous system damage, and the appearance of the optic disc usually remains normal.

We assume the result may correlate with the different retinal ganglion cells (RGCs) damage mechanisms in glaucoma and intracranial tumor. It is well-known that glaucoma is characterized by the damage to RGCs axons initialing at the optic nerve head with different mechanisms, such as intraocular pressure mechanical compression, vascular disorders, immunologic influence, and oxidative stress. That may lead to direct retrograde damage to the RGCs, followed by the RNFL thinning and VF defect. Also, some studies show glaucoma optic disk change correlated with the intra-orbital optic nerve measurement and chiasmal size (13–15), which suggests glaucoma may also lead to anterograde degeneration post optic disk. Therefore, glaucoma may produce a bidirectional nerve injury from the optic nerve head.

While intracranial tumors cause retrograde degeneration on the visual pathway, the pathologic changes start from the distal axonal and progress centripetally, which is also found in other central nervous system pathologies such as cerebral infarction, head trauma, and multiple sclerosis (16–18). That includes two conditions. Tumor arising near the sella turcica causing the axonal or terminal lesions between the eye and lateral geniculate body leads to the direct retrograde degeneration (6) _ENREF_6.

Whereas, tumors arising in the post lateral geniculate body cause damage to the optic radiation after the tertiary neurons in the visual pathway and lead to trans-synaptic retrograde retinal degeneration (TRD). It also causes the RNFL thinning and the optic nerve head vessel density to decrease (16, 19, 20). This is mechanically different from the damage to RGCs and axons in glaucoma.

Previous research showed the chiasmal lesion caused a more prominent optic nerve head vessel density decrease than the post-geniculate lesion, which indicated the direct retrograde degeneration might be more prominent than TRD (20). And our study shows the RNFL thinning is less prominent than glaucoma' RGCs' degeneration, both of the direct and trans-synaptic retrograde induced by the intracranial tumor. Whether the RNFL damage extent is negatively correlated with the distance from the initial site of injury to the RGCs remains unknown and needs more research to prove.

Another hypothesis is that the weak structure-function correlation in intracranial tumor patients is might due to the less injury of RNFL caused by direct or trans-synaptic retrograde. Our study yields two age and VF matched groups, of glaucoma and intracranial tumor, and shows more severe RNFL damage, smaller rim area, larger cup volume, and larger C/D ($p<0.05$) in the glaucoma patients. Also, some studies showed the optic chiasmal compression might cause the cell-inner plexiform layer to thin without RNFL changing in the early phase of some intracranial tumors (21, 22) _ENREF_21. However, Orman et al's study showed, pituitary tumors might have RNFL thinning and RGCs degeneration without VF defect (23). These inconsistencies in structure and function may also lead to the weak structure-function correlation in those intracranial tumor patients.

In the contrast to the intracranial tumor, in our study, at the same age range and VF MD levels, glaucoma patients have more severe RNFL and optic nerve head damage. The logistic regression analysis shows the RNFL loss tending to the diagnosis of glaucoma; the irregular VF damage is inclined to the diagnosis of intracranial tumor. Few studies had ever explored the RNFL difference between those two VF-affected diseases. This may provide some information for the differential diagnosis.

There are some limitations to our study. First, the smaller number of participants may introduce some selection bias. Second, there are not enough post-geniculate participants to analyze the direct and transsynaptic retrograde degeneration respectively. The same problem exists in the angle-closed and open glaucoma cases. Further study should be conducted to explore more detailed information.

In conclusion, due to few correlation coefficients, intracranial tumor has a weak correlation between the RNFL thickness and Octopus visual field MD, compared with glaucoma. RNFL and optic nerve head damage were more prominent in glaucoma patients when compared to intracranial tumor patients. OCT and Octopus visual field may provide more information for the differential diagnosis of intracranial tumor and glaucoma.

Data availability statement

The original contributions presented in the study are included in the article. Further inquiries can be directed to the corresponding author.

Ethics statement

The studies involving human participants were reviewed and approved by Peking University People's Hospital and Peking University International Hospital. The patients/participants provided their written informed consent to participate in this study.

Author contributions

XL, JQ, and XC wrote the main manuscript text, and prepared figures and tables. ZR, TC, and YB provided the data. All authors reviewed the manuscript. All authors contributed to the article and approved the submitted version.

Funding

This study was supported by the National Natural Science Foundation of China (NSFC, No. 21173012) and National Key R&D Program of China, No.2020YFC2008200.

Conflict of interest

The authors declare that the research was conducted in the absence of any commercial or financial relationships that could be construed as a potential conflict of interest.

Publisher's note

References

1. Moon J, Shin S. Segmented retinal layer analysis of chiasmal compressive optic neuropathy in pituitary adenoma patients. *Graefe's Arch Clin Exp Ophthalmol = Albrecht von Graefes Archiv fur klinische und experimentelle Ophthalmol* (2020) 258:419–25. doi: 10.1007/s00417-019-04560-3

2. Karl D, Gillan S, Goudie C, Sanders R. Giant prolactinoma mimicking low-tension glaucoma at presentation. *BMJ Case Rep* (2015). doi: 10.1136/bcr-2014-207634

3. Ahmed I, Feldman F, Kucharczyk W, Trope G. Neuroradiologic screening in normal-pressure glaucoma: Study results and literature review. *J Glaucoma* (2002) 11:279–86. doi: 10.1097/00061198-200208000-00002

4. Abd-Ellah M, Awad A, Khalaf A, Hamed H. A review on brain tumor diagnosis from MRI images: Practical implications, key achievements, and lessons learned. *Magnetic Resonance Imaging* (2019) 61:300–18. doi: 10.1016/j.mri.2019.05.028

5. Bialer O, Goldenberg-Cohen N, Toledano H, Snir M, Michowiz S. Retinal NFL thinning on OCT correlates with visual field loss in pediatric craniopharyngioma. *Can J Ophthalmol J Canadien d'ophtalmol* (2013) 48:494–9. doi: 10.1016/j.jcjo.2013.05.001

6. Jeong AR, Kim EY, Kim NR. Preferential ganglion cell loss in the nasal hemiretina in patients with pituitary tumor. *J Neuroophthalmol* (2016) 36:152–5. doi: 10.1097/WNO.0000000000000331

7. Monteiro M, Costa-Cunha L, Cunha L, Malta R. Correlation between macular and retinal nerve fibre layer Fourier-domain OCT measurements and visual field loss in chiasmal compression. *Eye London Engl* (2010) 24:1382–90. doi: 10.1038/eye.2010.48

8. Perdicchi A, de Paula A, Sordi E, Scuderi G. Cluster analysis of computerized visual field and optical coherence tomography-ganglion cell complex defects in high intraocular pressure patients or early stage glaucoma. *Eur J Ophthalmol* (2020) 30:475–9. doi: 10.1177/1120672119841774

9. Holló G. Comparison of structure-function relationship between corresponding retinal nerve fibre layer thickness and octopus visual field cluster defect values determined by normal and tendency-oriented strategies. *Br J Ophthalmol* (2017) 101:150–4. doi: 10.1136/bjophthalmol-2015-307759

10. Naghizadeh F, Garas A, Vargha P, Hollo G. Structure-function relationship between the octopus perimeter cluster mean sensitivity and sector retinal nerve fiber layer thickness measured with the RTVue optical coherence tomography and scanning laser polarimetry. *J Glaucoma* (2014) 23:11–8. doi: 10.1097/IJG.0b013e318264cda2

11. Ferreras A, Pablo L, Garway-Heath D, Fogagnolo P, García-Feijoo J. Mapping standard automated perimetry to the peripapillary retinal nerve fiber layer in glaucoma. *Invest Ophthalmol Visual Sci* (2008) 49:3018–25. doi: 10.1167/iovs.08-1775

12. Monsalve B, Ferreras A, Khawaja AP, Calvo P, Ara M, Fogagnolo P, et al. The relationship between structure and function as measured by OCT and octopus perimetry. *Br J Ophthalmol* (2015) 99:1230–5. doi: 10.1136/bjophthalmol-2014-305888

13. Kitsos G, Zikou A, Bagli E, Kosta P, Argyropoulou M. Conventional MRI and magnetisation transfer imaging of the brain and optic pathway in primary open-angle glaucoma. *Br J Radiol* (2009) 82:896–900. doi: 10.1259/bjr/55866125

14. Ramli NM, Sidek S, Rahman FA, Peyman M, Zahari M, Rahmat K, et al. Novel use of 3T MRI in assessment of optic nerve volume in glaucoma. *Graefe's Arch Clin Exp Ophthalmol = Albrecht von Graefes Archiv fur klinische und experimentelle Ophthalmol* (2014) 252:995–1000. doi: 10.1007/s00417-014-2622-6

15. Omodaka K, Murata T, Sato S, Takahashi M, Tatewaki Y, Nagasaka T, et al. Correlation of magnetic resonance imaging optic nerve parameters to optical coherence tomography and the visual field in glaucoma. *Clin Exp Ophthalmol* (2014) 42:360–8. doi: 10.1111/ceo.12237

16. Vien L, DalPorto C, Yang D. Retrograde degeneration of retinal ganglion cells secondary to head trauma. *Optometry Vision Sci* (2017) 94:125–34. doi: 10.1097/opx.0000000000000899

17. Gunes A, Inal E, Demirci S, Tok L, Tok O. Changes in retinal nerve fiber layer thickness in patients with cerebral infarction: Evidence of transneuronal retrograde degeneration. *Acta Neurol Belgica* (2016) 116:461–6. doi: 10.1007/s13760-015-0592-z

18. Huang-Link Y, Al-Hawasi A, Eveman I. Retrograde degeneration of visual pathway: hemimacular thinning of retinal ganglion cell layer in progressive and active multiple sclerosis. *J Neurol* (2014) 261:2453–6. doi: 10.1007/s00415-014-7538-x

19. Meier P, Maeder P, Kardon R, Borruat F. Homonymous ganglion cell layer thinning after isolated occipital lesion: Macular OCT demonstrates transsynaptic retrograde retinal degeneration. *J Neuro-Ophthalmol* (2015) 35:112–6. doi: 10.1097/wno.0000000000000182

20. Celik Buyuktepe T, Bingöl Kızıltunç P, Buyuktepe M, Atilla H. Direct and transsynaptic retrograde degeneration and optic nerve head microvascular changes in patients with hemianopia. *Eur J Ophthalmol* (2021) 31:1785–94. doi: 10.1177/1120672120951731

21. Blanch R, Micieli J, Oyesiku N, Newman N, Biousse V. Optical coherence tomography retinal ganglion cell complex analysis for the detection of early chiasmal compression. *Pituitary* (2018) 21:515–23. doi: 10.1007/s11102-018-0906-2

22. Chung Y, Na M, Yoo J, Kim W, Jung I, Moon JH, et al. Optical coherent tomography predicts long-term visual outcome of pituitary adenoma surgery: New perspectives from a 5-year follow-up study. *Neurosurgery* (2020) 88:106–12. doi: 10.1093/neuros/nyaa318

23. Orman G, Sungur G, Culha C. Assessment of inner retina layers thickness values in eyes with pituitary tumours before visual field defects occur. *Eye London Engl* (2021) 35:1159–64. doi: 10.1038/s41433-020-1032-8

frontiers | Frontiers in Endocrinology

TYPE Original Research
PUBLISHED 09 August 2022
DOI 10.3389/fendo.2022.947586

OPEN ACCESS

EDITED BY
Lian Zhao,
National Eye Institute (NIH),
United States

REVIEWED BY
Tao Li,
Zhongshan Ophthalmic Center, Sun Yat-sen University, China
Weihong Yu,
Peking Union Medical College Hospital (CAMS), China

*CORRESPONDENCE
Xuan Shi
drxuanshi@163.com

†These authorships have contributed equally to this work and share first authorship

SPECIALTY SECTION
This article was submitted to Molecular and Structural Endocrinology, a section of the journal Frontiers in Endocrinology

RECEIVED 18 May 2022
ACCEPTED 06 July 2022
PUBLISHED 09 August 2022

CITATION
Cai Y, Liu W-B, Zhou M, Jin Y-T, Sun G-S, Zhao L, Han F, Qu J-F, Shi X and Zhao M-W (2022) Diurnal changes of retinal microvascular circulation and RNFL thickness measured by optical coherence tomography angiography in patients with obstructive sleep apnea–hypopnea. *Front. Endocrinol.* 13:947586. doi: 10.3389/fendo.2022.947586

Diurnal changes of retinal microvascular circulation and RNFL thickness measured by optical coherence tomography angiography in patients with obstructive sleep apnea–hypopnea

Yi Cai[1†], Wen-Bo Liu[1†], Miao Zhou[1†], Yu-Tong Jin[2], Guo-Sheng Sun[1], Long Zhao[3], Fang Han[3], Jin-Feng Qu[1], Xuan Shi[1*] and Ming-Wei Zhao[1]

[1]Department of Ophthalmology, Peking University People's Hospital; Eye Diseases and Optometry Institute, Beijing Key Laboratory of Diagnosis and Therapy of Retinal and Choroid Diseases, College of Optometry, Peking University Health Science Center, Beijing, China, [2]Department of Biostatistics and Bioinformatics, Emory University, Atlanta, GA, United States, [3]Sleep Medicine Center, Department of Respiratory and Critical Care Medicine, Peking University People's Hospital, Beijing, China

Purpose: To evaluate capillaries perfusion and retinal nerve fiber layer (RNFL) thickness diurnal changes of macular/optic disc regions among participants with or without obstructive sleep apnea-hypopnea (OSA) using spectral-domain optical coherence tomography angiography (OCTA).

Methods: In this study, we enrolled a cohort of 35 participants including 14 patients with mild-to-moderate OSA, 12 patients with severe OSA, and 9 healthy individuals. All participants had Berlin questionnaire filled. At 20:00 and 6:30, right before and after the polysomnography examination, a comprehensive ocular examination was conducted. The systemic and ocular clinical characteristics were collected, and OCTA scans were performed repeatedly. Blood flow and RNFL thickness parameters were then exported using built-in software and analyzed accordingly.

Results: After sleep, the overall vessel density (VD) variables, especially macular and choriocapillaris VDs, were relatively comparative and stable. One exception was the RPC vessel density at the inside-disc region with a decreasing trend in the mild-to-moderate group (p=0.023). RNFL changes before and after sleep in the nasal-inferior and peripapillary region were statistically significant (p=0.003; p=0.043) among three groups. And multiple testing correction verified the significant difference in diurnal changes between the mild-to-moderate group and the control group in pairwise comparisons (p=0.006; p=0.02).

Conclusions: The changes of imperceptible blood flow and RNFL thickness overnight around optic disc areas could be observed in OSA patients. Despite physiological fluctuations, aberrant diurnal changes might be useful for identifying a decrease in micro-environmental stability associated with the development of various ocular diseases such as glaucoma. Other VD variables, especially macular and choriocapillaris VDs, are relatively stable in eyes of patients having OSA with different severity.

KEYWORDS

optical coherence tomography angiography, obstructive sleep apnea-hypopnea, retinal nerve fiber layer, deep capillary plexus, radial peripapillary capillary, vessel density, ocular diurnal changes

Introduction

Obstructive sleep apnea–hypopnea (OSA) is a highly prevalent systemic disorder characterized by episodes of obstruction or collapse of the upper airway and subsequent partial (hypopnea) or complete (apnea) cessation of airflow for more than 10 s despite the remaining respiratory effort. It is frequently related to aberrant blood-gas changes and is always associated with anomalous sleep patterns and cortical arousal (1). It is the most common type of sleep disorder in adults, and the prevalence is 3.62% for adults over 30 years in Shanghai, China, with a still increasing prevalence consistent with the rising trend of obesity (2, 3). Abnormal activation of the sympathetic nervous system and elevated serum catecholamines are the initiating factors for many vascular, metabolic, and inflammatory diseases (4, 5); furthermore, OSA is also the main cause of life quality impairment and is associated with an increased risk of traffic accidents. The high incidence and severe impact on life quality make it a huge burden on public health.

OSA has already been verified to be highly associated with neurological disorders such as stroke, depression, headache, elevated cranial pressure, and peripheral neuropathy (6). The higher incidence of neurological disorders in patients with OSA is thought to be possibly related to the frequency of apnea-induced hypoxemia (4). Besides, OSA can lead to various optic nerve impairments (7, 8), including non-arteritic ischemic optic neuropathy (NAION) and glaucoma, as well as pathological involvement of the retinal/choroidal tissue, such as retinal vein occlusion (RVO) (9, 10) and pachychoroidal diseases like central serous chorioretinopathy (CSC) and polypoidal choroidal vasculopathy (PCV) (9, 11). In the last few years, a large number of scientific reviews, meta-analyses, and articles have been published to verify the significant association between OSA and glaucoma/CSC in adults (12–15), serving as the evidence of a strong association with the development of certain eye diseases.

Up to now, the pathogenesis between OSA and ocular optic nerve-related diseases or pachychoroid diseases is still unclear (9), probably associated with the abnormal hypoxia-induced factors upregulation, hypercoagulable state, oxidative stress, and endothelial cell damage secondary to hypoxia episodes (9). The related studies are mainly of clinical nature because of the long period for animal modeling. Thanks to the transparency of retinal tissue, the microvasculature of the retina tissue is the only microvascular network that can be directly observed. With the advancement of OCTA technology in the last decade, we can perform not only morphological but also quantitative studies on retinal microvasculature (16) and speculate on the pathogenic mechanism of OSA *in vivo*.

Quantitative assessment of microvascular circulation changes in patients with OSA is scarce. The first study of quantitative OCTA measurements in patients with OSA was performed by Yu et al. in 2017, who concluded that vascular density (VD) in the macular and retinal regions differed significantly among groups classified by OSA severity. The severe group with an apnea–hypopnea index (AHI) of more than 30 breaths/hour had significantly lower VD in the peripapillary area. In addition, vessel densities in the parafoveal and peripapillary regions were significantly negatively correlated with AHI (17). However, Laura Moyal et al. (18) reported that OCTA parameters at the SCP level were comparable between groups regardless of the severity of OSA, although significant functional variations in FDT-Matrix^{TM} and Humphrey 24/2 were noted, suggesting that changes in functional examinations might occur before blood flow fluctuation emerged. Contradictory results emerged from these existing studies. Therefore, in our previous study, we also took VD in the deep capillary plexus (DCP) into account and performed another cross-sectional comparison of quantitative OCTA parameters in patients with OSA of different severities.

We found that the severe group had significantly higher VD in parafoveal and perifoveal regions at the level of DCP, whereas the mild-to-moderate group had a significantly lower radial peripapillary capillary (RPC) VD in the peripapillary area. We considered that blood flow changes in the macula may first appear in the DCP layer in patients with OSA in the cross-sectional comparison. Reduced VD in the peripapillary region of the RPC layer may lead to subsequent RNFL changes (19). However, considering that complex compensatory mechanisms might exist and lead to adaptive modulation of retinal microvasculature and tissues during chronic OSA, immediate circadian retinal microvascular changes after exposure to hypoxia attacks and sympathetic system activation may be more responsive to the instant ocular changes over a short period. However, studies on altered circadian OCT or OCTA parameters are relatively lacking.

Therefore, in this study, we investigated the diurnal variation of nerve fiber layer thickness near the optic disc and the microvascular VD in the optic disc and macular regions in OSA patients.

Methods

This prospective observational study consisted of 26 consecutive participants newly diagnosed with OSA and nine age-matched controls, all recruited from the Sleep Laboratory of the People's Hospital of Peking University. The study was performed between January 2018 and September 2020 and was approved by the ethics committee at mentioned university. The protocols adhered to the aims of the Declaration of Helsinki. All subjects participated voluntarily, and their written informed consent was obtained.

The general experimental method has been elaborated in the previous study (19). Participants were enrolled according to the following criteria: 1) aged between 25 and 65 years; 2) this was the first time of sleep monitoring and had no history of any sleep disorder; 3) no history of any ocular surgery or trauma; 4) no history or family history of primary glaucoma; and 5) spherical equivalence <-6.0 D. The exclusion criteria were as follows: 1) already received any treatment for OSA including continuous positive airway pressure (CPAP); 2) with history of coexisting systemic diseases, including diabetes, migraine, hypertension, coronary heart diseases, or already recently treated by any vasoactive medication; 4) with an axial length out of the range of 22.0 to 26.5 mm; 5) combined with other ocular diseases or previous intraocular surgery history, including amblyopia, macular degeneration, CSC, optic nerve diseases, retinal detachment, and uveitis; 6) compromised OCTA signal secondary to refractive media opacity; 7) poor cooperation in OCTA examinations due to inability to control eye movements like strabismus; 8) best-corrected visual acuity (BCVA, converted to LogMAR scores) greater than 0.1.

After filling out the Berlin questionnaire, ocular data were collected at around 20:00. Baseline demographic data including, sex, age, current cigarette smoking status, neck circumference, body mass index (BMI), and blood pressure were also documented. The examiner and the participants were unaware of the polysomnography (PSG) results at the time of receiving the ocular and body examination. The next morning after PSG, the same set of OCTA scans was repeated as soon as the PSG test was completed (at around 6:30 a.m.). The morning blood pressure and intraocular pressure (IOP) were also collected.

Ocular examination

All participants received comprehensive ocular examinations, including BCVA (transformed into LogMAR score), IOP measured using a non-contact tonometer (TX-F fully automated IOP meter, Canon Canada), anterior segment examination, fundus examination, axial length and central corneal thickness (CCT) measured using the optical method (ZEISS IOLMaster 500, Carl Zeiss Meditec, Jena, Germany), and OCTA scans (Optovue RTVue XR Avanti, Optovue Inc., Fremont, CA). All images and data were evaluated by the same expert examiner (YC). To ensure consistency of the longitudinal assessment, topical mydriatic eye drop was not applied and all OCT scans were performed inside a silent room with a few minutes of dark adaptation.

Optical coherence tomography angiography

We preferred the right eye as the study eye unless there were obvious motion artifacts difficult to eliminate despite repeating. High-definition (HD) imaging was conducted using the RTVue XR Avanti Spectral Domain OCT System (version 2017,1,0,155), which had been described in detail in our previous study (19). The macula area was imaged in a 6 mm × 6 mm square, and the corresponding flow data were directly processed based on the split-spectrum amplitude-decorrelation angiography (SSADA) algorithm. Vascular density was defined as the proportion of blood vessels in the corresponding segmental scan. The foveal region was surrounded by the parafoveal area, which was defined as a ring area with an inner radius of 0.5 mm and an outer radius of 1.5 mm (20, 21). The perifoveal region was another annulus area with a width of 1.5 mm outside the parafoveal region (19, 22). The superficial capillary plexus (SCP) was generated as the layer between 3 μm below the internal limiting membrane (ILM) to 15 μm below the inner plexiform layer (IPL), while the DCP was defined as the area from 15 to 70 μm below the IPL (19, 23, 24). The innermost borderline of the avascular zone (FAZ) at the level of SCP was automatically identified through the built-in software. The area of the FAZ, VD within the FAZ zone, and VD

of the area 300 μm beyond FAZ were also obtained from the integrated software AngioAnalytics. The optic nerve head VD of the RPC layer was analyzed separately after the acquisition of 4.5 mm × 4.5 mm scans. The inside-disc zone was defined as an elliptical region corresponding to the boundary of the optic nerve. The peripapillary region was defined as the 2–4-mm annulus region extending from the inside-disc region and automatically divided into eight zones (Temporal Superior, Superior Temporal, Superior Nasal, Nasal Superior, Nasal Inferior, Inferior Nasal, Inferior Temporal, and Temporal Inferior, abbreviated as GH-TS, GH-ST, GH-SN, GH-NS, GH-NI, GH-IN, GH-IT, and GH-TI sections, respectively) according to the modified Garway-Heath (GH) grids (25). RPCs, the most superficial capillary layer, refer to the capillaries sited from the inner limiting membrane with an offset of 0 μm to the base of the nerve fiber layer, which corresponds to the thickness of the entire nerve fiber layer. The macular choriocapillaris vessel density was obtained using the built-in flow measurement tool by calculating the mean ratio of the vascular area occupied in a circle of 36 mm^2 centered on the foveola (26). Each OCTA scan mentioned above was performed two times, and for quantitative parameters, the mean value of the corresponding area was calculated for subsequent analysis.

Polysomnography

All subjects were monitored using a standard polysomnography system (Alice 6 LDx; Philips Respironics, Andover, MA) with standard nocturnal polysomnography continuous electroencephalography recorded from 10 p.m. to 6 a.m. (Alice 6 LDx; Philips Respironics, Andover, MA). All subjects underwent nocturnal polysomnography (PSG) for at least 6 h in a quiet, individual room. The definition of apnea events obeys the sleep guidelines. The AHI (times/h) was assessed for each patient based on Academy of Sleep Medicine standards and used as the indicator of the severity of OSA (27). Participants diagnosed with OSA (AHI >5 times/h) (27) were divided into two groups according to the severity of OSA: participants with an AHI of 5 to 30 times/h were classified in the mild-to-moderate group; subjects with an AHI over 30 times/h were graded into the severe group. Subjects verified by an AHI of 5 or less served as the control group.

Statistical analysis

Statistical analyses were performed using R (version 4.0.3). Continuous data were expressed as mean ± SD (min, max). The Shapiro–Wilk test was used to verify normality for continuous data. One-way analysis of variance (ANOVA) was used to perform a cross-sectional comparison between three groups for normal distribution data; otherwise, Kruskal–Wallis was used as an alternative, and Tukey *post-hoc* tests were used for pairwise comparison. Circadian valuable change was analyzed using paired t-test or paired-sample Wilcoxon signed-rank test. For two continuous measurements of the same scan item, the intraclass correlation coefficient (ICC) was calculated to determine the consistency of the corresponding continuous variables. Correlation coefficients between sectional RNFL diurnal difference and other parameters were analyzed and adjusted in the multiple regression analysis. p-values <0.05 were considered statistically significant.

Results

A total of 14 subjects diagnosed with mild-to-moderate OSA, 12 subjects with severe OSA, and nine control subjects without a diagnosis of OSA were included in the final analysis. The systemic and ocular parameters regarding age, blood pressure, BMI, AL, CCT, and intraocular pressure that may affect the analysis of quantitative OCTA data were all comparable. The characteristics of the subjects' systemic and ocular parameters are shown in Table 1.

Considering the prevalence of nerve fiber layer defect in OSA patients in the previous studies as mentioned above, we first investigated the retinal nerve fiber layer thickness changes in different peripapillary subdivisions corresponding to the Garway-Heath mapping of the VF in the range of 2–4-mm dual-ring area centered on the optic disc among different groups. The results suggested that the mean total peripapillary RNFL thickness in the baseline examination before PSG showed a decreasing trend in the OSA group compared to the control group, although without any statistical significance. In contrast, in certain Garway-Heath subdivisions, there were significant differences in the mean RNFL thickness at baseline, including the inferior hemisection ($p = 0.048$) and IT section ($p = 0.009$), respectively. In the longitudinal observation of circadian nerve fiber layer thickness changes using paired t-test analysis, the severe group was found to have significant differences between nocturnal and morning RNFL thickness in both the peripapillary, GH-S-Hemi, and GH-IN sections ($p = 0.003$; $p = 0.003$; $p = 0.049$, respectively), with the thickness being significantly higher in the morning than measured at night. In contrast, there were no significant diurnal differences of other sections in other groups (Table 2).

The vascular densities at the level of SCP, DCP, and choriocapillaris in the macular area, RPC in different areas around the optic disc, FAZ area, and superficial FAZ VD were all comparable between the different groups. Vessel density in the areas and the corresponding layers mentioned above also maintained relatively diurnal stability, except for RPC vessel density in the inside-disc area: a significant decrease in RPC layer vessel density at the inside-disc area in the mild-to-moderate group occurred after an overnight sleep with apnea

TABLE 1 Systemic and ocular characteristics of subjects.

Variables	Control group (N = 9)	Mild-to-moderate group (N = 14)	Severe group (N = 12)	P value
Age (y)	41.78 ± 12.13 (25, 60)	37.29 ± 8.00 (31, 61)	43.33 ± 9.06 (28, 56)	0.260
Sex				
Female	5 (55.6%)	2 (14.3%)	2 (16.7%)	
Male	4 (44.4%)	12 (85.7%)	10 (83.3%)	
Eye				
OD	8 (88.9%)	13 (92.9%)	12 (100%)	
OS	1 (11.1%)	1 (7.1%)	0 (0%)	
Cigarette smoking (%)	2 (22.2%)	3 (21.4%)	3 (25%)	
BMI (kg/m^2)	23.64 ± 2.88 (18.60, 28.34)	25.39 ± 3.01 (20.55, 31.64)	28.56 ± 4.68 (21.88, 39.45)	0.058†
AHI (events/h)	2.76 ± 1.02 (1.00, 4.00)	17.20 ± 5.43 (9.70, 27.20)	54.98 ± 15.57 (34.90, 87.40)	**0.000***†
Lowest value of SpO_2 (%)	89.67 ± 6.52 (74.00, 95.00)	85.50 ± 4.55 (75.00, 93.00)	66.75 ± 10.94 (50.00, 84.00)	**0.000***†
Nocturnal systolic pressure (mmHg)	116.33 ± 11.75 (100.00, 135.00)	118.43 ± 12.28 (102.00, 140.00)	118.33 ± 15.13 (85.00, 140.00)	0.923
Nocturnal diastolic pressure (mmHg)	74.33 ± 9.70 (60.00, 85.00)	77.21 ± 9.29 (64.00, 90.00)	77.58 ± 10.14 (50.00, 90.00)	0.717†
Morning systolic pressure (mmHg)	112.56 ± 12.20 (90.00, 128.00)	116.57 ± 10.94 (100.00, 140.00)	120.17 ± 15.19 (88.00, 142.00)	0.923
Morning diastolic pressure (mmHg)	74.67 ± 7.94 (60.00, 84.00)	77.64 ± 8.13 (64.00, 94.00)	78.75 ± 11.53 (54.00, 92.00)	0.415
Nocturnal MAP (mmHg)	88.33 ± 9.45 (73.33, 101.67)	90.95 ± 9.69 (78.67, 106.00)	91.17 ± 11.18 (61.67, 104.67)	0.788
Morning MAP (mmHg)	87.30 ± 8.55 (70.00, 98.67)	90.62 ± 8.69 (78.67, 108.00)	92.56 ± 12.35 (65.33, 108.67)	0.501
Nocturnal MOPP (mmHg)	46.56 ± 6.89 (37.33, 56.78)	46.42 ± 6.66 (38.44, 60.67)	48.19 ± 9.97 (21.11, 59.89)	0.476†
Morning MOPP (mmHg)	46.31 ± 7.03 (30.67, 52.78)	46.44 ± 6.26 (37.33, 55.89)	49.70 ± 9.01 (28.56, 62.56)	0.471
Diurnal difference in MOPP (mmHg)	-0.25 ± 3.67 (-6.67, 4.44)	0.02 ± 4.10 (-6.11, 7.84)	1.51 ± 5.26 (-5.67, 11.00)	0.601
Neck circumference (cm)	34.67 ± 3.35 (31.00, 42.00)	38.36 ± 3.08 (32.00, 43.00)	39.17 ± 3.64 (34.00, 46.00)	**0.012***
AL (mm)	23.82 ± 1.04 (22.28, 25.27)	24.66 ± 1.17 (22.47, 26.00)	24.66 ± 0.79 (23.04, 25.84)	0.118
CCT (μm)	545.00 ± 48.35 (432.00, 609.00)	537.36 ± 32.39 (488.00, 598.00)	541.58 ± 35.71 (454.00, 594.00)	0.892
Nocturnal IOP (mmHg)	12.33 ± 2.35 (9.00, 16.00)	14.21 ± 2.55 (10.00, 19.00)	12.58 ± 3.85 (8.00, 20.00)	0.259
Morning IOP (mmHg)	11.89 ± 2.85 (8.00, 16.00)	13.97 ± 2.21 (11.00, 17.00)	12.00 ± 3.10 (8.00, 17.00)	0.109†

Values are expressed as mean ± SD (range) or no. (%) according to the variable types; † represents using Kruskal–Wallis rank test for analysis; * and bold values represents for data with $p < 0.05$; BMI, body mass index; AHI, apnea–hypopnea index; CCT, central corneal thickness; AL, axial length; Lowest value of SpO_2, the lowest value of oxyhemoglobin saturation during sleep; IOP, intraocular pressure; MAP, mean arterial pressure, calculated by 2/3×diastolic blood pressure + 1/3×systolic blood pressure; MOPP, mean ocular perfusion pressure, calculated by 2/3×MAP − IOP.

events emerging (p = 0.023). ICC of RPC VD at the inside-disc area revealed 0.80 (95% confidence interval: 0.644–0.896). Comparative and statistical analysis results are demonstrated in Table 3.

Comparisons of diurnal difference in OCTA vessel density and RNFL parameters between the three groups revealed that RNFL changes in the GH-NI and peripapillary regions were significantly different (p = 0.003; p = 0.043, respectively) among the three groups, and *post-hoc* tests verified a significant difference in diurnal changes between the mild-to-moderate group and the control group (p = 0.006; p = 0.02, respectively), which is demonstrated in Figure 1. ICC showed high reliability respectively (ICC = 0.94, 95% confidence interval: 0.89–0.971; ICC = 0.85, 95% confidence interval: 0.715–0.919).

Correlation analysis of the diurnal difference changes in RNFL thickness in the above two regions showed that nocturnal IOP and AL were significantly correlated with RNFL changes in the GH-NI region (p = 0.050; 0.021, respectively), but none of them was significant after being adjusted in the multiple linear regression (demonstrated in Table 4).

Discussion

In our previous study, we performed a cross-sectional analysis in subjects with OSA of different severity and age-matched controls and found spatial heterogeneity of VD changes in OSA patients (19). To further observe the immediate effects after apnea events, in the present study we investigated the diurnal variation of relevant RNFL/OCTA parameters in subjects with OSA of different severity and found significant diurnal VD changes at the RPC layer in the inside-disc region in the mild-to-moderate group rather than other groups, as well as intergroup differences in diurnal changes of the RNFL thickness at certain sections.

In the cross-sectional comparison of RNFL thickness around the optic disc area, we found a decreasing trend in mean peripapillary RNFL thickness among three groups, although this decreasing trend was not statistically significant, which could probably be attributed to the relatively small sample size. A statistically significant decrease in RNFL thickness occurred only in the GH-inferior and GH-

TABLE 2 RNFL parameters results of participates.

Valuables	Control group (N = 9)	Mild-to-moderate group (N = 14) Baseline (night)	Severe group (N = 12)	Control group (N = 9)	Mild-to-moderate group (N = 14) Morning	Severe group (N = 12)	p	p1	p2	p3
Peripapillary RNFLT (μm)	124.55 ± 8.99 (114.79, 139.00)	118.03 ± 13.75 (95.54, 141.79)	115.79 ± 6.36 (108.46, 124.80)	127.42 ± 7.90 (117.01, 138.68)	117.65 ± 13.92 (97.58, 143.28)	117.69 ± 7.83 (108.68, 134.78)	0.090†	0.760	0.572	**0.003*†**
GH-S-Hemi RNFLT (μm)	123.43 ± 11.19 (112.70, 144.47)	118.40 ± 13.88 (96.48, 141.58)	117.49 ± 7.27 (105.65, 131.56)	126.34 ± 8.95 (114.23, 142.88)	118.16 ± 14.43 (98.92, 144.38)	119.72 ± 8.45 (107.65, 136.23)	0.458	0.941	0.736	**0.003*†**
GH-I-Hemi RNFLT (μm)	125.76 ± 7.73 (115.86, 135.24)	117.61 ± 15.13 (94.52, 142.02)	113.96 ± 7.13 (104.14, 128.37)	128.61 ± 7.74 (117.42, 139.39)	117.10 ± 15.57 (96.15, 143.17)	115.49 ± 8.49 (105.40, 133.23)	**0.048*†**	0.995	0.506	0.092†
GH-NS RNFLT (μm)	115.60 ± 11.91 (103.51, 140.41)	113.63 ± 27.84 (80.17, 180.94)	109.83 ± 12.88 (90.41, 134.98)	118.34 ± 8.43 (103.86, 135.53)	112.26 ± 29.49 (77.90, 183.33)	110.99 ± 13.58 (87.48, 134.67)	0.863†	0.084	0.440	0.724†
GH-NI RNFLT (μm)	89.07 ± 9.64 (68.66, 102.02)	94.15 ± 22.40 (63.57, 133.32)	84.20 ± 10.90 (62.27, 97.97)	94.39 ± 6.40 (83.21, 102.72)	91.15 ± 25.56 (52.15, 128.44)	86.37 ± 12.05 (64.11, 105.38)	0.493†	0.613	0.529†	0.072
GH-IN RNFLT (μm)	159.37 ± 20.59 (134.29, 198.85)	149.71 ± 25.82 (107.93, 196.71)	148.49 ± 10.67 (132.89, 173.85)	163.03 ± 21.45 (132.50, 202.11)	150.38 ± 27.82 (110.74, 205.65)	151.90 ± 10.45 (138.54, 179.86)	0.523†	0.796	0.588	**0.049***
GH-IT RNFLT (μm)	172.06 ± 15.07 (150.75, 196.65)	150.61 ± 18.57 (105.95, 178.17)	146.91 ± 18.70 (120.47, 182.43)	174.22 ± 17.29 (144.26, 198.90)	152.58 ± 17.47 (110.48, 177.21)	147.58 ± 18.82 (124.75, 187.42)	**0.009*†**	0.385	0.107	0.555
GH-TI RNFLT (μm)	87.02 ± 17.80 (69.86, 119.83)	75.51 ± 11.74 (54.67, 92.26)	77.14 ± 11.72 (62.49, 105.46)	86.31 ± 17.75 (71.20, 116.79)	75.05 ± 11.38 (58.94, 90.09)	76.23 ± 10.65 (63.57, 94.37)	0.320†	0.895	0.600	0.733†

Values are expressed as mean ± SD (range); † represents using the Kruskal–Wallis rank test for independent analysis, or Wilcoxon signed-rank test for paired analysis; p: p value of baseline (night) variables among three groups; p1: p value for diurnal comparison of paired variables in the control group; p2: p value for diurnal comparison of paired variables in the mild-to-moderate group; p3: p value for diurnal comparison of paired variables in the severe group; * and bold values represents for data with $p < 0.05$.
RNFLT, retinal nerve fiber layer thickness; GH, Garway-Heath-based grids. Temporal Superior, Superior Temporal, Superior Nasal, Nasal Superior, Nasal Inferior, Inferior Nasal, Inferior Temporal, and Temporal Inferior, abbreviated as GH-TS, GH-ST, GH-SN, GH-NS, GH-NI, GH-IN, GH-IT, GH-TI sections, respectively.
RNFL thickness referred to the mean RNFL thickness in the ellipsoidal area outward the boundary of the nipple area referring to optic nerve based on the modified Garway-Heath of a 2–4-mm grid. The RNFL thickness was corrected for ocular magnification.

TABLE 3 OCTA and FAZ parameters of subjects.

Variables	Control group (N = 9)	Mild-to-moderate group (N = 14) Baseline (night)	Severe group (N = 12)	Control group (N = 9)	Mild-to-moderate group (N = 14) Morning	Severe group (N = 12)	p	p1	p2	p3
Macular										
SCP										
S Whole Image VD (%)	51.07 ± 2.67 (47.41, 54.15)	48.96 ± 2.49 (44.20, 52.20)	50.70 ± 3.23 (46.36, 54.95)	48.44 ± 3.98 (43.03, 53.87)	49.04 ± 3.29 (42.22, 54.00)	49.21 ± 4.69 (36.80, 54.86)	0.155	0.079	0.942	0.284
S Fovea VD (%)	17.38 ± 6.64 (6.05, 27.87)	18.48 ± 6.39 (9.93, 31.07)	18.58 ± 7.64 (5.59, 28.16)	16.36 ± 7.16 (8.33, 31.16)	17.99 ± 6.30 (10.33, 32.90)	18.17 ± 8.31 (6.45, 29.70)	0.912	0.337	0.495	0.585
S ParaFovea VD (%)	54.25 ± 3.38 (47.80, 58.09)	52.77 ± 3.46 (45.08, 57.22)	54.60 ± 3.38 (46.45, 58.64)	51.66 ± 3.94 (44.79, 57.67)	52.58 ± 2.81 (47.93, 56.05)	53.38 ± 4.71 (40.83, 59.28)	0.247†	0.114	0.884	0.419
S PeriFovea VD (%)	51.69 ± 2.86 (47.48, 55.13)	49.46 ± 2.72 (44.41, 52.97)	51.30 ± 3.68 (46.30, 56.20)	49.10 ± 4.01 (43.19, 54.54)	49.57 ± 3.67 (40.61, 54.81)	49.88 ± 5.11 (36.35, 56.01)	0.259†	0.101	0.926	0.335
DCP										
D Whole Image VD (%)	50.66 ± 5.87 (42.95, 57.67)	48.77 ± 4.25 (39.97, 55.68)	51.57 ± 4.97 (43.62, 58.69)	45.69 ± 8.49 (34.48, 58.92)	49.43 ± 5.20 (41.87, 61.72)	49.71 ± 6.28 (39.83, 58.67)	0.351	0.146	0.652	0.384
D Fovea VD (%)	32.64 ± 9.69 (15.12, 45.93)	35.12 ± 7.11 (24.74, 50.84)	37.11 ± 7.59 (25.39, 49.36)	32.24 ± 11.77 (14.98, 53.61)	35.04 ± 6.40 (27.96, 50.81)	36.13 ± 7.68 (25.48, 47.82)	0.454	0.793	0.902	0.110

(Continued)

TABLE 3 Continued

Variables	Control group (N = 9)	Mild-to-moderate group (N = 14) Baseline (night)	Severe group (N = 12)	Control group (N = 9)	Mild-to-moderate group (N = 14) Morning	Severe group (N = 12)	p	p1	p2	p3
D ParaFovea VD (%)	56.29 ± 4.13 (49.67, 61.56)	55.18 ± 2.89 (47.97, 59.47)	57.08 ± 3.23 (51.80, 61.24)	52.57 ± 5.55 (45.87, 60.24)	55.29 ± 2.82 (51.12, 61.12)	54.92 ± 4.03 (48.60, 60.53)	0.360	0.116	0.909	0.095
D PeriFovea VD (%)	51.84 ± 6.69 (42.66, 59.54)	49.94 ± 4.85 (40.46, 57.40)	53.21 ± 5.80 (42.92, 61.39)	46.73 ± 9.11 (33.89, 60.58)	50.41 ± 5.74 (41.82, 63.17)	51.37 ± 7.08 (40.74, 61.81)	0.351	0.160	0.769	0.435
Overall QI	7.89 ± 1.05 (6.00, 9.00)	7.50 ± 0.52 (7.00, 8.00)	7.75 ± 0.62 (7.00, 9.00)	7.22 ± 0.83 (6.00, 8.00)	7.71 ± 0.91 (6.00, 9.00)	7.75 ± 0.97 (6.00, 9.00)	0.393†	0.746†	0.336†	1.000
FAZ										
FAZ Area (mm^2)	0.33 ± 0.16 (0.12, 0.59)	0.31 ± 0.10 (0.11, 0.44)	0.30 ± 0.10 (0.16, 0.46)	0.33 ± 0.16 (0.09, 0.60)	0.31 ± 0.10 (0.11, 0.44)	0.30 ± 0.10 (0.16, 0.48)	0.841	0.765	0.114	0.699
Perimeter night	2.18 ± 0.55 (1.43, 3.01)	2.10 ± 0.36 (1.26, 2.62)	2.09 ± 0.37 (1.47, 2.61)	2.16 ± 0.57 (1.25, 3.04)	2.13 ± 0.38 (1.31, 2.62)	2.09 ± 0.38 (1.51, 2.70)	0.877	0.454	0.164	0.982
Acircularity Index	1.10 ± 0.04 (1.06, 1.18)	1.09 ± 0.02 (1.06, 1.14)	1.08 ± 0.02 (1.05, 1.11)	1.10 ± 0.03 (1.07, 1.17)	1.09 ± 0.02 (1.06, 1.13)	1.08 ± 0.02 (1.05, 1.13)	0.542†	0.447	0.273	0.878
FD-300 Area VD (%)	54.04 ± 5.59 (45.72, 63.01)	53.95 ± 4.00 (46.67, 58.74)	55.99 ± 2.95 (50.67, 60.48)	52.13 ± 5.83 (42.37, 61.16)	54.34 ± 3.89 (46.04, 60.63)	53.98 ± 3.87 (48.98, 60.84)	0.409	0.051	0.705	0.130
FD-300 LVD (%)	12.84 ± 1.45 (10.45, 14.59)	12.60 ± 1.14 (9.83, 13.76)	13.29 ± 1.05 (11.62, 14.79)	12.11 ± 1.35 (9.85, 14.24)	12.56 ± 1.71 (10.63, 17.53)	12.73 ± 1.52 (9.39, 14.97)	0.355	0.089	0.943	0.622†
Optic disc										
Whole Image RPC VD (%)	52.15 ± 2.38 (48.91, 56.51)	50.86 ± 2.48 (47.26, 53.72)	50.74 ± 1.94 (47.34, 53.68)	52.18 ± 1.53 (50.46, 54.92)	49.98 ± 2.05 (46.44, 53.48)	50.62 ± 2.49 (45.56, 54.68)	0.320	0.970	0.065	0.806
Inside Disc RPC VD (%)	53.75 ± 3.82 (48.21, 61.93)	54.78 ± 5.05 (43.69, 63.39)	54.27 ± 3.92 (46.84, 59.97)	52.89 ± 4.75 (47.93, 64.20)	52.91 ± 5.02 (41.77, 61.65)	54.10 ± 3.88 (46.61, 61.69)	0.860	0.371	**0.023***	0.885
Peripapillary RPC VD (%)	55.30 ± 2.16 (52.27, 59.81)	53.24 ± 2.41 (48.47, 56.61)	54.33 ± 2.71 (49.06, 58.26)	55.19 ± 2.63 (52.47, 59.36)	52.68 ± 2.51 (48.68, 56.45)	53.58 ± 3.15 (48.06, 58.27)	0.158	0.894	0.152	0.288
QI	8.22 ± 1.30 (5.00, 9.00)	8.14 ± 0.86 (7.00, 9.00)	8.25 ± 0.62 (7.00, 9.00)	8.22 ± 0.97 (7.00, 9.00)	8.00 ± 0.78 (6.00, 9.00)	8.33 ± 0.49 (8.00, 9.00)	0.721†	0.746†	0.530†	0.766†
Choriocapillaris										
Choriocapillaris VD (%)	70.40 ± 1.75 (66.67, 72.11)	70.87 ± 2.07 (67.00, 73.94)	70.41 ± 2.51 (66.00, 75.25)	69.58 ± 2.22 (65.72, 72.33)	70.71 ± 2.16 (67.33, 74.42)	70.44 ± 1.89 (67.67, 73.81)	0.826	0.117	0.728	0.948

Values are expressed in form of mean ± SD (range); † represents using Kruskal–Wallis rank test for independent analysis or Wilcoxon signed-rank test for paired analysis; p: p value of baseline (night) variables among three groups; p1: p value for diurnal comparison of paired variables in the control group; p2: p value for diurnal comparison of paired variables in the mild-to-moderate group; p3: p value for diurnal comparison of paired variables in the severe group; * and bold values represents for data with $p < 0.05$.
SCP, superficial capillary plexus; DCP, superficial capillary plexus; S, superficial; D, deep; RPC, radial peripapillary capillaries; VD, vessel density; LVD, length density; QI, quality index; FD-300, vessel density in the 300-μm region beyond the FAZ boundary.

IT sections, similar to previous studies. In our previous research, average peripapillary RNFL thickness was significantly different between different OSA groups, although no significant difference was observed in the *post-hoc* analysis (19). Sagiv et al. measured RNFL thickness changes in 62 moderate and 46 severe OSA participants in comparison to 108 age-matched controls using OCT. The results revealed that the mean, upper, lower, and temporal quadrants of RNFL thickness were significantly lower in the OSA group (28).

However, longitudinal observational studies on RNFL thickness in patients with OSA are relatively scarce. The decreasing trend of RNFL could also be reflected during the long-term follow-up. Mehmet Ozgur Zengin et al. found that the mean RNFL thickness at the last measurement (Month 12) was significantly lower in OSA patients than that of the first measurement and in controls during the 1-year follow-up of OSA patients and proposed that AHI was significantly correlated with retinal nerve fiber layer thickness (29). Besides, there was only one previous study on the diurnal variation of RNFL thickness in OSA patients: Chirapapaisn et al. proposed that RNFL thickness in the morning was significantly higher than in the evening in moderate OSA in the diurnal comparison (30). They speculated that swelling of RNFL might occur secondary to hypoxia episodes, increasing the cerebral spinal fluid pressure, and chronic hypercapnia and subclinical papilledema could only be detected on OCT images. Similar findings were also obtained in the present study, where we found a significant increase in the peripapillary RNFL thickness measured in the morning in the severe OSA group rather than in other groups, although similar changes were not seen in the mild-to-moderate group. We consider that the analogous result in the severe group may also be attributed to decreased optic nerve perfusion

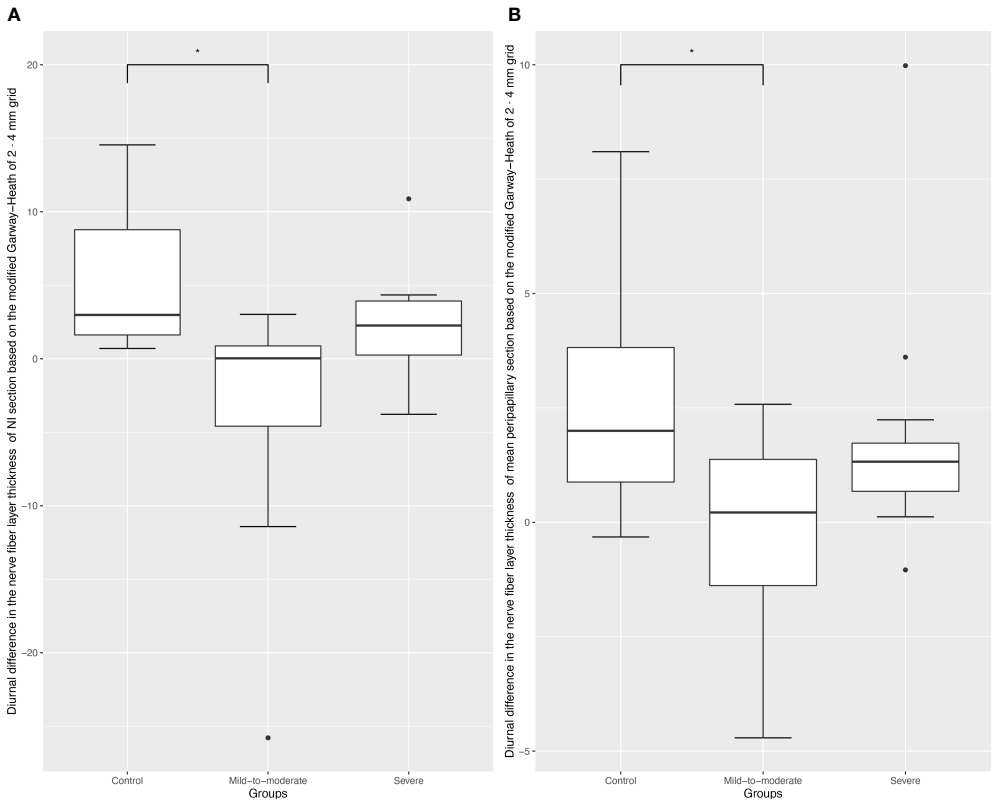

FIGURE 1
Box plots of diurnal RPC vessel density difference in different optic disc areas. Black dots indicate outliers (lower margin 5%, upper margin 5%). **(A)**, Box plots of diurnal RPC vessel density difference in the Garway-Heath-based-nasal inferior section; * refers to a Tukey *post-hoc* adjusted p value of 0.006. **(B)**, Box plots of diurnal RPC vessel density difference in the Garway-Heath-based-peripapillary section; * refers to a Tukey *post-hoc* adjusted p value of 0.02.

TABLE 4 Spearman's rank correlation analysis/multiple linear regression analysis of systemic and ocular factors associated with diurnal difference in sectional RNFLT.

Spearman's correlation analysis for diurnal difference in peripapillary RNFLT			Spearman's correlation analysis for diurnal difference in GH-NI RNFLT			Multiple linear regression analysis for diurnal difference in GH-NI RNFLT	
Variables	β	p	Variables	β	p	β′	p′
AHI	-0.182	0.295	AHI	-0.192	0.268		
Age	-0.005	0.978	Age	-0.010	0.956		
BMI	0.098	0.575	BMI	0.076	0.665		
Nocturnal systolic pressure	-0.0845	0.628	Nocturnal systolic pressure	-0.101	0.564		
Nocturnal diastolic pressure	-0.194	0.263	Nocturnal diastolic pressure	-0.116	0.507		
Morning systolic pressure	-0.062	0.724	Morning systolic pressure	0.078	0.658		
Morning diastolic pressure	-0.159	0.362	Morning diastolic pressure	0.002	0.991		
Neck circumference	-0.054	0.760	Neck circumference	-0.036	0.836		
AL	-0.263	0.127	AL	-0.331	**0.050***	-0.532	0.234
Nocturnal IOP	-0.354	0.057	Nocturnal IOP	-0.415	**0.021***	-0.399	0.129
Morning IOP	-0.040	0.821	Morning IOP	-0.233	0.177		

* and bold values represents data with a p value < 0.05. β: Spearman's rank correlation coefficient; β′: correlation coefficient in multiple linear regression analysis; p′: p value for the corresponding correlation coefficient in multiple linear regression analysis.
VD, vessel density; RNFLT, retinal nerve fiber layer thickness; GH, Garway-Heath-based grids; AL, axial length; IOP, intraocular pressure; AHI, apnea–hypopnea index; BMI, body mass index; NI, nasal inferior, I-Hemi, Inferior hemi; RPC, radial peripapillary capillaries; CCT, central corneal thickness.

secondary to repetitive mechanical obstruction of the upper airway and recurrent hypoxic episodes in severe OSA. This process might initiate retinal nerve fiber ischemia and subtle swelling, leading to slightly but significantly increased nerve fiber layer thickness in the early morning. In a three-group comparison of the difference in diurnal variation, we found a significant decrease in the diurnal difference at the peripapillary and GH-NI regions in the mild-to-moderate group compared to the control group. We consider that the different changes present in the mild-to-moderate group versus the control group may be related to regulation of blood flow in mild OSA subjects. In our previous study, it was confirmed that the mild-to-moderate group had a significantly lower VD in the peripapillary region on the RPC network (19). Yu et al. also demonstrated the decrease in VD of the peripapillary area in the moderate group when compared to the normal-to-mild group. Nerve fiber layer thickness remained relatively stable during the daytime, but there were some small diurnal rhythmic changes, although hardly statistically significant, probably related to superficial retinal blood flow changes. Lisanne J. Balk et al. revealed that the significant physiological slight variation in the RNFL thickness may be relevant to altered hemodynamic status after exercise and dehydration (31). Farideh Sharifipour et al. also documented non-significant slight changes in various parameters including RNFL thickness in the control group, with the highest values at 9 a.m. and lowest at 3p.m., although none of them showed a significantly absolute change over the daytime (32). These mentioned studies demonstrated that there might be very small and insignificant physiological diurnal fluctuations in RNFL thickness which could only be observed shortly after awakening in the physiological state, and in patients with mild-to-moderate OSA, such physiological fluctuations are significantly compromised probably because of abnormal nocturnal activation of the sympathetic system. The diameter of the retinal arterioles has also been verified to be narrowest in the nasal inferior arcade, which may be the reason for more significant impact in the GH-NI region rather than in other sections (33). In contrast, the significant increase of sectional RNFL thickness in awakening in patients with severe OSA may be the result of mild edema in the nerve fiber layer.

No research on the VD diurnal change in OSA was ever analyzed. In the present study, we did not find any significant diurnal variable in macular regions at the level of either SCP or DCP. VDs in macular regions were all comparable in three groups, regardless of the time collected. This was consistent with the previous research regarding the macular regions in normal participants (34, 35). We speculated that this might be due to the unique autoregulation mechanism of retinal microvascular circulation. The contradiction between the heavy demand and limited ocular total blood flow is addressed through the delicately structured bilayer macular capillary network and auto-regulation strategy (36), to nurture multiple layers of the cells effectively while maintaining the gradient tension of oxygen in different layers of retina tissue, which has been already mentioned in our previous work (19). During the hypoxia and hypercapnia episodes, vasoconstriction of arteries followed by the excretion of ET-1, a known powerful vasoconstrictor, reduces the choroidal large blood flow subsequently. The choroid tissue is richly innervated by parasympathetic and sympathetic nerve fibers (37), while retinal vessels branched from the central retinal artery are not. Autoregulation of blood flow is achieved mainly through perceiving changes in local oxygen/carbon dioxide concentration, which is also called metabolic coupling (36, 37). Besides, to compensate for this change in blood flow, vasomotion through small arterioles in SCP (myogenic mechanism) would increase the effective utilization of limited blood flow, and a bilayer microvessel network would also provide a buffer when coping with fluctuations in blood flow (38). In our previous study, we had found that compared to the control group, the severe group had significantly higher VD in the parafoveal and perifoveal regions at the level of deep capillary plexus (DCP), indicating that blood flow changes in macular areas might first appear at the DCP layer in OSA patients (19), probably due to long-term adaptive compensation. However, the metabolic coupling regulation mechanism is sensitive; we speculated that macular VD changes within 12 h between night and morning could be negligible, especially in the patient without pathological vascular changes such as atherosclerosis or hypertension.

Regarding VD in the optic disc areas, we found that the RPC vessel density at the inside-disc region decreased significantly in the mild-to-moderate group in the morning, although the decline was slight, while other groups remained relatively stable during the day and night. In our previous cross-sectional study, we had noticed that VD decreased significantly in the moderate-mild group compared to the control group in the peripapillary region on the radial peripapillary capillary (RPC) network (19). The same conclusion was also noted in various previous studies (18, 39, 40). Yu et al. also mentioned that, compared to the parafoveal area, VD reduction was more pronounced in the peripapillary area (17). Although the baseline peripapillary VD measurements at night were relatively comparable among the three groups, which may be due to the relatively smaller population in the present study, after at least a 6-h-long sleep and overnight PSG examination, inside-disc VD demonstrated a significant difference in the mild-to-moderate group. However, the diurnal VD difference calculated in disc areas was also comparable in the three groups. We speculated that, compared to macular regions, VD changes in disc areas were more vulnerable to the total blood flow changes, especially in the RPC layer, which nurtures nerve fiber bundles sited in the RNFL layer of the inner retina. This might be attributed to the radial distribution of microvascular in the RPC layer. They radiated directly out of the central retinal artery in the optic nerve head section; in this way, VD at the level of the RPC layer in disc areas will be directly influenced by the blood flow changes. However, the residual time for retaining the change in optic disc blood flow did not last as long as RNFL thickness changes did.

In the analysis of blood flow changes at the level of choriocapillaris in the macular area, no significance was noticed

between the three groups, and VD differences between day and night were also comparable. As mentioned above, the choroid tissue is richly innervated by autonomic vasoactive innervation and thus vulnerable to blood flow change in larger vessels and activation of the sympathetic nervous system, however, it can also regulate blood flow quickly at the same time. In one meta-study analysis of CSCR and OSA, findings suggested that patients with CSCR were more likely to have OSA, while patients with moderate/severe OSA had decreased subfoveal choroidal measurements on EDI-OCT scans (41). Besides, He et al. also reported that blood supply in choroid significantly decreased in moderate and severe OSA patients (42), Serpil Yazgan et al. (43) also noted that the peripapillary choroidal thickness of all quadrants was significantly thinner in the moderate and severe subgroups of OSA, and central macular choroidal thickness was significantly thinner in all subgroups of OSA subjects (43). However, Mehmet Özgür Zenginet al. (44) demonstrated that no significant variations in choroidal thickness were observed between patients with OSA and healthy subjects. Emine Esra Karaca et al. (45) also found no significant correlation between the severity of OSA and choroidal thickness in macular areas in a prospective study of 74 OSA patients and 33 normal subjects. They concluded that patients with OSA were able to protect choroidal thickness despite hypoxia to some extent. In our study, we also did not observe any change in the diurnal choriocapillaris VD analysis. We speculated that changes in choriocapillaris blood flow in patients with different severities of OSA did not have a relatively clear trend like VD and RNFL changes in disc areas. We considered that it could be related to fast vascular self-regulatory capacity in the early onset of OSA especially in young patients.

This study has several limitations. First, the subjects included in the study were relatively young and the population was small. Given the large number of examinations performed on every subject, to control the total time of the ophthalmic examination for better cooperation, and to meet the independence condition in statistical analysis, we performed OCTA measurements in only one eye, which further affects the sample size, although there was no evidence of differences in choosing different eyes. Second, considering that this is an exploratory study, we did not correct for multiple testing for various macula and optic disc subregions, which may lead to an inevitable increase in false discovery rate. Third, given the sitting position required to perform OCTA, the OCTA examination could not be performed in the sleeping or supine position. During episodes of apnea and hypopnea events, dynamic vascular changes cannot be captured. Also, changes in body position, light stimulation during transfer, etc., may have some impact on OCTA quantification. Future studies with larger populations and more accurate and reproducible OCTA algorithms are needed to further investigate the effects of OSA on retinal and optic disc microcirculation.

In conclusion, microcirculation blood flow and overnight RNFL thickness change around the optic disc areas might emerge in OSA patients. Although there may be physiological fluctuations, aberrant diurnal changes may signal a decrease in microenvironmental stability that may be associated with the development of various ocular diseases such as glaucoma. Other vessel density (VD) variables, especially macular VDs and FAZ parameters, are relatively stable in the eyes of patients with OSA of different severity.

Data availability statement

The raw data supporting the conclusions of this article will be made available by the authors, without undue reservation. The data supporting this study are available upon request from Prof. XS (e-mail: drxuanshi@163.com).

Ethics statement

The studies involving human participants were reviewed and approved by the Human Research Ethics Committee of Peking University People's Hospital. The patients/participants provided their written informed consent to participate in this study.

Author contributions

XS, J-FQ, and FH designed this study. XS, G-SS, and YC defined the criteria for inclusion and exclusion. W-BL, MZ, LZ, G-SS, and YC performed examinations. Y-TJ and YC analyzed and interpreted the patient data, and YC, Y-TJ, and MZ drafted this manuscript and made the figures and tables. XS, FH, and M-WZ modified the manuscript. All authors read and approved the final manuscript.

Funding

This study was supported by the National Natural Science Foundation of China (Grant No. 81970815), and National Key R&D Program of China, No. 2020YFC2008200.

Acknowledgments

The authors are grateful to all the subjects who participated in this study.

Conflict of interest

The authors declare that the research was conducted in the absence of any commercial or financial relationships that could be construed as a potential conflict of interest.

Publisher's note

References

1. Suzuki M. Obstructive sleep apnea -consideration of its pathogenesis. *Auris Nasus Larynx* (2022) 49(3):313–21. doi: 10.1016/j.anl.2021.10.007

2. Su L, Xiao Y. Application of personalized medicine to obstructive sleep apnea in China. *Sleep Med* (2021) 87:22–9. doi: 10.1016/j.sleep.2021.08.014

3. Huang SG, Li QY. [Prevalence of obstructive sleep apnea-hypopnea syndrome in Chinese adults aged over 30 yr in shanghai]. *Zhonghua Jie He He Hu Xi Za Zhi* (2003) 26(5):268–72. doi: 10.1023/A:1022289509702

4. Liu X, Ma Y, Ouyang R, Zeng Z, Zhan Z, Lu H, et al. The relationship between inflammation and neurocognitive dysfunction in obstructive sleep apnea syndrome. *J Neuroinflammation* (2020) 17(1):229. doi: 10.1186/s12974-020-01905-2

5. Almendros I, Basoglu ÖK, Conde SV, Liguori C, Saaresranta T. Metabolic dysfunction in OSA: Is there something new under the sun? *J Sleep Res* (2022) 31 (1):e13418. doi: 10.1111/jsr.13418

6. Fraser CL. Update on obstructive sleep apnea for neuro-ophthalmology. *Curr Opin Neurol* (2019) 32(1):124–30. doi: 10.1097/WCO.0000000000000630

7. Wong B, Fraser CL. Obstructive sleep apnea in neuro-ophthalmology. *J Neuroophthalmol* (2019) 39(3):370–9. doi: 10.1097/WNO.0000000000000728

8. Farahvash A, Micieli JA. Neuro-ophthalmological manifestations of obstructive sleep apnea: Current perspectives. *Eye Brain* (2020) 12:61–71. doi: 10.2147/EB.S247121

9. Al Saeed AA, AlShabib NS, Al Taisan AA, Kreary YA. Association of retinal vascular manifestation and obstructive sleep apnea (OSA): A narrative review. *Clin Ophthalmol* (2021) 15:3315–20. doi: 10.2147/OPTH.S305968

10. Leroux les Jardins G, Glacet-Bernard A, Lasry S, Housset B, Coscas G, Soubrane G. [Retinal vein occlusion and obstructive sleep apnea syndrome]. *J Fr Ophtalmol* (2009) 32(6):420–4. doi: 10.1016/j.jfo.2009.04.012

11. Mazzeo T, Leber HM, da Silva AG, Freire RCM, Barbosa GCS, Criado GG, et al. Pachychoroid disease spectrum: review article. *Graefes Arch Clin Exp Ophthalmol* (2022) 260(3):723–35. doi: 10.1007/s00417-021-05450-3

12. Scarinci F, Patacchioli FR, Parravano M. Exploring the biopsychosocial pathways shared by obstructive sleep apnea (OSA) and central serous chorioretinopathy (CSC): A literature overview. *J Clin Med* (2021) 10(7):1521. doi: 10.3390/jcm10071521

13. García-Sánchez A, Villalaín I, Asencio M, García J, García-Rio F. Sleep apnea and eye diseases: evidence of association and potential pathogenic mechanisms. *J Clin Sleep Med* (2022) 18(1):265–78. doi: 10.5664/jcsm.9552

14. Yu BE, Cheung R, Hutnik C, Malvankar-Mehta MS. Prevalence of obstructive sleep apnea in glaucoma patients: A systematic review and meta-analysis. *J Curr Glaucoma Pract* (2021) 15(3):109–16. doi: 10.5005/jp-journals-10078-1301

15. Rao DP, Senthil S, Choudhari N. Meta-analysis of association of obstructive sleep apnea (OSA) with glaucoma. *J Glaucoma* (2017) 26(3):e130. doi: 10.1097/IJG.0000000000000525

16. de Carlo TE, Romano A, Waheed NK, Duker JS. A review of optical coherence tomography angiography (OCTA). *Int J Retina Vitreous* (2015) 1:5. doi: 10.1186/s40942-015-0005-8

17. Yu J, Xiao K, Huang J, Sun X, Jiang C. Reduced retinal vessel density in obstructive sleep apnea syndrome patients: An optical coherence tomography angiography study. *Invest Ophthalmol Vis Sci* (2017) 58(9):3506–12. doi: 10.1167/iovs.17-21414

18. Moyal L, Blumen-Ohana E, Blumen M, Blatrix C, Chabolle F, Nordmann JP. Parafoveal and optic disc vessel density in patients with obstructive sleep apnea syndrome: an optical coherence tomography angiography study. *Graefes Arch Clin Exp Ophthalmol* (2018) 256(7):1235–43. doi: 10.1007/s00417-018-3943-7

19. Cai Y, Sun GS, Zhao L, Han F, Zhao MW, Shi X. Quantitative evaluation of retinal microvascular circulation in patients with obstructive sleep apnea-hypopnea using optical coherence tomography angiography. *Int Ophthalmol* (2020) 40 (12):3309–21. doi: 10.1007/s10792-020-01518-x

20. Dimitrova G, Chihara E, Takahashi H, Amano H, Okazaki K. Quantitative retinal optical coherence tomography angiography in patients with diabetes without diabetic retinopathy. *Invest Ophthalmol Vis Sci* (2017) 58(1):190–6. doi: 10.1167/iovs.16-20531

21. Chen FK, Menghini M, Hansen A, Mackey DA, Constable IJ, Sampson DM. Intrasession repeatability and interocular symmetry of foveal avascular zone and retinal vessel density in OCT angiography. *Transl Vis Sci Technol* (2018) 7(1):6. doi: 10.1167/tvst.7.1.6

22. Fu D, Tong H, Zheng S, Luo L, Gao F, Minar J. Retinal status analysis method based on feature extraction and quantitative grading in OCT images. *BioMed Eng Online* (2016) 15(1):87. doi: 10.1186/s12938-016-0206-x

23. Hassan M, Sadiq MA, Halim MS, Afridi R, Soliman MK, Sarwar S, et al. Evaluation of macular and peripapillary vessel flow density in eyes with no known pathology using optical coherence tomography angiography. *Int J Retina Vitreous* (2017) 3:27. doi: 10.1186/s40942-017-0080-0

24. Falavarjani KG, Shenazandi H, Naseri D, Anvari P, Kazemi P, Aghamohammadi F, et al. Foveal avascular zone and vessel density in healthy subjects: An optical coherence tomography angiography study. *J Ophthalmic Vis Res* (2018) 13(3):260–5. doi: 10.4103/jovr.jovr_173_17

25. Wang E, Chen Y, Li N, Min H. Effect of silicone oil on peripapillary capillary density in patients with rhegmatogenous retinal detachment. *BMC Ophthalmol* (2020) 20(1):268. doi: 10.1186/s12886-020-01533-7

26. Sarwar S, Hassan M, Soliman MK, Halim MS, Sadiq MA, Afridi R, et al. Diurnal variation of choriocapillaris vessel flow density in normal subjects measured using optical coherence tomography angiography. *Int J Retina Vitreous* (2018) 4:37. doi: 10.1186/s40942-018-0140-0

27. Kapur VK, Auckley DH, Chowdhuri S, Kuhlmann DC, Mehra R, Ramar K, et al. Clinical practice guideline for diagnostic testing for adult obstructive sleep apnea: An American academy of sleep medicine clinical practice guideline. *J Clin Sleep Med* (2017) 13(3):479–504. doi: 10.5664/jcsm.6506

28. Sagiv O, Fishelson-Arev T, Buckman G, Mathalone N, Wolfson J, Segev E, et al. Retinal nerve fibre layer thickness measurements by optical coherence tomography in patients with sleep apnoea syndrome. *Clin Exp Ophthalmol* (2014) 42(2):132–8. doi: 10.1111/ceo.12145

29. Zengin MO, Tuncer I, Karahan E. Retinal nerve fiber layer thickness changes in obstructive sleep apnea syndrome: one year follow-up results. *Int J Ophthalmol* (2014) 7(4):704–8. doi: 10.3980/j.issn.2222-3959.2014.04.22

30. Chirapapaisan N, Likitgorn T, Pleumchitchom M, Sakiyalak D, Banhiran W, Saiman M, et al. Diurnal changes in retinal nerve fiber layer thickness with obstructive sleep apnea/hypopnea syndrome. *Int J Ophthalmol* (2016) 9(7):979–83. doi: 10.18240/ijo.2016.07.07

31. Balk LJ, Sonder JM, Strijbis EM, Twisk JW, Killestein J, Uitdehaag BM, et al. The physiological variation of the retinal nerve fiber layer thickness and macular volume in humans as assessed by spectral domain-optical coherence tomography. *Invest Ophthalmol Vis Sci* (2012) 53(3):1251–7. doi: 10.1167/iovs.11-8209

32. Sharifipour F, Farrahi F, Moghaddasi A, Idani A, Yaseri M. Diurnal variations in intraocular pressure, central corneal thickness, and macular and retinal nerve fiber layer thickness in diabetics and normal individuals. *J Ophthalmic Vis Res* (2016) 11(1):42–7. doi: 10.4103/2008-322X.180708

33. Wang YX, Panda-Jonas S, Jonas JB. Optic nerve head anatomy in myopia and glaucoma, including parapapillary zones alpha, beta, gamma and delta: Histology and clinical features. *Prog Retin Eye Res* (2021) 83:100933. doi: 10.1016/j.preteyeres.2020.100933

34. Rommel F, Rothe M, Kurz M, Prasuhn M, Grisanti S, Ranjbar M. Evaluating diurnal variations in retinal perfusion using optical coherence tomography angiography. *Int J Retina Vitreous* (2020) 6:22. doi: 10.1186/s40942-020-00227-y

35. Wu JH, Penteado RC, Moghimi S, Zangwill LM, Proudfoot JA, Weinreb RN. Diurnal variation of retinal vessel density in healthy human eyes. *J Glaucoma* (2021) 30(9):820–6. doi: 10.1097/IJG.0000000000001903

36. Luo X, Shen YM, Jiang MN, Lou XF, Shen Y. Ocular blood flow autoregulation mechanisms and methods. *J Ophthalmol* (2015) 2015:864871. doi: 10.1155/2015/864871

37. Reiner A, Fitzgerald MEC, Del Mar N, Li C. Neural control of choroidal blood flow. *Prog Retin Eye Res* (2018) 64:96–130. doi: 10.1016/j.preteyeres.2017.12.001

38. Pournaras CJ, Rungger-Brändle E, Riva CE, Hardarson SH, Stefansson E. Regulation of retinal blood flow in health and disease. *Prog Retin Eye Res* (2008) 27 (3):284–330. doi: 10.1016/j.preteyeres.2008.02.002

39. Ucak T, Unver E. Alterations in parafoveal and optic disc vessel densities in patients with obstructive sleep apnea syndrome. *J Ophthalmol* (2020) 2020:4034382. doi: 10.1155/2020/4034382

40. Wang XY, Li M, Ding X, Han DM. [Application of optical coherence tomography angiography in evaluation of retinal microvascular changes in patients with obstructive sleep apnea syndrome]. *Zhonghua Yi Xue Za Zhi* (2017) 97 (32):2501–5. doi: 10.3760/cma.j.issn.0376-2491.2017.32.006

41. Wu CY, Riangwiwat T, Rattanawong P, Nesmith BLW, Deobhakta A. ASSOCIATION OF OBSTRUCTIVE SLEEP APNEA WITH CENTRAL SEROUS CHORIORETINOPATHY AND CHOROIDAL THICKNESS: A systematic review and meta-analysis. *Retina* (2018) 38(9):1642–51. doi: 10.1097/IAE.0000000000002117

42. He M, Han X, Wu H, Huang W. Choroidal thickness changes in obstructive sleep apnea syndrome: a systematic review and meta-analysis. *Sleep Breath* (2016) 20(1):369–78. doi: 10.1007/s11325-015-1306-8

43. Yazgan S, Erboy F, Celik HU, Ornek T, Ugurbas SH, Kokturk F, et al. Peripapillary choroidal thickness and retinal nerve fiber layer in untreated patients with obstructive sleep apnea-hypopnea syndrome: A case-control study. *Curr Eye Res* (2017) 42(11):1552–60. doi: 10.1080/02713683.2016.1266661

44. Zengin M, Öz T, Baysak A, Çinar E, Küçükerdönmez C. Changes in choroidal thickness in patients with obstructive sleep apnea syndrome. *Ophthalmic Surg Lasers Imaging Retina* (2014) 45(4):298–304. doi: 10.3928/23258160-20140624-02

45. Karaca EE, Ekici F, Yalçın NG, Çiftçi TU, Özdek Ş. Macular choroidal thickness measurements in patients with obstructive sleep apnea syndrome. *Sleep Breath* (2015) 19(1):335–41. doi: 10.1007/s11325-014-1025-6

frontiers | Frontiers in Endocrinology

TYPE Original Research
PUBLISHED 25 August 2022
DOI 10.3389/fendo.2022.949827

OPEN ACCESS

EDITED BY
Lian Zhao,
National Eye Institute (NIH),
United States

REVIEWED BY
Huaizhou Wang,
Beijing Tongren Hospital, Capital Medical University, China
Peng Zhou,
Parkway Health, China
Xianru Hou,
Peking University People's Hospital, China

*CORRESPONDENCE
Yi Ning
yi.ning@meinianresearch.com

SPECIALTY SECTION
This article was submitted to Molecular and Structural Endocrinology, a section of the journal Frontiers in Endocrinology

RECEIVED 21 May 2022
ACCEPTED 02 August 2022
PUBLISHED 25 August 2022

CITATION
Liu X, Pan X, Ma Y, Jin C, Wang B and Ning Y (2022) Variation in intraocular pressure by sex, age, and geographic location in China: A nationwide study of 284,937 adults.
Front. Endocrinol. 13:949827.
doi: 10.3389/fendo.2022.949827

Variation in intraocular pressure by sex, age, and geographic location in China: A nationwide study of 284,937 adults

Xuan Liu[1], Xue Pan[2], Yuan Ma[3], Cheng Jin[3], Bo Wang[3] and Yi Ning[4]*

[1]Beijing Tsinghua Changgung Hospital, School of Clinical Medicine, Tsinghua University, Beijing, China, [2]Department of Ophthalmology, Beijing Shijitan Hospital, Capital Medical University, Beijing, China, [3]Peking University Health Science Center, Meinian Public Health Research Institute, Beijing, China, [4]School of Public Health, Hainan Medical University, Haikou, China

Objective: To investigate the distribution characteristics of intraocular pressure (IOP) by sex, age, and geographic location in China and to build the corresponding reference intervals (RIs).

Material and methods: A cross-sectional, multi-centered, population-based study was conducted. All data were collected from participants without eye diseases who underwent ophthalmological examinations in 170 Health Screening Centers in mainland China in 2018. The non-contact tonometer was used to measure IOP. The age-, sex-, and province-specific RIs of IOP were investigated. The IOP of different age–sex groups was further explored by stratifying according to height, body mass index (BMI), blood pressure, altitude, and geographic area.

Results: During the study, a population-based sample of 284,937 participants was included. The distribution of measured IOP followed an approximately Gaussian distribution, with a higher mean value in men than in women. The IOP showed a general trend of decline with age for both men and women and varied across geographical locations. The mean IOP was 15.4 (95% CI: 9.1-21.6) mmHg for men and 14.9 (95% CI: 9.0-20.8) mmHg for women. For men, it decreased from 11.0-23.5 mmHg at age 18-24 years to 10.5-20.5 mmHg at age ≥70 years. For women, it decreased from 10.5-22.0 to mmHg at age 18-24 years to 10.0-21.0 mm Hg at age ≥70 years.

Conclusions: The IOP varied with age, sex, metabolic disorders and geographic location. These RIs should be considered in the clinical process of glaucoma diagnosis and treatment.

KEYWORDS

intraocular pressure (IOP), sex, age, geographic distribution, reference interval

Introduction

Glaucoma is the most common cause of irreversible blindness worldwide (1, 2), with the number of patients expected to reach 111.8 million by 2040 (2). From a pathophysiological and therapeutic point of view, intraocular pressure (IOP) is the primary modifiable risk factor, since progression of glaucoma usually stops if IOP is lowered by 30-50% from baseline (3). Assessment of IOP helps to make decisions for prevention, diagnosis, and treatment of glaucoma.

The prevalence of glaucoma varies with sex (4, 5), age (4, 6, 7), and across geographic regions (2, 8, 9). Glaucoma prevalence varies from 2.93% in Europe to 3.40% in Asia and 4.79% in Africa (2). Previous studies have defined a normal range of IOP as 10 to 21 mmHg (10). However, participants in these studies were Caucasians, and the normal reference interval (RI) may be different for Asians. An ophthalmologically normal Japanese population-based study reported an average IOP of 14.1 ± 2.3 mmHg (11). Additionally, a positive correlation between age and IOP in Caucasians (12), and an inverse correlation between age and IOP in Japanese have been reported (11). Although a few studies have examined the variation of IOP by age, gender, and geographic location across China (13, 14), they did not capture the heterogeneity due to relatively small sample sizes. One study (15) investigated the association of IOP with age and sex; however, geographic distribution and metabolic factors were ignored. In order to investigate the distribution characteristics of IOP and to provide specific RI, we conducted this study using available data from 170 Screening Centers located across the majority of provinces in mainland China.

Methods

Study population

The Meinian OneHealth Group is a public company with health screening centers located in most provinces in mainland China, which provide annual or periodic health examinations for their members. All screening equipment for eye examinations were approved by the authorities. All participants (aged ≥18 years) underwent a brief interview about demographic information, medical history, and health checkup.

Participants (n=17,983,184) underwent ophthalmological examinations (including visual acuity, IOP measurements, slit-lamp examination, and fundus photography) in 267 screening centers from January 1st to December 31st, 2018. We included 974,300 participants aged ≥18 years with no missing values for age, sex, and intraocular pressure of both eyes. We excluded 234,372 participants with previously diagnosed glaucoma, history of eye surgery (including cataract surgery, retinal detachment surgery, vitrectomy, corneal refractive surgery), cataract, trachoma, hypochromatopsia, conjunctivitis, or corrected visual acuity below 0.3. To explore the IOP RI for healthy people, we further excluded 425,671 participants with certain diseases, including cardio-cerebro-vascular diseases, hypertension, diabetes, dyslipidemia, obesity, hyperuricemia, severe hepatic disease, severe renal disease, osteoporosis, and anemia (detailed diagnostic criteria described in the measurement of covariates). For those who attended two screenings or more, results from the most recent checkup were included to ensure the independency of data. Therefore, we included 284,937 participants from 170 health screening centers across 81 cities in mainland China in our study (Figure 1).

This study complies with the tenets of the Declaration of Helsinki, and institutional review board (IRB)/Ethics Committee approval was obtained. This study was approved by the Ethics Committee of Beijing Tsinghua Changgung Hospital, affiliated with Tsinghua University (Ethics number 18181-0-01). All participants provided informed consent. Data were centrally managed and stored. Individual identifiers were removed and remained anonymous during the entire study process.

Measurements

Measurements of IOP

Ophthalmic examination consisted of slit-lamp examination (cornea, lens, iris, and aqueous), non-mydriatic fundus photography, and IOP measurement. The IOP was measured with an auto non-contact tonometer (HNT-7000 Non-Contact Tonometer made in Korea, Reichert 7CR Auto Non-Contact Tonometer made in USA, or Topcon CT-80A Non-Contact Computerized Tonometer made in Japan), and all procedures were performed strictly according to instructions and unified operation specifications.

Measurements of covariates

All laboratories in this study successfully completed a standardization and certification program. Blood samples were drawn by venipuncture after 8–12 h of overnight fasting. Fasting blood glucose (FBG), total cholesterol (TC), triglyceride (TG), high-density lipoprotein (HDL), low-density lipoprotein (LDL), creatinine (Cr), alanine transaminase (ALT), and aspartate transaminase (AST) were measured using automatic biochemical analyzers with commercially available reagents at the clinical biochemical laboratories in each center.

Estimated glomerular filtration rate (E-GFR) was calculated according to the Chronic Kidney Disease Epidemiology Collaboration creatinine equation (16), and severe chronic kidney disease was defined as eGFR less than 30 ml/min/1.73 m^2 or with proteinuria. Diabetes was defined as a self-reported physician-diagnosis history, currently treated with insulin or

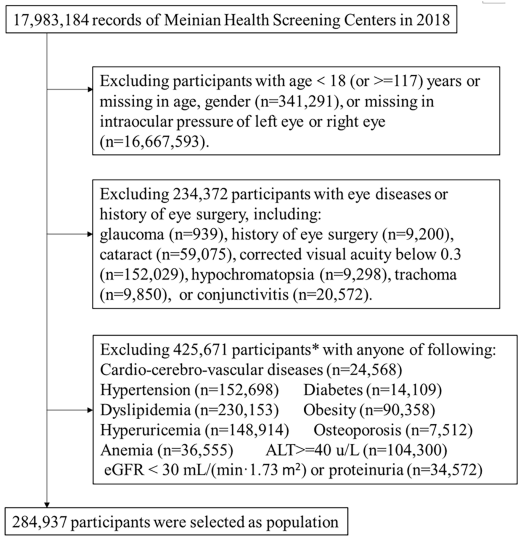

FIGURE 1
Flowchart of selection of the study participants.

oral hypoglycemic agents, or *via* FBG concentrations ≥7.0 mmol/L. Dyslipidemia was defined as a self-reported dyslipidemia history, TC ≥6.22 mmol/L, TG ≥2.26 mmol/L, HDL <1.04 mmol/L, or LDL ≥4.92 mmol/L. Hyperuricemia was defined as a uric acid concentration of ≥360 μmol/L in women and ≥420 μmol/L in men. Severe hepatic insufficiency was defined as an ALT concentration ≥40 U/L. Hemoglobin levels were measured *via* blood cell analysis (5-Part Differential), and levels <120 g/L in men or <110 g/L in women was regarded as anemia.

Left ventricular hypertrophy, atrial flutter, or atrial fibrillation was diagnosed by electrocardiogram. Severe valvular heart disease was diagnosed by echocardiography, including mitral valve stenosis (mitral valve area <1.5 cm^2), mitral regurgitation (regurgitant fraction ≥30%), aortic stenosis (aortic valve area <1.0 cm^2), aortic regurgitation (regurgitant fraction ≥30%), tricuspid valve stenosis, tricuspid regurgitation, pulmonary valve stenosis, and pulmonary valve regurgitation. Stroke was diagnosed by cranial computed tomography or magnetic resonance imaging. Carotid artery stenosis was diagnosed by carotid color Doppler ultrasound.

Obesity was defined as a body mass index (BMI) of 28 kg/m^2 or higher. Systolic blood pressure (SBP), diastolic blood pressure (DBP), and heart rate (HR) were measured using a digital automatic blood pressure (BP) monitor after participants were seated for at least 5 min. The mean values of the two BP and HR readings were recorded. Hypertension was defined as a self-reported physician-diagnosis history, currently treated with antihypertensive agents. Prehypertension was defined as 120 mm Hg ≤ SBP <140 mmHg or 80 mm Hg ≤ DBP <90 mmHg without a history of hypertension. Tachycardia was defined as an HR >100 beats/min and bradycardia was defined as an HR of <60 beats/min. Data on gross domestic product per capita (GDP) were collected from the China Statistical Yearbook for 2018 (17).

Statistical analysis

The IOP reported for the participants was the mean value of IOP in the left and right eyes without specific indication. As the distribution of IOP differed between men and women, we performed separate analyses between sexes. Besides age, sex, and geographical regions, the distribution of IOP according to height, BMI, blood pressure, altitude, and north or south geographic area were also explored. Height and altitude were divided by tertiles, and geographic area was divided by latitude of 33°N.

To describe IOP distribution, the mean and 95% confidence interval (mean ± 1.96 SD) were calculated, where SD denotes standard deviation. The medians (2.5^{th}-97.5^{th} percentiles) were also presented, which were used as the reference intervals (RIs) in this study, since the Clinical and Laboratory Standards Institute (18) recommends the non-parametric computation of a 0.95 coverage interval. The analysis of variance and the SNK test were applied to compare IOP levels among different age groups (the rank of IOP values were used when median values were compared). A general linear model was constructed to

estimate age-GDP-adjusted IOP mean values. Choropleth maps were produced by R software to visually examine the geographical variation in IOP. Statistical analyses were conducted using SAS software (SAS, Inc., Cary, NC, USA, version 9.4) and R software (version 3.6.1). A p-value of <0.05 was considered statistically significant.

Results

Basic characteristics and IOP distribution for all participants

Among the 284,937 participants included, approximately 33.9% were men. The average age was 39.9 ± 11.9 years (mean± SD) for men and 38.7 ± 10.7 years for women (Table 1). The mean IOP was 15.4 (95% CI: 9.1-21.6) mmHg for men and 14.9 (95% CI: 9.0-20.8) mmHg for women. A higher proportion of men than women were prehypertensive, prediabetic, and overweight. The distribution of IOP followed an approximately Gaussian distribution, with a slight right-ward skew in both sexes (Figure 2).

The IOP showed a general trend of decline with age in both sexes (Figure 3). The median IOP of men decreased gradually from 15.5 (RI: 11.0-23.5) mmHg at ages 18-24 to 14.0 (RI: 10.5-20.5) mmHg at age ≥70 years. The median IOP of women decreased gradually from 15.0 (RI: 10.5-22.0) mmHg at ages 18-24 to 14.0 (RI: 10.0-21.0. mmHg at age ≥70 years. After the age of 65 years, the IOP of men was similar to that of women. According to the multiple comparison of IOP levels among different age groups using the SNK test in Figure 3, there was a significant difference between all the age groups of 18-24, 25-29,

TABLE 1 Sociodemographic and clinical characteristics of study participants (N=284,937) by sex.

	Men	Women
N	96,517	188,420
Age (years), Mean ± SD	39.93 ± 11.91	38.66 ± 10.66
<30, n (%)	21,292 (22.1)	41,772 (22.2)
30-39, n (%)	32,504 (33.7)	69,050 (36.6)
40-49, n (%)	20,028 (20.8)	44,129 (23.4)
50-59, n (%)	15,352 (15.9)	25,402 (13.5)
60-69, n (%)	6,611 (6.8)	7,571 (4.0)
>=70, n (%)	730 (0.8)	496 (0.3)
IOP (mmHg), Mean ± SD	15.35 ± 3.20	14.88 ± 3.01
Right IOP	15.26 ± 3.37	14.80 ± 3.16
Left IOP	15.44 ± 3.40	14.95 ± 3.20
Gross Domestic Product per capita (CNY), n (%)		
Quintiles 1	19,935 (20.7)	39,855 (21.2)
Quintiles 2	20,160 (20.9)	34,252 (18.2)
Quintiles 3	27,515 (28.5)	63,625 (33.8)
Quintiles 4	9,551 (9.90)	12,913 (6.85)
Quintiles 5	19,356 (20.1)	37,775 (20.0)
Hypertension, n (%)		
Normal	49,961 (53.0)	133,373 (72.7)
Prehypertension	44,335 (47.0)	50,163 (27.3)
Diabetes, n (%)		
Normal	15,004 (77.2)	30,324 (83.3)
Prediabetes	4,422 (22.8)	6,099 (16.7)
BMI† (kg/m^2), Mean ± SD	22.79 ± 2.55	21.79 ± 2.51
<18.5, n (%)	4,989 (5.35)	16,150 (8.92)
<24, n (%)	56,586 (60.7)	128,591 (71.1)
<28, n (%)	31,699 (34.0)	36,230 (20.0)
Height (cm), n (%)		
Tertile 1	4,737 (5.08)	109,019 (60.2)
Tertile 2	31,123 (33.4)	63,965 (35.4)
Tertile 3	57,416 (61.6)	7,989 (4.41)

(Continued)

TABLE 1 Continued

	Men	Women
City size*, n (%)		
Small or medium sized city	12,513 (13.0)	28,075 (14.9)
Large city	42,899 (44.4)	80,922 (42.9)
Mega city and above	41,105 (42.6)	79,423 (42.2)
Geographical region**, n (%)		
North China	11,247 (11.7)	19,041 (10.1)
East China	59,749 (61.9)	120,677 (64.0)
Central China	944 (0.98)	1,735 (0.92)
South China	5,409 (5.60)	11,411 (6.06)
Northeast China	3,870 (4.01)	8,516 (4.52)
Northwest China	9,666 (10.01)	16,800 (8.92)
Southwest China	5,632 (5.84)	10,240 (5.43)

*According to the new standards in 2014, urban populations are more than 10 million for megacity behemoth, 5-10 million for mega city, 1-5 million for large cities (3-5 million for type I large cities, 1-3 million for type II large cities), 0.5-1 million for medium-sized cities, and less than 0.5 million for small cities (0.2-0.5 million for type I small cities, and less than 0.2 million for the type II small cities). The city size was divided according to the sixth census in 2010.
**Seven geographical regions of China: https://www.chinacheckup.com/blogs/articles/regions-of-china
†BMI was categorized according to Chinese guidelines: underweight (BMI<18.5 kg/m^2), normal (18.5-23.9 kg/m^2), overweight (24-27.9 kg/m^2), and obesity (≥28 kg/m^2).

30-34, 45-49, 50-54, 60-64, and ≥65 years in men and age groups–18-24, 25-29, 30-34, 60-64, and ≥70 years in women.

IOP levels varied across geographical locations. The age-GDP adjusted mean IOP is presented for both sexes in Figure 4. In men, the lowest standardized 95% reference interval was 9.0-22.5 mmHg in Guangxi and the highest 95% reference interval was 11.5-23.2 mmHg in Yunnan province. For women, the lowest standardized 95% reference interval was 8.7-20.0 mmHg in Guizhou province and the highest 95% reference interval was 11.2-21.5 mmHg in the Yunnan province.

Stratification analysis results

Certain factors may influence IOP levels, such as height and blood pressure. We further calculated the IOP (RIs) in subgroups of height tertiles, normal or overweight, normal or prehypertension, altitude tertiles, and north or south geographic location for different age groups (Table 2). The results in the general population (participants with certain diseases) are also displayed (Table S2).

The IOP reference intervals varied with BMI (Table 2). The highest IOP levels were found in the higher BMI and younger age groups, while the lowest IOP levels were found in the lower BMI and older age groups in both sexes (Table 2). Higher BMI tended to have higher IOP in the same age group. In male participants, the highest IOP levels (15.5 (10.5-23.0) mmHg) were found in the overweight group and age <30 years, while the lowest IOP levels (13.5 (10.0-20.0) mm Hg) were found in those with BMI <24 kg/m^2 and age ≥60 years. Similar results were observed in female participants.

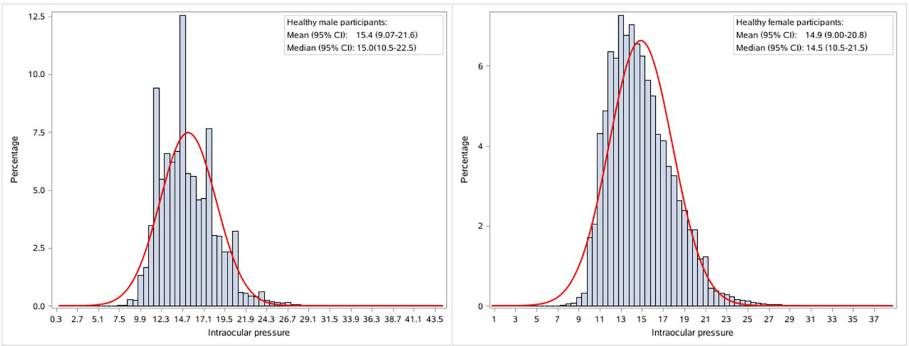

FIGURE 2
Sex specific distribution of intraocular pressure in healthy participants. The red curve denotes the normal distribution density curve.

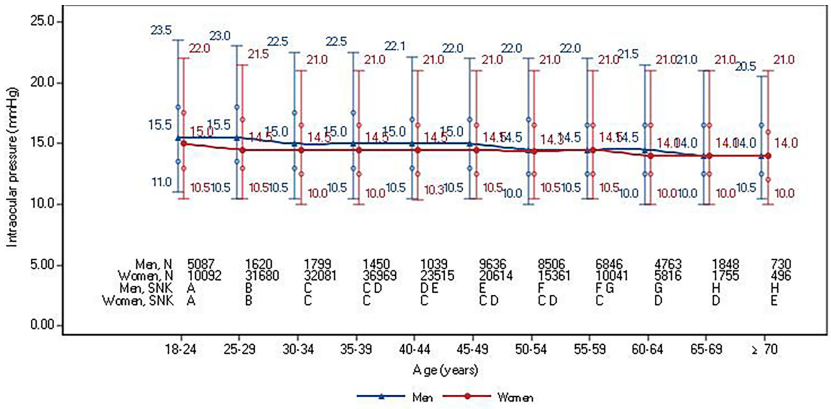

FIGURE 3
Median and 95% reference intervals of intraocular pressure in healthy participants according to sex and age stratifications. Circles denote interquartile ranges. Student-Newman-Keuls (SNK) test was used for multiple comparison of IOP levels among different age groups by gender and age. The same capital letters indicated different means of the index groups were equal, but different capital letters indicated different means of index groups were not equal.

pt?>IOP RIs varied with blood pressure (Table 2). The highest IOP levels were found in the higher blood pressure and younger age groups, while the lowest IOP levels were found in the lower blood pressure and older age groups in both sexes. Higher blood pressure tended to have higher IOP in the same age group. In male participants, the highest IOP levels (16.0 (11.0-24.0) mmHg) were found in those with the highest blood pressure and age <30 years, while the lowest IOP levels (14.5(10.5-21.5) mmHg) were found in

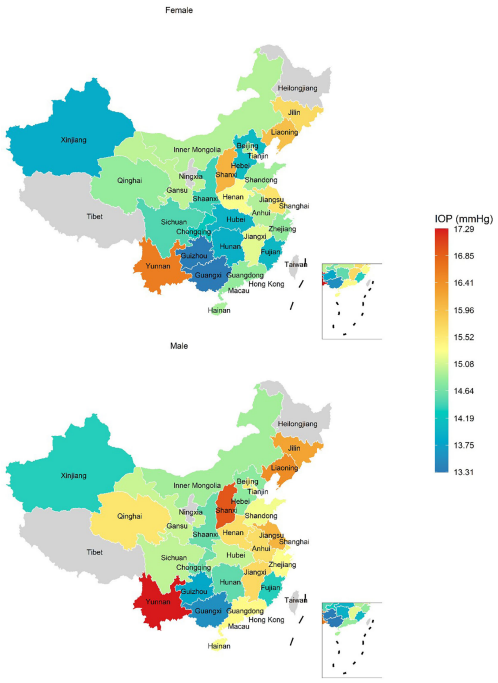

FIGURE 4
The adjusted mean of intraocular pressure in healthy participants. Intraocular pressure was adjusted for age and gross domestic product by a general linear model. Choropleth maps were produced within R software according to the decile of province intraocular pressure levels.

TABLE 2 Median and 95% reference interval of intraocular pressure of participants in the study.

	Men				Women			
	All (N=96,517)	<30 years (N=21,292)	30-60 years (N=67,884)	≥60 years (N=7,341)	All (N=188,420)	<30 years (N=41,772)	30-60 years (N=138,581)	≥60 years (N=8,067)
Height*,cm								
Tertile 1	14.5(10.5-21.5)	16.0(11.0-22.5)	14.5(10.5-21.5)	14.0(10.0-21.5)	14.5(10.5-21.0)	15.0(10.5-22.0)	14.5(10.5-21.0)	14.0(10.0-21.0)
Tertile 2	14.5(10.5-22.0)	15.5(10.5-23.5)	14.5(10.5-22.0)	14.0(10.0-21.0)	14.5(10.5-21.5)	15.0(10.5-21.5)	14.5(10.5-21.0)	14.0(10.5-21.5)
Tertile 3	15.0(10.5-22.5)	15.5(10.5-23.0)	15.0(10.5-22.5)	14.5(10.0-21.5)	14.5(10.0-21.5)	15.0(10.5-22.0)	14.5(10.0-21.0)	14.5(10.5-20.5)
BMI[&], kg/m^2								
<24	14.5(10.5-21.5)	15.0(10.5-22.0)	14.5(10.3-21.3)	13.5(10.0-20.0)	14.5(10.0-21.5)	14.5(10.5-21.5)	14.0(10.0-21.0)	14.0(10.0-20.5)
24-27.9	15.0(10.5-22.3)	15.5(10.5-23.0)	14.5(10.5-22.0)	14.0(10.0-21.0)	14.5(10.5-21.0)	15.0(10.5-22.0)	14.5(10.1-21.0)	14.0(10.0-21.0)
Blood pressure								
Normal	14.5(10.5-22.0)	15.0(10.5-22.5)	14.5(10.5-21.5)	14.0(10.0-21.0)	14.5(10.0-21.0)	14.5(10.5-21.5)	14.0(10.0-21.0)	14.0(10.0-20.5)
Pre-hypertension	15.5(10.5-23.0)	16.0(11.0-24.0)	15.0(10.5-23.0)	14.5(10.5-21.5)	15.0(10.5-22.0)	15.5(11.0-23.0)	15.0(10.5-22.0)	14.5(10.5-21.0)
Altitude*, m								
Tertile 1	15.5(10.5-23.0)	16.0(10.5-23.7)	15.5(10.5-22.5)	14.5(10.5-22.0)	15.0(10.5-21.1)	15.0(10.5-22.5)	14.5(10.5-21.0)	14.5(10.5-21.0)
Tertile 2	14.5(10.5-22.5)	15.5(10.5-23.0)	14.5(10.0-22.0)	14.0(10.0-21.5)	14.0(10.0-21.0)	14.5(10.5-21.5)	14.0(10.0-21.0)	13.5(10.0-20.5)
Tertile 3	14.5(10.5-22.4)	15.0(11.0-23.0)	14.5(10.5-22.0)	14.0(10.0-21.0)	14.5(10.5-21.5)	14.5(10.5-22.0)	14.5(10.5-21.5)	14.0(10.5-21.5)
Geographic area†								
North	15.0(10.5-22.5)	15.0(11.0-23.0)	15.0(11.0-22.5)	14.5(10.5-21.5)	14.5(10.5-21.5)	14.5(10.5-22.0)	14.5(10.5-21.5)	14.5(10.5-21.5)
South	15.0(10.5-22.5)	15.5(10.5-23.0)	15.0(10.5-22.0)	14.0(10.0-21.5)	14.5(10.0-21.0)	15.0(10.5-22.0)	14.5(10.0-21.0)	14.0(10.0-21.0)

*Height and altitude are divided by tertiles.
[&]BMI: Body mass index.
†Geographic area divided by latitude of 33°N.

those with the lowest blood pressure and age ≥60 years. Similar results were observed in female participants.

The IOP RIs varied with altitude (Table 2). The highest IOP levels were found in the lower altitude and younger age groups, while the lowest IOP levels were found in higher altitude and older age groups in both sexes. Lower altitude groups tended to have higher IOP in the same age group. In male participants, the highest IOP levels (16.0 (10.5-23.7) mmHg) were found in the group from the lowest altitude and with age <30 years, while the lowest IOP levels (14.0 (10.0-21.0) mm Hg) were found in groups from the highest altitude and with age ≥60 years.

However, IOP reference intervals did not show any differences by height tertiles and geographic area divided by latitude of 33° N in all three age groups.

Discussion

To the best of our knowledge, the current study is the largest investigation using national data to examine nuanced IOP differences by sex, age, and geographic location in China. We found that the distribution of IOP varied with all three factors. BMI, blood pressure, and altitude also influenced IOP.

IOP is an important factor for glaucoma pathogenesis, and is also crucial for monitoring the treatment of glaucoma. Therefore, it is important to identify the variations in IOP by sex, age, and geographical location. Investigation of specific RIs of IOP will help to distinguish normal eyes from glaucomatous eyes based on IOP readings and contribute to setting precise IOP RIs for glaucoma treatments in diverse patients.

This study suggests that the association between sex and IOP may be modified by age. We found that below 60 years of age, men had a higher IOP than women. However, men and women over 60 years of age had similar IOP values. The association between sex and IOP was inconsistent in previous studies (6, 11). This could be due to the studies reporting no gender difference in IOP being performed with participants aged 55 years and over (6, 11), while others observing higher IOP values in men being performed in younger participants aged about 40 years (4). The gender difference may be influenced by hormonal regulation (5, 19). However, further research is warranted to better understand the mechanisms underlying sex differences in IOP.

The IOP showed a general trend of decline with age in both sexes. There are studies that show IOP increasing with age (6), decreasing with aging (7), and not associated with age after adjustment (20, 21). Several factors, such as a narrow age span, limited amounts of samples, and a lack of sex-specific analysis, may lead to inconsistent results. In our study, we found that the median IOP decreased from 18 years (15.5 mmHg) to 70 years of

age and over (14.0 mmHg) in male participants. The general trend among women is similar to men.

The diverse IOP distribution in different locations has been reported in previous studies (2, 22–24). The IOP was reported as 17.1 ± 3.1 mmHg (22) in the Baltimore Eye Survey in the United States, 14.5 ± 2.6 mmHg in the Tehran Eye Study in Iran (23), and 12.9 ± 3.1 mmHg in the Shihpai eye study (24) in Shihpai, Taiwan. Here, the IOP distribution in China also varied from 15.6 ± 3.0 mmHg in Beijing to 15.3 ± 2.3 mmHg in Guangzhou (25). Previous spatially orientated research was limited by comparisons across singular and coarse geographic scales. In the current study, we were able to investigate the variation of IOP RIs across China, accounting for administrative regions, altitude, and latitude, by the data from 170 health screening centers covering 81 cities in mainland China. We found that the IOP values varied from 8.7-20.0 mmHg in Guizhou to 11.2-21.5 mmHg in Yunnan province. The study has shown that IOP levels are higher at lower altitudes for different genders and ages, with the exception that the highest IOP occurred in Yunnan Province, which has a higher average altitude. An investigation of IOP from a geographical perspective will provide the necessary information for allocation of health resources to prevent and control glaucoma.

Several studies have shown that IOP is influenced by risk factors in metabolic disorders such as diabetes (26), blood pressure levels (27),obesity (28), and dyslipidemia (29). We found that participants with certain metabolic disorders, such as being overweight and pre-hypertension, have higher IOP. This may indicate that IOP levels were influenced by diseases or risk factors of metabolic disorders. Another possible explanation is that obesity may affect breathing, which may influence the measurement of intraocular pressure when the non-contact IOP is usually measured in sitting posture.

The distribution of IOP varied with sex, age, and geographic location, suggesting that the variation in IOP should be corrected according to these factors in medical practice. The traditional normal range of IOP (10 to 21 mmHg) was based on a hospital-based study performed by Leydhecker and colleagues (12) in 1958 and an investigation conducted by Hollows and Graham in 1966 (10). These studies were limited to Caucasians, and the results were not stratified by sex, age, or geographic area. Hypertension, diabetes, obesity, and other metabolic disorders, which also can alter IOP dramatically, were not taken into account. Especially in the diagnosis of “normal tension glaucoma”, the “normal range of intraocular pressure” may need to be further precisely defined according to age, sex, metabolic disorders and geographic location.

The limitations of this study need to be acknowledged. First, IOP was measured using a non-contact tonometer, and the central corneal thickness was not taken into account in IOP measurements; however, the non-contact tonometers in our study have good quality control and are still widely used as a screening tool for glaucoma in China and other countries (30). Second, the participants of this study were mainly those selected for health screening, and thus do not represent the general population. However, the number of people undergoing health screening in China reached 575 million in 2018, accounting for 42% of its population in 2018. The results of this study may provide insights into this special population. Thirdly, the Figure 4 indicated there were some IOP variations in certain ethnic minority areas, such as Yunnan and Xinjing. However, there was no available information on race for individuals in this real-world data. The influence of race on the variation in IOP should be further studied.

In summary, the IOP varied with age, sex, metabolic disorders and geographic location. These RIs should be considered in the clinical process of glaucoma diagnosis and treatment.

Data availability statement

The raw data supporting the conclusions of this article will be made available by the authors, without undue reservation.

Ethics statement

The studies involving human participants were reviewed and approved by The Ethics Committee of Beijing Tsinghua Changgung Hospital, affiliated with Tsinghua University (Ethics number 18181-0-01). The patients/participants provided their written informed consent to participate in this study.

Author contributions

XL, XP, and YM wrote the main manuscript text, and prepared figures and tables. CJ, BW, and YN provided the data. All authors reviewed the manuscript.

Funding

This work was supported by the National Natural Science Foundation of China (91846303) and the Ministry of Science and Technology of China (2020YFC2003400).

Acknowledgments

We thank all study participants and appreciate the contributions made by all health professionals in Meinian health screening centers.

Conflict of interest

The authors declare that the research was conducted in the absence of any commercial or financial relationships that could be construed as a potential conflict of interest.

Publisher's note

Supplementary material

The Supplementary Material for this article can be found online at: https://www.frontiersin.org/articles/10.3389/fendo.2022.949827/full#supplementary-material

SUPPLEMENTARY TABLE 1
Sociodemographic and clinical characteristics of the general population‡ (N=739,928) by sex

SUPPLEMENTARY TABLE 2
Median and 95% reference interval of intraocular pressure of the general population‡ according to sex and age and further stratified by height, body mass index, blood pressure, altitude, geographic area

References

1. Jonas JB, Aung T, Bourne RR, Bron AM, Ritch R, Panda-Jonas S. Glaucoma. *Lancet* (2017) 390(10108):2183–93. doi: 10.1016/S0140-6736(17)31469-1

2. Tham Y-C, Li X, Wong TY, Quigley HA, Aung T, Cheng CY. Global prevalence of glaucoma and projections of glaucoma burden through 2040: a systematic review and meta-analysis. *Ophthalmology* (2014) 121(11):2081–90. doi: 10.1016/j.ophtha.2014.05.013

3. Singh K, Shrivastava A. Early aggressive intraocular pressure lowering, target intraocular pressure, and a novel concept for glaucoma care. *Surv Ophthalmol* (2008) 53(6):S33–8. doi: 10.1016/j.survophthal.2008.08.007

4. Zhao D, Kim MH, Pastor-Barriuso R, Chang Y, Ryu S, Zhang Y, et al. A longitudinal study of age-related changes in intraocular pressure: the kangbuk Samsung health study. *Invest Ophthalmol Visual Sci* (2014) 55(10):6244–50. doi: 10.1167/iovs.14-14151

5. Panchami SRP, Shenoy JP, Shivakumar J, Kole SB. Postmenopausal intraocular pressure changes in south Indian females. *J Clin Diagn Res: JCDR* (2013) 7(7):1322. doi: 10.7860/JCDR/2013/5325.3145

6. Han X, Zhao H, Wu C, Liu C, Yan W, Hu Y, et al. Ten-year changes of intraocular pressure in adults: the liwan eye study. *Clin Exp Ophthalmol* (2019) 47 (1):41–8. doi: 10.1111/ceo.13372

7. Chua J, Chee ML, Chin CWL, Tham YC, Tan N, Lim SH, et al. *Inter-relationship between ageing, body mass index, diabetes, systemic blood pressure* and intraocular pressure in asians: 6-year longitudinal study. *Br J Ophthalmol* (2019) 103(2):196–202. doi: 10.1136/bjophthalmol-2018-311897

8. Tielsch JM, Sommer A, Katz J, Royall RM, Quigley HA, Javitt J. Racial variations in the prevalence of primary open-angle glaucoma: the Baltimore eye survey. *Jama* (1991) 266(3):369–74. doi: 10.1001/jama.1991.03470030069026

9. Rudnicka AR, Mt-Isa S, Owen CG, Cook DG, Ashby D. Variations in primary open-angle glaucoma prevalence by age, gender, and race: a Bayesian meta-analysis. *Invest Ophthalmol Visual Sci* (2006) 47(10):4254–61. doi: 10.1167/iovs.06-0299

10. Hollows F, Graham P. Intra-ocular pressure, glaucoma, and glaucoma suspects in a defined population. *Br J Ophthalmol* (1966) 50(10):570. doi: 10.1136/bjo.50.10.570

11. Fukuoka S, Aihara M, Iwase A, Araie M . Intraocular pressure in an ophthalmologically normal Japanese population. *Acta Ophthalmol* (2008) 86 (4):434–9. doi: 10.1111/j.1600-0420.2007.01068.x

12. Bonomi L, Marchini G, Marraffa M, Bernardi P, Franco ID, Perfetti S, et al. Prevalence of glaucoma and intraocular pressure distribution in a defined population: The egna-neumarkt study. *Ophthalmology* (1998) 105(2):209–15. doi: 10.1016/s0161-6420(98)92665-3

13. Song W, Shan L, Cheng F, Fan P, Zhang LJ, Qu W, et al. Prevalence of glaucoma in a rural northern china adult population: a population-based survey in kailu county, inner mongolia. *Ophthalmology* (2011) 118(10):1982–8. doi: 10.1016/j.ophtha.2011.02.050

14. Wang YX, Xu L, Yang H, Jonas JB. Prevalence of glaucoma in north China: the Beijing eye study. *Am J Ophthalmol* (2010) 150(6):917–24. doi: 10.1016/j.ajo.2010.06.037

15. Yassin SA, Al-Tamimi ER. Age, gender and refractive error association with intraocular pressure in healthy Saudi participants: A cross-sectional study. *Saudi J Ophthalmol* (2016) 30(1):44–8. doi: 10.1016/j.sjopt.2015.11.007

16. Stevens LA, Claybon MA, Schmid CH, Chen J, Horio M, Imai E, et al. Evaluation of the chronic kidney disease epidemiology collaboration equation for estimating the glomerular filtration rate in multiple ethnicities. *Kidney Int* (2011) 79(5):555–62. doi: 10.1038/ki.2010.462

17. National Health Commission. *China Statistical yearbook 2018*. Beijing, China: Peking Union Medical College Press (2018).

18. Clinical and L.S. Institute. *Defining, establishing, and verifying reference intervals in the clinical laboratory; approved guideline, 3rd Edition*. Wayne, PA: CLSI (2008).

19. Tint NL, Alexander P, Tint KM, Vasileiadis GT, Yeung AM, Azuara-Blanco A. Hormone therapy and intraocular pressure in nonglaucomatous eyes. *Menopause* (2010) 17(1):157–60. doi: 10.1097/gme.0b013e3181b82fb4

20. Carel RS, Korczyn AD, Rock M, Goya I. Association between ocular pressure and certain health parameters. *Ophthalmology* (1984) 91(4):311–4. doi: 10.1016/S0161-6420(84)34282-8

21. Rochtchina E, Mitchell P, Wang JJ. Relationship between age and intraocular pressure: the blue mountains eye study. *Clin Exp Ophthalmol* (2002) 30(3):173–5. doi: 10.1046/j.1442-9071.2002.00519.x

22. Sommer A, Tielsch JM, Katz J, Quigley HA, Gottsch JD, Javitt J, et al. Relationship between intraocular pressure and primary open angle glaucoma among white and black americans: the Baltimore eye survey. *Arch Ophthalmol* (1991) 109(8):1090–5. doi: 10.1001/archopht.1991.01080080050026

23. Hashemi H, Kashi A, Fotouhi A, Mohammad K. Distribution of intraocular pressure in healthy Iranian individuals: the Tehran eye study. *Br J Ophthalmol* (2005) 89(6):652–7. doi: 10.1136/bjo.2004.058057

24. Lin H-Y, Hsu W-M, Chou P, Liu CJ, Chou JC, Tsai S-Y, et al. Intraocular pressure measured with a noncontact tonometer in an elderly Chinese population: the shihpai eye study. *Arch Ophthalmol* (2005) 123 (3):381–6. doi: 10.1001/archopht.123.3.381

25. Wang YX, Xu L, Zhang XH, You QS, Zhao L, Jonas JB. Five-year change in intraocular pressure associated with changes in arterial blood pressure and body mass index. *Beijing eye study PloS One* (2013) 8(10):e77180. doi: 10.1371/journal.pone.0077180

26. Wu S-Y, Nemesure B, Hennis A, Leske MCBarbados Eye Studies Group. Nine-year changes in intraocular pressure: the Barbados eye studies. *Arch Ophthalmol* (2006) 124(11):1631–6. doi: 10.1001/archopht.124.11.1631

27. Klein B, Klein R, Knudtson M. Intraocular pressure and systemic blood pressure: longitudinal perspective: the beaver dam eye study. *Br J Ophthalmol* (2005) 89(3):284–7. doi: 10.1136/bjo.2004.048710

28. Nakano T, Tatemichi M, Miura Y, Sugita M, Kitahara K. Long-term physiologic changes of intraocular pressure: a 10-year longitudinal analysis in young and middle-aged Japanese men. *Ophthalmology* (2005) 112(4):609–16. doi: 10.1016/j.ophtha.2004.10.046

29. Wang YX, Xu L, Wei WB, Jonas JB. Intraocular pressure and its normal range adjusted for ocular and systemic parameters. the Beijing eye study 2011. *PloS One* (2018) 13(5):e0196926. doi: 10.1371/journal.pone.0196926

30. Reznicek L, Muth D, Kampik A, Neubauer AS, Hirneiss C. Evaluation of a novel scheimpflug-based non-contact tonometer in healthy subjects and patients with ocular hypertension and glaucoma. *Br J Ophthalmol* (2013) 97(11):1410–4. doi: 10.1136/bjophthalmol-2013-303400

frontiers | Frontiers in Endocrinology

TYPE Original Research
PUBLISHED 14 September 2022
DOI 10.3389/fendo.2022.943275

OPEN ACCESS

EDITED BY
Stephen A. Whelan,
Cedars-Sinai, United States

REVIEWED BY
Yun Feng,
Peking University Third Hospital, China
Pir Salim Mahar,
Aga Khan University, Pakistan
Mohd Radzi Hilmi,
International Islamic University Malaysia, Malaysia

*CORRESPONDENCE
Lvzhen Huang
huanglvzhen@126.com
Zhengxuan Jiang
jiangzhengxuan@ahmu.edu.cn

†These authors share first authorship

SPECIALTY SECTION
This article was submitted to Molecular and Structural Endocrinology, a section of the journal Frontiers in Endocrinology

RECEIVED 13 May 2022
ACCEPTED 24 August 2022
PUBLISHED 14 September 2022

CITATION
Li J, Tao T, Yu Y, Xu N, Du W, Zhao M, Jiang Z and Huang L (2022) Expression profiling suggests the involvement of hormone-related, metabolic, and Wnt signaling pathways in pterygium progression. *Front. Endocrinol.* 13:943275. doi: 10.3389/fendo.2022.943275

Expression profiling suggests the involvement of hormone-related, metabolic, and Wnt signaling pathways in pterygium progression

Jiarui Li[1,2,3†], Tianchang Tao[1,2,3†], Yingying Yu[1,2,3], Ningda Xu[1,2,3], Wei Du[1,2,3], Mingwei Zhao[1,2,3], Zhengxuan Jiang[4*] and Lvzhen Huang[1,2,3*]

[1]Department of Ophthalmology, Peking University People's Hospital Eye diseases, and Optometry Institute, Beijing, China, [2]Beijing Key Laboratory of Diagnosis and Therapy of Retinal and Choroid Diseases, Peking University People's Hospital, Beijing, China, [3]College of Optometry, Peking University Health Science Center, Beijing, China, [4]Department of Ophthalmology, The Second Affiliated Hospital of Anhui Medical University, Hefei, China

Background: Pterygium is an ocular surface disease that can cause visual impairment if it progressively invades the cornea. Although many pieces of research showed ultraviolet radiation is a trigger of pterygium pathological progress, the underlying mechanism in pterygium remains indistinct.

Methods: In this study, we used microarray to evaluate the changes of transcripts between primary pterygium and adjacent normal conjunctiva samples in China. Then, we performed Gene Ontology (GO) and Kyoto Encyclopedia of Genes and Genomes (KEGG) functional enrichment analyses. Moreover, we constructed protein-protein interaction (PPI) and miRNA-mRNA regulatory networks to predict possible regulatory relationships. We next performed gene set enrichment analysis (GSEA) to explore the similarities and differences of transcripts between Asian studies from the Gene Expression Omnibus database. Furthermore, we took the intersection of differentially expressed genes (DEGs) with other data and identified hub genes of the development of pterygium. Finally, we utilized real-time quantitative PCR to verify the expression levels of candidate genes.

Results: A total of 49 DEGs were identified. The enrichment analyses of DEGs showed that pathways such as the Wnt-signaling pathway and metabolism-related pathways were upregulated, while pathways such as hormone-related and transcription factor-associated pathways were downregulated. The PPI and miRNA-mRNA regulatory networks provide ideas for future research directions. The GSEA of selecting Asian data revealed that epithelial-mesenchymal transition and myogenesis existed in the pathology of pterygium in the Asian group. Furthermore, five gene sets (interferon-gamma response, Wnt beta-catenin signaling, oxidative

phosphorylation, DNA repair, and MYC targets v2) were found only in our Chinese datasets. After taking an intersection between selecting datasets, we identified two upregulated (*SPP1* and *MYH11*) and five downregulated (*ATF3*, *FOS*, *EGR1*, *FOSB*, and *NR4A2*) hub genes. We finally chose night genes to verify their expression levels, including the other two genes (*SFRP2* and *SFRP4*) involved in Wnt signaling; Their expression levels were significantly different between pterygium and conjunctiva.

Conclusions: We consider hormone-related, metabolic, and Wnt signaling pathways may be important in the pathology of pterygium development. Nine candidate genes we identified deserve further study and can be potential therapeutic targets.

KEYWORDS

Pterygium, microarray, ocular surface disease, conjunctiva, hormone, metabolism

1 Introduction

Pterygium is a benign ocular surface disease that typically appears as a fibrovascular conjunctiva thickening from the nasal side and may progressively extend onto the cornea, causing visual impairment (1, 2). The incidence of pterygium was 1.4% in the Asian population and 2.1% in the Chinese (3). Ultraviolet (UV) radiation, male gender, older age, ethnicity, outdoor occupation, and air pollution were associated with the occurrence and development of pterygium (3–5). Pterygium excision with conjunctival autograft and adjuvant therapy is the conventional treatment (6). Using fibrin glue in place of sutures for attaching conjunctival autograft during the surgery could further reduce the recurrence rate (0-4.5%) and surgical duration and help recover the cornea (7–9). Although many efforts have made progress, more surgical and non-surgical approaches are needed to be explored to decrease the recurrence further.

Currently, the underlying mechanism in pterygium remains indistinct. UV radiation is a well-recognized major cause of pterygium, and many research studies believe it triggers oxidative stress leading to DNA damage and subsequently stimulates multiple pathogenic factors (such as tumor suppressor P53, growth factors, pro-inflammatory cytokines, and extracellular matrix modulation) to induce a hyperproliferative state (10–15). On the other hand, hereditary factors and viruses (e.g., human papillomavirus) are also reported to contribute to the disease, so pterygium is considered an outcome of a combination of genetic and environmental factors (1, 15). Moreover, pterygium is regarded as a limbal stem cell disorder with precancerous features (16). In short, despite many studies on pterygium, there are lots of unsolved puzzles that need to be unraveled.

Many studies have utilized transcriptome technologies to identify changes in transcripts of pterygium in recent years (17–23). They have greatly advanced the research on pterygium and identified several groups of abnormally expressed genes in pterygium, such as keratins (*KRT3*, *KRT4*, *KRT6B*, *KRT13*, *KRT14*, *KRT16*, and *KRT24*); S100 calcium-binding proteins (*S100A8*, *S100*A9, *S100A11*, and *S100P*); collagens (*COL1A1*, *COL8A1*, and *COL10A1*). Furthermore, other studies have reported the involvement of various matrix metalloproteinases in the progression of pterygium (*MMP1*, *MMP2*, *MMP3*, *MMP9*, and *MMP13*) (24–26). On the other hand, it has been reported that the Chinese have a higher incidence of the disease than the whole Asian population (3), so the transcriptomic information needs to be more abundant. Moreover, identifying the similarities and differences of transcripts between Asian studies is necessary to reveal the underlying mechanisms of pterygium.

In this study, we used microarray to evaluate the changes of transcripts between primary pterygium samples and adjacent normal conjunctiva samples in China and perform multiple bioinformatic analyses. Next, we took the intersection of differentially expressed genes with other data in Asian countries and identified hub genes. Finally, we verified the expression levels of candidate genes from microarray data. Our study hopes to provide more evidence of the progression of pterygium and find potential treatment targets.

2 Material and methods

2.1 Specimens preparation

This study approval was provided by the Ethics Committee of the second affiliated hospital of Anhui Medical University in accordance with the Helsinki Declaration of 1975. Sixteen nasal primary pterygium samples and fourteen adjacent normal conjunctiva samples were obtained from 16 participants (aged 47-70 years, five males and 11 females) through pterygium excision surgery. All the procedures were performed by an experienced ophthalmologist in the second affiliated hospital, Anhui Medical University. All of the participants in this study signed the informed consent before they were enrolled in the study. After pterygium excision, the whole part of the tissues was immediately placed in RNALater™ RNA Stabilization Reagent for Animal Tissue (Beyotime, China, R0118) and infiltrated overnight at four degrees, then all of the tissues were stored at a −80 °C refrigerator until RNA extraction.

2.2 RNA isolation

The total RNA of the tissues was isolated using TRIzol™ Reagent (Invitrogen, USA, 15596026) according to the manufacturer's protocol. For microarray analysis, two pairs of pterygium and adjacent normal conjunctiva samples were used. The other tissues were used in real-time quantitative polymerase chain reaction (qPCR). The quality control and quantification of RNA were performed by electrophoresis on 1% agarose gels and NanoDrop 2000 (Thermo Fisher Scientific, USA).

2.3 Microarray analysis

After the quality test of RNA, gene expression profiling was conducted by Shanghai Baygene Biotechnology Co.Ltd (Shanghai, China) using GeneChip® Human Transcriptome Array 2.0 (HTA 2.0). cDNA was synthesized, amplified, fragmented, and labeled for hybridization using the GeneChip® WT PLUS Reagent Kit (Affymetrix, USA, 902280) from 2 ugs isolated RNA following the manufacturer's protocols. Then, GeneChip® Expression Wash, Stain, and Scan were performed following protocol from GeneChip® Hybridization Wash and Stain Kit (Affymetrix, USA, 900720). Probe cell intensity data (CEL) from microarrays are analyzed and normalized by Signal Space Transformation Robust Multichip Analysis (SST-RMA) algorithm in the Affymetrix® Expression Console™ software (v1.4). The normalized data were then subjected to R package limma (v3.42.2) to identify differentially expressed genes (DEGs) (27). Genes with $|\log2FC| > 1$ and p-value < 0.05 were identified as DEGs. Volcano plot visualization was exerted by ggplot2 (v3.3.0). Next, the DEGs were submitted to execute the Gene Ontology (GO) and the Kyoto Encyclopedia of Genes and Genomes (KEGG) functional enrichment analyses utilizing the R package ClusterProfiler (v3.14.3) (28). For Protein-protein interaction (PPI) network construction, we used the STRING database (https://string-db.org/cgi/input.pl) to recognize the possible connections between DEGs, the data exported from the STRING database was visualized by Cytoscape (v3.8.2), and the MCODE (v2.0.0) plugin of Cytoscape was applied to identify a key module of PPI network (29).

2.4 Data collection

For further bioinformatic analyses, we collected miRNA and microarray data from PubMed and the Gene Expression Omnibus database (GEO, www.ncbi.nlm.nih.gov/geo) based on our selection criteria. As for miRNA selection, we used "Pterygium" and "miRNA" as keywords to search on Pubmed and screen research from Asia. Next, we included 14 miRNAs that were validated by qPCR or could be found in at least two microarray data. The information on miRNA enrolled in our study is listed in Table 1 (30–37). The selection of microarray datasets for this study was based on screening the GEO database, and datasets from Asia were selected. The details of these microarray datasets are shown in Table 2.

2.5 The miRNA-mRNA regulatory network construction

All enrolled miRNAs were submitted to ENCORI (the encyclopedia of RNA Interactomes, https://starbase.sysu.edu.cn/) to predict and acquire their targeted mRNAs (38). The ENCORI could also connect to seven other target mRNA-predicted programs (microT, miRanda, miRmap, PITA, RNA22, PicTar, and TargetScan); the mRNAs we selected were overlapped in at least four predicted programs. The miRNAs usually perform as negative regulators to affect the expression of the target mRNAs, upregulated miRNA led to downregulated target mRNA and vice versa. Considering such a regulatory pattern, we took the intersection of the acquired mRNAs with our microarray data based on the expression change direction. The visualization of the miRNA-mRNA regulatory network was carried out by TBtools (v1.0986988) (39).

2.6 Gene set enrichment analysis

The gene set enrichment analysis (GSEA) based on Hallmark gene sets in the molecular signatures database (v7.5.1) was performed by GSEA software (v4.2.3). The results

TABLE 1 The information on miRNA for further analysis.

miRNA	Change	p.value	Country	Verification	Source
hsa-miR-221	Up	<0.0001	China	qPCR	PMID:25053875 (30)
hsa-miR-21	Up	<0.01	China	qPCR	PMID:30967746 (31)
hsa-miR-143-3p	Up	<0.005	China	qPCR	PMID:29360447 (32)
hsa-miR-145-5p	Up	<0.05	China	qPCR	
hsa-miR-30a-5p	Up	0.043	China	qPCR	PMID:32867783 (33)
hsa-miR-143-5p	Up	0.001		qPCR	
hsa-miR-199-3p	Up	0.001		qPCR	
hsa-miR-199-5p	Up	0.002		qPCR	
hsa-miR-486-3p	Up	0.001		qPCR	
hsa-miR-215	Down	0.028	Singapore	qPCR	
hsa-miR-200a	Down	0.015	China	qPCR	PMID:26995143 (35)
hsa-miR-218-5p	Down	<0.01	China	qPCR	PMID:30243568 (36)
hsa-miR-122	Down	<0.05	China	qPCR	PMID:27415790 (37)
hsa-miR-1298-5p	Up	0.046	Singapore/China	–	From the intersection of GSE21346 and PMID:27415790

of GSEA were subjected to TBtools to visualize as a heat map, and data was clustered using Euclidean distances with complete hierarchical clustering.

2.7 Hub genes identification and enrichment analysis

To identify hub genes, we processed microarray datasets GSE83627, GSE51995, and GSE2513 by limma (v3.42.2). Besides, the microarray dataset GSE151872 only has one pterygium sample and is not applicable for limma's protocol, so we discarded this dataset to recognize hub genes. We took the intersection of DEGs from our microarray data and the above datasets, then submitted the results to the STRING database to perform further enrichment analysis. The visualizations were conducted by TBtools, Cytoscape, and ggplot2.

2.8 Real-time quantitative polymerase chain reaction

cDNA was synthesized from a total of 1 μg RNA with the ReverTra Ace® qPCR RT Master Mix with gDNA Remover (Toyobo Co., Ltd., Japan, Code No.FSQ-301). Real-time quantitative polymerase chain reactions (qPCR) were carried out using SYBR® Green Real-time PCR Master Mix (Toyobo Co., Ltd., Japan, Code No. QPK-201) with Roche LightCycler 480 (Roche Diagnostics Lid. Switzerland). Evaluating relative mRNA expression by using *GAPDH* as endogenous control *via*

TABLE 2 The descriptions of GEO datasets used to perform subsequent analyses.

Datasets ID	Country	Samples	Platforms	Microarray types	DEGs	
GSE83627	Singapore	4 Conjunctiva cases 4 Pterygium cases	GPL14550 SurePrint G3 Human GE 8x60K Microarray	mRNA	Up	523
					Down	0
GSE51995	Singapore	4 Conjunctiva cases 4 Pterygium cases	GPL14550 SurePrint G3 Human GE 8x60K Microarray	mRNA	Up	508
					Down	231
GSE2513	Singapore	4 Conjunctiva cases 8 Pterygium cases	GPL96 Affymetrix Human Genome U133A Array	mRNA	Up	114
					Down	73
GSE151872	Japan	1 Conjunctiva cases 3 Pterygium cases	GPL17077 Agilent-039494 SurePrint G3 Human GE v2 8x60K Microarray	mRNA	Up	–
					Down	–
GSE21346	Singapore	3 Conjunctiva cases 3 Pterygium cases	GPL7723 miRCURY LNA microRNA Array, v.11.0	microRNA	Up	4
					Down	1

GEO, Gene Expression Omnibus; DEGs, Differentially expressed genes.

the $2^{-\triangle CT}$ methods. The experiments were repeated using three technical replicates. Table 3 lists all primers.

2.9 Statistical analysis

Analyses were performed and visualized by GraphPad Prism 8.3.0. After failing to pass the Shapiro-Wilk normality test, then comparisons of data were made using the Mann–Whitney nonparametric test. A p-value of <0.05 was considered a significant difference.

3 Results

3.1 Results of microarray data analysis

3.1.1 The differential gene expression analysis

The differential gene expression analysis identified a total of 49 DEGs (|log2FC| >1 and p-value < 0.05) on primary pterygium samples vs. adjacent normal conjunctiva samples. Among them, 21 were upregulated, and 28 were downregulated; all the DEGs and details are listed in Supplementary Table 1. The volcano plot (shown in Figure 1A) of the microarray data indicated the distribution of the DEGs. The upregulated DEGs were shown in yellow and downregulated were shown in green.

3.1.2 KEGG and GO pathway enrichment analysis

To get more bioinformatic signatures of the pterygium, we next performed enrichment analyses of the DEGs. Figure 1B presented the results of the KEGG pathway enrichment analysis. The upregulated pathways were related to infection and metabolism, and the downregulated were associated with inflammation, hormone, and cell differentiation. As for GO analysis, a total number of 195 GO terms of upregulated DEGs and 237 GO terms of downregulated DEGs were enriched (Supplementary Table 2 listed all the GO terms), the top 30 of them in different classifications (cellular component, molecular function, and biological process) were shown in Figures 1C, D for the up- and downregulated GO terms respectively. Negative regulation of the Wnt-signaling pathway, peroxide and oxygen related, and metabolism-related pathways could be found in upregulated GO terms (Figure 1C). Additionally, hormone and skeletal muscle related and transcription factor associated pathways were enriched in downregulated GO terms (Figure 1D).

3.1.3 PPI network construction

For protein-coding genes of the DEGs, we next put them into the STRING for a PPI network (Figure 2A). There were 32 nodes and 188 interacted edges in the PPI network. Then, we used MCODE to identify a key module for the whole network (Figure 2B); this cluster scoring 8.444 had ten nodes and 76 edges and might play a role in the pterygium.

TABLE 3 Primers for real-time quantitative PCR.

Gene Symbol	EnsemblID		Sequence (5' -> 3')	Amplicon Size
SPP1	ENSG00000118785	Fp	TTCTGATTGGGACAGCCGTG	199bp
		Rp	TCTCATCATTGGCTTTCCGCT	
MYH11	ENSG00000133392	Fp	CGCCAAGAGACTCGTCTGG	129bp
		Rp	TCTTTCCCAACCGTGACCTTC	
ATF3	ENSG00000162772	Fp	CCTCTGCGCTGGAATCAGTC	111bp
		Rp	TTCTTTCTCGTCGCCTCTTTTT	
FOSB	ENSG00000125740	Fp	GCTGCAAGATCCCCTACGAAG	249bp
		Rp	ACGAAGAAGTGTACGAAGGGTT	
FOS	ENSG00000170345	Fp	GGGGCAAGGTGGAACAGTTAT	126bp
		Rp	CCGCTTGGAGTGTATCAGTCA	
NR4A2	ENSG00000153234	Fp	GCACTCCGGGTCGGTTTAC	129bp
		Rp	GCCACGTAGTTCTGGTGGAA	
EGR1	ENSG00000120738	Fp	GGTCAGTGGCCTAGTGAGC	149bp
		Rp	GTGCCGCTGAGTAAATGGGA	
SFRP2	ENSG00000145423	Fp	ATGCTTGAGTGCGACCGTTT	99bp
		Rp	TACCTTTGGAGCTTCCTCGG	
SFRP4	ENSG00000106483	Fp	ACGAGCTGCCTGTCTATGAC	99bp
		Rp	TGTCTGGTGTGATGTCTATCCAC	
GAPDH	ENSG00000111640	Fp	ACAACTTTGGTATCGTGGAAGG	101bp
		Rp	GCCATCACGCCACAGTTTC	

Fp, Forward primer; Rp, Reverse primer.

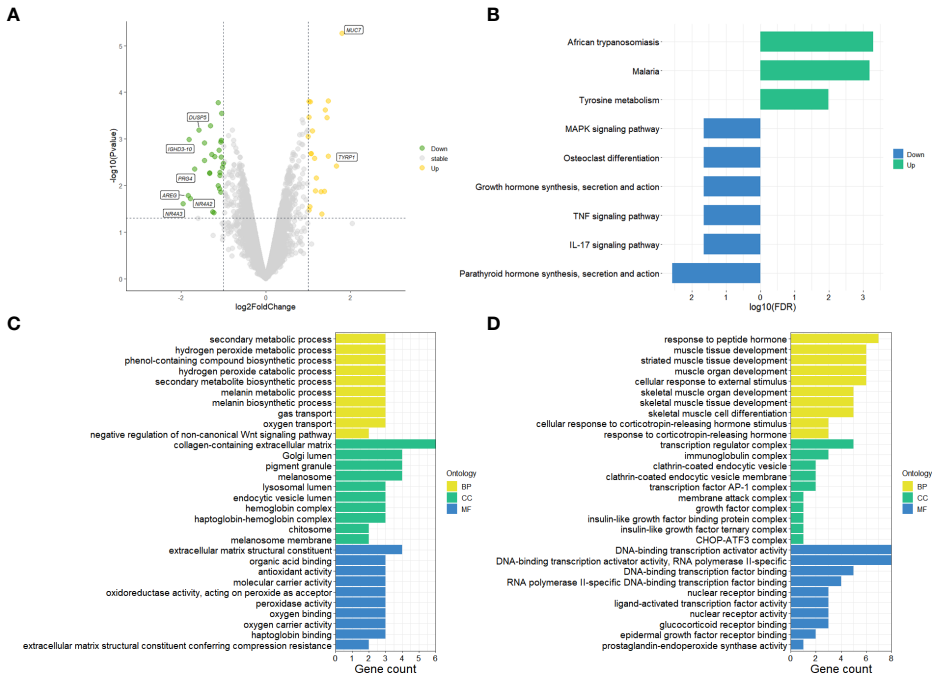

FIGURE 1
Results of microarray data analysis. **(A)** Volcano plot of microarray data, upregulated genes fill with yellow while downregulated genes fill with green. Grey dots mean genes are stable. The dotted horizontal lines indicate a p.value of 0.05, and the vertical lines indicate a log2FC of 1. Genes (|log2FC| > 1.5) labeled with their gene symbol are shown in the Figure. **(B)** KEGG analysis of DEGs of pterygium. The green color indicates upregulation, and blue indicates downregulation. **(C)** Top 30 upregulated GO terms for DEGs in different classifications. **(D)** Top 30 downregulated GO terms for DEGs in different classifications. The selection criteria of significant pathways or GO terms was FDR < 0.05. log2FC, log2foldchange; GO, Gene Ontology; KEGG, Kyoto Encyclopedia of Genes and Genomes (http://www.genome.jp/kegg/); FDR, false discovery rate. BP, biological process; CC, cellular component; MF, molecular function.

3.2 The miRNA-mRNA regulatory network construction

We searched on PubMed using the keywords "Pterygium" AND "miRNA" for all years, then selected the miRNAs in pterygium from Asian research based on the selection criteria. Table 1 summarizes the information on the selected miRNAs. Next, we put these miRNAs into ENCORI to predict the targeted mRNA and merged the results with our microarray data according to the screening criteria. Finally, a total of eight miRNAs and twelve mRNAs constructed 17 regulatory pairs. The miRNA-mRNA regulatory network was shown in Figure 3, and there existed a one-to-many regulatory relationship.

3.3 To compare the similarities and differences between Asian studies by gene set enrichment analysis

We found four datasets from Gene Expression Omnibus (GEO) in Asia (Singapore and Japan) to perform the following analysis (Table 2). We subjected the whole expression matrixes of our data and four datasets from GEO to GSEA software (v4.2.3), selecting Hallmark gene sets in the molecular signatures database (v7.5.1) to find similar and different biological processes of pterygium in Asia. As shown in Figure 4, only two gene sets were enriched in all datasets (epithelial-mesenchymal transition and myogenesis). Three gene sets were in the results of the other four datasets but not ours (inflammatory response, angiogenesis, and coagulation). Moreover, five gene sets were found only in our microarray data (interferon-gamma response, Wnt beta-catenin signaling, oxidative phosphorylation, DNA repair, and MYC targets v2). Furthermore, there were several gene sets in our data that were enriched in the other three data. Our microarray data was indicated as a separate clustering in cluster analysis based on Euclidean distance. The complete results of GSEA are demonstrated in Supplementary Table 3. The bigger the NES, the stronger the effect. NES > 0 meant upregulated while NES < 0 represented downregulated.

3.4 Identifying the hub genes by taking intersection with other microarray data

To identify the hub genes in the development of pterygium, we took an intersection between our data and other data from GEO datasets (Figures 5A, B). There were only two upregulated and five

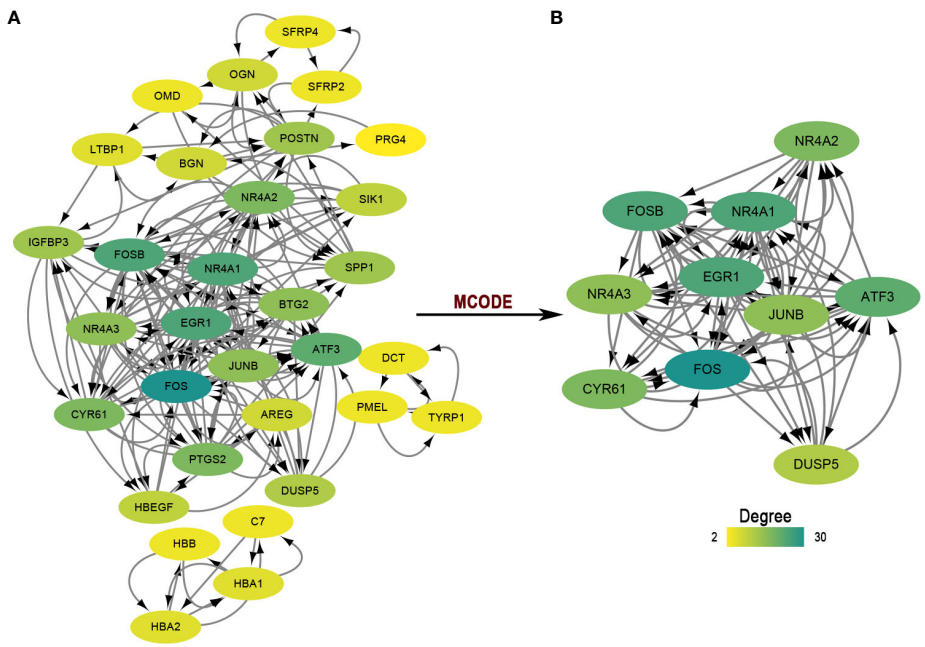

FIGURE 2
The PPI network and module analysis. **(A)** The entire PPI network of DEGs. Total of 32 nodes and 188 interacted edges in the PPI network. **(B)** A significant module of the PPI network. PPI, protein-protein interaction.

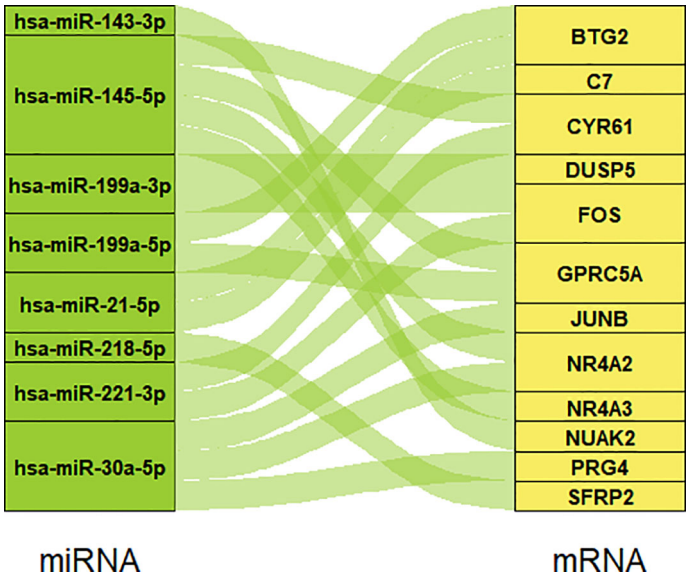

FIGURE 3
The miRNA-mRNA regulatory network. Eight miRNAs and 12 mRNAs construct 17 regulatory pairs.

downregulated genes at the intersection of four microarray datasets (Table 4). All of them were protein-coding genes. Strikingly, all five downregulated genes were in the key cluster that MCODE identified (Figure 2B), so we next put these hub genes into STRING again and performed network enrichment analysis. Two upregulated genes showed no interaction, while five downregulated genes displayed a strong connection (Figure 5C). Moreover, the network enrichment analysis (Figures 5D, E) of these five genes showed similarity with enrichment analysis of downregulated DEGs (e.g., Parathyroid hormone synthesis, secretion, and action; IL-17

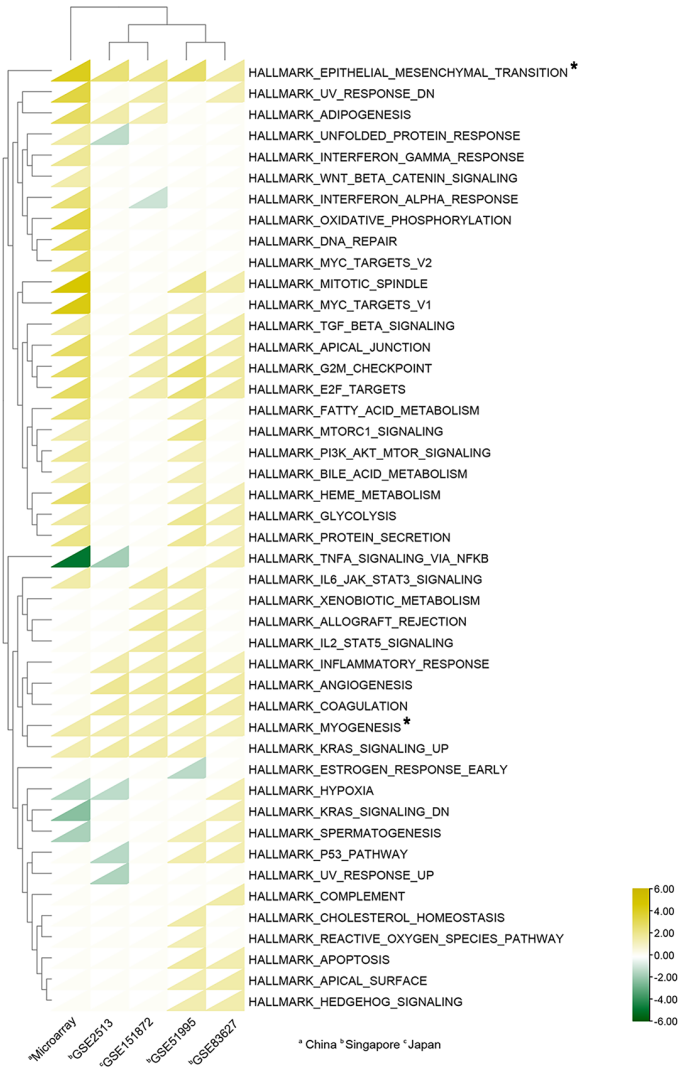

FIGURE 4
Heat map of Gene sets enriched in GSEA analysis. A total of 45 gene sets were enriched. The triangles in yellow indicate upregulated gene sets (NES > 0), while the triangles in green indicate downregulated gene sets (NES < 0); Triangles in white show no enrichment. Asterisks mean gene sets enriched in all datasets. The cluster analyses were based on Euclidean distance.

signaling pathway; Osteoclast differentiation). Some pathways associated with the organic and abiotic substance or stimulus resulted from network enrichment analysis but not from the whole DEGs'.

3.5 Validation of the mRNA expression levels of candidate genes by qPCR

Based on the previous analysis, we chose seven hub genes to verify their expression levels. We enrolled *SFRP2* and *SFRP4* in further analysis because they were DEGs involved in Wnt signaling. As illustrated in Figures 6A–I, the mRNA expression levels of candidate genes (*SFRP2*, *SFRP4*, *SPP1*, *ATF3*, *FOS*, *EGR1*, *FOSB*, *NR4A2*, and *MYH11)* were significantly different in primary pterygium samples compared to conjunctiva samples. Additionally, the correlation analysis of log2 foldchange between microarray and the qPCR quantitative data demonstrated a high correlation (R^2 = 0.8934, Figure 6J) which presented the accuracy of our microarray data.

4 Discussion

Pterygium is a common fibrovascular degeneration of conjunctiva, and ultraviolet radiation is the main cause. The best way of treating pterygium is to perform surgery with some adjuvant treatments (6, 40). Currently, the concrete mechanisms of onset and progression of pterygium still remain obscure.

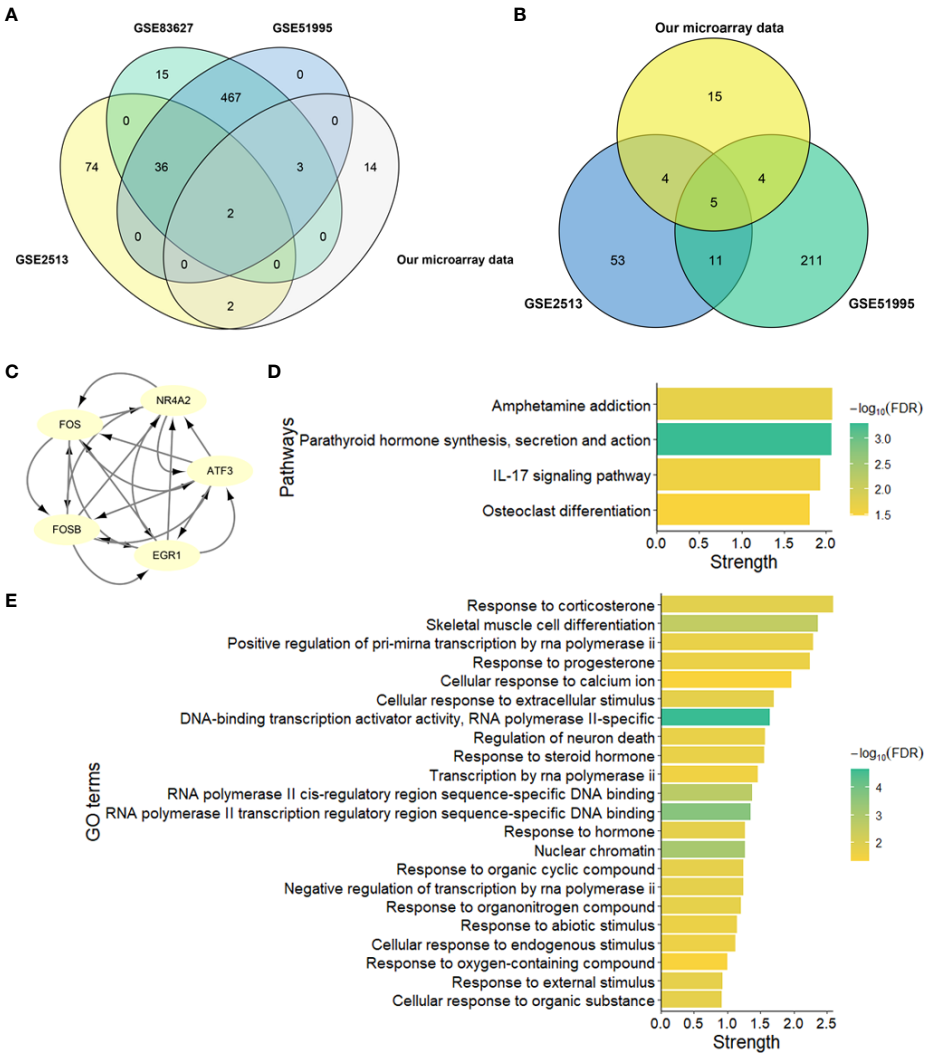

FIGURE 5
Identification and network enrichment analysis of hub genes. **(A)** Venn plot of upregulated genes of four microarray data. **(B)** Venn plot of downregulated genes of four microarray data. **(C)** PPI network of five downregulated hub genes. There are five nodes and ten edges. **(D)** KEGG pathway network enrichment analysis of five downregulated hub genes. **(E)** GO network enrichment analysis of five downregulated hub genes. Strength describes how significant the enrichment effect is.

TABLE 4 The gene cluster in the intersection of datasets.

Gene symbol	Description	Change
SPP1	secreted phosphoprotein 1	Up
MYH11	myosin heavy chain 11	Up
ATF3	activating transcription factor 3	Down
FOSB	FosB proto-oncogene, AP-1 transcription factor subunit	Down
FOS	Fos proto-oncogene, AP-1 transcription factor subunit	Down
NR4A2	nuclear receptor subfamily 4 group A member 2	Down
EGR1	early growth response 1	Down

10.3389/fendo.2022.943275

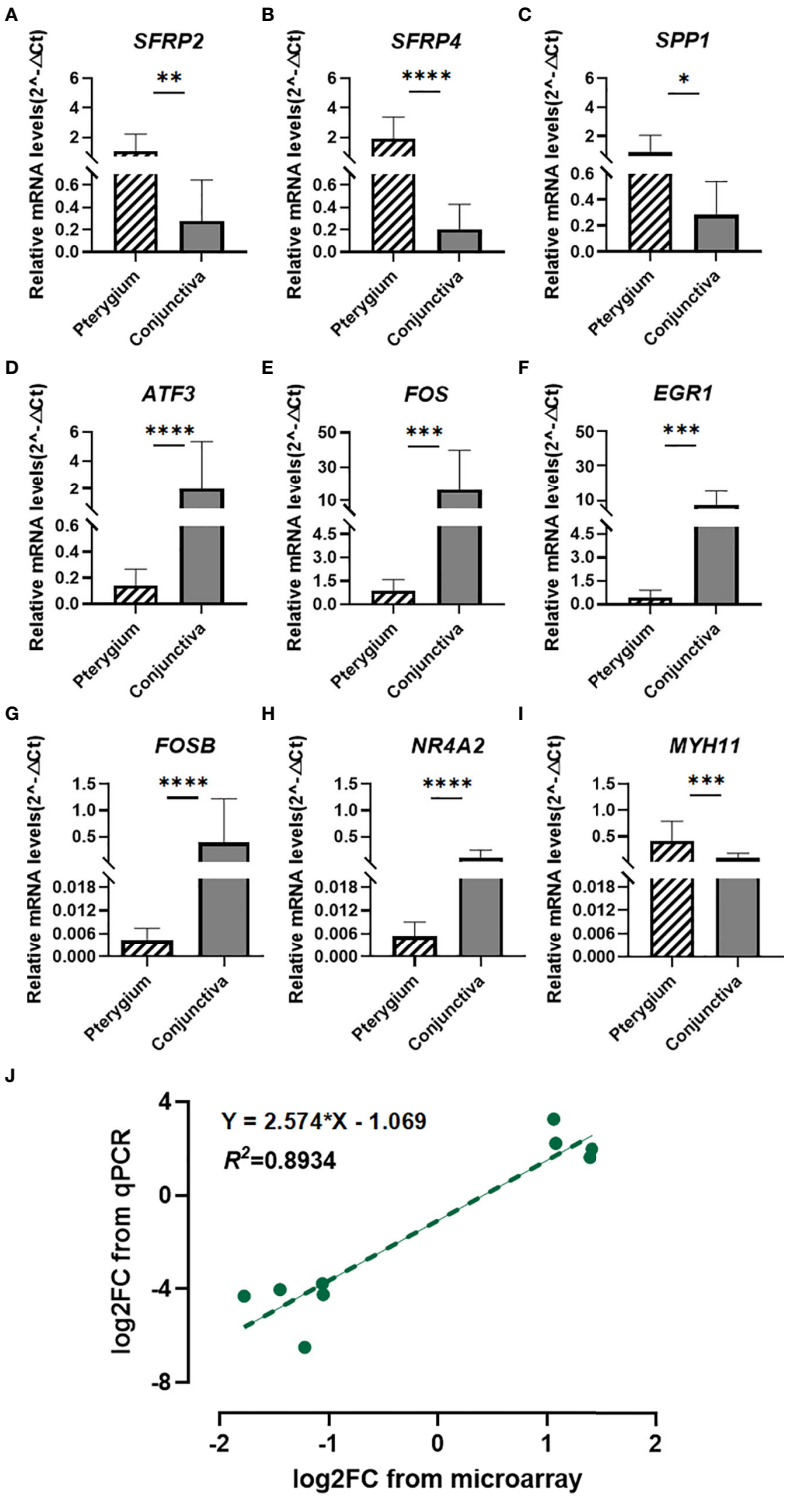

FIGURE 6
Quantitative real-time PCR verification and Correlation analysis. **(A–I)** Quantitative real-time PCR validation for *SFRP2, SFRP4, SPP1, ATF3, FOS, EGR1, FOSB, NR4A2,* and *MYH11*. n = 14 for primary pterygium samples and n = 12 for normal conjunctiva samples. *p < 0.05, **p < 0.01, ***p < 0.001, ****p < 0.0001. **(J)** Correlation analysis between microarray and qPCR data of candidate genes. Linear regression model (green dotted line): y = 2.574x - 1.069, R2 = 0.8934.

To explore the underlying mechanism of pterygium, we used microarray to compare changes in transcripts between primary pterygium samples and conjunctiva samples. 49 DEGs were identified in our study, and we next conducted multiple enrichment analyses to find the potential pathways of the disease. In the results, numbers of the metabolic and biosynthetic processes were upregulated (seven of the top ten GO BP terms), and these processes represent that the cells in pterygium were actively reacting to the compounds (e.g., hydrogen peroxide) involved in them. As part of reactive oxygen species, hydrogen peroxide is responsible for oxidative stress, while oxidative stress is considered a pathogenic mechanism of pterygium (12, 41). Additionally, metabolites from healthy and diseased cells can be directly released to tear, making the difference in tear proteome between pterygium and other diseases (42). The Wnt-signaling pathway, which can control stem cell biology and growth, is also upregulated; the changes in gene expression associated with Wnt-signaling in pterygium have been reported; however, how this pathway affects the development of pterygium needs to be studied in depth (43, 44). Downregulated pathways also provide us with pieces of evidence of disease progression. Hormone-related pathways are significantly downregulated; some research reported that hormone-related growth factors and receptors are implicated in pterygium (45, 46). Even though some hormones can affect corneal morphology, physiology, and metabolism, there is few of evidence indicating that hormones directly participate in the development of pterygium (47, 48). On the other hand, long-term UVA radiation to the eyes can affect the level of corticotropin-releasing hormone in the brain (49). So, we infer that the changes in hormone-related pathways are the response to UVA radiation. Furthermore, growth factors are also downregulated. Much evidence suggests that multiple growth factors are involved in pterygium, and their expression pattern may lead to a wide variation in the growth of pterygium (15). Other downregulated pathways (e.g., tumor necrosis factor (TNF) signaling, mitogen-activated protein kinase (MAPK) signaling, and transcription factor) have strong relationships with UV radiation or pterygium (50–52). The above results, to some extent, confirmed the reliability of our microarray data.

Nowadays, the PPI network and miRNA-mRNA regulatory network have been constructed in many studies (53–55). Since our new microarray data and new miRNA data from PubMed became available, we constructed new networks based on recent data. Our PPI network and miRNA-mRNA regulatory network hope to provide a new basis for further study of pterygium. Moreover, hsa-miR-199a-3p targets *DUSP5* in our network have been confirmed in pterygium (33).

Besides performing analyses of our microarray data, we also compare our data with other Asian datasets from GEO. The hallmark gene sets include 50 gene sets, while 45 gene sets were enriched through GSEA. As displayed in Figure 4, epithelial-mesenchymal transition (EMT) and myogenesis are found upregulated in all datasets. EMT, playing an essential role in wound healing and tissue remodeling, is a biological process that induces the transition of polarized and immotile epithelial cells into motile mesenchymal fibroblast-like cells (56). EMT and myogenesis in our results represent epithelial cells converted to myofibroblasts, serving as a key feature of pathological tissue repair and playing an essential role in pterygium progression (33, 57). As for the differences between our data and other Asian data, we found five significant pathways only upregulated in our results: interferon-gamma response, Wnt beta-catenin signaling, oxidative phosphorylation, DNA repair, and MYC targets v2. As outlined previously, oxidative phosphorylation and DNA repair are related to oxidative stress and DNA damage which are downstream of UV radiation. Interferon-gamma response belongs to immune responses which have been associated with pterygium (58). MYC, as a proto-oncogene is also involved in the disease (59). The result of Wnt beta-catenin signaling is consistent with our previous GO analysis. On the other hand, three pathways (inflammatory response, angiogenesis, and coagulation) correlating with pterygium are not present in our data but exist in the other four datasets (15). Interestingly, three datasets show upregulation of the pathways named UV response downregulated. This result probably shows that the response to UV radiation is different between pterygium cells and healthy cells, while pterygium epithelium possibly has resistance to UV-induced apoptosis (14). In conclusion, the results of GSEA have offered a shred of potential evidence for the cause of differences in pterygium incidence in Asia. The pathways that are unique and absent in our datasets should be worth attention.

To further investigate the common mechanism of pathogenesis in pterygium, we took the intersection between our data and other GEO datasets we selected. A total of seven genes were identified as hub genes. The two upregulated genes show no interactions, and the network enrichment analysis shows no results. We later subjected them to ClusterProfiler, and the results were similar to previous GO terms that they involved (data not shown). *SPP1* encodes osteopontin playing important roles in wound healing. Osteopontin is suggested to affect metalloproteinase (MMP) secretion and influence fibroblast proliferation dependent on the growth factors (60). This process is highly concordant with mechanisms that are reported in the progression of pterygium (25). *MYH11* encoding myosin heavy chain 11 has been confirmed its involvement in several types of cancer and is probably related to metabolism-related genes (61). Five downregulated hub genes are included in the key module that MCODE identified and have interactions with each other, which means they are in the important section of disease development. These five hub genes are transcription factors. Network enrichment analysis shows they are also significantly associated with hormone-related pathways. Among them, *FOS* and *FOSB*, as members of the AP-1 transcription factor complex, were upregulated in corneal epithelial cell layers when under UV exposure for one to six hours (62). Furthermore, the c-fos mRNA level is intermediate-early induced by UV radiation in cultured pterygium epithelial cells but downregulated after 12h (52). Additionally, after applying oxidative stress to human retinal pigment epithelium, the changes of expression of *ATF3* (another member of AP-1 transcription

factors), *FOS*, and *FOSB* are in a dose-dependent manner (63). Moreover, overexpression of *SPP1* in cells can downregulate the level of c-fos, and *SPP1* plays a role in wound healing (64). So, since AP-1 transcription factors are downregulated in this study, we infer that their levels depend on the balance of effects of UV exposure and wound healing. *EGR1* encodes early growth response, critically participating in neovascularization, tumor angiogenesis, and growth, together with *ATF3, which* can influence the limbal epithelial cell proliferation (65, 66). *NR4A2* is also associated with tumor proliferation, migration, and invasion (67). In summary, we speculate these hub genes are associated with pterygium proliferation and may response for resistance to UV exposure, these effects may be involved in inactivation of hormone-related pathways.

Finally, we verified the mRNA levels of nine candidate genes through qPCR. Correlation analysis shows the qPCR data are consistent with microarray data, suggesting the credibility of our results. Besides seven hub genes, we also validated two upregulated gene expressions (*SFRP2* and *SFRP4*). They are served as classical antagonists of Wnt signaling and can interact with Wnt protein directly through both autocrine and paracrine modes. In some cases, they also can promote Wnt signaling (68). Wnt signaling can control adult stem cell biology and growth (69); meanwhile, pterygium is thought to be a limbal stem cell disorder (16). The results of these two genes remind us that genes located upstream of the Wnt signaling pathway are involved in the progression of pterygium and probably can be used as therapeutic targets. Additionally, the Wnt beta-catenin signaling is the unique gene set in the results of GSEA in our data, so further in-depth studies are required, especially for the Chinese. Three hub genes (*FOS*, *NR4A2*, and *SFRP2*) are also in our miRNA-mRNA network; the predicted regulatory relationships are worthy of future research.

There were some deficiencies in our study. 1) Our sample size was insufficient and may cause a potential bias. 2) The validations of protein levels of our candidate genes were not conducted. The following study is currently ongoing to remedy the shortcomings of this study.

In conclusion, we consider hormone-related, metabolic, and Wnt signaling pathways may be important in developing pterygium besides its classical mechanisms. Nine candidate genes we identified deserve further study and can be potential therapeutic targets. In short, our findings shed important light on the further study of pterygium.

Data availability statement

The data presented in the study are deposited in the GEO repository, accession number GSE208384.

Ethics statement

The studies involving human participants were reviewed and approved by The Ethics Committee of The Second Affiliated Hospital of Anhui Medical University. The patients/participants provided their written informed consent to participate in this study.

Author contributions

JL and TT wrote this manuscript and performed bioinformatic analyses. YY, NX, and WD conducted data collection and experiment process. ZJ carried out a surgical procedure. MZ and LH provided the idea for this study, and LH revised this manuscript. JL and TT have contributed equally to this work. All authors contributed to the article and approved the submitted version.

Funding

This work was supported by the Beijing-Tianjin-Hebei Special Project (Grant Number J200014), the Science and technology innovation project of the Chinese Academy of medical sciences (2019-RC-HL-019), the National Natural Science Foundation of China (Grant Number 81670870). National Key R&D Program of China (Grant No. 2020YFC2008200). The funders had no role in the study design, data collection, analysis, decision to publish, or manuscript preparation.

Acknowledgments

We are grateful to all the participants and their families for their generosity and support.

Conflict of interest

The authors declare that the research was conducted in the absence of any commercial or financial relationships that could be construed as a potential conflict of interest.

Publisher's note

Supplementary material

The Supplementary Material for this article can be found online at: https://www.frontiersin.org/articles/10.3389/fendo.2022.943275/full#supplementary-material

References

1. Liu T, Liu Y, Xie L, He X, Bai J. Progress in the pathogenesis of pterygium. *Curr Eye Res* (2013) 38(12):1191–7. doi: 10.3109/02713683.2013.823212

2. Van Acker SI, Van den Bogerd B, Haagdorens M, Siozopoulou V, Ni Dhubhghaill S, Pintelon I, et al. Pterygium-the good, the bad, and the ugly. *Cells* (2021) 10(7):1567. doi: 10.3390/cells10071567

3. Fang XL, Chong CCY, Thakur S, Da Soh Z, Teo ZL, Majithia S, et al. Ethnic differences in the incidence of pterygium in a multi-ethnic Asian population: The Singapore epidemiology of eye diseases study. *Sci Rep* (2021) 11(1):501. doi: 10.1038/s41598-020-79920-9

4. Moran DJ, Hollows FC. Pterygium and ultraviolet radiation: A positive correlation. *Br J Ophthalmol* (1984) 68(5):343–6. doi: 10.1136/bjo.68.5.343

5. Fu Q, Mo Z, Gu Y, Lu B, Hao S, Lyu D, et al. Association between outpatient visits for pterygium and air pollution in hangzhou, China. *Environ pollut* (2021) 291:118246. doi: 10.1016/j.envpol.2021.118246

6. Fonseca EC, Rocha EM, Arruda GV. Comparison among adjuvant treatments for primary pterygium: A network meta-analysis. *Br J Ophthalmol* (2018) 102(6):748–56. doi: 10.1136/bjophthalmol-2017-310288

7. Ghiasian L, Samavat B, Hadi Y, Arbab M, Abolfathzadeh N. Recurrent pterygium: A review. *J Curr Ophthalmol* (2021) 33(4):367–78. doi: 10.4103/joco.joco_153_20

8. Lan A, Xiao F, Wang Y, Luo Z, Cao Q. Efficacy of fibrin glue versus sutures for attaching conjunctival autografts in pterygium surgery: A systematic review with meta-analysis and trial sequential analysis of evidence. *Oncotarget* (2017) 8(25):41487–97. doi: 10.18632/oncotarget.17195

9. Hilmi MR, Kamal K, Azemin M. Pterygium recurrence and corneal stabilization point after pterygium excision using the controlled partial avulsion fibrin glue technique. *Makara J Health Res* (2020) 24:140–6. doi: 10.7454/msk.v24i2.1195

10. Yajima H, Lee KJ, Zhang S, Kobayashi J, Chen BP. DNA Double-strand break formation upon uv-induced replication stress activates atm and DNA-pkcs kinases. *J Mol Biol* (2009) 385(3):800–10. doi: 10.1016/j.jmb.2008.11.036

11. Zhou WP, Zhu YF, Zhang B, Qiu WY, Yao YF. The role of ultraviolet radiation in the pathogenesis of pterygia (Review). *Mol Med Rep* (2016) 14(1):3–15. doi: 10.3892/mmr.2016.5223

12. Kormanovski A, Parra F, Jarillo-Luna A, Lara-Padilla E, Pacheco-Yepez J, Campos-Rodriguez R. Oxidant/Antioxidant state in tissue of prymary and recurrent pterygium. *BMC Ophthalmol* (2014) 14:149. doi: 10.1186/1471-2415-14-149

13. Han SJ, Min HJ, Yoon SC, Ko EA, Park SJ, Yoon JH, et al. Hmgb1 in the pathogenesis of ultraviolet-induced ocular surface inflammation. *Cell Death Dis* (2015) 6:e1863. doi: 10.1038/cddis.2015.199

14. Di Girolamo N, Chui J, Coroneo MT, Wakefield D. Pathogenesis of pterygia: Role of cytokines, growth factors, and matrix metalloproteinases. *Prog Retin Eye Res* (2004) 23(2):195–228. doi: 10.1016/j.preteyeres.2004.02.002

15. Bradley JC, Yang W, Bradley RH, Reid TW, Schwab IR. The science of pterygia. *Br J Ophthalmol* (2010) 94(7):815–20. doi: 10.1136/bjo.2008.151852

16. Chui J, Coroneo MT, Tat LT, Crouch R, Wakefield D, Di Girolamo N. Ophthalmic pterygium: A stem cell disorder with premalignant features. *Am J Pathol* (2011) 178(2):817–27. doi: 10.1016/j.ajpath.2010.10.037

17. Shibata N, Ishida H, Kiyokawa E, Singh DP, Sasaki H, Kubo E. Relative gene expression analysis of human pterygium tissues and uv radiation-evoked gene expression patterns in corneal and conjunctival cells. *Exp Eye Res* (2020) 199:108194. doi: 10.1016/j.exer.2020.108194

18. Jaworski CJ, Aryankalayil-John M, Campos MM, Fariss RN, Rowsey J, Agarwalla N, et al. Expression analysis of human pterygium shows a predominance of conjunctival and limbal markers and genes associated with cell migration. *Mol Vis* (2009) 15:2421–34.

19. Hou AH, Lan WW, Law KP, Khoo SCJ, Tin MQ, Lim YP, et al. Evaluation of global differential gene and protein expression in primary pterygium: S100a8 and S100a9 as possible drivers of a signaling network. *PloS One* (2014) 9(5):e97402. doi: 10.1371/journal.pone.0097402

20. Wolf J, Hajdu RI, Boneva S, Schlecht A, Lapp T, Wacker K, et al. Characterization of the cellular microenvironment and novel specific biomarkers in pterygia using rna sequencing. *Front Med-Lausanne* (2021) 8:714458. doi: 10.3389/fmed.2021.714458

21. de Guimaraes JA, Hounpke BW, Duarte B, Boso ALM, Viturino MGM, de Carvalho Baptista L, et al. Transcriptomics and network analysis highlight potential pathways in the pathogenesis of pterygium. *Sci Rep* (2022) 12(1):286. doi: 10.1038/s41598-021-04248-x

22. Liu J, Ding X, Yuan L, Zhang X. Identification of pterygium-related mrna expression profiling by microarray analysis. *Eye (Lond)* (2017) 31(12):1733–9. doi: 10.1038/eye.2017.116

23. Chen Y, Wang H, Jiang Y, Zhang X, Wang Q. Transcriptional profiling to identify the key genes and pathways of pterygium. *PeerJ* (2020) 8:e9056. doi: 10.7717/peerj.9056

24. Kim YH, Jung JC, Jung SY, Kim YI, Lee KW, Park YJ. Cyclosporine a downregulates mmp-3 and mmp-13 expression in cultured pterygium fibroblasts. *Cornea* (2015) 34(9):1137–43. doi: 10.1097/Ico.0000000000000477

25. Yang SF, Lin CY, Yang PY, Chao SC, Ye YZ, Hu DN. Increased expression of gelatinase (Mmp-2 and mmp-9) in pterygia and pterygium fibroblasts with disease progression and activation of protein kinase c. *Invest Ophth Vis Sci* (2009) 50(10):4588–96. doi: 10.1167/iovs.08-3147

26. Li DQ, Lee SB, Gunja-Smith Z, Liu YQ, Solomon A, Meller D, et al. Overexpression of collagenase (Mmp-1) and stromelysin (Mmp-3) by pterygium head fibroblasts. *Arch Ophthalmol-Chic* (2001) 119(1):71–80.

27. Ritchie ME, Phipson B, Wu D, Hu Y, Law CW, Shi W, et al. Limma powers differential expression analyses for rna-sequencing and microarray studies. *Nucleic Acids Res* (2015) 43(7):e47. doi: 10.1093/nar/gkv007

28. Yu G, Wang LG, Han Y, He QY. Clusterprofiler: An r package for comparing biological themes among gene clusters. *OMICS* (2012) 16(5):284–7. doi: 10.1089/omi.2011.0118

29. Shannon P, Markiel A, Ozier O, Baliga NS, Wang JT, Ramage D, et al. Cytoscape: A software environment for integrated models of biomolecular interaction networks. *Genome Res* (2003) 13(11):2498–504. doi: 10.1101/gr.1239303

30. Wu CW, Cheng YW, Hsu NY, Yeh KT, Tsai YY, Chiang CC, et al. Mirna-221 negatively regulated downstream P27kip1 gene expression involvement in pterygium pathogenesis. *Mol Vis* (2014) 20:1048–56.

31. Li X, Dai Y, Xu J. Mir-21 promotes pterygium cell proliferation through the Pten/Akt pathway. *Mol Vis* (2018) 24:485–94.

32. Teng Y, Yam GH, Li N, Wu S, Ghosh A, Wang N, et al. Microrna regulation of Mdm2-P53 loop in pterygium. *Exp Eye Res* (2018) 169:149–56. doi: 10.1016/j.exer.2018.01.015

33. He S, Huang Y, Dong S, Qiao C, Yang G, Zhang S, et al. Mir-199a-3p/5p participated in tgf-beta and egf induced emt by targeting Dusp5/Map3k11 in pterygium. *J Transl Med* (2020) 18(1):332. doi: 10.1186/s12967-020-02499-2

34. Lan W, Chen S, Tong L. Microrna-215 regulates fibroblast function: Insights from a human fibrotic disease. *Cell Cycle* (2015) 14(12):1973–84. doi: 10.1080/15384101.2014.998077

35. Wu CW, Peng ML, Yeh KT, Tsai YY, Chiang CC, Cheng YW. Inactivation of P53 in pterygium influence mir-200a expression resulting in Zeb1/Zeb2 up-regulation and emt processing. *Exp Eye Res* (2016) 146:206–11. doi: 10.1016/j.exer.2016.03.012

36. Han S, Chen Y, Gao Y, Sun B, Kong Y. Microrna-218-5p inhibit the migration and proliferation of pterygium epithelial cells by targeting egfr *Via* Pi3k/Akt/Mtor signaling pathway. *Exp Eye Res* (2019) 178:37–45. doi: 10.1016/j.exer.2018.09.010

37. Cui YH, Li HY, Gao ZX, Liang N, Ma SS, Meng FJ, et al. Regulation of apoptosis by mir-122 in pterygium *Via* targeting bcl-W. *Invest Ophthalmol Vis Sci* (2016) 57(8):3723–30. doi: 10.1167/iovs.16-19402

38. Li JH, Liu S, Zhou H, Qu LH, Yang JH. Starbase V2.0: Decoding mirna-cerna, mirna-ncrna and protein-rna interaction networks from Large-scale clip-seq data. *Nucleic Acids Res* (2014) 42:D92–7. doi: 10.1093/nar/gkt1248

39. Chen C, Chen H, Zhang Y, Thomas HR, Frank MH, He Y, et al. Tbtools: An integrative toolkit developed for interactive analyses of big biological data. *Mol Plant* (2020) 13(8):1194–202. doi: 10.1016/j.molp.2020.06.009

40. Chu WK, Choi HL, Bhat AK, Jhanji V. Pterygium: New insights. *Eye (Lond)* (2020) 34(6):1047–50. doi: 10.1038/s41433-020-0786-3

41. Ahmad A, Ahsan H. Biomarkers of inflammation and oxidative stress in ophthalmic disorders. *J Immunoassay Immunochem* (2020) 41(3):257–71. doi: 10.1080/15321819.2020.1726774

42. de Almeida Borges D, Alborghetti MR, Franco Paes Leme A, Ramos Domingues R, Duarte B, Veiga M, et al. Tear proteomic profile in three distinct ocular surface diseases: Keratoconus, pterygium, and dry eye related to graft-Versus-Host disease. *Clin Proteomics* (2020) 17(1):42. doi: 10.1186/s12014-020-09307-5

43. Li J, Li C, Wang G, Liu Z, Chen P, Yang Q, et al. Apr-246/Prima-1met inhibits and reverses squamous metaplasia in human conjunctival epithelium. *Invest Ophthalmol Vis Sci* (2016) 57(2):444–52. doi: 10.1167/iovs.15-17519

44. Zhu CP, Pan FY, Ge LP, Zhou J, Chen LLL, Zhou T, et al. Serpina3k plays antioxidant roles in cultured pterygial epithelial cells through regulating ros system. *PloS One* (2014) 9(10):e108859. doi: 10.1371/journal.pone.0108859

45. Solomon A, Grueterich M, Li DQ, Meller D, Lee SB, Tseng SC. Overexpression of insulin-like growth factor-binding protein-2 in pterygium body fibroblasts. *Invest Ophthalmol Vis Sci* (2003) 44(2):573–80. doi: 10.1167/iovs.01-1185

46. Qin YJ, Chu WK, Huang L, Ng CHY, Chan TCY, Cao D, et al. Induction of apoptosis in pterygium cells by antagonists of growth hormone-releasing hormone receptors. *Invest Ophthalmol Vis Sci* (2018) 59(12):5060–6. doi: 10.1167/iovs.18-24751

47. Baser H, Cuhaci N, Topaloglu O, Yulek F, Ugurlu N, Ersoy R, et al. Is there any association between primary hyperparathyroidism and ocular changes, such as central corneal thickness, retinal thickness, and intraocular pressure? *Endocrine* (2016) 51(3):545–50. doi: 10.1007/s12020-015-0724-5

48. Stuard WL, Titone R, Robertson DM. The Igf/Insulin-igfbp axis in corneal development, wound healing, and disease. *Front Endocrinol (Lausanne)* (2020) 11:24. doi: 10.3389/fendo.2020.00024

49. Hiramoto K, Yamate Y. Long-term uva exposure to the eye compromises memory and learning ability in mice *Via* corticotropin-releasing hormone type 2 receptor. *Int J Biol Sci* (2020) 16(12):2170–9. doi: 10.7150/ijbs.45967

50. Kuo CH, Miyazaki D, Yakura K, Araki-Sasaki K, Inoue Y. Role of periostin and interleukin-4 in recurrence of pterygia. *Invest Ophthalmol Vis Sci* (2010) 51 (1):139–43. doi: 10.1167/iovs.09-4022

51. Siak JJ, Ng SL, Seet LF, Beuerman RW, Tong L. The nuclear-factor kappab pathway is activated in pterygium. *Invest Ophthalmol Vis Sci* (2011) 52(1):230–6. doi: 10.1167/iovs.10-5735

52. Di Girolamo N, Coroneo M, Wakefield D. Epidermal growth factor receptor signaling is partially responsible for the increased matrix metalloproteinase-1 expression in ocular epithelial cells after uvb radiation. *Am J Pathol* (2005) 167 (2):489–503. doi: 10.1016/s0002-9440(10)62992-6

53. He S, Sun H, Huang Y, Dong S, Qiao C, Zhang S, et al. Identification and interaction analysis of significant genes and microrna in pterygium. *BioMed Res Int* (2019) 2019:2767512. doi: 10.1155/2019/2767512

54. Xu Y, Qiao C, He S, Lu C, Dong S, Wu X, et al. Identification of functional genes in pterygium based on bioinformatics analysis. *BioMed Res Int* (2020) 2020:2383516. doi: 10.1155/2020/2383516

55. Xu N, Cui Y, Dong J, Huang L. Exploring the molecular mechanisms of pterygium by constructing lncrna-Mirna-Mrna regulatory network. *Invest Ophthalmol Vis Sci* (2020) 61(8):12. doi: 10.1167/iovs.61.8.12

56. Yang J, Weinberg RA. Epithelial-mesenchymal transition: At the crossroads of development and tumor metastasis. *Dev Cell* (2008) 14(6):818–29. doi: 10.1016/j.devcel.2008.05.009

57. Shu DY, Lovicu FJ. Myofibroblast transdifferentiation: The dark force in ocular wound healing and fibrosis. *Prog Retin Eye Res* (2017) 60:44–65. doi: 10.1016/j.preteyeres.2017.08.001

58. Liu L, Yang D. Immunological studies on the pathogenesis of pterygium. *Chin Med Sci J* (1993) 8(2):84–8.

59. Cui D, Pan Z, Zhang S, Zheng J, Huang Q, Wu K. Downregulation of c-myc in pterygium and cultured pterygial cells. *Clin Exp Ophthalmol* (2011) 39(8):784–92. doi: 10.1111/j.1442-9071.2011.02531.x

60. Icer MA, Gezmen-Karadag M. The multiple functions and mechanisms of osteopontin. *Clin Biochem* (2018) 59:17–24. doi: 10.1016/j.clinbiochem.2018.07.003

61. Wang J, Xu P, Hao Y, Yu T, Liu L, Song Y, et al. Interaction between Dnmt3b and Myh11 *Via* hypermethylation regulates gastric cancer progression. *BMC Cancer* (2021) 21(1):914. doi: 10.1186/s12885-021-08653-3

62. Gillardon F, Zimmermann M, Uhlmann E. Expression of c-fos and c-jun in the cornea, lens, and retina after ultraviolet irradiation of the rat eye and effects of topical antisense oligodeoxynucleotides. *Br J Ophthalmol* (1995) 79(3):277–81. doi: 10.1136/bjo.79.3.277

63. Chaum E, Yin J, Yang H, Thomas F, Lang JC. Quantitative ap-1 gene regulation by oxidative stress in the human retinal pigment epithelium. *J Cell Biochem* (2009) 108(6):1280–91. doi: 10.1002/jcb.22358

64. Liu X, Sun Y, Li H, Li Y, Li M, Yuan Y, et al. Effect of Spp1 on nerve degeneration and regeneration after rat sciatic nerve injury. *BMC Neurosci* (2017) 18(1):30. doi: 10.1186/s12868-017-0348-1

65. Hsueh YJ, Kuo PC, Chen JK. Transcriptional regulators of the Deltanp63: Their role in limbal epithelial cell proliferation. *J Cell Physiol* (2013) 228(3):536–46. doi: 10.1002/jcp.24160

66. Fahmy RG, Dass CR, Sun LQ, Chesterman CN, Khachigian LM. Transcription factor egr-1 supports fgf-dependent angiogenesis during neovascularization and tumor growth. *Nat Med* (2003) 9(8):1026–32. doi: 10.1038/nm905

67. Jing CY, Fu YP, Zhou C, Zhang MX, Yi Y, Huang JL, et al. Hepatic stellate cells promote intrahepatic cholangiocarcinoma progression *Via* Nr4a2/Osteopontin/Wnt signaling axis. *Oncogene* (2021) 40(16):2910–22. doi: 10.1038/s41388-021-01705-9

68. Pawar NM, Rao P. Secreted frizzled related protein 4 (Sfrp4) update: A brief review. *Cell Signal* (2018) 45:63–70. doi: 10.1016/j.cellsig.2018.01.019

69. Nusse R, Clevers H. Wnt/Beta-catenin signaling, disease, and emerging therapeutic modalities. *Cell* (2017) 169(6):985–99. doi: 10.1016/j.cell.2017.05.016

frontiers | Frontiers in Endocrinology

TYPE Original Research
PUBLISHED 15 September 2022
DOI 10.3389/fendo.2022.973962

OPEN ACCESS

EDITED BY
Lvzhen Huang,
Department of Ophthalmology, Peking University People's Hospital, China

REVIEWED BY
Omer Iqbal,
Loyola University Chicago, United States
Xiuming Jin,
Zhejiang University, China
Yifei Huang,
First Affiliated Hospital of Chinese PLA General Hospital, China
Guigang Li,
Huazhong University of Science and Technology, China

*CORRESPONDENCE
Jing Hong
hongjing196401@163.com
Yun Feng
fengyun@bjmu.edu.cn

SPECIALTY SECTION
This article was submitted to Molecular and Structural Endocrinology, a section of the journal Frontiers in Endocrinology

RECEIVED 20 June 2022
ACCEPTED 29 August 2022
PUBLISHED 15 September 2022

CITATION
Yu H, Zeng W, Zhao G, Hong J and Feng Y (2022) Response of tear cytokines following intense pulsed light combined with meibomian gland expression for treating meibomian gland dysfunction-related dry eye. *Front. Endocrinol.* 13:973962. doi: 10.3389/fendo.2022.973962

Response of tear cytokines following intense pulsed light combined with meibomian gland expression for treating meibomian gland dysfunction-related dry eye

Haozhe Yu, Weizhen Zeng, Gezheng Zhao, Jing Hong* and Yun Feng*

Department of Ophthalmology, Peking University Third Hospital, Beijing, China

Purpose: This study compared the changes in tear inflammatory cytokine levels after intense pulsed light (IPL) combined with meibomian gland expression (MGX) (IPL group) and instant warm compresses combined with MGX (physiotherapy group) as treatments for meibomian gland dysfunction (MGD)-related dry eye disease (DED) to explore their similarities and differences in therapeutic mechanisms.

Methods: This study was a *post-hoc* analysis of a randomized controlled trial. Thirteen patients with MGD-related DED were enrolled in each group and received three treatments correspondingly with 3-week intervals. The levels of 20 tear cytokines, namely, TNF-α, IL-6, MMP-9, CXCL8/IL-8, CXCL10/IP-10, IL-10, EGF, IL-6R, IL-1β, IFN-γ, lactoferrin, Fas ligand, IL-17A, LT-α, S100A9, LCN2/NGAL, IL-13, IL-12/IL-23p40, Fas, and CCL11/Eotaxin, were measured at baseline, before the second and third treatments, and 3 weeks after the third treatment. The primary outcome was the difference in cytokine levels between baseline and the last measurement, and the trends were analyzed at each measurement point.

Results: At the last measurement, a significant decrease was observed in all tear cytokines for both IPL and physiotherapy groups compared with baseline. The IPL group showed greater reductions in IL-6, IL-6R, IL-1β, IL-13, and CCL11/Eotaxin than the physiotherapy group. TNF-α, CXCL8/IL-8, CXCL10/IP-10, IL-10, EGF, IL-1β, IFN-γ, and Lipocalin-2/NGAL levels continued to decrease with treatment time. Important interactions were found in the changes of IL-6 and IL-13 levels, where the levels first decreased and then slightly increased in the physiotherapy group after treatment, while they continued to decrease in the IPL group.

Conclusions: The mechanisms of IPL and physiotherapy in treating MGD-related DED were both associated with reducing inflammation, and the superiority of IPL could be attributed to its better inhibitory effect on inflammatory cytokines like IL-6. In addition, several cytokines were on a

downward trend during treatment, suggesting that the vicious cycle of DED was suppressed.

KEYWORDS

meibomian gland dysfunction, intense pulsed light, cytokine, tear, MGD, IPL

Introduction

Dry eye disease (DED) has been recognized as a high incidence of ocular surface disease over the past few decades with its estimated prevalence of nearly 12% around the world, and the trend continuously increases rapidly (1, 2). In clinical practice, DED can be divided into two types: aqueous-deficient due to low tear production and evaporative due to meibomian gland dysfunction (MGD). The latter is the most common type, with more than 80% of patients belonging to this type (3). MGD usually presents as an abnormal quantity and quality of secreted meibum, mainly caused by epithelial hyperkeratinization and high viscosity of meibomian lipids, which will further lead to ongoing chronic inflammation, resulting in meibomian gland dropout and atrophy (4, 5). In this case, the stability of the lipid layer of the tear film will decrease, thereby exhibiting high evaporation and hyperosmolarity of the tear (6, 7).

Many therapies targeted to the lipid composition and chronic inflammatory state of meibomian glands have been proposed including artificial tears, omega-3 supplements, anti-inflammatories like cyclosporine A, and antibiotics like doxycycline (8, 9). Recently, non-pharmaceutical interventions for MGD including warm compress, manual physical expression, and intraductal probing which act directly on meibomian glands have attracted more and more attention with their favorable clinical effect (10). Of these, intense pulsed light (IPL) treatment based on non-laser and high-intensity light sources is considered to be a possible better option (11, 12). In addition, several randomized clinical trials reported a better improvement of combination therapy of IPL with other approaches such as meibomian gland expression (MGX), which therefore has been widely used in clinical practice nowadays (13–15).

Several possible mechanisms have been proposed to explain the symptomatic improvement of MGD and DED after IPL treatment, including inhibition of bacteria growth in the eyelid, reduction of viscosity in the meibum through heating, and dilation and reconstruction of meibomian gland ducts through electromagnetic waves (16). However, their exact mechanisms are still unclear and controversial due to a lack of evidence at the molecular level; clinical studies reported different correlations between decreased levels of inflammatory cytokines and improvement in MGD (17, 18). The photothermal effect of IPL on meibomian glands has not been confirmed by *in-vivo* experiments. Li et al. (19) further proposed neurogenic mechanisms on this basis. In addition, a recent study found that although IPL could activate fibroblasts and immune cells, it might also skew the metabolic pathway of targeted cells toward a glycolytic phenotype, thereby promoting oxidative stress and apoptosis (20). Such results affect the assessment of the safety and efficacy of IPL and limit its further application (21, 22). On the contrary, instant warm compresses are considered to be a conservative measure that was worth promoting with excellent safety although its mechanism is also not well understood (23, 24). Nowadays, the multiplex assay of cytokines in tears has been recognized as an effective means to explore the mechanism of ocular surface diseases such as DED and keratoconus as well as monitor their progress of treatment (25, 26). In this study, we explored the interaction of the IPL and common physical therapy with the ocular surface by comparing their changes in tear cytokine profiles based on our previous randomized control trial, with a view to providing a reference for the mechanistic interpretation and choice of therapy for MGD.

Method

Study design and subjects

This is a *post-hoc* analysis based on our previous randomized controlled trial which aimed to compare the efficacy of IPL and instant warm compresses in combination with MGX in improving DED. The study was registered on the Chinese Clinical Trial Registry (ChiCTR1800014787), and its detailed design and primary outcome have been reported elsewhere (15). In short, 120 patients with DED caused by MGD from four centers were randomized to receive either IPL + MGX or instant warm compresses + MGX therapy, and each subject was treated three times at 3-week intervals. All subjects had no additional drug interventions other than the use of artificial tears three times a day. The clinical parameters considered mainly included tear film break-up time (TBUT), self-evaluated Standard Patient Evaluation of Eye Dryness (SPEED) questionnaire score, meibomian gland yielding secretion score (MGYSS), and

corneal staining score, and the primary outcome was the improvement of tear break-up time of the right eye at 3 weeks after the last treatment compared to baseline.

In the current study, 26 patients from a single center at Peking University Third Hospital were included with a 1:1 ratio of IPL + MGX (IPL) to instant warm compresses + MGX (physiotherapy) groups. Their tears were collected at different time points (baseline and before/after treatment), which was consistent with previous randomized trials, and the cytokine levels of their tears were measured. The primary endpoint was the change in cytokine levels of tears at 3 weeks after the third therapy from baseline. The study was approved by Peking University Third Hospital Medical Science Research Ethics Committee and conducted under the guidance of the Declaration of Helsinki. All subjects signed an informed consent.

Tear collection and cytokine concentration measurement

The subjects' tears were collected at 0 to 14 days before the first treatment (baseline), before the second (first repeated measurement) and third interventions (second repeated measurement), and 3 weeks after the third treatment (third repeated measurement). For each time point, a total of 6.6 μl of basal tear samples were collected carefully from the lower lateral tear meniscus of each eye of the subjects using 2.2 μl of microcapillaries. The tears from the different patients and eyes were independently transferred to 0.5-ml microcentrifuge tubes and stored at −80°C until further analysis.

The concentration of a set of 20 cytokines, namely, tumor necrosis factor α (TNF-α), interleukin 6 (IL-6), matrix metalloproteinase-9 (MMP-9), interleukin 8 (CXCL8/IL-8), chemokine C-X-C ligand 10 (CXCL10/IP-10), interleukin 10 (IL-10), epidermal growth factor (EGF), interleukin 6 receptor (IL-6R), interleukin 1 beta (IL-1β), interferon gamma (IFN-γ), lactoferrin, Fas ligand, interleukin 17A (IL-17A), lymphotoxin-alpha (LT-α), S100 calcium binding protein A9 (S100A9), Lipocalin-2 (LCN2/NGAL), interleukin 13 (IL-13), interleukin 12 (IL-12/IL-23p40), Fas, and chemokine C-C motif ligand 11 (CCL11/Eotaxin), was measured through a microsphere-based immunoassay according to the instructions of the manufacturers (17, 27).

Statistical analysis

The statistical analysis was conducted using IBM SPSS 24.0 and R 4.0.4 software. The changes in the cytokine levels were presented as the ratio of cytokine levels at different time points compared to baseline for further repeated measurement analysis. The reductions in cytokine levels at baseline and last measurement in patients assigned to the IPL and physiotherapy groups, as well as their trends during ongoing treatment, were analyzed through generalized estimating equations based on the compound symmetric correlation matrix, respectively (28). The age, sex, SPEED score of patients as well as TBUT, fluorescein staining of the cornea, MGYSS score, and baseline tear cytokine levels were included in the model as covariates. The nominal P <0.05 was considered statistically significant.

Results

Figure 1 shows the changes in tear cytokine levels of patients during the three follow-up visits after IPL and physiotherapy. There were significant decreases in all tear cytokine levels at the last measurement after treatment. The IPL group had significantly greater decreases in IL-6, IL-6R, IL-1β, IL-13, and CCL11/Eotaxin than the physiotherapy group. A superior cytokine-lowering effect of physiotherapy was found for EGF, FasL, IL-17A, and Fas; however, these differences disappeared after adjusting for baseline covariates.

Repeated measures analysis further indicated that there were group differences in the effect of IPL and physiotherapy on decreasing IL-6 and CCL11/Eotaxin concentrations in tears, and their levels continued to decrease with treatment time. However, the interaction of CCL11/Eotaxin was marginally significant, suggesting that IPL was more effective than physiotherapy in reducing CCL11/Eotaxin, and their differences further increased over time. In addition, between-group and time-point differences were found for FasL and IL-17A, while there was no difference in the primary outcome, implying that these cytokine levels varied differently with time and reached similar levels at the last measurement.

Although there were no between-group differences, significant time effects were found in the decreases of TNF-α, CXCL8/IL-8, CXCL10/IP-10, IL-10, EGF, IL-1β, IFN-γ, and Lipocalin-2/NGAL, indicating that their levels continued to decline with treatment. A marginally significant interaction was also found for IL-1β, demonstrating a higher cytokine-lowering effect in the IPL group. No significant between-group and time effects were found for MMP-9, lactoferrin, IL-17A, S100A9, IL-12/IL-23p40, or Fas, suggesting that the lowering effects of these cytokines were similar between groups and did not change with prolonged treatment.

Furthermore, significant interaction effects were found for IL-6R, LT-α, and IL-13. IL-6R and IL-13 gradually decreased in the IPL group, while they first decreased and then increased in the physiotherapy group. LT-α levels in both groups tended to first decrease and then increase, but the increase in the IPL group was delayed compared with the physiotherapy group.

Discussion

Several emerging therapies, such as IPL, have been proposed for MGD and its related DED; however, their superiority and specific mechanisms are still controversial. In the current study,

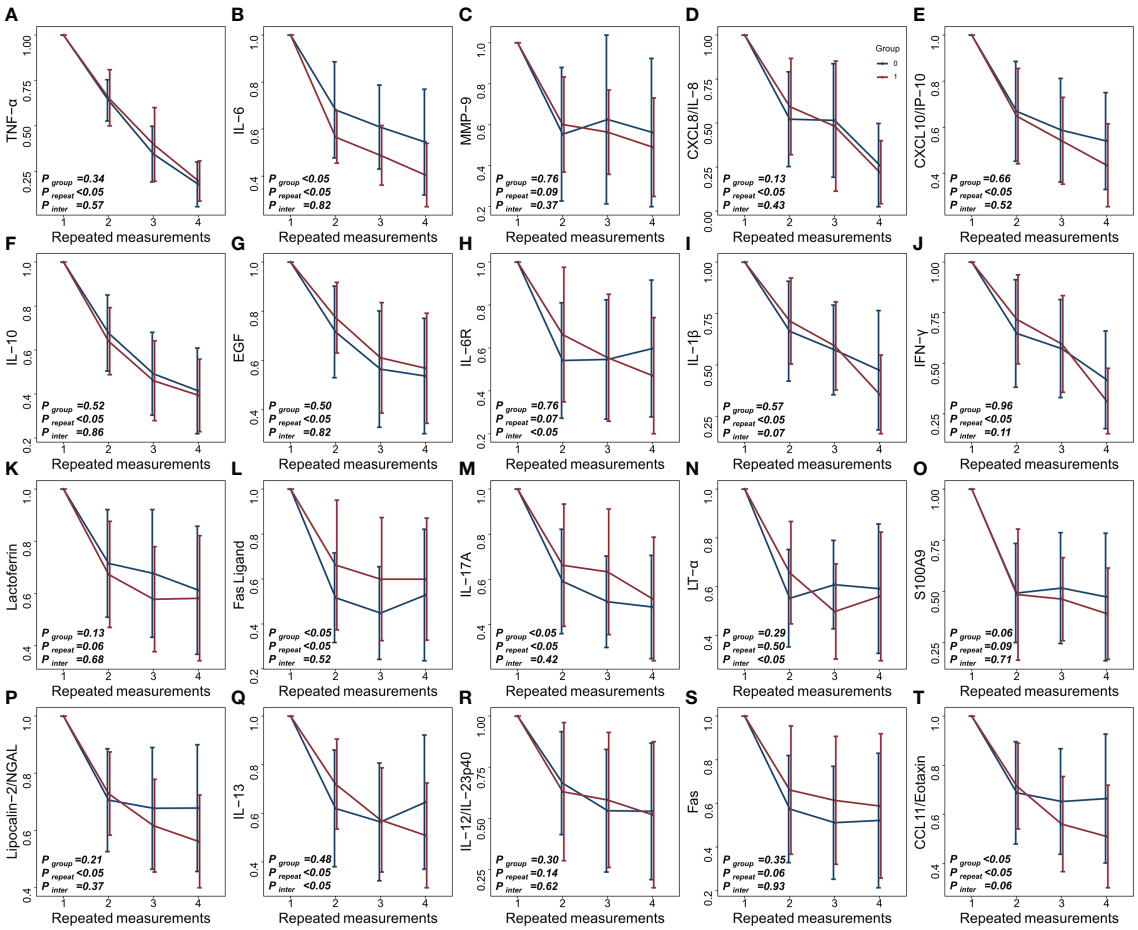

FIGURE 1
(A–T) Longitudinal changes in tear cytokine levels under different treatments (red: IPL group, blue: physiotherapy group).

we compared the changes in the levels of inflammatory cytokines in the tears of patients with MGD undergoing IPL treatment versus physiotherapy over time. Both the IPL and physiotherapy groups had reduced levels of all tested cytokines, and IPL demonstrated superior ability in reducing the levels of IL-6, IL-6R, IL-1β, IL-13, and CCL11/Eotaxin.

Proinflammatory cytokine levels in tears are closely related to the occurrence and development of MGD through a vicious inflammatory cycle, and many studies have tried to speculate on the mechanism of treatment of MGD through changes in these cytokines (29). Liu et al. (17) and Li et al. (30) reported significant decreases in the levels of IL-17A, IL-6, prostaglandin E2, CXCL1, CCL11, TNF-α, IFN-γ, IL-2, and TIMP-1 in the tears of MGD patients, suggesting that the therapeutic effect of IPL on MGD might be achieved by regulating inflammation. Our study further expanded the cytokine profile of the therapeutic mechanism of IPL. In this context, it is inappropriate to reveal the therapeutic mechanism of IPL or physiotherapy for MGD through only one or a few specific signaling pathways, while determining the interaction between signaling pathways and exploring their inflammatory cytokine networks through omics approaches might be promising (31, 32). In addition, we found that physiotherapy alone could also change the levels of inflammatory cytokines in tears, indicating that the combination of anti-inflammatory drugs or antibiotics with physiotherapy might not be necessary, thus avoiding the potential side effects of related drugs such as ocular hypertension (33).

IL-6 is an important signature molecule of MGD and MGD-related DED, which is associated with signs like meibography score, meibum quality, and Schirmer I test (34, 35). In addition, it also plays a key role in the pathological mechanisms by regulating lipid metabolism and the differentiation of Th17 cells that could induce severe DED (36, 37). IL-1β is thought to be involved in the vicious cycle of MGD because it could be recruited to the ocular surface by bone marrow-derived cells and further promote the secretion of more inflammatory cytokines by epithelial cells (38). Therefore, the better therapeutic effect of

IPL on MGD and MGD-related DED might be related to its improved ability to reduce the levels of these cytokines. In addition, recent studies have reported the potential roles of IL-6R, IL-13, and CCL11/Eotaxin in autoimmune diseases such as primary Sjögren's syndrome through T and B helper cells (39–43). Further exploration of the application of IPL for ocular surface symptoms of other immune-related diseases in this context is worth considering.

The levels of several cytokines that are generally thought to be anti-inflammatory were also reduced, such as IL-10 secreted by regulatory B cells (44–46). One possible reason for this is the duality of IL-10 in the ocular surface immune response to DED and MGD. For instance, Fukushima et al. (47) reported that IL-10 promoted the infiltration of eosinophils into the conjunctiva, and Roda et al. (48) found that IL-10 levels in tears were higher in DED patients. However, a previous study found no association between the reduction of IL-10 in tears after IPL with meibum expression improvement (18). In addition, IPL was shown to be unable to regulate IL-10 mRNA expression *in vivo*; therefore, its decrease might be affected by physiotherapy or a cascade reaction of inflammatory cytokines (49). Further exploration of the roles of such cytokines and their interactions in DED and MGD patients will help to reveal the mechanisms of therapeutic change.

There has been no agreement on the periods of treatment for MGD. It is generally accepted that long-term treatment for MGD is necessary when considering physiotherapy; however, there is considerable variation in the number and duration of IPL treatments, ranging from every few weeks or months to a single session (14, 50–53). Our current results show that during the treatment process, although some cytokines reached the lowest levels after the first treatment, there were still some cytokines whose concentration continued to decline, revealing the necessity for prolonged therapy to some extent. Most of these sustained response cytokines were involved in the vicious cycle of MGD and DED, such as TNF-α and IFN-γ, thereby reducing the inflammatory cascade reaction, which could also be used to explain the low levels of MMP-9, an inflammatory cytokine mainly secreted by corneal epithelial cells, after the first treatment.

It is worth noting that after treatment, the decrease in cytokine levels varied widely between patients, suggesting that the treatment benefit varied considerably among patients. Several studies have reported similar results, where the extent of meibomian gland dropout would greatly affect the patient's response to treatment, and those patients with early-stage MGD were more suitable for IPL/MGX therapy; however, its mechanism remains unclear (54–56). In addition, MGX and instant warm compresses are not standardized clinical procedures, which can also affect a patient's response to therapy. It has been proven that the type of meibum squeezed from MGX as well as the ambient temperature and type of equipment in warm compress therapy could affect the improvement of MGD (57, 58). Although almost all patients in this study demonstrated benefits from physiotherapy, Villani et al. (59) showed that physiotherapy was ineffective for nearly one-third of patients due to compliance and standardization. In this context, standardized IPL treatment procedures are recommended.

There are some limitations to this study. Although the current results were obtained through a *post-hoc* analysis of a rigorous prospective randomized controlled trial to avoid potential bias, the single-center sample size was relatively small. We also only reported nominal *P*-values that were not adjusted for multiple hypothesis testing because of the exploratory nature of this study; therefore, the results should be interpreted with caution. In addition, both experimental and control groups included MGX treatment, and while it is expected that its effects could be counteracted in clinical trials to reflect the true effects of IPL, it is difficult to rule out its potential interactions with IPL or instant warm compresses. Furthermore, the last time point in this study was set at 3 weeks after the third treatment, and a longer follow-up is still required to determine the long-term effect of IPL and physiotherapy on MGD and DED.

Data availability statement

The raw data supporting the conclusions of this article will be made available by the authors, without undue reservation.

Ethics statement

This study was reviewed and approved by Peking University Third Hospital medical science research ethics committee. The patients/participants provided their written informed consent to participate in this study.

Author contributions

JH, YF, and HY designed the study. HY wrote the initial draft. WZ collated and organized the data from the clinical trial. WZ, GZ, and YF revised the manuscript. All the authors made a substantial contribution to the article and approved the final submitted version.

Funding

This study was supported by grants from the National Natural Science Foundation of China (Nos. 81700799 and 82070926).

Conflict of interest

The authors declare that the research was conducted in the absence of any commercial or financial relationships that could be construed as a potential conflict of interest.

Publisher's note

References

1. Chatterjee S, Agrawal D, Sanowar G, Kandoi R. Prevalence of symptoms of dry eye disease in an urban Indian population. *Indian J Ophthalmol* (2021) 69 (5):1061–6. doi: 10.4103/ijo.IJO_1796_20

2. Papas EB. The global prevalence of dry eye disease: A Bayesian view. *Ophthalmic Physiol Opt* (2021) 41(6):1254–66. doi: 10.1111/opo.12888

3. Rouen PA, White ML. Dry eye disease: Prevalence, assessment, and management. *Home Healthc Now* (2018) 36(2):74–83. doi: 10.1097/NHH.0000000000000652

4. Chan TCY, Chow SSW, Wan KHN, Yuen HKL. Update on the association between dry eye disease and meibomian gland dysfunction. *Hong Kong Med J* (2019) 25(1):38–47. doi: 10.12809/hkmj187331

5. Sabeti S, Kheirkhah A, Yin J, Dana R. Management of meibomian gland dysfunction: a review. *Surv Ophthalmol* (2020) 65(2):205–17. doi: 10.1016/j.survophthal.2019.08.007

6. Liu H, Begley C, Chen M, Bradley A, Bonanno J, McNamara NA, et al. A link between tear instability and hyperosmolarity in dry eye. *Invest Ophthalmol Visual Sci* (2009) 50(8):3671–9. doi: 10.1167/iovs.08-2689

7. Messmer EM, Bulgen M, Kampik A. Hyperosmolarity of the tear film in dry eye syndrome. In: *Developments in ophthalmology* (Basel: Karger) (2010). doi: 10.1159/000315026

8. Suzuki T. Inflamed obstructive meibomian gland dysfunction causes ocular surface inflammation. *Invest Ophthalmol Visual Sci* (2018) 59(14 Special Issue): DES94–DES101. doi: 10.1167/iovs.17-23345

9. Kang MS, Shin J, Kwon JM, Huh J, Lee JE. Efficacy of 0.05% cyclosporine a on the lipid layer and meibomian glands after cataract surgery: A randomized, double-masked study. *PloS One* (2021) 16(1):e0245329. doi: 10.1371/journal.pone.0245329

10. Arita R, Fukuoka S. Non-pharmaceutical treatment options for meibomian gland dysfunction. *Clin Exp Optom* (2020) 103(6):742–55. doi: 10.1111/cxo.13035

11. Li D, Lin SB, Cheng B. Intense pulsed light treatment for meibomian gland dysfunction in skin types III/IV. *Photobiomodul Photomed Laser Surg* (2019) 37 (2):70–6. doi: 10.1089/photob.2018.4509

12. Lam PY, Shih KC, Fong PY, Chan TCY, Ng ALK, Jhanji V, et al. A review on evidence-based treatments for meibomian gland dysfunction. *Eye Contact Lens* (2020) 46(1):3–16. doi: 10.1097/ICL.0000000000000680

13. Huang X, Qin Q, Wang L, Zheng J, Lin L, Jin X. Clinical results of intraductal meibomian gland probing combined with intense pulsed light in treating patients with refractory obstructive meibomian gland dysfunction: A randomized controlled trial. *BMC Ophthalmol* (2019) 19(1):211. doi: 10.1186/s12886-019-1219-6

14. Shin KY, Lim DH, Moon CH, Kim BJ, Chung TY. Intense pulsed light plus meibomian gland expression versus intense pulsed light alone for meibomian gland dysfunction: A randomized crossover study. *PloS One* (2021) 16(3):e0246245. doi: 10.1371/journal.pone.0246245

15. Yan X, Hong J, Jin X, Chen W, Rong B, Feng Y, et al. The efficacy of intense pulsed light combined with meibomian gland expression for the treatment of dry eye disease due to meibomian gland dysfunction: A multicenter, randomized controlled trial. *Eye Contact Lens* (2021) 47(1):45–53. doi: 10.1097/ICL.0000000000000711

16. Suwal A, Hao JL, Zhou DD, Liu XF, Suwal R, Lu CW. Use of intense pulsed light to mitigate meibomian gland dysfunction for dry eye disease. *Int J Med Sci* (2020) 17(10):1385–92. doi: 10.7150/ijms.44288

17. Liu R, Rong B, Tu P, Tang Y, Song W, Toyos R, et al. Analysis of cytokine levels in tears and clinical correlations after intense pulsed light treating meibomian gland dysfunction. *Am J Ophthalmol* (2017) 183:81–90. doi: 10.1016/j.ajo.2017.08.021

18. Choi M, Han SJ, Ji YW, Choi YJ, Jun I, Alotaibi MH, et al. Meibum expressibility improvement as a therapeutic target of intense pulsed light treatment in meibomian gland dysfunction and its association with tear inflammatory cytokines. *Sci Rep* (2019) 9(1):7648. doi: 10.1038/s41598-019-44000-0

19. Li D, Lin SB, Cheng LHH, Zhang MZ, Cheng B. Intense pulsed light treatment for itch associated with allergic keratoconjunctivitis: A retrospective study of 35 cases. *Photobiomodul Photomed Laser Surg* (2021) 39(3):196–203. doi: 10.1089/photob.2020.4826

20. Ferreira L, Vitorino R, Neuparth MJ, Rodrigues D, Gama A, Faustino-Rocha AI, et al. Intense pulsed light: Friend or foe? molecular evidence to clarify doubts. *Anticancer Res* (2018) 38(2):779–86. doi: 10.21873/anticanres.12284

21. Cote S, Zhang AC, Ahmadzai V, Maleken A, Li C, Oppedisano J, et al. Intense pulsed light (IPL) therapy for the treatment of meibomian gland dysfunction. *Cochrane Database Syst Rev* (2020) 2020(3):CD013559. doi: 10.1002/14651858.CD013559

22. Valencia-Nieto L, Novo-Diez A, Blanco-Vázquez M, López-Miguel A. Therapeutic instruments targeting meibomian gland dysfunction. *Ophthalmol Ther* (2020) 9(4):797–807. doi: 10.1007/s40123-020-00304-3

23. Murphy O, O' Dwyer V, Lloyd-Mckernan A. The efficacy of warm compresses in the treatment of meibomian gland dysfunction and demodex folliculorum blepharitis. *Curr Eye Res* (2020) 45(5):563–75. doi: 10.1080/02713683.2019.1686153

24. Zhou X, Shen Y, Shang J, Zhou X. Effects of warm compress on tear film, blink pattern and meibomian gland function in dry eyes after corneal refractive surgery. *BMC Ophthalmol* (2021) 21(1):330. doi: 10.1186/s12886-021-02091-2

25. Willems B, Tong L, Minh TDT, Pham ND, Nguyen XH, Zumbansen M. Novel cytokine multiplex assay for tear fluid analysis in sjogren's syndrome. *Ocul Immunol Inflammation* (2020) 29:1639–44. doi: 10.1080/09273948.2020.1767792

26. Zhang H, Cao X, Liu Y, Wang P, Li X. Tear levels of inflammatory cytokines in keratoconus: A meta-analysis of case-control and cross-sectional studies. *BioMed Res Int* (2021) 2021:6628923. doi: 10.1155/2021/6628923

27. Chen H, Chen H, Liang L, Zhong Y, Liang Y, Yu Y, et al. Evaluation of tear protein markers in dry eye disease with different lymphotoxin-alpha expression levels. *Am J Ophthalmol* (2020) 217:198–211. doi: 10.1016/j.ajo.2020.03.013

28. Ying GS, Maguire MG, Glynn R, Rosner B. Tutorial on biostatistics: Statistical analysis for correlated binary eye data. *Ophthalmic Epidemiol* (2018) 25(1):1–12. doi: 10.1080/09286586.2017.1320413

29. Yamaguchi T. Inflammatory response in dry eye. *Invest Ophthalmol Visual Sci* (2018) 59(14 Special Issue):DES192–9. doi: 10.1167/iovs.17-23651

30. Li Q, Liu J, Liu C, Piao J, Yang W, An N, et al. Effects of intense pulsed light treatment on tear cytokines and clinical outcomes in meibomian gland dysfunction. *PloS One* (2021) 16(8):e0256533. doi: 10.1371/journal.pone.0256533

31. Pieragostino D, D'Alessandro M, di Ioia M, Di Ilio C, Sacchetta P, Del Boccio P. Unraveling the molecular repertoire of tears as a source of biomarkers: Beyond ocular diseases. *Proteomics - Clin Appl* (2015) 9(1-2):169–86. doi: 10.1002/prca.201400084

32. Bakker OB, Aguirre-Gamboa R, Sanna S, Oosting M, Smeekens SP, Jaeger M, et al. Integration of multi-omics data and deep phenotyping enables prediction of cytokine responses. *Nat Immunol* (2018) 19(7):776–86. doi: 10.1038/s41590-018-0121-3

33. Gao YF, Liu RJ, Li YX, Huang C, Liu YY, Hu CX, et al. Comparison of anti-inflammatory effects of intense pulsed light with tobramycin/dexamethasone plus warm compress on dry eye associated meibomian gland dysfunction. *Int J Ophthalmol* (2019) 12(11):1708–13:101442. doi: 10.18240/ijo.2019.11.07

34. Massingale ML, Li X, Vallabhajosyula M, Chen D, Wei Y, Asbell PA. Analysis of inflammatory cytokines in the tears of dry eye patients. *Cornea* (2009) 28(9):1023–7. doi: 10.1097/ICO.0b013e3181a16578

35. Li M, Zhang L. IL-6 and TNF-α expression in the ocular surface of aqueous tear deficiency dry eye-type rat. *Int J Ophthalmol* (2010) 10(7):1281–3. doi: 10.3969/j.issn.1672-5123.2010.07.013

36. Lehrskov LL, Christensen RH. The role of interleukin-6 in glucose homeostasis and lipid metabolism. *Semin Immunopathol* (2019) 41(4):491–9. doi: 10.1007/s00281-019-00747-2

37. Foulsham W, Mittal SK, Taketani Y, Chen Y, Nakao T, Chauhan SK, et al. Aged mice exhibit severe exacerbations of dry eye disease with an amplified

memory Th17 cell response. *Am J Pathol* (2020) 190(7):1474–82. doi: 10.1016/j.ajpath.2020.03.016

38. Lam H, Bleiden L, de Paiva CS, Farley W, Stern ME, Pflugfelder SC. Tear cytokine profiles in dysfunctional tear syndrome. *Am J Ophthalmol* (2009) 147 (2):198–205.e191. doi: 10.1016/j.ajo.2008.08.032

39. Pflugfelder SC, Corrales RM, de Paiva CS. T Helper cytokines in dry eye disease. *Exp Eye Res* (2013) 117:118–25. doi: 10.1016/j.exer.2013.08.013

40. Nocturne G, Seror R, Fogel O, Belkhir R, Boudaoud S, Saraux A, et al. CXCL13 and CCL11 serum levels and lymphoma and disease activity in primary sjögren's syndrome. *Arthritis Rheumatol* (2015) 67(12):3226–33. doi: 10.1002/art.39315

41. Mao YM, Zhao CN, Leng J, Leng RX, Ye DQ, Zheng SG, et al. Interleukin-13: A promising therapeutic target for autoimmune disease. *Cytokine Growth Factor Rev* (2019) 45:9–23. doi: 10.1016/j.cytogfr.2018.12.001

42. Wang S, Zhang H. Upregulation of the IL-33/ST2 pathway in dry eye. *Mol Vision* (2019) 25:583–92.

43. Ramamoorthy P, Khanal S, XXXJ. Nichols J. Inflammatory proteins associated with contact lens-related dry eye. *Contact Lens Anterior Eye* (2022) 45 (3). doi: 10.1016/j.clae.2021.101442

44. Lin X, Wang X, Xiao F, Ma K, Liu L, Wang X, et al. IL-10-producing regulatory b cells restrain the T follicular helper cell response in primary sjögren's syndrome. *Cell Mol Immunol* (2019) 16(12):921–31. doi: 10.1038/s41423-019-0227-z

45. Kim DS, Woo JS, Min HK, Choi JW, Moon JH, Park MJ, et al. Short-chain fatty acid butyrate induces IL-10-producing b cells by regulating circadian-clock-related genes to ameliorate sjögren's syndrome. *J Autoimmun* (2021) 119:102611. doi: 10.1016/j.jaut.2021.102611

46. Mielle J, Nutz A, Guillpain P, Audo R, Gaujoux-Viala C, Combe B, et al. IL-10-producing regulatory b cells are present and functional in primary sjögren patients. *Immunol Res* (2021) 69(1):107–13. doi: 10.1007/s12026-021-09171-x

47. Fukushima A, Sumi T, Fukuda K, Kumagai N, Nishida T, Yagita H, et al. Interleukin 10 and transforming growth factor β contribute to the development of experimentally induced allergic conjunctivitis in mice during the effector phase. *Br J Ophthalmol* (2006) 90(12):1535–41. doi: 10.1136/bjo.2006.100180

48. Roda M, Corazza I, Reggiani MLB, Pellegrini M, Taroni L, Giannaccare G, et al. Dry eye disease and tear cytokine levels— a meta-analysis. *Int J Mol Sci* (2020) 21(9):3111. doi: 10.3390/ijms21093111

49. Taylor M, Porter R, Gonzalez M. Intense pulsed light may improve inflammatory acne through TNF-α down-regulation. *J Cosmet Laser Ther* (2014) 16(2):96–103. doi: 10.3109/14764172.2013.864198

50. Albietz JM, Schmid KL. Intense pulsed light treatment and meibomian gland expression for moderate to advanced meibomian gland dysfunction. *Clin Exp Optom* (2018) 101(1):23–33. doi: 10.1111/cxo.12541

51. Tashbayev B, Yazdani M, Arita R, Fineide F, Utheim TP. Intense pulsed light treatment in meibomian gland dysfunction: A concise review. *Ocul Surf* (2020) 18(4):583–94. doi: 10.1016/j.jtos.2020.06.002

52. Xue AL, Wang MTM, Ormonde SE, Craig JP. Randomised double-masked placebo-controlled trial of the cumulative treatment efficacy profile of intense pulsed light therapy for meibomian gland dysfunction: Intense pulsed light therapy for meibomian gland dysfunction. *Ocul Surf* (2020) 18(2):286–97. doi: 10.1016/j.jtos.2020.01.003

53. Solomos L, Bouthour W, Malclès A, Thumann G, Massa H. Meibomian gland dysfunction: Intense pulsed light therapy in combination with low-level light therapy as rescue treatment. *Med (Lithuania)* (2021) 57(6):619. doi: 10.3390/medicina57060619

54. Vegunta S, Patel D, Shen JF. Combination therapy of intense pulsed light therapy and meibomian gland expression (IPL/MGX) can improve dry eye symptoms and meibomian gland function in patients with refractory dry eye: A retrospective analysis. *Cornea* (2016) 35(3):318–22. doi: 10.1097/ICO.0000000000000735

55. Zhao Y, Veerappan A, Yeo S, Rooney DM, Acharya RU, Tan JH, et al. Clinical trial of thermal pulsation (LipiFlow) in meibomian gland dysfunction with preteatment meibography. *Eye Contact Lens* (2016) 42(6):339–46. doi: 10.1097/ICL.0000000000000228

56. Tang Y, Liu R, Tu P, Song W, Qiao J, Yan X, et al. A retrospective study of treatment outcomes and prognostic factors of intense pulsed light therapy combined with meibomian gland expression in patients with meibomian gland dysfunction. *Eye Contact Lens* (2021) 47(1):38–44. doi: 10.1097/ICL.0000000000000704

57. Wang MTM, Gokul A, Craig JP. Temperature profiles of patient-applied eyelid warming therapies. *Contact Lens Anterior Eye* (2015) 38(6):430–4. doi: 10.1016/j.clae.2015.06.002

58. Lee H, Kim M, Park SY, Kim EK, Seo KY, Kim TI. Mechanical meibomian gland squeezing combined with eyelid scrubs and warm compresses for the treatment of meibomian gland dysfunction. *Clin Exp Optom* (2017) 100(6):598–602. doi: 10.1111/cxo.12532

59. Villani E, Garoli E, Canton V, Pichi F, Nucci P, Ratiglia R. Evaluation of a novel eyelid-warming device in meibomian gland dysfunction unresponsive to traditional warm compress treatment: an *in vivo* confocal study. *Int Ophthalmol* (2015) 35(3):319–23. doi: 10.1007/s10792-014-9947-3

frontiers | Frontiers in Endocrinology

TYPE Review
PUBLISHED 29 September 2022
DOI 10.3389/fendo.2022.946915

OPEN ACCESS

EDITED BY
Lian Zhao,
National Eye Institute (NIH),
United States

REVIEWED BY
Yanwu Xu,
Baidu, China
Xibo Ma,
Institute of Automation (CAS), China

*CORRESPONDENCE
Yong Tao
taoyong@bjcyh.com

†These authors share first authorship

SPECIALTY SECTION
This article was submitted to Molecular and Structural Endocrinology, a section of the journal Frontiers in Endocrinology

RECEIVED 18 May 2022
ACCEPTED 12 September 2022
PUBLISHED 29 September 2022

CITATION
Huang X, Wang H, She C, Feng J, Liu X, Hu X, Chen L and Tao Y (2022) Artificial intelligence promotes the diagnosis and screening of diabetic retinopathy. *Front. Endocrinol.* 13:946915. doi: 10.3389/fendo.2022.946915

Artificial intelligence promotes the diagnosis and screening of diabetic retinopathy

Xuan Huang[1,2†], Hui Wang[1†], Chongyang She[1], Jing Feng[1], Xuhui Liu[1], Xiaofeng Hu[1], Li Chen[1] and Yong Tao[1*]

[1]Department of Ophthalmology, Beijing Chaoyang Hospital, Capital Medical University, Beijing, China, [2]Medical Research Center, Beijing Chaoyang Hospital, Capital Medical University, Beijing, China

Deep learning evolves into a new form of machine learning technology that is classified under artificial intelligence (AI), which has substantial potential for large-scale healthcare screening and may allow the determination of the most appropriate specific treatment for individual patients. Recent developments in diagnostic technologies facilitated studies on retinal conditions and ocular disease in metabolism and endocrinology. Globally, diabetic retinopathy (DR) is regarded as a major cause of vision loss. Deep learning systems are effective and accurate in the detection of DR from digital fundus photographs or optical coherence tomography. Thus, using AI techniques, systems with high accuracy and efficiency can be developed for diagnosing and screening DR at an early stage and without the resources that are only accessible in special clinics. Deep learning enables early diagnosis with high specificity and sensitivity, which makes decisions based on minimally handcrafted features paving the way for personalized DR progression real-time monitoring and in-time ophthalmic or endocrine therapies. This review will discuss cutting-edge AI algorithms, the automated detecting systems of DR stage grading and feature segmentation, the prediction of DR outcomes and therapeutics, and the ophthalmic indications of other systemic diseases revealed by AI.

KEYWORDS

diabetic retinopathy, artificial intelligence, classification, segmentation, diagnosis, screening, prediction

Introduction

Diabetic retinopathy (DR), an eye disease that is associated with severe visual impairment, is the leading cause of blindness in diabetics (1). DR occurrence is attributed to chronic high blood glucose levels that lead to retinal capillary damage hindering light perception and signal transmission. DR, whose incidence is high in the working-age population, prevails all over the world and is estimated to reach 191 million

cases by 2030 (2). Despite the progression of DR leading to blindness, the detection of DR in early stages is challenging due to its imperceptible visual signs. Hereby, regular screening and early diagnosis can reduce the visual loss risk by 57.0% as well as treatment costs (2). The screening tests for DR (usually retinal photography) are safe, simple, acceptable, and benefit-validated by many longitudinal studies (3, 4). Efficacious treatments, such as the intravitreal injections of antivascular endothelial growth factor (VEGF) agents and laser therapies for severe DR, are available for patients identified through early detection. However, many countries lack the resources for nationwide screening. Therefore, a simple and scalable community screening solution is needed with insufficiently trained ophthalmology. As an important public healthcare problem, DR meets all the criteria for screening that has long been recommended by many international societies (5).

The new technology based on artificial intelligence (AI), which permits to implement large-scale detection and personalized predictive models, is shifting screening strategies and enhancing the cost-effectiveness of screening (6). Advances in computer-aided diagnostic (CAD) techniques in modern ophthalmology are efficient in saving time and human resources as well as costs for routine DR screening and are associated with low diagnostic errors (7). CAD has also been shown to effectively handle the rising number of referable DR patients and diagnosis of DR at an early stage with few sight-threatening effects (8). Variations in these techniques are based on different non-invasive imaging systems, including ultrawide-field fundus (UWF), optical coherence tomography (OCT), OCT angiography (OCTA), standard 45° fundus photography, and even the camera equipped in smartphones applied to in-time DR screening (9). Machine learning (ML)–based algorithms, especially deep learning (DL), are not only efficient for the detection, localization, and quantification of pathological features mimicking the path of the human brain for target recognition in DR but could also diagnose or classify DR stages from patterns recognized independently, by unsupervised convolutional neural networks (CNNs) (10). Although AI-based retinal analysis methods widely differ in their applicability, reliability, and interpretability in different diseases and datasets, recently, fully automated AI-based systems have been further developed and initially approved for DR screening (11, 12).

In this review, we will analyze the applications of ML/DL comprehensively for the screening and diagnostic grading of DR and the mechanistic features of DR progression revealed by AI, as well as the AI guidance of the prognosis and therapy systems with an automated identification of disease activity, recurrence, and therapeutic effect evaluation. In addition, the use of retinal examination to establish the risks for other diseases will be commented, thus expanding the role in the diagnosis and screening of DR.

Development of artificial intelligence algorithm

With increased computational power and the availability of new datasets, DL has experienced a dramatic resurgence recently as a subfield of machine learning. The diagnosis and therapeutics of DR have benefited greatly from DL owing to the volume of big data and the increasing application of ophthalmic devices as well as digital record systems. Scaling to large datasets, DL models show successive improvements with more data, which enable them to outperform many classical ML approaches. The majority of available models are trained by supervised learning, whereby datasets have data points (e.g., fundus lesion) as input and the matched data labels (e.g., mild or severe) as output. Commonly first, the algorithm uses the large data amounts to learn the natural features of statistics in images, like curves, straight lines, and colorations among others. Additionally, in the second step, in order to differentiate among diagnostic cases, the higher-level layers of algorithms are involved to be retrained. Moreover, the identification of the specific image parts that correspond to specific diagnostic objects is based on target detecting and segmentation algorithms. The image data are taken as input by CNN approaches that iteratively warp the pixels *via* multiple convolutional and non-linear operations until the original raw data matrix is transmuted into a probability distribution over potential image classes (13) (Figure 1). Aside from the CNN as a feed-forward neural network designed to process data with network structures, the recurrent neural network (RNN) is a specialized neural network for processing sequential data, such as time series. In addition, the long short-term memory (LSTM) algorithm is a variant of RNN that aims to prevent the vanishing gradient problem in RNN by using a memory gating mechanism (Figure 1). They all have contributed to the application of AI across the human lifespan (14).

Image-level diagnostics could employ CNN-based approaches, including Inception V3, Xception, InceptionResNet V2, ResNeXt101, and NASNetLarge, applying transfer learning from ImageNet. We have proposed multiple algorithms for DR detection and grading based on deep ensemble learning and attention mechanisms to integrate the classic algorithms (15). Relative to the traditional single network model detection algorithm, the area under the receiver operating characteristic curve (AUC), accuracy, and recall of the suggested approach are respectively improved to 95%, 92%, and 92%, proving the optimization and adaptability of fusion algorithms for fundus photographs. For OCT images, we have also applied a fusion network algorithm to the retinal lesion classification of choroidal neovascularization (CNV), diabetic macular edema (DME), drusen, and normal groups. The result showed that the developed fusion algorithm can significantly improve the

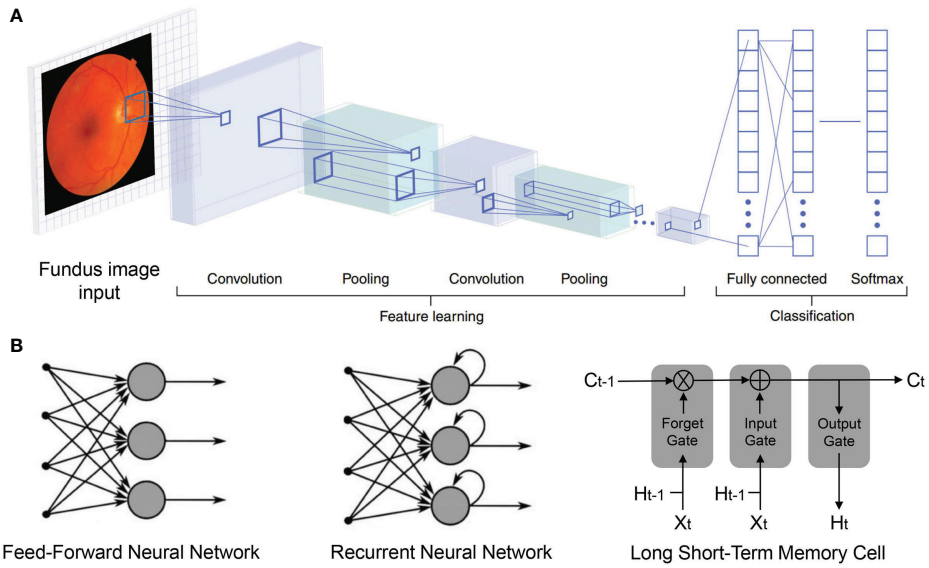

FIGURE 1
Deep neural network structures. **(A)** Convolutional neural network (CNN) imaging flow: Fundus images are input and sequentially transformed by convolution, pooling, and fully connected layers, into flattened vectors. Output vector (Softmax layer) elements denote the probabilities for disease presence. In training, lower layers (left) learn features to influence the high-level representations (right), by which internal network layer parameters are iteratively adjusted to enhance accuracy. **(B)** General architectures of deep learning models in mainstream.

performance of classifiers compared to traditional algorithms while providing a powerful tool and theoretical support to assist with the diagnosis of retinal OCT images (16).

For a long time, two types of learning tasks have been used to construct AI models: supervised learning with training from known patterns and labeled input data commonly referred to as ground truths and unsupervised learning from unknown patterns without labeled input data. Unsupervised learning has limited power up to date, while an automatic supervised solution is challenging due to the requirement of a large amount of training data and the laborious annotations for medical images. Therefore, novel self-supervised learning frameworks for retinal disease diagnosis are presented nowadays (17–20). This so-called unsupervised visual representation learning derives labels from a co-occurring input to relate information, thus reducing the annotation efforts by learning the visual features from the unlabeled images. For instance, Xiaomeng Li et al. developed a self-supervised method surpassing the supervised baseline for the classification of pathologic myopia (PM) and age-associated macular degeneration (AMD) (21).

Another solution to the training need for large, criterion standard–annotated retinal datasets is few-shot deep learning. This algorithm aims to learn from a relatively low number of training data, which is beneficial for clinical situations involving rare retinal diseases or when addressing potential bias resulting from data that may not adequately represent certain groups for training. Tae Keun Yoo et al. demonstrated that few-shot learning using a generative adversarial network (GAN) could improve the applicability of DL in the OCT diagnosis of rare retinal diseases (22). The potential benefits of using low-shot methods for AI retinal diagnostics due to a limited number of annotated training retinal images have been confirmed as feasible (23).

Automated detection and classification of diabetic retinopathy

New ML and DL approaches are viable for automated DR diagnosis. Various performance metrics, including accuracy, specificity, AUC, sensitivity or recall, precision, F1 score, and Kappa score, have been used for the evaluation of grading, namely, classification performance. The International Council of Ophthalmology classification for DR considers five retinopathy stages (none, non-proliferative: mild, moderate, severe, and proliferative), while DME is classified as no DME, non-center involving DME, and center-involving DME (6). These clinical standards are widely used in the practice of AI-based implementation.

In 2016, Gulshan et al. (24) established a potent DL algorithm for DR assessment. Approximately 0.13 million images from two public databases (EyePAC-1 and Messidor-2) were used to train their model. As a result, 0.97–0.99 AUC values were acquired from tests using two distinct datasets to detect referable (moderate or worse) DR achieving physician-level

accuracy. To facilitate translation and develop DL for clinical applications using multiform retinal images of inhomogeneous qualities from different camera types in the representative screening populations sensitive to DR, Ting D.S.W. et al. (25) built a diagnostic model for DR based on larger datasets that consist of approximately 0.5 million images from a multiethnic community. In the primary validation dataset (14, 880 patients; 71, 896 images), the automated model had high sensitivity (90.5, 100, 96.4, 93.2%) and specificity (91.6, 91.1, 87.2, 88.7%) for distinguishing vision-threatening DR from referable DR and for the identification of related eye diseases, such as referable glaucoma and referable AMD. Based on a solid evaluation of retinal images by trained professional graders, the performance of this model was comparable to that of the current first class. Using various reference standards to assess DR by professional graders, retinal specialists, and optometrists, there was fair consistency in the 10 external validation datasets of multiethnicities and diverse settings.

Similarly, Abramoff et al. (26) developed an automated system for DR detection with a sensitivity of 96.8% and specificity of 59.4% using the CNN algorithm on a publicly available dataset (Messidor-2), considered as pathbreaking work in this field. Subsequently, studies have further assessed the suitability of the DL technology for DR detection (27) and grading (28, 29). Gargeya and Leng (27) reported optimal DL diagnostic performance in the detection of DR achieving a 0.97 AUC with a specificity and sensitivity of 98% and 94%, respectively, based on two publicly available databases (E-Ophtha and Messidor-2). Likewise, Philip et al. (30) documented a sensitivity and specificity of 86.2% and 76.8%, respectively, for predicting disease versus no disease on their own dataset of 14, 406 images of DR screening. High-quality datasets with precise DR grading are essential to developing a DL system for automated detection and classification (31), so we present an overview of the available and high-level datasets that are public open access (OA) or access upon request (AUR) (Table 1).

Conventional fundus photography used by most studies takes the images of the macula area and optic nerve with a field of view (FOV) between 20◦ and 50◦. Although conventional FOV covers the vital region of interest for DR diagnosis and detection, there is still a large portion of uncaptured retinal surface that also matters. Takahashi et al. (42) used four-field non-mydriatic 45° fundus images to integrate into a wide retinal area for DR stage grading through a DL algorithm. With regard to DR grading, the four-field fundus photography exhibited a better performance compared to single-field conventional fundus photography. Nevertheless, four-field fundus photography in practice is laborious and time consuming, which limits its feasibility. Due to retinal imaging technology advances, a new fundus photography expanding to 200° of retinal surface images in a single shot called UWF has made a figure (51), thus providing the peripheral and posterior pole retinal region. Actually, UWF retinal images, such as UWF fluorescein angiography, have been widely used in DR diagnosis as well as treatment, attaining peripheral ischemic and neovascularization areas (52). For instance, detecting proliferative DR (PDR) *via* the DL algorithm using UWF fundus photography was proven effective by Nagasawa et al. (53).

With its unprecedented resolution, OCT permits the non-invasive visualization of the fine retinal structures. As one of the most dominant *in vivo* diagnostic tools in modern ophthalmology, spectral domain (SD)–OCT is the gold standard approach for the diagnostic imaging of macular diseases, including DME and CNV. A model based on the CNN using OCT images was shown to be able to effectively distinguish cases with advanced AMD or DME that need timely treatment, from less severe cases (54). By contrast, AI performed as well as six specialists who made ground-truth referrals using the same scans. Similarly, Chan et al. (55) integrated several DL architectures for the automatic classification of normal and DME through OCT images from a screening program in Singapore called SIDRP, thereby yielding an accuracy of 93.75%. Based on SIDRP, one of the largest DR datasets around the world, Alsaih et al. (56) compared the kinds of mainstream ML and figured out the best one to detect DME with a sensitivity and specificity of 87.5% and 87.5%, respectively. Additionally, Gerendas et al. (57) found the potential of ML/DL in the prognosis of DME patients' best corrected visual acuity (BCVA) by OCT.

Mechanistic interpretation of diabetic retinopathy features by artificial intelligence

AI application performing at an expert level without information on how the AI system make its decision cannot be considered as sufficient to apply. The ML/DL uses multiple representation levels to assess every retinal image operating as a black-box model without showing the actual DR lesions (e.g., microaneurysms and retinal hemorrhages). Such black-box issues may affect their clinical use negatively. Therefore, the mechanistic interpretation of DR features by AI is necessary and helpful for both clinical application and etiology research in depth. These features can likely be the contour or shape of the optic disc and tortuosity or caliber of the retinal vessels, which indicate the mechanism of certain disease progression.

For models based on digital fundus photography, we reviewed the general segmentation approaches of the DR lesions such as microaneurysm, hard exudate, intraretinal hemorrhage, vitreous hemorrhage, preretinal hemorrhage, neovascularization, cotton wool spots, intraretinal microvascular abnormalities, and venous beads. At the end of the network, a convolutional visualization

10.3389/fendo.2022.946915

TABLE 1 Datasets for diabetic retinopathy (DR) detection, segmentation, and grading.

Dataset	No. of images	No. of subjects	Device used	Access	Country	Year	Type	Remarks
DRIVE (32)	40	400	Canon CR5 non-mydriatic 3CCD camera with a 45° FOV	OA	Netherlands	2004	CFP	Retinal vessel segmentation and ophthalmic diseases
DIARETDB0 (33)	130	NA	50° FOV DFC	OA	Finland	2006	CFP	DR detection and grading
DIARETDB1 (34)	89	NA	50° FOV DFC	OA	Finland	2007	CFP	DR detection and grading
HEI-MED (35)	169	910	Visucam PRO fundus camera (Zeiss, Germany)	OA	USA	2010	CFP	DR detection and grading
DRiDB (36)	50	NA	Zeiss Visucam 200 DFC at a 45° FOV	OA	Croatia	2013	CFP	DR grading
E-Ophtha (37)	463	NA	NA	OA	France	2013	CFP	Lesion detection
DRIMDB (38)	216	NA	CF-60UVi fundus camera (Canon)	OA	Turkey	2014	CFP	DR detection and grading
MESSIDOR 1 (39)	1,200	NA	Topcon TRC NW6 non-mydriatic at a 45° FOV	OA	France	2014	CFP	DR and DME grading
Srinivasan (40)	3,231	45	SD-OCT (Heidelberg Engineering, Germany)	OA	USA	2014	OCT	DR detection and grading, DME, and AMD
EyePACS (41)	88,702	NA	Centervue DRS (Italy), Optovue iCam (USA), Canon CR1/DGi/CR2 and Topcon NW	OA	USA	2015	CFP	DR grading
JICHI DR (42)	9,939	2,740	AFC-230 fundus camera (Nidek)	OA	Japan	2017	CFP	DR grading
Rotterdam Ophthalmic Data Repository DR (43)	1,120	70	TRC-NW65 non-mydriatic DFC (Topcon)	OA	Netherlands	2017	CFP	DR detection
IDRID (44)	516	NA	NA	OA	India	2018	CFP	DR grading and lesion
OCTID (45)	500	NA	Cirrus HD-OCT machine (Carl Zeiss Meditec)	OA	Multiethnic	2018	OCT	DR, AMD, and hypertension
APTOS (46)	5,590	NA	DFC	OA	India	2019	CFP	DR grading
OCTAGON (47)	213	213	DRI OCT Triton (Topcon)	AUR	Spain	2019	OCTA	DR detection
ODIR-2019 (48)	8,000	5,000	DFC (Canon, ZEISS, Kowa)	OA	China	2019	CFP	DR, AMD, glaucoma, and hypertension
OIA-DDR (49)	13,673	9,598	NA	OA	China	2019	CFP	DR grading and lesion segmentation
FGADR (50)	2,842	NA	NA	OA	UAE	2021	CFP	DR and DME grading
MESSIDOR 2 (26)	1,748	874	Topcon TRC NW6 non-mydriatic at a 45° FOV	AUR	France	Update	CFP	DR and DME grading

DFC, digital fundus camera; OA, open access; FOV, field of view; DR, diabetic retinopathy; DME, diabetic macular edema; AMD, age-related macular degeneration; AUR, access upon request; CFP, color fundus photography; OCT, optical coherence tomography; OCTA, OCT angiography; NA, not available.

layer was used to illustrate the prognostic regions of the fundus for DR diagnosis (27) (Figures 2A, B). The retinal landmarks for this mechanistic interpretation are large retinal vessels, optic discs, and sometimes foveal location as they can be found equally in each fundus image (58, 59) (Figures 2C, D). Ali Shah et al. (60) could detect microaneurysms in color, with Hessian and curvelet-based feature extraction achieving a sensitivity of 48.2%. Huang et al. (61) used the extreme learning machine (ELM) to localize neovascularization. They made use of standard deviation, differential invariant, Gabor, and anisotropic filters with a final classifier using ELM. Together with the support vector machine (SVM), this network performed well and resulted in lower computational time applicable to run on a personal computer (PC) or smartphone. For segmentation tasks, the preprocessing step conformed to a central rule that had direct effects on outputs. Variations in preprocessing techniques were dependent on the dataset quality and lesion type. Orlando et al. (62) combined the deep CNN (DCNN) with the manually designed features by means of illumination correction, color equalization, and Contrast Limited Adaptive Histogram Equalization (CLAHE) contrast enhancement. These high-dimensional feature vectors were fed into a random forest classifier for DR lesion detection, thus achieving an AUC score of 0.93, which was equivalent to other DCNN models (63, 64). The DCNN applied to fundus images could clearly show the lesions on retinal surfaces. For instance, Lam et al. (65) have implemented a state-of-the-art DCNN to identify DR lesions in image patches *via* VGG16, AlexNet, GoogleNet, ResNet, and Inception V3. They achieved 98.0% accuracy based on 243 fundus images from EyePACS. Wang et al. (66) have also used Inception V3 as a feature map and FCN-32s as the segmentation part. As a result, they found the sensitivity values of 60.7%, 49.5%, 28.3%, 36.3%, 57.3%, 8.7%, 79.8%, and 16.4% over preretinal hemorrhage, exudate, vitreous hemorrhage, neovascularization, cotton wool spots, fibrous

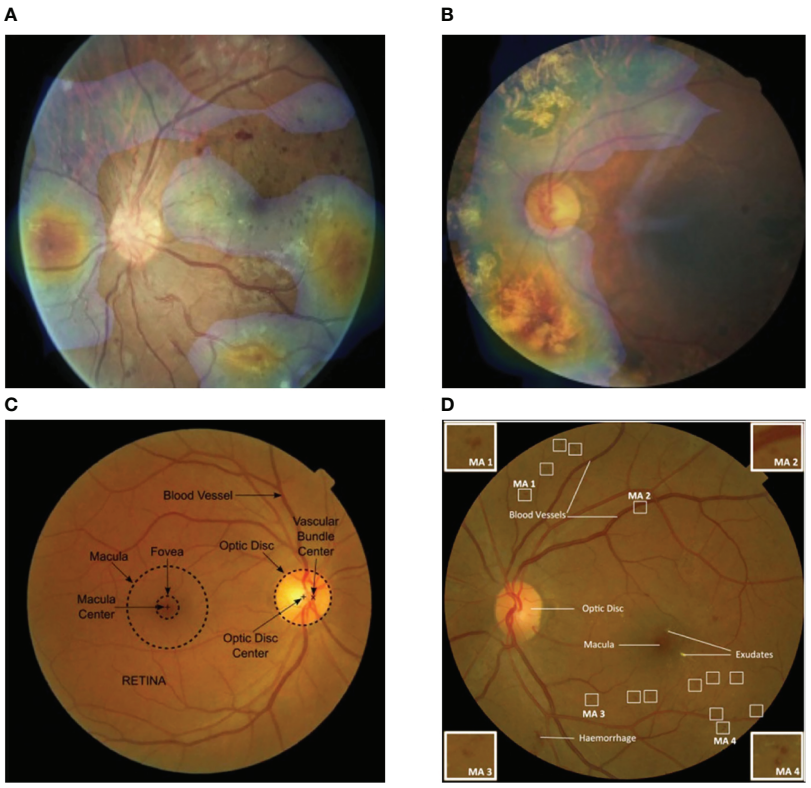

FIGURE 2
Visualization features generated automatically from color fundus photography. **(A)** Fundus heat map overlaid on a fundus image, pathologic regions of interest are in temporal and nasal quadrants as shown. **(B)** Pathologic findings are distributed in lower and upper-left quadrants as highlighted. **(C)** General anatomic landmarks for orientation in retina are labeled automatically. **(D)** Relevant pathologic structures: hemorrhage, exudates, and microaneurysms are shown. Image patches at four corners display the representative features of microaneurysm changes detected by artificial intelligence (AI) [Adapted from Ursula Schmidt-Erfurth et al. (10)].

proliferation, intraretinal hemorrhage, and microaneurysm, respectively. Similarly, Quellec et al. (63) focused on four lesions, i.e., cotton wool spots, exudate, hemorrhage, and microaneurysm using a predefined DCNN and reported the values of 62.4%, 52.2%, 44.9%, and 31.6% over cotton wool spots, exudate, hemorrhage, and microaneurysm for sensitivity, respectively. In comparison, this model showed slightly better performance for cotton wool spots and microaneurysm than that of Wang et al (66), while Wang et al.'s performed better in hemorrhage detection.

For OCT-based models, fovea detection is of great significance as it can also be used for orientation, especially in DME (67). Kermany et al. (54) performed an occlusion test to determine areas in the OCT image that contribute most to the decision of the neural network for DME and AMD (Figure 3). In OCT, the detection of intra- and subretinal macular fluid (IRF and SRF) is most applicable for exudative diseases, including DME (68) (Figure 3). IRF or SRF may be essential for the determination of disease activities from OCT scans and initial diagnosis of whether there is disease activity as binary. Combining fundus photographs and OCT images, Holmberg et al. (69) suggested a retinal layer extraction pipeline to assess retinal thickness, using segmentation algorithm Unet for OCT and self-supervised ResNet50 for fundus. Based on OCTA images, Yukun Guo et al. (70) used DCNNs to segment avascular zones and achieved 87.0% accuracy for mild-to-moderate DR and 76.0% accuracy for severe DR. Furthermore, Hecht et al. (71) developed ML algorithms to build a predictive classifier to diagnose DME and diabetic cystoid macular edema using SD-OCT. In order to confirm a diabetic etiology, ME pattern, hard exudates, subretinal fluid, hyperreflective foci, and cyst location within retinal layers are differentiated by the developed algorithm, resulting in a specificity of 95%, sensitivity of 96%, and AUC of 0.937. Thus, a clinical decision flowchart for uncertainty cases may support intravitreal injections rather than topical treatment.

These approaches greatly facilitate the clinical understanding of DR. In classification, real-word trust in the performance of AI and identification of probable model biases are established when physicians know which discriminative features informed decision-making. In prediction, establishing the role of individual predictive factors in AI will elucidate it further on the underlying

10.3389/fendo.2022.946915

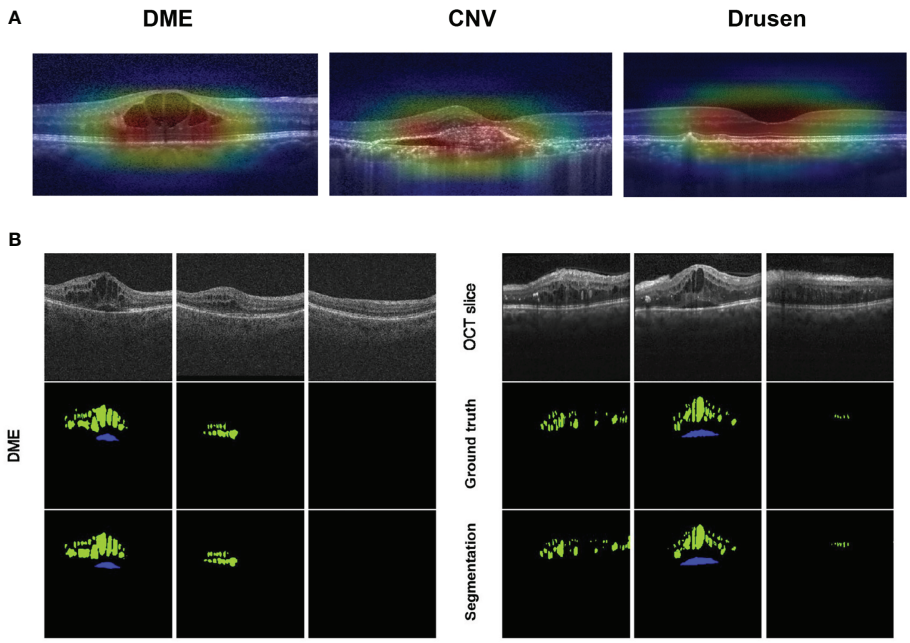

FIGURE 3
Visualization features generated automatically from optical coherence tomography (OCT). **(A)** Feature areas of pathology in diabetic macular edema (DME), choroidal neovascularization, and drusen are highlighted, superimposed on the input image to show the areas that the AI model considered as vital in a diagnosis. **(B)** Segmentation findings of DME on OCT scans acquired with Cirrus (left) or Spectralis (right) devices: the upper row shows OCT raw slices; the middle row shows manual labels by certified graders considered as ground truth; the lower row shows automated results segmented by AI. (IRF, intraretinal cystoid fluid in green; SRF, subretinal fluid in blue) [Adapted from Schlegl et al., 2018 (68)].

pathophysiology. Owing to the mechanistic interpretation of DR features by AI or telemedical CAD, the black box between imaging and diagnosis becomes more and more transparent, revealing the etiological mechanism of DR. Visual explanation techniques such as Grad-CAM and Integrated Gradients are applied to generate saliency maps in order to enhance the interpretability of the algorithms. Using different methods for feature weight calculation, they generate color heat maps that highlight regions that play a critical role in the classification judgment. By visualizing the saliency maps, the contribution of different regions in the image to the final prediction could help us understand the underlying associations between ocular features and DR indicating the mechanism of disease. For DR grading, a novel multiresolution network was developed to focus on the lesion regions, providing a lesion activation map with lesion consistency as an additional evidence for clinical diagnosis (72).

Prognosis and therapeutics guided by artificial intelligence

With respect to pattern recognition in prior data, AI methods can be used to predict the future like an experienced physician. Therefore, AI has the ability to improve the quality of care for DR patients by informing optimal therapies and to reduce healthcare costs by managing treatment prognosis. Major prediction objectives include not only functional outcomes posttherapy but also the future natural course of DR progression. Of note, AI produces and acquires knowledge that can be reproduced and accessed from data more effectively than the majority of experienced experts. Thus, clinicians are empowered to access and use prior experience from hundreds of thousands of previous cases by the ML/DL model to inform optimal treatment.

Although intravitreal anti-VEGF therapy has generated good results for the last decades and is deemed as one of the most promising medical interventions in retina, it is sometimes costly with the ever-growing number of implementations and faces challenges in the therapeutic schedule without a clear indication of benefit limiting its clinical adoption. Prahs et al. (73) trained a DCNN for the prediction of anti-VEGF indications based on central retinal OCT scans without human interventions, thus offering the clinician support in the decision-making of whether anti-VEGF is necessary or not. In the situation of DME, the implementation of anti-VEGF therapy is recommended to treat only if the intraocular fluid remains stable (74). Anti-VEGF agents can also be used to treat pigment epithelial detachment (PED) if the volume of fluid shows active growth (75, 76). Moreover, investigators propose various roles

for different fluid types. For instance, IRF is a retreatment indication, while up to a definite cutoff (200 μm in height at the foveal center), but as to SRF, it may not be so (77). For these models, microstructural alterations in retina are necessary to be analyzed using efficient AI processing beyond manpower. The pathological quantification of images may also be crucial for prognoses as various biomarkers exhibit tight correlations with visual acuity and vision outcomes (78).

Reasonable retreatment intervals are important to manage healthcare effectively. As for intravitreal therapy, there is a need to achieve complete disease control while, as much as possible, avoiding the potential anti-VEGF therapy-associated morbidity including endophthalmitis (79). AI approaches will make a difference in predictive models to inform efficient treatment resolving the dilemma. Theoretically, images and clinical features at both the baseline and post-first injection time of a given patient should be obtained by AI models. The trained model will provide extendibility probability up to a certain interval, namely, overall expected treatment needs as well as optimal extension length over a definite time frame. Administered in clinical practice, these models boosted by AI will enhance the plannability of anti-VEGF treatments, such as reducing healthcare costs and managing the expectations of physicians and patients, resulting in better outcomes due to the prevention of under- or overtreatment widely.

With the advancing guidance of AI in the prognosis and therapeutics of DR, more and more stakeholders, including scientists, clinicians, regulatory agencies, and patients, consider it necessary to pave the road toward the development and implementation of an updated staging system for DR. Given the complexities of diabetic pathways and pathology, most systems may need diverse information from AI to be included in updated staging systems for DR (80). Advanced AI-based disease models will elucidate on DR pathophysiology and further explore the neglected knowledge by interpreting the microstructural features from predictive analyses.

From diabetic retinopathy to systemic diseases

As a relatively simple, safe, validated, and acceptable routine test, retinal photography for DR screening easily accumulated to the largest medical image-level dataset. That would be an access to relevant endocrine disease or even other systemic diseases data-driven by AI technology potentially. The development of automated analysis software using AI-based deep neural learning for retinal images will allow the development of specific software to define cardiovascular risks in diabetic individuals on the basis of retinal structures as well as functional microvasculature changes (81, 82).

By ophthalmoscopy the diagnoses of various systemic diseases start to be part of eye specialists' work, including CMV infection, hypertension, syphilis, tuberculosis, sarcoidosis, and other autoimmune diseases. For DR complication, Kang Zhang et al. (83) found that the identification of chronic kidney disease (CKD) and type 2 diabetes (T2DM) could be attained by DL models using only fundus images or multimodal information combined with clinical metadata (sex, age, height, body mass index, weight, and blood pressure) achieving the AUCs of 0.85–0.93. This study also assessed the feasibility of predicting CKD progression in a longitudinal cohort. Especially, the estimated glomerular filtration rate (eGFR), as an important biomarker to diagnose, could be accurately predicted by an AI model using their fundus images alone, expanding the scope of DR screening insightfully.

Patients with T2DM have higher than average risks for neurodegenerative disease development, especially cognitive dysfunctions, including Alzheimer's disease (84). Since the retina is embryonically a brain-derived tissue, the eye is supposed to provide an efficient window into the brain, facilitating easy, non-invasive investigations of neurodegenerative comparisons between the brain and retina. The measurement of neuroretina or retinal fiber layer thickness by SD-OCT (85), or the evaluation of retinal sensitivity (86) as well as gaze fixation by microperimetry (87), are proven to be indicative for the identification of T2DM patients with mild cognitive impairments, which may be a prodromal sign of Alzheimer's disease. These results elucidate on strategies for DR screening in individuals older than 60 years, as screening for retinopathy may not be limited to keeping from sight-threatening disease but may also be used to early detect the individual risk of severe cognitive decline.

It is said that eyes are the windows to the mind. Exactly, the retina is fairly special as it is the only place of the human body where vascular tissues can be rapidly and non-invasively visualized. Efforts have been aimed deeply at improving the risk prediction of cardiovascular disease (CVD), especially by integrating phenotypic features to promote and the addition of retinal imaging. CVD-associated conditions, including cholesterol emboli and hypertensive retinopathy, can often manifest in the eye. Several retinal features were used to predict cardiovascular events, such as stroke (88) or chronic kidney disease (89), previously. These specific features include vessel caliber, bifurcation, and tortuosity, which could easily be detected by advanced ML/DL. A DL model predicting cardiovascular risk factors was built by Poplin and Varadarjan et al. (90) using retinal fundus images from 48,101 patients from the UK Biobank study dominated by Caucasians without diabetes and 236,234 patients from the EyePACS population of mainly diabetic Hispanics. The validation of these models was carried out using images from 999 patients in EyePACS, 12,026 patients in UK Biobank, and an external cohort comprising Asian patients (91). The model was then established to be fairly accurate for various predictions, including age (mean absolute error ± 3.26 years), sex (AUC = 0.97), systolic blood

pressure (mean absolute error within 11 mmHg), and smoking status (AUC = 0.71). In addition, a model was trained for the prediction of the onset of major adverse cardiovascular events within 5 years, achieving an AUC of 0.70 (95% CI: 0.65, 0.74) from retinal fundus images independently, which is equivalent to the AUC of 0.72 (95% CI: 0.67, 0.76) for the European SCORE risk calculator.

Populations with more cardiovascular events or a markedly larger dataset will enable DL models to be more accurate, evaluated, and trained with high confidence. The use of larger datasets for training and more clinical demonstrations will inform whether retinal fundus images will augment or replace some conventional costly or invasive markers (92). DL systems have the potential of accepting multiple data types as inputs to unearth specific relevance for heterogeneous healthcare data, such as genomic profiling, time-series information, and clinical features, to yield more robust accuracy in disease identifications and predictions (Figure 4). As a window to health, once extensively "exploited" by AI approaches, the retina is expected to be a new focus of both non- and ophthalmological research.

Conclusion

Translating AI to ophthalmic clinic still faces some problems in reality. Although there are many representative international datasets of DR available to build the diagnosis model, they were designed with insufficient consideration for clinical adaptability. The data quality was uneven and the labeling standards varied. Therefore, a standardized dataset with a large sample size needs to be constructed with authoritative and recognized high-quality annotations, which is prerequisite to improve the performance of AI systems finally. In addition, the regulatory mechanism and evaluation criteria have not yet formed a complete and unified system. It is also necessary to establish and improve an AI product evaluation system that conforms to medical evaluation standards before the large-scale clinical use of AI, in order to ensure its safety and effectiveness.

Since DR has seen the first FDA clearance named IDx-DR for an autonomous AI diagnostic system without an image interpretation provided by a specialist, more and more commercial products are developed and believed to come into the market in the near future. In China, training and validation data for AI algorithms are vast due to a rather centralized healthcare system and the largest population of DR (93). Hundreds of new start-up companies working on AI applications to healthcare in China have emerged to improve business, and several DR AI-based screening tools have acquired the certificate of medical device Class III approved by NMPA as pioneers, e.g., Silicon Intelligence, Airdoc, Vistel, and especially Intelligent Healthcare of Baidu that developed the first granted algorithm working robustly with various fundus camera models and achieving high accuracies for detecting multiple ophthalmic diseases (94, 95). Undoubtedly, the real-world deployment of these new systems in multiple settings will be full of challenges not only in AI diagnostic technologies but also in the marketing pattern and policy-making. The combination of telemedicine aided by 5G technology and automated retinal image analysis will enhance the convenience of DR care by

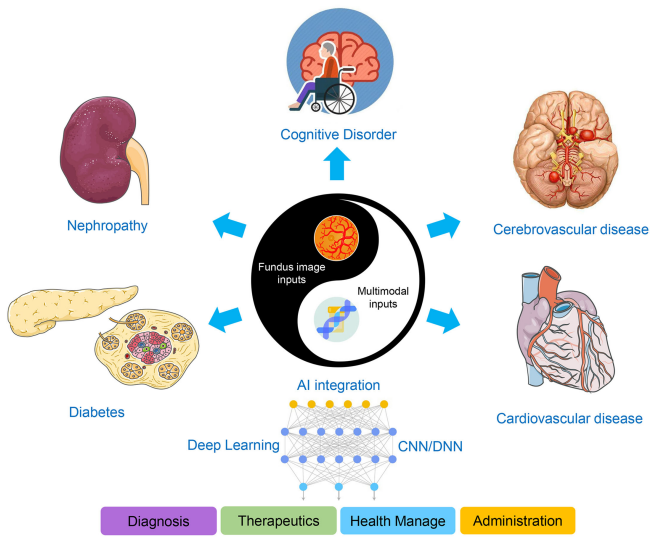

FIGURE 4
Scheme of the AI-based applications integrating DR screening with multimodal features. Fundus image inputs, including digital fundus photography and OCT, integrated with multimodal features, are indicative for diverse systemic diseases such as diabetes, nephropathy, cognitive disorder, and cerebro- or cardiovascular disease, facilitating the four perspectives of medical practice concerned.

providing automated real-time assessment in a more personalized way, supporting commercial interests to promote the whole industry. Additionally, multicenter, head-to-head, real-world validation, multimodality, and improved algorithm studies are imperative and encouraged to conduct, which might magnify the significance of DR screening beyond preventing sight-threatening diseases to the new strategies of systemic diagnosis in metabolism and endocrinology.

Author contributions

XH and HW contributed to the writing of the manuscript under YT's supervision. CS, JF, XL, XFH, and LC do data collection, reference updating and checking. All authors contributed to the article and approved the submitted version.

Funding

National Natural Science Foundation of China (Award number(s): 32000485, 62006161, 82070948). Scientific Research Program of Beijing Municipal Commission of Education (KM202010025020) and Shunyi District "Beijing Science and technology achievements transformation coordination and service platform" construction fund (SYGX202010).

Conflict of interest

The authors declare that the research was conducted in the absence of any commercial or financial relationships that could be construed as a potential conflict of interest.

Publisher's note

References

1. G. B. D. Blindness, C. Vision Impairment and S. Vision Loss Expert Group of the Global Burden of Disease. Causes of blindness and vision impairment in 2020 and trends over 30 years, and prevalence of avoidable blindness in relation to VISION 2020: the right to sight: an analysis for the global burden of disease study. *Lancet Glob Health* (2021) 9:e144–60. doi: 10.1016/S2214-109X(20)30489-7

2. Oh K, Kang HM, Leem D, Lee H, Seo KY, Yoon S. Early detection of diabetic retinopathy based on deep learning and ultra-wide-field fundus images. *Sci Rep* (2021) 11:1897. doi: 10.1038/s41598-021-81539-3

3. Yau JW, Rogers SL, Kawasaki R, Lamoureux EL, Kowalski JW, Bek T, et al. Global prevalence and major risk factors of diabetic retinopathy. *Diabetes Care* (2012) 35:556–64. doi: 10.2337/dc11-1909

4. Ting DS, Cheung GC, Wong TY. Diabetic retinopathy: global prevalence, major risk factors, screening practices and public health challenges: a review. *Clin Exp Ophthalmol* (2016) 44:260–77. doi: 10.1111/ceo.12696

5. Wong TY, Bressler NM. Artificial intelligence with deep learning technology looks into diabetic retinopathy screening. *JAMA* (2016) 316:2366–7. doi: 10.1001/jama.2016.17563

6. Vujosevic S, Aldington SJ, Silva P, Hernandez C, Scanlon P, Peto T, et al. Screening for diabetic retinopathy: new perspectives and challenges. *Lancet Diabetes Endocrinol* (2020) 8:337–47. doi: 10.1016/S2213-8587(19)30411-5

7. Vasudevan L, Hoda K, Arya S, Janarthanam JB. Automated Detection and Diagnosis of Diabetic Retinopathy: A Comprehensive Survey. *J Imaging* (2021) 7(9):1–26. doi: 10.3390/jimaging7090165

8. Selvachandran G, Quek SG, Paramesran R, Ding W, Son LH. Developments in the detection of diabetic retinopathy: a state-of-the-art review of computer-aided diagnosis and machine learning methods. *Artif Intell Rev* (2022) 1–50. doi: 10.1007/s10462-022-10185-6

9. Majumder S, Deen MJ. Smartphone sensors for health monitoring and diagnosis. *Sensors (Basel)* (2019) 19:1–45. doi: 10.3390/s19092164

10. Schmidt-Erfurth U, Sadeghipour A, Gerendas BS, Waldstein SM, Bogunovic H. Artificial intelligence in retina. *Prog Retin Eye Res* (2018) 67:1–29. doi: 10.1016/j.preteyeres.2018.07.004

11. Yang WH, Zheng B, Wu MN, Zhu SJ, Fei FQ, Weng M, et al. An evaluation system of fundus photograph-based intelligent diagnostic technology for diabetic retinopathy and applicability for research. *Diabetes Ther* (2019) 10:1811–22. doi: 10.1007/s13300-019-0652-0

12. Abramoff MD, Lavin PT, Birch M, Shah N, Folk JC. Pivotal trial of an autonomous AI-based diagnostic system for detection of diabetic retinopathy in primary care offices. *NPJ Digit Med* (2018) 1:39. doi: 10.1038/s41746-018-0040-6

13. Esteva A, Robicquet A, Ramsundar B, Kuleshov V, DePristo M, Chou K, et al. A guide to deep learning in healthcare. *Nat Med* (2019) 25:24–9. doi: 10.1038/s41591-018-0316-z

14. Topol EJ. High-performance medicine: the convergence of human and artificial intelligence. *Nat Med* (2019) 25:44–56. doi: 10.1038/s41591-018-0300-7

15. Ai Z, Huang X, Fan Y, Feng J, Zeng F, Lu Y. DR-IIXRN : Detection algorithm of diabetic retinopathy based on deep ensemble learning and attention mechanism. *Front Neuroinform* (2021) 15:778552. doi: 10.3389/fninf.2021.778552

16. Ai Z, Huang X, Feng J, Wang H, Tao Y, Zeng F, et al. FN-OCT: Disease detection algorithm for retinal optical coherence tomography based on a fusion network. *Front Neuroinform* (2022) 16:876927. doi: 10.3389/fninf.2022.876927

17. Burlina P, Paul W, Liu TYA, Bressler NM. Detecting anomalies in retinal diseases using generative, discriminative, and self-supervised deep learning. *JAMA Ophthalmol* (2022) 140:185–9. doi: 10.1001/jamaophthalmol.2021.5557

18. He Y, Carass A, Zuo L, Dewey BE, Prince JL. Autoencoder based self-supervised test-time adaptation for medical image analysis. *Med Image Anal* (2021) 72:102136. doi: 10.1016/j.media.2021.102136

19. Yang J, Tao Y, Xu Q, Zhang Y, Ma X, Yuan S, et al. Self-supervised sequence recovery for semi-supervised retinal layer segmentation. *IEEE J BioMed Health Inform* (2022) 26:3872–83. doi: 10.1109/JBHI.2022.3166778

20. Chen Z, Xiong Y, Wei H, Zhao R, Duan X, Shen H. Dual-consistency semi-supervision combined with self-supervision for vessel segmentation in retinal OCTA images. *BioMed Opt Express* (2022) 13:2824–34. doi: 10.1364/BOE.458004

21. Li X, Hu X, Qi X, Yu L, Zhao W, Heng PA, et al. Rotation-oriented collaborative self-supervised learning for retinal disease diagnosis. *IEEE Trans Med Imaging* (2021) 40:2284–94. doi: 10.1109/TMI.2021.3075244

22. Yoo TK, Choi JY, Kim HK. Feasibility study to improve deep learning in OCT diagnosis of rare retinal diseases with few-shot classification. *Med Biol Eng Comput* (2021) 59:401–15. doi: 10.1007/s11517-021-02321-1

23. Hunt MS, Kihara Y, Lee AY. Novel low-shot deep learning approach for retinal image classification with few examples. *JAMA Ophthalmol* (2020) 138:1077–8. doi: 10.1001/jamaophthalmol.2020.3256

24. Gulshan V, Peng L, Coram M, Stumpe MC, Wu D, Narayanaswamy A, et al. Development and validation of a deep learning algorithm for detection of diabetic

retinopathy in retinal fundus photographs. *JAMA* (2016) 316:2402–10. doi: 10.1001/jama.2016.17216

25. Ting DSW, Cheung CY, Lim G, Tan GSW, Quang ND, Gan A, et al. Development and validation of a deep learning system for diabetic retinopathy and related eye diseases using retinal images from multiethnic populations with diabetes. *JAMA* (2017) 318:2211–23. doi: 10.1001/jama.2017.18152

26. Abramoff MD, Lou Y, Erginay A, Clarida W, Amelon R, Folk JC, et al. Improved automated detection of diabetic retinopathy on a publicly available dataset through integration of deep learning. *Invest Ophthalmol Vis Sci* (2016) 57:5200–6. doi: 10.1167/iovs.16-19964

27. Gargeya R, Leng T. Automated identification of diabetic retinopathy using deep learning. *Ophthalmology* (2017) 124:962–9. doi: 10.1016/j.ophtha.2017.02.008

28. Sayres R, Taly A, Rahimy E, Blumer K, Coz D, Hammel N, et al. Using a deep learning algorithm and integrated gradients explanation to assist grading for diabetic retinopathy. *Ophthalmology* (2019) 126:552–64. doi: 10.1016/j.ophtha.2018.11.016

29. Sahlsten J, Jaskari J, Kivinen J, Turunen L, Jaanio E, Hietala K, et al. Deep learning fundus image analysis for diabetic retinopathy and macular edema grading. *Sci Rep* (2019) 9:10750. doi: 10.1038/s41598-019-47181-w

30. Philip S, Fleming AD, Goatman KA, Fonseca S, McNamee P, Scotland GS, et al. The efficacy of automated "disease/no disease" grading for diabetic retinopathy in a systematic screening programme. *Br J Ophthalmol* (2007) 91:1512–7. doi: 10.1136/bjo.2007.119453

31. Khan SM, Liu X, Nath S, Korot E, Faes L, Wagner SK, et al. A global review of publicly available datasets for ophthalmological imaging: barriers to access, usability, and generalisability. *Lancet Digit Health* (2021) 3:e51–66. doi: 10.1016/S2589-7500(20)30240-5

32. *Drive-grand challenge official website* . Available at: https://drive.grand-challenge.org (Accessed 23/5/2021).

33. Kauppi T, Kalesnykiene V, Kamarainen J, Lensu L, Sorri I. *DIARETDB0 : Evaluation database and methodology for diabetic retinopathy algorithms* (2006). Mach Vis Pattern Recognit Res Group, Lappeenranta Univ Technol Finland. Available at: http://www.siue.edu/~sumbaug/RetinalProjectPapers (Accessed 25/5/2021).

34. Kauppi T, Kalesnykiene V, Kamarainen JK, Lensu L, Sorri I, Raninen A. The DIARETDB1 diabetic retinopathy database and evaluation protocol. *BMVC 2007 - Proc Br Mach Vis Conf* (2007) 2007:1–18. doi: 10.5244/C.21.15

35. Giancardo L, Meriaudeau F, Karnowski TP, Li Y, Garg S, Tobin KWJr., et al. Exudate-based diabetic macular edema detection in fundus images using publicly available datasets. *Med Image Anal* (2012) 16:216–26. doi: 10.1016/j.media.2011.07.004

36. Prentasic P, Loncaric S, Vatavuk Z, Bencic G, Subasic M, Tomislav R. Diabetic retinopathy image database(DRiDB): A new database for diabetic retinopathy screening programs research. *Int Symp Image Signal Process Anal ISPA* (2013) 711:711–6. doi: 10.1109/ISPA.2013.6703830

37. Decencière E, Cazuguel G, Zhang X, Thibault G, Klein JC, Meyer F. TeleOphta: Machine learning and image processing methods for teleophthalmology. *Irbm* (2013) 34:196–203. doi: 10.1016/j.irbm.2013.01.010

38. Sevik U, Kose C, Berber T, Erdol H. Identification of suitable fundus images using automated quality assessment methods. *J BioMed Opt* (2014) 19:046006. doi: 10.1117/1.JBO.19.4.046006

39. Decencière E, Zhang X, Cazuguel G, Laÿ B, Cochener B, Caroline T. Feedback on a publicly distributed image database: The messidor database. *Image Anal Stereol* (2014) 33:231–4. doi: 10.5566/ias.1155

40. Srinivasan PP, Kim LA, Mettu PS, Cousins SW, Comer GM, Izatt JA, et al. Fully automated detection of diabetic macular edema and dry age-related macular degeneration from optical coherence tomography images. *BioMed Opt Express* (2014) 5:3568–77. doi: 10.1364/BOE.5.003568

41. *Kaggle.com* . Available at: https://www.kaggle.com/c/diabetic-retinopathy-detection/data (Accessed 26/05/2021).

42. Takahashi H, Tampo H, Arai Y, Inoue Y, Kawashima H. Applying artificial intelligence to disease staging: Deep learning for improved staging of diabetic retinopathy. *PloS One* (2017) 12:e0179790. doi: 10.1371/journal.pone.0179790

43. *Rotterdam Ophthalmic data repository. re3data.org* . Available at: https://www.re3data.org/repository/r3d100012445 (Accessed 22/06/2021).

44. Porwal P, Pachade S, Kamble R, Kokare M, Deshmukh G, Sahasrabuddhe V. Indian Diabetic retinopathy image dataset (IDRiD): A database for diabetic retinopathy screening research. *Data* (2018) 3:1–8. doi: 10.3390/data3030025

45. Gholami P, Roy P, Parthasarathy MK, Lakshminarayanan V. OCTID: Optical coherence tomography image database. *Comput Electr Eng* (2020) 81:1–8. doi: 10.1016/j.compeleceng.2019.106532

46. *Kaggle.com*. Available at: https://www.kaggle.com/c/aptos2019-blindness-detection (Accessed 23/05/2021).

47. Diaz M, Novo J, Cutrin P, Gomez-Ulla F, Penedo MG, Ortega M. Automatic segmentation of the foveal avascular zone in ophthalmological OCT-a images. *PloS One* (2019) 14:e0212364. doi: 10.1371/journal.pone.0212364

48. *ODIR-2019*. Available at: https://odir2019.grand-challenge.org/ (Accessed 22/06/2021).

49. Li T, Gao Y, Wang K, Guo S, Liu H, Kang H. Diagnostic assessment of deep learning algorithms for diabetic retinopathy screening. *Inform Sci* (2019) 501:511–22. doi: 10.1016/j.ins.2019.06.011

50. Zhou Y, Wang B, Huang L, Cui S, Shao L. A benchmark for studying diabetic retinopathy: Segmentation, grading, and transferability. *IEEE Trans Med Imaging* (2021) 40:818–28. doi: 10.1109/TMI.2020.3037771

51. Soliman AZ, Silva PS, Aiello LP, Sun JK. Ultra-wide field retinal imaging in detection, classification, and management of diabetic retinopathy. *Semin Ophthalmol* (2012) 27:221–7. doi: 10.3109/08820538.2012.708812

52. Kaines A, Oliver S, Reddy S, Schwartz SD. Ultrawide angle angiography for the detection and management of diabetic retinopathy. *Int Ophthalmol Clin* (2009) 49:53–9. doi: 10.1097/IIO.0b013e31819fd471

53. Nagasawa T, Tabuchi H, Masumoto H, Enno H, Niki M, Ohara Z, et al. Accuracy of ultrawide-field fundus ophthalmoscopy-assisted deep learning for detecting treatment-naive proliferative diabetic retinopathy. *Int Ophthalmol* (2019) 39:2153–9. doi: 10.1007/s10792-019-01074-z

54. Kermany DS, Goldbaum M, Cai W, Valentim CCS, Liang H, Baxter SL, et al. Identifying medical diagnoses and treatable diseases by image-based deep learning. *Cell* (2018) 172:1122–1131 e1129. doi: 10.1016/j.cell.2018.02.010

55. Chan GCY, Kamble R, Muller H, Shah SAA, Tang TB, Meriaudeau F. Fusing results of several deep learning architectures for automatic classification of normal and diabetic macular edema in optical coherence tomography. *Annu Int Conf IEEE Eng Med Biol Soc* (2018) 2018:670–3. doi: 10.1109/EMBC.2018.8512371

56. Alsaih K, Lemaitre G, Rastgoo M, Massich J, Sidibe D, Meriaudeau F. Machine learning techniques for diabetic macular edema (DME) classification on SD-OCT images. *BioMed Eng Online* (2017) 16:68. doi: 10.1186/s12938-017-0352-9

57. Gerendas BS, Bogunovic H, Sadeghipour A, Schlegl T, Langs G, Waldstein SM, et al. Computational image analysis for prognosis determination in DME. *Vision Res* (2017) 139:204–10. doi: 10.1016/j.visres.2017.03.008

58. Molina-Casado JM, Carmona EJ, Garcia-Feijoo J. Fast detection of the main anatomical structures in digital retinal images based on intra- and inter-structure relational knowledge. *Comput Methods Programs BioMed* (2017) 149:55–68. doi: 10.1016/j.cmpb.2017.06.022

59. Moccia S, De Momi E, El Hadji S, Mattos LS. Blood vessel segmentation algorithms - review of methods, datasets and evaluation metrics. *Comput Methods Programs BioMed* (2018) 158:71–91. doi: 10.1016/j.cmpb.2018.02.001

60. Ali Shah SA, Laude A, Faye I, Tang TB. Automated microaneurysm detection in diabetic retinopathy using curvelet transform. *J BioMed Opt* (2016) 21:101404. doi: 10.1117/1.JBO.21.10.101404

61. Huang H, Ma H, Qian W. Automatic parallel detection of neovascularization from retinal images using ensemble of extreme learning machine(.). *Annu Int Conf IEEE Eng Med Biol Soc* (2019) 2019:4712–6. doi: 10.1109/EMBC.2019.8856403

62. Orlando JI, Prokofyeva E, Del Fresno M, Blaschko MB. An ensemble deep learning based approach for red lesion detection in fundus images. *Comput Methods Programs BioMed* (2018) 153:115–27. doi: 10.1016/j.cmpb.2017.10.017

63. Quellec G, Charriere K, Boudi Y, Cochener B, Lamard M. Deep image mining for diabetic retinopathy screening. *Med Image Anal* (2017) 39:178–93. doi: 10.1016/j.media.2017.04.012

64. He A, Li T, Li N, Wang K, Fu H. CABNet: Category attention block for imbalanced diabetic retinopathy grading. *IEEE Trans Med Imaging* (2021) 40:143–53. doi: 10.1109/TMI.2020.3023463

65. Lam C, Yu C, Huang L, Rubin D. Retinal lesion detection with deep learning using image patches. *Invest Ophthalmol Vis Sci* (2018) 59:590–6. doi: 10.1167/iovs.17-22721

66. Wang Y, Yu M, Hu B, Jin X, Li Y, Zhang X, et al. Deep learning-based detection and stage grading for optimising diagnosis of diabetic retinopathy. *Diabetes Metab Res Rev* (2021) 37:e3445. doi: 10.1002/dmrr.3445

67. Liefers B, Venhuizen FG, Schreur V, van Ginneken B, Hoyng C, Fauser S, et al. Automatic detection of the foveal center in optical coherence tomography. *BioMed Opt Express* (2017) 8:5160–78. doi: 10.1364/BOE.8.005160

68. Schlegl T, Waldstein SM, Bogunovic H, Endstrasser F, Sadeghipour A, Philip AM, et al. Fully automated detection and quantification of macular fluid in OCT using deep learning. *Ophthalmology* (2018) 125:549–58. doi: 10.1016/j.ophtha.2017.10.031

69. Holmberg OG, Köhler ND, Martins T, Siedlecki J, Herold T, Keidel L, et al. Self-supervised retinal thickness prediction enables deep learning from unlabelled data to boost classification of diabetic retinopathy. *Nat Mach Intell* (2020) 2:719–26. doi: 10.1038/s42256-020-00247-1

70. Guo Y, Camino A, Wang J, Huang D, Hwang TS, Jia Y. MEDnet, a neural network for automated detection of avascular area in OCT angiography. *BioMed Opt Express* (2018) 9:5147–58. doi: 10.1364/BOE.9.005147

71. Hecht I, Bar A, Rokach L, Noy Achiron R, Munk MR, Huf W, et al. Optical coherence tomography biomarkers to distinguish diabetic macular edema from pseudophakic cystoid macular edema using machine learning algorithms. *Retina* (2019) 39:2283–91. doi: 10.1097/IAE.0000000000002342

72. Li X, Jiang Y, Zhang J, Li M, Luo H, Yin S. Lesion-attention pyramid network for diabetic retinopathy grading. *Artif Intell Med* (2022) 126:102259. doi: 10.1016/j.artmed.2022.102259

73. Prahs P, Radeck V, Mayer C, Cvetkov Y, Cvetkova N, Helbig H, et al. OCT-based deep learning algorithm for the evaluation of treatment indication with anti-vascular endothelial growth factor medications. *Graefes Arch Clin Exp Ophthalmol* (2018) 256:91–8. doi: 10.1007/s00417-017-3839-y

74. Diabetic Retinopathy Clinical Research N, Wells JA, Glassman AR, Ayala AR, Jampol LM, Aiello LP, et al. Aflibercept, bevacizumab, or ranibizumab for diabetic macular edema. *N Engl J Med* (2015) 372:1193–203. doi: 10.1056/NEJMoa1414264

75. Penha FM, Gregori G, Garcia Filho CA, Yehoshua Z, Feuer WJ, Rosenfeld PJ. Quantitative changes in retinal pigment epithelial detachments as a predictor for retreatment with anti-VEGF therapy. *Retina* (2013) 33:459–66. doi: 10.1097/IAE.0b013e31827d2657

76. Schmidt-Erfurth U, Waldstein SM, Deak GG, Kundi M, Simader C. Pigment epithelial detachment followed by retinal cystoid degeneration leads to vision loss in treatment of neovascular age-related macular degeneration. *Ophthalmology* (2015) 122:822–32. doi: 10.1016/j.ophtha.2014.11.017

77. Arnold JJ, Markey CM, Kurstjens NP, Guymer RH. The role of sub-retinal fluid in determining treatment outcomes in patients with neovascular age-related macular degeneration–a phase IV randomised clinical trial with ranibizumab: the FLUID study. *BMC Ophthalmol* (2016) 16:31. doi: 10.1186/s12886-016-0207-3

78. Waldstein SM, Philip AM, Leitner R, Simader C, Langs G, Gerendas BS, et al. Correlation of 3-dimensionally quantified intraretinal and subretinal fluid with visual acuity in neovascular age-related macular degeneration. *JAMA Ophthalmol* (2016) 134:182–90. doi: 10.1001/jamaophthalmol.2015.4948

79. Silva R, Berta A, Larsen M, Macfadden W, Feller C, Mones J, et al. Treat-and-Extend versus monthly regimen in neovascular age-related macular degeneration: Results with ranibizumab from the TREND study. *Ophthalmology* (2018) 125:57–65. doi: 10.1016/j.ophtha.2017.07.014

80. Sun JK, Aiello LP, Abramoff MD, Antonetti DA, Dutta S, Pragnell M, et al. Updating the staging system for diabetic retinal disease. *Ophthalmology* (2021) 128:490–3. doi: 10.1016/j.ophtha.2020.10.008

81. Cheung CY, Xu D, Cheng CY, Sabanayagam C, Tham YC, Yu M, et al. A deep-learning system for the assessment of cardiovascular disease risk *via* the measurement of retinal-vessel calibre. *Nat BioMed Eng* (2021) 5:498–508. doi: 10.1038/s41551-020-00626-4

82. Seidelmann SB, Claggett B, Bravo PE, Gupta A, Farhad H, Klein BE, et al. Retinal vessel calibers in predicting long-term cardiovascular outcomes: The atherosclerosis risk in communities study. *Circulation* (2016) 134:1328–38. doi: 10.1161/CIRCULATIONAHA.116.023425

83. Zhang K, Liu X, Xu J, Yuan J, Cai W, Chen T, et al. Deep-learning models for the detection and incidence prediction of chronic kidney disease and type 2 diabetes from retinal fundus images. *Nat BioMed Eng* (2021) 5:533–45. doi: 10.1038/s41551-021-00745-6

84. Simo R, Ciudin A, Simo-Servat O, Hernandez C. Cognitive impairment and dementia: a new emerging complication of type 2 diabetes-the diabetologist's perspective. *Acta Diabetol* (2017) 54:417–24. doi: 10.1007/s00592-017-0970-5

85. Cheung CY, Ikram MK, Chen C, Wong TY. Imaging retina to study dementia and stroke. *Prog Retin Eye Res* (2017) 57:89–107. doi: 10.1016/j.preteyeres.2017.01.001

86. Ciudin A, Simo-Servat O, Hernandez C, Arcos G, Diego S, Sanabria A, et al. Retinal microperimetry: A new tool for identifying patients with type 2 diabetes at risk for developing Alzheimer disease. *Diabetes* (2017) 66:3098–104. doi: 10.2337/db17-0382

87. Simo-Servat O, Ciudin A, Ortiz-Zuniga AM, Hernandez C, Simo R. Usefulness of eye fixation assessment for identifying type 2 diabetic subjects at risk of dementia. *J Clin Med* (2019) 8:1–12. doi: 10.3390/jcm8010059

88. Cheung CY, Tay WT, Ikram MK, Ong YT, De Silva DA, Chow KY, et al. Retinal microvascular changes and risk of stroke: the Singapore Malay eye study. *Stroke* (2013) 44:2402–8. doi: 10.1161/STROKEAHA.113.001738

89. Yip W, Ong PG, Teo BW, Cheung CY, Tai ES, Cheng CY, et al. Retinal vascular imaging markers and incident chronic kidney disease: A prospective cohort study. *Sci Rep* (2017) 7:9374. doi: 10.1038/s41598-017-09204-2

90. Poplin R, Varadarajan AV, Blumer K, Liu Y, McConnell MV, Corrado GS, et al. Prediction of cardiovascular risk factors from retinal fundus photographs *via* deep learning. *Nat BioMed Eng* (2018) 2:158–64. doi: 10.1038/s41551-018-0195-0

91. Ting DSW, Wong TY. Eyeing cardiovascular risk factors. *Nat BioMed Eng* (2018) 2:140–1. doi: 10.1038/s41551-018-0210-5

92. Ting DSW, Peng L, Varadarajan AV, Keane PA, Burlina PM, Chiang MF, et al. Deep learning in ophthalmology: The technical and clinical considerations. *Prog Retin Eye Res* (2019) 72:100759. doi: 10.1016/j.preteyeres.2019.04.003

93. He J, Baxter SL, Xu J, Xu J, Zhou X, Zhang K. The practical implementation of artificial intelligence technologies in medicine. *Nat Med* (2019) 25:30–6. doi: 10.1038/s41591-018-0307-0

94. Li F, Pan J, Yang D, Wu J, Ou Y, Li H, et al. A multicenter clinical study of the automated fundus screening algorithm. *Transl Vis Sci Technol* (2022) 11:22. doi: 10.1167/tvst.11.7.22

95. Han R, Cheng G, Zhang B, Yang J, Yuan M, Yang D, et al. Validating automated eye disease screening AI algorithm in community and in-hospital scenarios. *Front Public Health* (2022) 10:944967. doi: 10.3389/fpubh.2022.944967

frontiers | Frontiers in Endocrinology

TYPE Original Research
PUBLISHED 16 November 2022
DOI 10.3389/fendo.2022.945446

OPEN ACCESS

EDITED BY
Jing Li,
Capital Normal University, China

REVIEWED BY
Weihong Yu,
Peking Union Medical College Hospital (CAMS), China
Yuqin Wang,
Wenzhou Medical University, China

*CORRESPONDENCE
Qin Xiao
hanxiaoqin1981@163.com

†These authors have contributed equally to this work

SPECIALTY SECTION
This article was submitted to Molecular and Structural Endocrinology, a section of the journal Frontiers in Endocrinology

RECEIVED 16 May 2022
ACCEPTED 25 July 2022
PUBLISHED 16 November 2022

CITATION
Xiao Q, Sun Y-Y, Lu Z-J, Li S-s, Su R, Chen W-L, Ran L-L, Zhang S, Deng K, Yu W-Z and Chen W (2022) Protective effects of safranal on diabetic retinopathy in human microvascular endothelial cells and related pathways analyzed with transcriptome sequencing. *Front. Endocrinol.* 13:945446. doi: 10.3389/fendo.2022.945446

Protective effects of safranal on diabetic retinopathy in human microvascular endothelial cells and related pathways analyzed with transcriptome sequencing

Qin Xiao[1*†], Yao-Yao Sun[2,3,4,5†], Zhan-Jun Lu[1], Shan-shan Li[1], Riguga Su[6], Wen-Lin Chen[6], Lin-Lin Ran[6], Surina Zhang[7], Kaixin Deng[8], Wen-Zhen Yu[2,3,4,5] and Wenqian Chen[2,3,4,5]

[1]Department of Ophthalmology, Affiliated Hospital of Inner Mongolia University for Nationalities, Tongliao, China, [2]Department of Ophthalmology, Peking University People's Hospital, Beijing, China, [3]Eye diseases and Optometry Institute, Beijing, China, [4]Beijing Key Laboratory of Diagnosis and Therapy of Retinal and Choroid Diseases, Beijing, China, [5]College of Optometry, Peking University Health science center, Beijing, China, [6]College of Clinical (Mongolian) Medicine, Inner Mongolia University for Nationalities, Tongliao, China, [7]Department of Hematology, Affiliated Hospital of Inner Mongolia University for Nationalities, Tongliao, China, [8]Department of Ophthalmology, Beijing Jishuitan Hospital, Beijing, China

Aim: To determine the effect of safranal on diabetic retinopathy *in vitro* and its possible mechanisms.

Methods: We used human retinal microvascular endothelial cells (HRMECs) to test the influence of safranal *in vitro*. High glucose damage was established and an safranal was tested at various concentrations for its potential to reduce cell viability using the MTT assay. We also employed apoptosis detection, cell cycle detection, a transwell test, and a tube formation assay to look into safranal's inhibitory effects on high glucose damage at various doses. Furthermore, mRNA transcriptome sequencing was performed. mRNA expression levels in a high glucose damage model, a high glucose damage model treated with safranal, and a blank control were compared to find the possible signaling pathway. Western blotting was used to confirm the expressions of several molecules and the levels of phosphorylation in each for the newly discovered pathway.

Results: Cell proliferation was inhibited under a high glucose condition but could be protected by safranal at different concentrations ($P<0.001$). Flow cytometry results suggested safranal also protected cells from apoptosis ($P=0.006$). A transwell test demonstrated reduced invasiveness of safranal-treated cells in a high glucose condition ($P<0.001$). In a tube formation investigation, there were noticeably more new branches in the high gloucose group compared to a high glucose treated with safranal group ($P<0.001$). In mRNA expression patterns on transcriptome sequencing, the MAPK signaling pathway showed an expression ratio. With western blotting, the phosphorylation level of p38-AKT was elevated

under a high glucose condition but could be inhibited by safranal. The expression of molecules associated with cell adhesion, including E-cadherin, N-cadherin, Snail, Twist, and fibronectin also changed significantly after safranal treatment under a high glucose condition.

Conclusion: Safranal can protect diabetic retinopathy *in vitro*, and the p38-AKT signaling pathway was found to be involved in the pathogenesis of diabetic retinopathy and could be inhibited by safranal. This pathway may play a role by influencing cell migration and adhesion.

KEYWORDS

diabetic retinopathy, safranal, high glucose, transcriptomics, human retinal microvascular endothelial cells

Introduction

Diabetic retinopathy (DR) is the most prevalent and distinct microvascular diabetic complication. In individuals aged 20 to 74 years, it is still the major cause of vision loss and preventable blindness, especially in middle- and high-income nations (1, 2). According to Zhen et al., in 2020, 103.12 million adults worldwide were forecast to have DR. By 2045, that figure is expected to rise to 160.50 million (3). The number of persons who lose their vision due to DR is likely to continue to climb and will become an even more critical issue in the future.

DR is thought to be a microvascular disease. Through influences on cellular metabolism, signaling, and growth factors, several biochemical processes have been postulated to modulate the pathogenesis of DR (4). Recently, people have investigated the mechanisms of high glucose damage on vascular alterations and DR development (5). As an illustration, it was discovered that high glucose causes the production of inflammatory intermediates, the breaching of the blood-retina barrier, the demise of pericytes, and an increase in vascular permeability, all of which contribute to the progression of DR phases and the development of vascular dysfunctions (6, 7).

Attempts to uncover novel therapeutic targets have been made despite tremendous breakthroughs in the treatment of DR. Antioxidative stress is gaining attention as a potential treatment for DR. A classical antioxidant; i.e., safranal (systematic name 2,6,6-trimethylcyclohexa3,1-din-1-carboxaldehyde), is a compound of volatile carboxaldehyde (8) and a major constituent of saffron. Safranal has a wide spectrum of biological actions, including anti-inflammatory, anti-cancer, and antigenotoxic characteristics (9, 10).. In DR patients, precursors of safranal, such as crocin, have been reported to be utilized to reduce microglial activation (11). It can also reduce central macular thickness and increase best-corrected visual acuity (12). Our previous study revealed an inhibitory function for safranal on chroidal neovascularization. However, the role of safranal in DR and the mechanisms involved have not been well investigated.

This study aimed to ascertain whether safranal was protective for DR *in vitro* and to elucidate the mechanism behind this effect. With human retinal microvascular endothelial cells(HRMECs), we verified the protective effect of safranal on DR under severe glucose damage *in vitro*. Finally, we identified and confirmed the potential pathway involved in using transcriptome sequencing.

Methods

Cell viability

Cellular viability of HRMECs was analyzed using an MTT assay (MTT Cell Proliferation and Cytotoxicity Assay Kit; Beyotime, Shanghai, China) according to the manufacturer's instructions and as previously reported (13). Cells were plated at 5×10^4 per well in 96-well plates, and cell proliferation was measured. High glucose was added to the wells at different concentrations. 10 μL of safanal were added to create an experimental group and 10 μL of added phosphate-buffered saline (PBS) was used as the blank control. Cells were cultured at 37°C. 10 μL of MTT were added into each well and incubated at 37°C for 4 h and then the absorbance (A) of each well was estimated at 568 nm. Each experiment was repeated in five wells and was duplicated at least three times. Optical density (OD) values were obtained and the inhibition rate was calculated as (1-OD experiment group/OD negative control group) ×100% As

previously reported, the MTT assay (MTT Cell Proliferation and Cytotoxicity Assay Kit; Beyotime, Shanghai, China) was used to evaluate the cellular viability of HRMECs. Cell proliferation was assessed after cells were plated in 96-well plates at a density of 5×10^4 per well. The wells received additions of high glucose at various concentrations. The experimental group received 10 μL of safanal, and the blank control received 10 μL of phosphate-buffered saline (PBS). At 37°C, cells were cultured. Each well received 10 μL of MTT, which was then added, and each well's absorbance (A) was calculated at 568 nm after being incubated at 37°C for 4 hours. Each experiment was done at least three times in 5 distinct wells. The inhibition rate was estimated as (1-OD experiment group/OD negative control group) 100% using the optical density (OD) values (10, 14).

Flow cytometric analysis

A FITC Annexin V Apoptosis Detection Kit (BD Biosciences, San Diego, CA) was used to quantify apoptosis in accordance with the manufacturer's recommendations. In summary, HRMECs (1×10^6) were plated in six-well plates and exposed to high glucose, high glucose with safranal, or a control solution for 24, 48, or 72 hours. Following EDTA-mediated cell detachment, the cells were washed in cold PBS and stained with annexin V-FITC and propidium iodide (PI). Flow cytometry analysis was carried out immediately (excitation 488 nm; emission 530 nm). CellQuest software was used to analyze the samples using flow cytometry (FACSCalibur; BD Biosciences) (BD Biosciences). The percentage of early apoptotic cells (LR) plus late apoptotic cells was used to compute the apoptotic rate (UR) (15). The CycleTESTTM Plus DNA Reagent Kit (BD Biosciences) was used to stain cells with PI for cell cycle analysis, and FACScan was used to analyze the results. Cells in the G0/G1, S, and G2/M stages were enumerated, and their percentages were compared.

Migration

As previously mentioned (14, 15), migration was evaluated using a transwell (Corning Life Sciences, Lowell, MA) with an 8.0 m pore size. Briefly, 2×10^4 cells in 200 μL of serum-free media were added to the transwell's top. A final amount of 600 μL of DMEM (with 10% FBS) was added to the bottom chamber. Every migration test was run for 5 hours at 37°C. The cells were stained with 4,6-diamidino-2- phenylindole (DAPI; Roche Diagnostics, Indianapolis, IN) for 15 minutes after the assay and then fixed in 4% paraformaldehyde. A cotton swab was used to remove the immobile cells so the membrane could be photographed. Five arbitrary fields of view's worth of cells were counted.

Tube formation

Cells were grown with high glucose, high glucose plus safranal, or a negative control solution at a density of 2×10^5 cells per well. According to the manufacturer's directions and our earlier research, 48-well plates were filled with 150 μL of matrigel (Cat# 354234; BD Sciences, Franklin Lakes, NJ) solution and incubated at 37°C for 0.5 h. The matrigel was seeded with HRMECs (5×10^4 per well), which were then cultivated for 2–8 hours. Matrigel networks were counted and taken pictures of. Image J software was used to count the new branches and branch nodes (National Institutes of Health, Bethesda, MD). Three times the experiments were conducted (10, 16).

Transcriptome sequencing

Three groups were created after counting the cells: Negative control, high glucose damage model treated with high glucose (10 μL, 25 mol/L), and high glucose damage model treated with safranal (10 μL, 80 g/mL) are the three options. As previously mentioned, cells were cultured. As previously reported (10, 16), RNA samples were isolated and identified. With the use of oligo (dT)-coupled magnetic beads, mRNA was amplified; random hexamers were used to create single-stranded cDNA; and buffer, dNTPs, DNA polymerase I, and RNase H were used to create double-stranded cDNA. The end of the purified double-stranded cDNA was first repaired, then an A tail addition was added, the sequencing connector was connected, and finally the fragment size was chosen using AMPure XP beads.The final step was performing PCR amplification and purifying the PCR output with AMPure XP beads to create the final library. Different libraries were pooled into the flow cell in accordance with the effective concentration and the demands of the target dismount data volume after the library detection was qualified. Following cBOT clustering, sequencing was carried out using an Illumina high-throughput sequencing platform.

Western blotting

HRMECs were counted and separated into three groups: a negative control; a high glucose damage model treated with safranal (10 μL, 80 g/mL); and a high glucose damage model treated with high glucose (10 μL, 25 mol/L). A Bio-Rad test kit was used to extract the cells' total protein and evaluate the protein content (Bio-Rad, Hercules, CA, USA). Equal amounts of protein (30 μg) were resolved on polyacrylamide gels containing 12% Tris-HCl before being transferred to a PVDF blotting membrane (Millipore, Billerica, MA, USA). After blocking, specific antibodies against phosphate-extracellular

regulated protein kinases (p-ERK), total-ERK (t-ERK), p-P38, t-P38, p-serine/threonine kinase (AKT), t-AKT (1:2000, Santa Cruz, CA, USA), E-cadherin, N-cadherin, Snail, Twist, Fibronectin(1:2000, Santa Cruz, CA, USA) and beta actin (1:2,000, Abcam, Cambridge, MA, USA), were treated with the membranes. The protein bands were detected by chemiluminescence after the blots had been carefully washed and treated with peroxidase-conjugated goat anti-rabbit or anti-mouse secondary antibodies (1:1,000, ZSGB-Bio, Beijing, China) (Pierce, Rockford, IL, USA). Three times the experiment was conducted (10).

Statistical analysis

Each of the tests were conducted three times, and the data are shown as the mean standard error of the mean (SEM). A one-way ANOVA was used for three groups or more and the Student's t test was used for two groups. Statistics were considered significant if $P<0.05$. Using SPSS 17.0, all data analysis were carried out (Chicago, IL, USA).

Results

Safranal shows a protective effect of cell proliferation on high glucose damage in HRMECs

In order to determine the appropriate glucose concentration for construction of the high glucose damage model, we investigated the effect of different concentrations of glucose on cells of 0 μM, 5 μM, 10 μM, 15 μM, 20 μM, 25 μM, 30 μM, 35 μM, 40 μM, 45 μM, and 50 μM. We found a dose-dependent effect on cell proliferation, where the IC50 of glucose was 26.95 (Figure 1A). Combining our result with previous report, we chose 25 μM as the concentration for subsequent experiments, we chose 25 μM as the concentration for subsequent experiments (17). At a high glucose concentration of 25 μM, we screened different safranal concentration gradients (5 μM, 10 μM, 20 μM, 40 μM, 80 μM, 160 μM, and 320 μM). After three days of cell culture, we found a similar dose-dependent effect of safranal on cell proliferation. Although high glucose inhibited cell proliferation, this inhibitory effect was ameliorated with higher safranal doses. When the concentration exceeded 160 μM, however, there was an effect of toxicity (Figure 1B). Therefore, we chose 80 μM as the final concentration for further study. We further investigated cell proliferation, and after five days of co-culture, we found that, cell growth was decreased in the presence of high glucose damage, but safranal exhibited a protective impact in comparison to the control, and this protective effect became more pronounced with longer safranal incubation time. ($P<0.001$; Figure 1C).

Safranal protects HRMECs from apoptosis and affects the cell cycle under a high glucose condition and *in vitro*

The effects of safranal on apoptosis in HRMECs was assessed by A FITC Annexin V Apoptosis Detection Kit. As shown in Figures 2A, B, under high sugar conditions, more cells underwent apoptosis. However, this apoptosis was inhibited after the treatment with safranal. Under a high glucose condition, HRMECs treated with safranal showed a significantly lower percentage of apoptotic cells ($P=0.006$).

Next, we examined the effect of safranal on the cell cycle G1 or S phase by using flow cytometry analysis. From Figures 2C, D, we found that high glucose reduced the cell number in phase G1, while the number in phase S were increased. After safranal treatment, however, we found more cells in the G1 phase and fewer cells in phase S ($P<0.001$). These results suggested that safranal could inhibit cell apoptosis and affect the cell cycle.

Safranal inhibits cell migration of HRMECs *in vitro*

Along with the cell proliferation investigation, we also investigated into whether safranal affects HRMEC migration, a critical stage in the creation of vessels. The modified Boyden chamber test was used. According to Figures 3A, B, more cells went through the membrane under the high glucose condition than they did under the negative control. Cellular migration was, however, inhibited by safranal. The high glucose group and the high glucose group treated with safranal differed significantly. ($P<0.001$; Figures 3A, B).

Safranal inhibits tube formation of HRMECs *in vitro*

In the *in vitro* tube formation investigation, higher tube development was seen when the glucose level was high. However, the 80 μM safranal-cultured HRMECs showed a reduced ability to develop a normal vascular network. In comparison to the control groups, the network's number of new branches and branch nodes dramatically dropped. ($P<0.001$; Figures 3C, D).

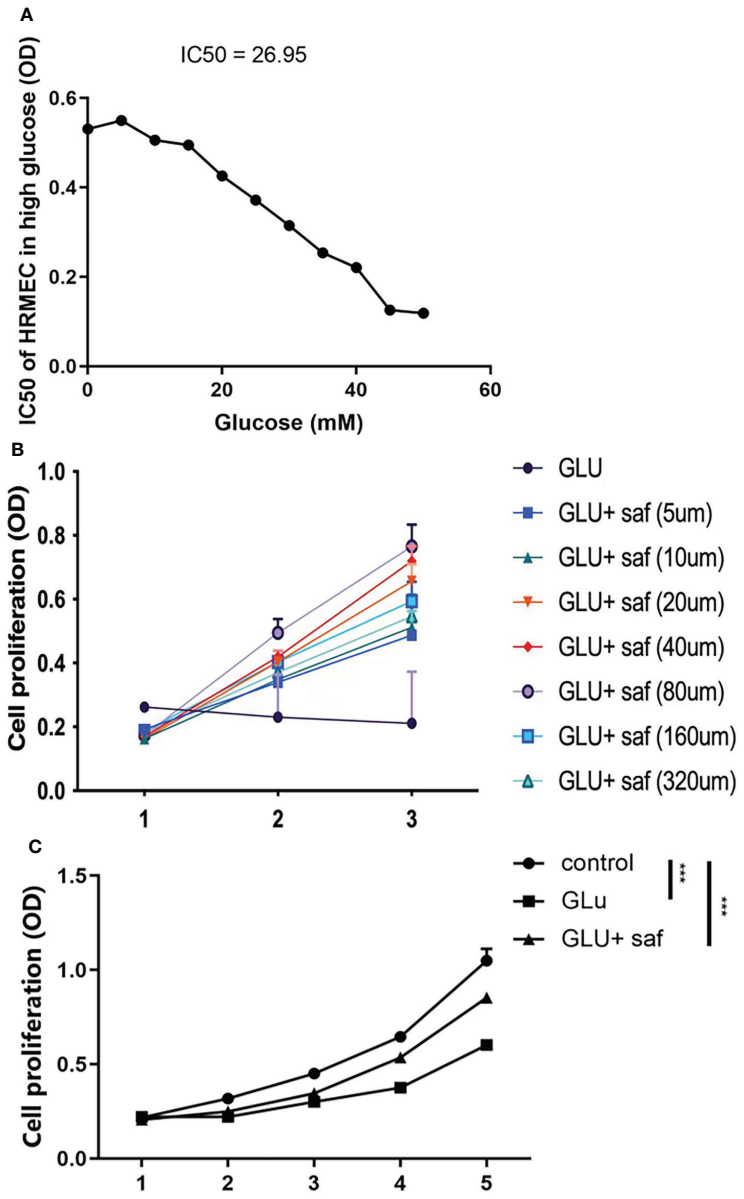

FIGURE 1
Safranal's protective effect on cell proliferation in HRMECs in high glucose damage conditions. **(A)** shows that under different concentrations of glucose, cell proliferation was inhibited with an IC50 of 26.95. Cell proliferation was protected under different concentration of safranal while 80 μM demonstrated the best protection effect **(B)**. After five days of incubation, safranal had a better protective effect on cell proliferation over time $P<0.001$; **(C)**.

Pathways involved in cellular high glucose damage and the effect of safranal identified with transcriptome sequencing

Figure 4A shows the heat map of the three groups, including the negative control, high glucose group, and high glucose treated with the safranal group. Figures 4B, C demonstrate the Kyoto Encyclopedia of Genes and Genomes (KEGG) and Gene Ontology (GO) results between the high glucose group and high glucose treated with the safranal group. From the KEGG results for these two groups, after safranal treatment, the ribosome pathway, Parkinson's disease-related pathway, and cytokine receptor interaction pathways are the major activation pathways. In contrast, the dilated cardiomyophaty pathway and phosphatidylinositol signalings system pathway are the major inhibition pathways. From the GO results for these two groups, after safranal treatment, the ribosome pathway,

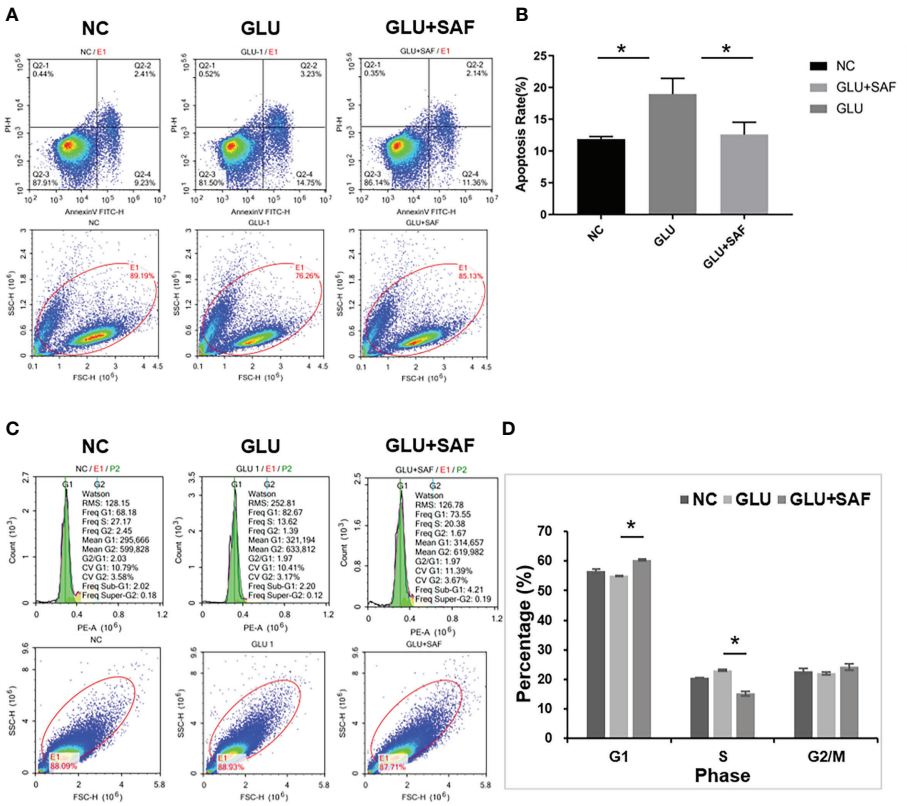

FIGURE 2
Flow cytometry results. The apoptosis rate varied indifferent groups:negative control, high glucose group, and high glucose group treated with safranal P=0.006, **(A, B)**. Regarding the cell cycle, compared with the high glucose group, there were more cells in phase G1 but fewer cells in phase S in the high glucose treated with safranal group P<0.001; **(C, D)**. * means a statistically significant difference.

structural constituent of the ribosome pathway, ribosomal subunit pathway, and response to bacterium were the major activation pathways, while mitochondrial outer membrane permeabilization, the cellular amino acid biosynthetic process pathway, and the serine metabolic process pathway were the major inhibition pathways. After analyzing the data from both the KEGG results and GO results, the mitogen-activated protein kinase (MAPK) signaling pathway was activated in the high glucose group and suppressed in the safranal-treated group; it is suggested that safranal treatment DR through this signaling pathway (Figure 4D). Figure 4E demonstrates the changes in the specific and detailed signaling of the MAPK pathways from KEGG and GO results.

P38-AKT signaling pathway confirmed by western blotting

Western blot analysis was used to confirm the MAPK members, including P38 and the ERK-related pathway, that transcriptome sequencing had identified. Basically, western blot analysis of p-P38, t-P38, p-ERK, t-ERK, p-PDK1/2, p-AKT, and t-AKT was carried out, with beta actin serving as an internal loading control. We found that under a high glucose condition or after safranal treatment, there was no difference in protein expressions for both p-ERK and t-ERK. On the other hand, the phosphorylation levels of p38 and AKT were elevated in the high glucose group compared with the levels in the negative control group. Under safranal treatment, however, the phosphorylation levels of P38 and AKT were downregulated. As a result, p38-AKT but not the ERK pathway was shown to be possibly involved in the protective effect of safranal on DR. However, further experiments are still needed to explore the intracellular mechanisms (Figure 5).

E-cadherin, N-cadherin, snail, twist, and fibronectin were found to involve in the protection of DR by safranal

Factors related to cell adhesion and migration, including E-cadherin, N-cadherin, Snail, Twist, and fibronectin were also

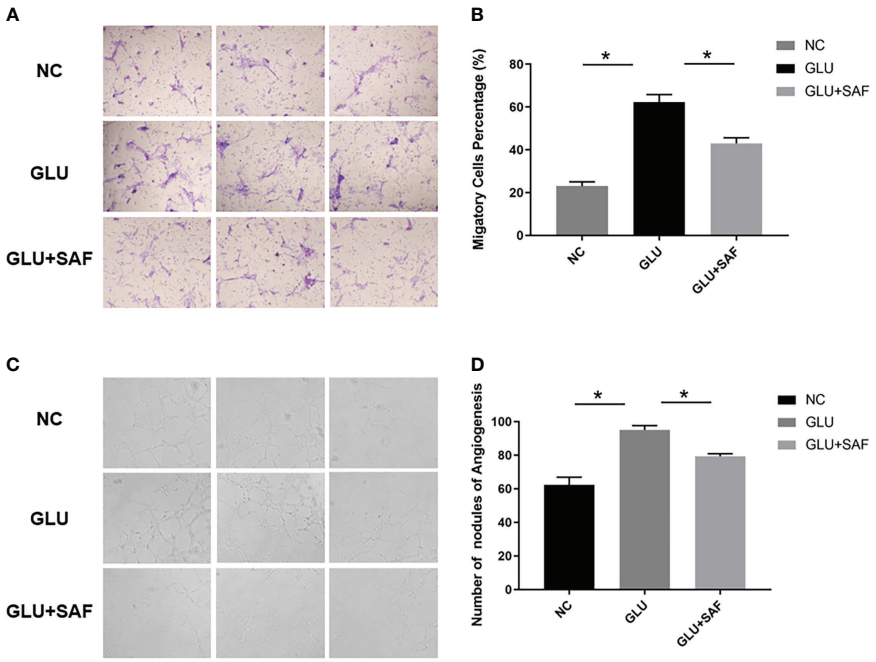

FIGURE 3
Cell migration and tube formation results. Under high glucose, more cells were found to migrate through the membrane. After safranal treatment, the migration rate decreased significantly P<0.001, **(A, B)**. There were more new vessel branches and nodes in the high glucose group but both decreased after safranal treatment P<0.001, **(C, D)**. * means a statistically significant difference.

analyzed. Under a high glucose condition, the protein expressions of all these factors were upregulated, except for E-cadherin, demonstrating that high glucose could promote cell adhesion and migration. After safranal treatment, however, the protein expression was decreased for all the factors investigated, except for E-cadherin. E-cadherin demonstrated a total reversed change in that the expression was decreased under a high glucose condition but was increased after safranal treatment. These results indicated that safranal inhibits DR mainly by inhibiting cell adhesion and migration in the presence of high glucose.

Discussion

In the present research, we demonstrated that safranal had a protective effect on DR *in vitro*. The function of safranal was verified in cells under hyper-glucose conditions. Transcriptome sequencing has been used to further investigate the potential signaling pathway, and it revealed the P38-AKT pathway as being connected to hyper-glucose damage in cells, with the potential for safranal to block this effect. Furthermore, this pathway mainly affects the adhesion and migration-related molecules of cells. Our results confirm that safranal may have a protective effect against DR *in vitro* and that the P38-AKT pathway may be involved. This is the first report on this pathway having a protective effect with safranal treatment for DR.

There have been many attempts to explore ways to slow the progression of DR to the proliferative stage. Many drugs are still being studied, and their preventive or therapeutic properties need to be investigated further. Pharmaceutical investigations have revealed saffron's component; i.e., safranal, which possesses antioxidant, anti-apoptotic, and anti-inflammatory properties (10). Safranal decreased caspase-3, tumor necrosis factor-alpha (TNF-), or superoxide dismutase (SOD) activity in diabetic rats, according to Malekzadeh et al. (18). In our study, the protective influence of safranal on DR was verified. Safranal could protect cells from the effects of high glucose on cell proliferation, reduce apoptosis, and inhibit cell migration and tube formation, similar to the previous report.

To determine the possible mechanism of how safranal protects DR, transcriptome sequencing was performed to learn more about how safranal functions in cells under high glucose circumstances. The P38-AKT signaling pathway was discovered to be involved in the hyper-glucose injury process in cells after Western blotting confirmed it. Additionally, safranal has the potential to block this signaling pathway. The mitogen-activated protein kinase (MAPK)/p38 signaling pathway is widely known for playing a pivotal role in cell survival and death (19, 20).

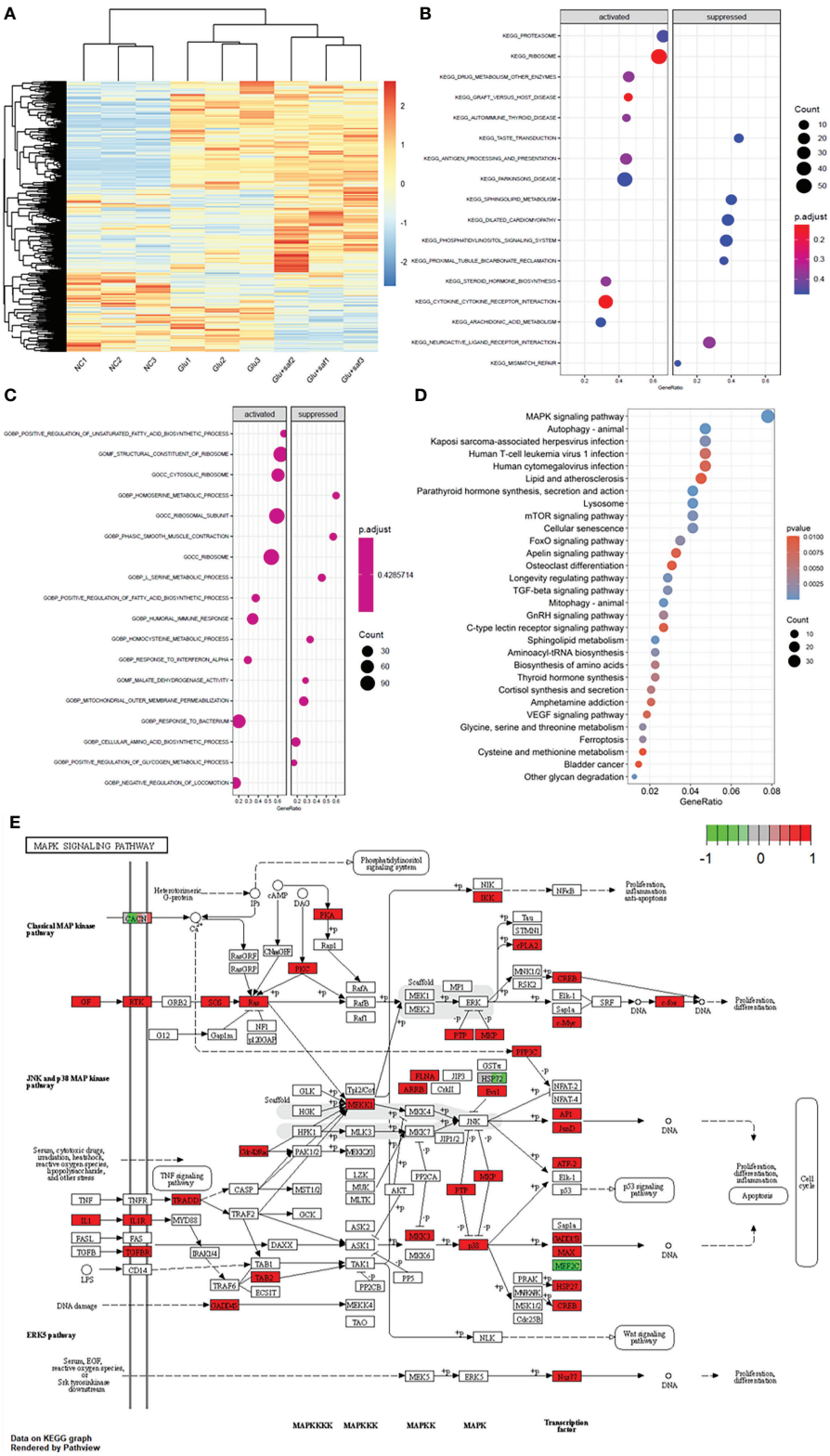

FIGURE 4
Transcriptome sequencing results. **(A)** shows the heat map of the three groups including the negative control, high glucose group, and high glucose treated with safranal group. **(B, C)** demonstrate the Kyoto Encyclopedia of Genes and Genomes (KEGG) and Gene Ontology (GO) results between the high glucose group and high glucose treated with safranal group. From the bubble graph, the MAPK signaling pathway demostrateda high gene ratio **(D)** and the detailed pathway was demonstrated in **(E)**.

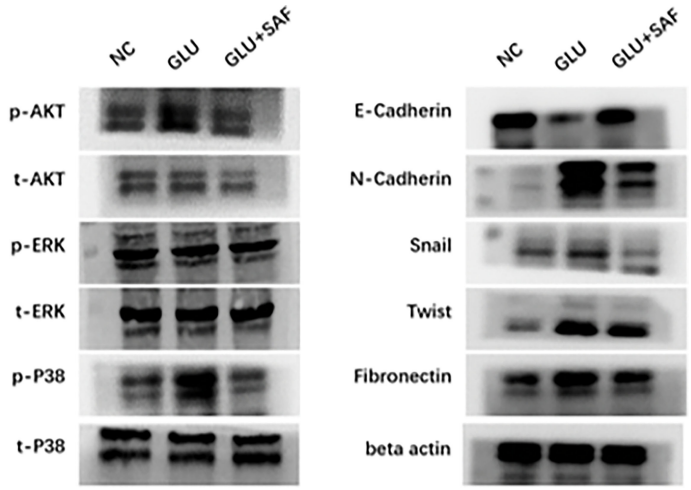

FIGURE 5
Western blot results. Western blot results showing the phosphorylation changes in the p38-AKT signaling pathway. The phosphorylation level of p38 was elevated in the high glucose condition but was inhibited by safranal. However, there was no change in the phosphorylation level of ERK. Under a high glucose condition, the protein expression of factors related to cell migration and adhesion, including N-cadherin, Snail, Twist, and fibronectin were upregulated in a high glucose condition and could be inhibited by safranal. E-cadherin, on the other hand, demonstrated an opposite expression trend.

Targeting the p38 signaling pathway has been shown to influence pathological angiogenesis and tissue repair in other investigations (21). Thus far, research had been conducted on the relationship between P38 and DR. In DR, for example, Zou et al. discovered that p38 might increase retinal micro-angiogenesis by upregulating RUNX1 expression. The p38-MAPK pathway was also found to be activated in diabetic rat model retinopathy with microvascular disease (22). These results confirm our findings, which show that the p38 signaling pathway contributes to the development of DR and that safranal effectively inhibits p38 expression in a model of cellular damage brought on by excess glucose, thus avoiding DR.

When p38 is activated, it causes a cascade of events in downstream signaling pathways, including the phosphorylation of AKT. Cell proliferation, migration, adhesion, apoptosis, and angiogenesis are all regulated by the conventional AKT signaling pathway. In ophthalmological research, the AKT pathway has also been linked to the onset and progression of neovascularization (23, 24). For example, changes in p38 and AKT have been widely shown to be involved in the pathology of DR. However, the ability of the pathogenic effect of this pathway on DR to be protected by safranal is the first report. In our study, however, molecules associated with cell migration and adhesion, including E-cadherin, N-cadherin, Snail, Twist, and fibronectin were also found to participate in safranal protection against DR, so we suggest that changes in AKT mainly affect cell adhesion and migration and thus DR formation. These factors ultimately affect the formation of neovascularization in DR by participating in the migration and adhesion of vascular endothelium cells. When exposed to high glucose, Zhou et al. found that the expression of Snail and N-cadherin levels were increased in Müller cells, which suggested those mesenchymal proteins play an important role in the development of DR. E-cadherin, on the other hand, demonstrated a total opposite expression trend. E-cadherin is closely related to the tight junction of vascular endothelium cells and inner blood-retinal barrier (25). Under the condition of high glucose, the decrease in E-cadherin expression indicates the potential destruction of iBRB (26), while safranal increased the expression of E-cadherin, thus protecting iBRB. Further research is necessary to determine whether safranal's intervention in DR also involves these other signaling pathways.

This study was unable to determine whether safranal's effect on DR is directly related to suppression of the P38-AKT pathway. More research is needed to determine the significance of this signaling pathway in safranal's protection against DR. In addition, other potential DR pathways, such as the VEGF signaling system, were not examined in this study. Further research on the pathophysiology of DR and potential treatment targets is required. Another limitation of the present experiment is that we only performed *in vitro* experiments but not *in vivo* experiments. In future, we need to conduct further *in vivo* experiments to further validate the protective effect of safranal on DR and related pathways.

Data availability statement

The data presented in the study are deposited in the link as https://datadryad.org/stash/share/K2mdS4ReytQYjgRa5sT-C_4OVs7bF3aKv46rjcvibEM.

Author contributions

All the authors contributed to Conceptualization, Methodology, Software, Investigation, Formal Analysis, Writing - Original Draft. SL has helped with the data analysis and writing of the paper. All authors contributed to the article and approved the submitted version.

Funding

This study was supported by the National Natural Science Foundation of China (No.82160815); Inner Mongolia Autonomous Region Science and Technology Project(NO.2022YFSH0061); Research Project of Affiliated Hospital of Inner Mongolia University for Nationalities(NO.KJGGJC202108)

Conflict of interest

The authors declare that the research was conducted in the absence of any commercial or financial relationships that could be construed as a potential conflict of interest.

Publisher's note

References

1. Vujosevic S, Aldington S.J, Silva P, Hernandez C, Scanlon P, Peto T, et al. Screening for diabetic retinopathy: new perspectives and challenges. *Lancet Diabetes Endocrinol* (2020) 8(4):337–47. doi: 10.1016/S2213-8587(19)30411-5

2. Cheung N, Mitchell P, Wong TY. Diabetic retinopathy. *Lancet* (2010) 376 (9735):124–36. doi: 10.1016/S0140-6736(09)62124-3

3. Teo ZL, Tham YC, Yu M, Chee ML, Rim TH, Cheung N, et al. Global prevalence of diabetic retinopathy and projection of burden through 2045: Systematic review and meta-analysis. *Ophthalmology* (2021) 128(11):1580–91. doi: 10.1016/j.ophtha.2021.04.027

4. Fong DS, Aiello LP, Ferris FL3rd, Klein R. Diabetic retinopathy. *Diabetes Care* (2004) 27(10):2540–53. doi: 10.2337/diacare.27.10.2540

5. Rodriguez ML, Perez S, Mena-Molla S, Desco MC, Ortega AL, et al. Oxidative stress and microvascular alterations in diabetic retinopathy: Future therapies. *Oxid Med Cell Longev* (2019) 2019:4940825. doi: 10.1155/2019/4940825

6. Shafabakhsh R, Aghadavod E, Mobini M, Heidari-Soureshjani R, Asemi Z. Association between microRNAs expression and signaling pathways of inflammatory markers in diabetic retinopathy. *J Cell Physiol* (2019) 234(6):7781–7. doi: 10.1002/jcp.27685

7. Semeraro F, Morescalchi F, Cancarini A, Russo A, Rezzola S, Costagliola C, et al. Diabetic retinopathy, a vascular and inflammatory disease: Therapeutic implications. *Diabetes Metab* (2019) 45(6):517–27. doi: 10.1016/j.diabet.2019.04.002

8. Rameshrad M, Razavi BM, Hosseinzadeh H. Saffron and its derivatives, crocin, crocetin and safranal: a patent review. *Expert Opin Ther Pat* (2018) 28 (2):147–65. doi: 10.1080/13543776.2017.1355909

9. Zeinali M, Zirak MR, Rezaee SA, Karimi G, Hosseinzadeh H. Immunoregulatory and anti-inflammatory properties of crocus sativus (Saffron) and its main active constituents: A review. *Iran J Basic Med Sci* (2019) 22(4):334–44. doi: 1022038/ijbms2019343658158

10. Qin X, Sun YY, Lu ZJ, Zhang TZ, Li SS, Hua T, et al. Inhibitory effects of safranal on laser-induced choroidal neovascularization and human choroidal microvascular endothelial cells and related pathways analyzed with transcriptome sequencing. *Int J Ophthalmol* (2021) 14(7):981–9. doi: 1018240/ijo20210704

11. Yang X, Huo F, Liu B, Liu J, Chen T, Li J, et al. Crocin inhibits oxidative stress and pro-inflammatory response of microglial cells associated with diabetic retinopathy through the activation of PI3K/Akt signaling pathway. *J Mol Neurosci* (2017) 61(4):581–9. doi: 10.1007/s12031-017-0899-8

12. Sepahi S, Mohajeri SA, Hosseini SM, Khodaverdi E, Shoeibi N, Namdari M, et al. Effects of crocin on diabetic maculopathy: A placebo-controlled randomized clinical trial. *Am J Ophthalmol* (2018) 190:89–98. doi: 10.1016/j.ajo.2018.03.007

13. Zhao M, Bai Y, Xie W, Shi X, Li F, Yang F, et al. Interleukin-1beta level is increased in vitreous of patients with neovascular age-related macular degeneration (nAMD) and polypoidal choroidal vasculopathy (PCV). *PloS One* (2015) 10(5): e0125150. doi: 101371/journalpone0125150

14. Wu K, Yuan LH, Xia W. Inhibitory effects of apigenin on the growth of gastric carcinoma SGC-7901 cells. *World J Gastroenterol* (2005) 11(29):4461–4. doi: 10.3748/wjg.v11.i29.4461

15. Wang F, Bai Y, Yu W, Han N, Huang L, Zhao M, et al. Anti-angiogenic effect of KH902 on retinal neovascularization. *Graefes Arch Clin Exp Ophthalmol* (2013) 251(9):2131–9. doi: 10.1007/s00417-013-2392-6

16. Zhu X, Bai Y, Yu W, Pan C, Jin E, Song D, et al. The effects of pleiotrophin in proliferative diabetic retinopathy. *PloS One* (2015) 10(1):e0115523. doi: 10.1371/journal.pone.0115523

17. Aggarwal A, Yuan Z, Barletta JA, Lorch JH, Nehs MA. Ketogenic diet combined with antioxidant n-acetylcysteine inhibits tumor growth in a mouse model of anaplastic thyroid cancer. *Surgery* (2020) 167(1):87–93. doi: 10.1016/j.surg.2019.06.042

18. Alavi MS, Fanoudi S, Fard AV, Soukhtanloo M, Hosseini M, Barzegar H, et al. Safranal attenuates excitotoxin-induced oxidative OLN-93 cells injury. *Drug Res (Stuttg)* (2019) 69(6):323–9. doi: 10.1055/a-0790-8200

19. Sun Y, Liu YX. LncRNA HOTTIP improves diabetic retinopathy by regulating the p38-MAPK pathway. *Eur Rev Med Pharmacol Sci* (2018) 22 (10):2941–8. doi: 1026355/eurrev_201809_15904

20. Bailey KA, Moreno E, Haj FG, Simon SI, Passerini AG. Mechanoregulation of p38 activity enhances endoplasmic reticulum stress-mediated inflammation by arterial endothelium. *FASEB J* (2019) 33(11):12888–99. doi: 10.1096/fj.201900236R

21. Ekberg NR, Eliasson S, Li YW, Zheng X, Chatzidionysiou K, Falhammar H, et al. Protective effect of the HIF-1A Pro582Ser polymorphism on severe diabetic retinopathy. *J Diabetes Res* (2019) 2019:2936962. doi: 10.1155/2019/2936962

22. Huang C, Zhu HJ, Li H, Li QX, Li FM, Cheng L. p38-MAPK pathway is activated in retinopathy of microvascular disease of STZ-induced diabetic rat model. *Eur Rev Med Pharmacol Sci* (2018) 22(18):5789–96. doi: 1026355/eurrev_201805_15048

23. Xie H, Zhang C, Liu D, Yang Q, Tang L, Wang T, et al. Erythropoietin protects the inner blood-retinal barrier by inhibiting microglia phagocytosis *via* Src/Akt/cofilin signalling in experimental diabetic retinopathy. *Diabetologia* (2021) 64(1):211–25. doi: 10.1007/s00125-020-05299-x

24. Wang N, Zhang C, Xu Y, Tan HY, Chen H, Feng Y, et al. Berberine improves insulin-induced diabetic retinopathy through exclusively suppressing Akt/mTOR-mediated HIF-1alpha/VEGF activation in retina endothelial cells. *Int J Biol Sci* (2021) 17(15):4316–26. doi: 10.7150/ijbs.62868

25. Navaratna D, McGuire PG, Menicucci G, Das A. Proteolytic degradation of VE-cadherin alters the blood-retinal barrier in diabetes. *Diabetes* (2007) 56 (9):2380–7. doi: 10.2337/db06-1694

26. Liu D, Xu H, Zhang C, Xie H, Yang Q, Li W, et al. Erythropoietin maintains VE-cadherin expression and barrier function in experimental diabetic retinopathy *via* inhibiting VEGF/VEGFR2/Src signaling pathway. *Life Sci* (2020) 259:118273. doi: 10.1016/j.lfs.2020.118273

Frontiers in Endocrinology

Explores the endocrine system to find new therapies for key health issues

The second most-cited endocrinology and metabolism journal, which advances our understanding of the endocrine system. It uncovers new therapies for prevalent health issues such as obesity, diabetes, reproduction, and aging.

Discover the latest Research Topics

See more →

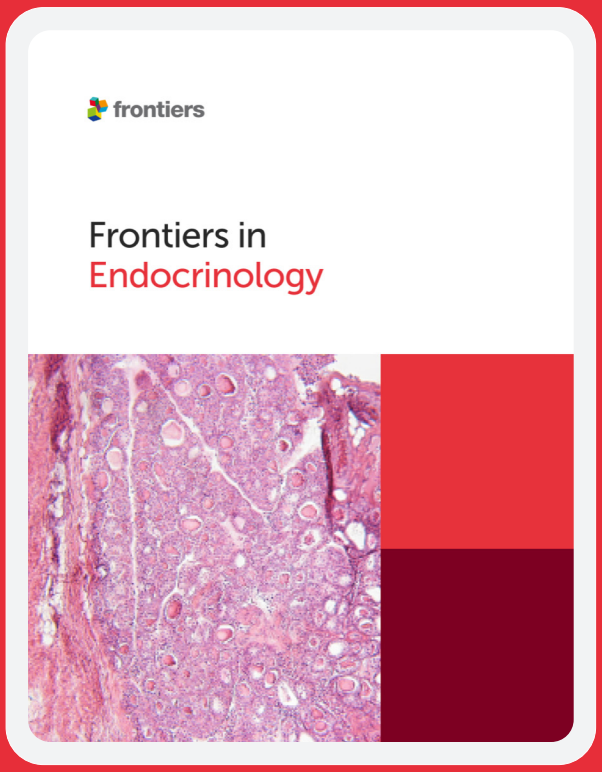

Frontiers

Avenue du Tribunal-Fédéral 34
1005 Lausanne, Switzerland
frontiersin.org

Contact us

+41 (0)21 510 17 00
frontiersin.org/about/contact